Dipl.-Ing. Thomas Gruber BSc

CFD-based modeling approaches for high-temperature corrosion in biomass fired boilers

DOCTORAL THESIS

to achieve the university degree of

Doktor der technischen Wissenschaften

submitted to

Graz University of Technology

Supervisor

Dipl.-Ing. Dr.techn. Univ.-Doz. Prof., Ingwald Obernberger

Institute of Process and Particle Engineering

Graz, December 2015

AFFIDAVIT

I declare that I have authored this thesis independently, that I have not used other than the declared sources/resources, and that I have explicitly marked all material which has been quoted either literally or by content from the sources used. The text document uploaded to TUGRAZonline is identical to the present doctoral thesis.

December, 2015
Date


Signature

Acknowledgement

At the very beginning of this work a want to take the chance to thank several people without their professional as well as emotional help I wouldn't have been able to prepare the work presented. I would like to express my sincere gratitude to all of them.

First I want to thank all colleagues at BIOENENERGY 2020+ for their support in the past years. At this point I want to address a special thanks to Stefan Retschitzegger for his never-ceasing support throughout all upcoming questions, problems and serious throwbacks. Further, I want to thank Kai Schulze and Robert Scharler for their support, the enjoyable working atmosphere as well as the opportunity to incorporate own ideas into the project. Further, I want to thank Prof. Ingwald Obernberger for his guidance, fruitful discussions and helpful remarks be it regarding representative combustion conditions for the test runs or relevant literature.

In addition I want to thank Prof. Ferdinand Haider for the hours of exited discussion on all relevant aspects of high-temperature corrosion. Also the helpful input of Prof. Wolfgang Sprengel on the oxidation of metals shall be highlighted.

Thanks to Angelika Reichmann for carrying out the SEM/EDX analyses presented in this work as well as for her support during the interpretation of the data.

A special thank goes to my family and friends for supporting me through rough times, inspiring me to carry on, and finish the work started. Last but not least I want to thank my companion Rieke for her outstanding patience and support throughout good and bad times.

Abstract

Material corrosion of heat exchanger steel surfaces in biomass fired boilers is of major importance. Especially when firing biomass fuels with high contents of chlorine, sulphur and alkali metals (waste wood as well as agricultural fuels) but also for conventional wood fuels (wood chips, bark) with respect to increasing the steam parameters and thus the efficiency of future biomass combined heat and power plants. Presently, due to the high complexity of the underlying processes no simulation tools sufficiently describing high-temperature corrosion in biomass fired boilers in dependence on the influencing parameters are available.

Therefore, the main goal of the work presented was the development of two basic models for the prediction of the local high-temperature corrosion potential of the common boiler steel 13CrMo4-5 in woody biomass fired boilers in dependence of the most relevant influencing parameters. The models developed are designed to be used together with computational fluid dynamic simulations of flue gas flow and heat transfer. To gain input data for the model development two online corrosion probe two test runs have been carried out in a specially designed biomass fired drop tube reactor. To investigate the influence of different fuel compositions chemically untreated wood chips and waste wood A1-A2 (according to German standards), have been used as fuels in these test runs. Firstly, an empirical model was developed based on the experimental data gained. This rather simple model only needs input data from the flow and heat transfer simulations. Additional test runs had to be carried out, using a newly developed mass loss probe, to gain information regarding the dominating corrosion mechanism. Based on these test runs a more sophisticated computational fluid dynamics based model, the so-called detailed model, was developed, which considers transport processes and chemical reactions between the steel surface, surrounding deposit layer and gas phase for the most relevant high-temperature corrosion processes in woody biomass fired combustion plants. For this purpose the detailed model had to be coupled with a deposit formation model, which provides necessary information regarding the local deposits formed.

After validating the models, using the experimental data gained in the test runs, they have been applied for the simulation of the local high-temperature corrosion potential of selected woody biomass fired boilers. The models are well applicable to investigate the influence of different live steam temperatures, plant geometries or interconnections of the superheater tube bundles on the high-temperature corrosion potential. The empirical model is especially well suited to quickly estimate if high-temperature corrosion is of relevance for a certain plant. However, the application of the model is strictly limited to comparable flue gas, and therefore also fuel compositions as in the test runs and the usage of a low alloy steel like 13CrMo4-5. Furthermore, the model does not provide any information regarding the local corrosion mechanism prevailing. The detailed model on the other hand gives important information regarding the dominating corrosion mechanism. It could be shown that the oxidation of the steel, active Cl-induced oxidation and hot corrosion are the most relevant mechanisms for woody biomass fuels in the temperature range investigated. Since the dominating mechanism may vary locally, depending on the aggregate state as well as the chemical composition of the ash deposits, this additional information of the detailed model is of special interest. However the detailed model has the drawback that it is computationally expensive. Concluding, both models are well applicable to estimate the local high-temperature corrosion in biomass fired boilers and hence, represent helpful tools for plant manufactures and engineers.

Kurzfassung

Die Hochtemperatur-Korrosion von Überhitzerstahl in mit Biomasse befeuerten Kesseln stellt ein weitverbreitetes Problem dar. Besonders betroffen von korrosionsbedingten Problemen sind dabei Anlagen, welche Brennstoffe reich an Chlor, Schwefel oder Alkalimetallen (z.B. Altholz, landwirtschaftliche Restbrennstoffe, halmgutartige Brennstoffe) verbrennen. Darüber hinaus weisen auch Anlagen, welche konventionelle holzartige Brennstoffe (z.B. Hackschnitzel, Rinde) verfeuern ein hohes Korrosionsrisiko auf, wenn sie mit hohen Dampfparametern betrieben werden, um so den Wirkungsgrad zu steigern. Aufgrund der Komplexität der zugrundeliegenden Prozesse gibt es zurzeit noch kein zuverlässiges Simulationswerkzeug, um Hochtemperaturkorrosion in mit Biomasse befeuerten Kesseln in Abhängigkeit der wichtigsten Einflussgrößen zu bewerten.

Aus diesem Grund stellt das Hauptziel der vorliegenden Arbeit die Entwicklung zweier Modellierungsansätze dar, um das lokale Hochtemperatur-Korrosionspotential des verbreiteten Kesselstahls 13CrMo4-5, in mit holzartiger Biomasse befeuerten Kesseln bewerten zu können. Dabei sollten die beiden Modellansätze zusammen mit CFD-basierten Strömungs- und Wärmeübergangssimulation verwendet werden können.

Die hierfür nötigen Basisdaten stammen aus Online-Korrosionssondentestläufen, welche in einem speziell entwickelten mit Biomasse befeuerten Fallrohr-Reaktor (DropTube) durchgeführt wurden. Dabei wurden die beiden Brennstoffe Waldhackgut, sowie Altholz der Klasse A1-A2 (nach Deutschem-Standard) verwendet, um den Einfluss von unterschiedlichen Brennstoffen auf das Korrosionsverhalten zu untersuchen.

Auf Basis dieser Messdaten wurde zuerst ein empirisches Korrosionsmodell entwickelt. Dieses erlaubt die Berechnung eines lokalen Hochtemperatur-Korrosionspotentials anhand der Einflussgrößen: Stahltemperatur, Rauchgastemperatur und -geschwindigkeit. Um Aufschluss über den dominierenden Korrosionsmechanismus im stationären Betrieb zu erlangen, wurden weitere Testläufe mit einer neuen Masseverlustsonde durchgeführt. Darauf basierend wurde das sogenannte detaillierte Modell entwickelt, welches auch Transportprozesse und chemische Reaktionen zwischen der Stahloberfläche, der umgebenden Depositionsschicht und der Gasphase berücksichtigt. Zu diesem Zweck wurde das detaillierte Modell mit einem bereits verfügbaren Depositions-Modell gekoppelt, welches die nötigen Randbedingungen für die Simulation liefert.

Nach Validierung der Modelle, mit Hilfe der experimentellen Daten aus den Testläufen, wurde mit ihrer Hilfe das lokale Hochtemperatur-Korrosionspotential ausgewählter mit Biomasse befeuerter Dampfkesseln berechnet. Dabei erwiesen sich die entwickelten Modelle als nützliche Werkzeuge um den Einfluss von geänderten Dampftemperaturen, Kessel-Geometrien oder Verschaltungen der Überhitzerbündel, auf das Hochtemperatur-Korrosionspotential zu bewerten. Das empirische Modell eignet sich besonders für eine schnelle Erstbewertung, ob für einen Kessel unter bestimmten Betriebsparametern ein Risiko für Hochtemperatur-Korrosion besteht. Dabei unterliegt das empirische Modell gewissen Anwendungseinschränkungen. So kann es zum Beispiel nur für vergleichbare Brennstoff- sowie Rauchgaszusammensetzungen wie sie in den Testläufen vorherrschten, sowie den dabei verwendeten Überhitzerstahl 13CrMo4-5 verwendet werden. Des Weiteren liefert es keine Informationen bezüglich des lokalen Korrosionsmechanismus.

Das detaillierte Modell hingegen unterliegt nicht der strikten Beschränkung von vergleichbaren Rauchgas- und Brennstoffzusammensetzungen wie in den Testläufen und liefert darüber hinaus noch relevante Informationen bezüglich des lokal vorherrschenden Korrosionsmechanismus. Hierbei stellen die Oxidation des Stahles, aktive Cl-induzierte Korrosion, sowie Korrosion durch Ascheschmelzen die relevantesten Korrosions-mechanismen für holzartige Biomasse, im untersuchten Temperaturbereich, dar. Das detaillierte Modell hat allerdings den Nachteil, dass es sehr rechen- und somit zeitintensiv ist. Zusammenfassend sind beide Modellierungsansätze dazu geeignet um das lokale Hochtemperatur-Korrosionspotential in mit Biomasse befeuerten Kesseln, innerhalb ihrer Anwendungsgrenzen, zu bewerten. Sie stellen somit nützliche Werkzeuge für Kesselhersteller dar, um das Hochtemperatur-Korrosionsrisiko bereits in der Planungsphase eines Kessels bewerten zu können.

CFD-based modeling approaches for high-temperature corrosion in biomass fired boilers

Thomas Gruber

Institute of Process and Particle Engineering
Graz University of Technology
Inffeldgasse 21b, A 8010 Graz

This thesis is based on the following appended papers, in the text referred to by their Roman numerals I-III:

I **Investigation of the corrosion behaviour of 13CrMo4–5 for biomass fired boilers with coupled online corrosion and deposit probe measurements**

T. Gruber, K. Schulze, R. Scharler, I. Obernberger
Fuel 2015;144:15-24

II **Application of an empirical model in CFD simulations to predict the local high temperature corrosion potential in biomass fired boilers**

T. Gruber, R. Scharler, I. Obernberger
Biomass & Bioenergy 2015; 79:145:154

III **Dominating high temperature corrosion mechanisms in low alloy steels in wood chips fired boilers**

T. Gruber, S. Retschitzegger, R. Scharler, I. Obernberger
Submitted to Energy & Fuels, Oct. 2015

Author's contribution

Paper I
The author performed the online corrosion test runs as well as the deposit probe measurements. Further the author developed and validated the empirical high-temperature corrosion model. The author performed the data post-processing and was responsible for preparation of the manuscript.

Paper II
The author performed the CFD simulations as well as the application of the empirical high-temperature corrosion model. The author made the simulation post-processing and was responsible for preparation of the manuscript.

Paper III
The author performed the literature survey as well as the mass loss probe test runs. The author performed the data post-processing and was responsible for preparation of the manuscript.

Additional publication of relevance although not included in the thesis:

Papers in peer reviewed journals

S. Retschitzegger, T. Gruber, T. Brunner, I. Obernberger. Short term online corrosion measurements in biomass fired boilers. Part 1: Application of a newly developed mass loss probe. Fuel Processing Technology 2015; 137:148-156.

S. Retschitzegger, T. Gruber, T. Brunner, I. Obernberger. Short term online corrosion measurements in biomass fired boilers. Part 2: Investigation of the corrosion behavior of three selected superheater steels for two biomass fuels. Fuel Processing Technology 2016; 142:59-70.

Content

1 Introduction and objectives ---------- 1

2 Theoretical background on high-temperature corrosion ---------- 4

2.1 High-temperature corrosion rate laws ---------- 4
2.1.1 Linear rate law ---------- 5
2.1.2 Parabolic rate law ---------- 5
2.1.3 Paralinear rate law ---------- 6

2.2 High-temperature corrosion mechanisms ---------- 6
2.2.1 Oxidation of metals ---------- 7
2.2.2 Active Cl-induced oxidation ---------- 8
2.2.3 Molten salt corrosion ---------- 10

2.3 Influencing factors ---------- 11

2.4 Existing model ---------- 12

3 Methodology ---------- 14

3.1 Experimental section ---------- 14
3.1.1 Steel 13CrMo4-5 ---------- 14
3.1.2 Drop Tube reactor ---------- 14
3.1.3 Online corrosion probe measurements ---------- 16
3.1.4 Mass loss probe measurements ---------- 17
3.1.5 Deposit probe measurements ---------- 17
3.1.6 Biomass fuel and ash analyses ---------- 18
3.1.7 HCl/SO_x measurements ---------- 18
3.1.8 SEM/EDX analyses and sample preparation ---------- 19

3.2 Basic CFD models applied ---------- 20
3.2.1 Empirical packed bed model ---------- 20
3.2.2 Heat exchanger model ---------- 21
3.2.3 Deposit formation model ---------- 22

4 Empirical model ---------- 27

4.1 Online corrosion probe test runs ---------- 27
4.1.1 Test run and operating conditions ---------- 27
4.1.2 Fuel ---------- 30
4.1.3 Deposit formation ---------- 31
4.1.4 SEM/EDX analyses ---------- 34

4.2 Corrosion rates measured and empirical model development ---------- 37

4.3 Possible high-temperature corrosion mechanisms ---------- 42

4.4 Application range of the empirical model ---------- 44

4.5 Application of the model in a combined heat and power plant ---------- 45
4.5.1 Description of the case study ---------- 46
4.5.2 Results of the flow and heat transfer ---------- 48

4.5.3 Results of the empirical high-temperature corrosion model ---- 52

4.6 Summary and recommendations ---- 54

5 Detailed model ---- 57

5.1 Mass loss probe test runs ---- 57
5.1.1 Test run and operating conditions ---- 58
5.1.1 Fuel ---- 60
5.1.2 Mass loss over time ---- 61
5.1.3 Deposit formation ---- 61
5.1.4 SEM/EDX analyses ---- 63

5.2 Corrosion mechanism and model development ---- 65
5.2.1 Oxidation of the steel 13CrMo4-5 in air environment ---- 65
5.2.2 Influence of corrosive gases (HCl, SO_x) ---- 67
5.2.3 Influence of water vapor on high-temperature corrosion ---- 68
5.2.4 Influence of KCl on high-temperature corrosion ---- 69
5.2.5 Overall corrosion mechanism and detailed high-temperature corrosion model ---- 70

5.3 Implementation of the detailed corrosion model in the coupled heat exchanger/deposit formation model ---- 74

5.4 Comparison of selected results from the detailed high-temperature corrosion model with experimental data 78

5.5 Application of the model ---- 83
5.5.1 Description of the case study ---- 83
5.5.2 Simulation results ---- 85

5.6 Summary and recommendations ---- 90

6 Overall summary and conclusions ---- 93

7 Outlook ---- 97

Bibliography ---- 98

8 ANNEX ---- 109

8.1 Boundary Conditions of the CFD case studies ---- 109
8.1.1 Case study 1: Application of the empirical high-temperature corrosion model (see Section 4.5) ---- 109
8.1.2 Case study 2: Test case to demonstrate the detailed corrosion model (see Section 5.3) ---- 113
8.1.3 Case study 3: Simulation of the drop tube reactor (see Section 5.4) ---- 115
8.1.4 Case study 4: Application of the detailed model (see Section 5.5) ---- 120

8.2 Scientific journal papers ---- 123

List of Figures

Figure 2.1: Schematic figure of the oxidation of iron for temperatures higher than 570 °C. Below this temperature the formation of wustit is disabled [39]. *8*

Figure 2.2: Mechanisms of chloride sulphation in deposits as well as the subsequent active Cl-induced oxidation on boiler tubes (adapted from [48]) *10*

Figure 3.1: Schematic view of the combined packed bed/drop tube reactor with relevant units and measurement ports (adapted from [Paper I]). *15*

Figure 3.2: Schematic view of the corrosion probe (left) and the sensor probe head (right) with the electrodes (1–3) and the mass loss ring (M) [69] *16*

Figure 3.3: Scheme of the deposit probe [31] *18*

Figure 3.4: Schematic illustration of the models used within this work and their interactions. *26*

Figure 4.1: Results of the EDX-analysis of the deposits formed during the deposit probe measurements for forest wood chips (left) and waste wood (right) [Paper I] *32*

Figure 4.2: Photo of the corrosion probes after the forest wood chips test run (left) and after the waste wood test run (right) [Paper I]. *33*

Figure 4.3: Chemical composition of the deposits found on the corrosion probes after the test runs [Paper I]. *34*

Figure 4.4: SEM/EDX element mappings through the cross section of a corrosion probe ring on the windward side. Results for forest wood chips are shown left and for waste wood right [Paper I]. *35*

Figure 4.5: SEM/EDX element mappings through the cross section of a corrosion probe ring on the windward + 50° side. Results for forest wood chips are shown left and for waste wood right. *35*

Figure 4.6: SEM/EDX element mappings through the cross section of a corrosion probe ring on the leeward side. Results for forest wood chips are shown left and for waste wood right. *36*

Figure 4.7: SEM image of the deposit layer and corrosion products of the wood chips corrosion probe test ring (left) and quantitative results of the EDX analysis of different zones (right). *36*

Figure 4.8: Two examples of measured corrosion rates over a testing day (wood chips test run). *37*

Figure 4.9: Two examples of measured corrosion rates over a testing day (waste wood test run). *38*

Figure 4.10: Example of a time curve of the measured corrosion rate and flue gas velocity for waste wood [Paper I]. *39*

Figure 4.11: Empirical model in comparison to measurement values for forest wood chips (left) and for waste wood (right) as a function of flue gas temperature [Paper I]. *40*

Figure 4.12: Empirical model in comparison to measurement values for forest wood chips (left) and for waste wood (right) as a function of steel temperature [Paper I]. *41*

Figure 4.13: Empirical model in comparison to measurement values for forest wood chips (left) and for waste wood (right) as a function of flue gas temperature for various flue gas velocities [Paper I]. *41*

Figure 4.14: Two examples of measured corrosion rates in comparison with the calculated corrosion rate over a testing day (wood chips test run). *42*

Figure 4.15: Two examples of measured corrosion rates in comparison with the calculated corrosion rate over a testing day (waste wood test run)..... *42*

Figure 4.16: Schematic view of the simulated CHP plant..... *47*

Figure 4.17: Streamlines of the flue gas colored by the temperature (°C) (left) and profiles of flue gas velocity (m/s) (right) in the symmetry plane of the simulated plant (case CS1) (Figure adapted from [Paper II]) *49*

Figure 4.18: Profiles of the assumed steam temperatures (°C) (left) and the calculated total heat transfer coefficients on the flue gas side (W/m²K) (right) in the symmetry plane of the simulated plant (case CS1) (Figure adapted from [Paper II])..... *49*

Figure 4.19: Steel temperature (°C) of the heat exchangers in the symmetry plane of the simulated plant (case CS1) (Figure adapted from [Paper II]) *50*

Figure 4.20: Calculated local corrosion potential (mm/1000h) of SH3 in the symmetry plane of the simulated plant under full load conditions (CS1) for wood chips [Paper II] (left) and waste wood (right)..... *53*

Figure 4.21: Calculated local corrosion potential (mm/1000h) of SH3 in the symmetry plane of the simulated plant for a changed flow in the final superheater (CS2) for wood chips [Paper II] (left) and waste wood (right)..... *53*

Figure 4.22: Calculated local corrosion potential (mm/1000h) of SH3 in the symmetry plane of the simulated plant for enhanced steam temperatures (from 453 °C to 480 °C) (CS3) for wood chips [Paper II] (left) and waste wood (right)..... *54*

Figure 5.1: Mass loss for various test runs as a function of time [Paper III]. *61*

Figure 5.2: Photos of the MLP after the test runs [Paper III] *62*

Figure 5.3: EDX elemental mappings of the deposit and corrosion layer on the windward side of the MLP sample rings for the test runs: Retschitzegger et al. (left), gas burner (middle) and wood chips at elevated temperatures and velocities (right) [Paper III]. *63*

Figure 5.4: EDX elemental mappings of the deposit and corrosion layer on the leeward side of the MLP sample rings for the test runs: Retschitzegger et al. (left), gas burner (middle) and wood chips at elevated temperatures and velocities (right). *64*

Figure 5.5: O_2 activities at the Fe_3O_4 oxide interfaces as a function of temperature. *66*

Figure 5.6: Arrhenius plot of $k_{p,Cl}$ as a function of the reciprocal mean deposit temperature. *72*

Figure 5.7: Exemplary results of the coupled heat exchanger/deposit formation/detailed corrosion potential model. The figure shows the most relevant parameters (A: flue gas temperature (°C); B: steel temperature (°C); C: mass of ash deposition (kg/m²); D: mass of Cl deposition (kg/m²); E: mass fraction of chlorine (kg/kg); F: liquid salt fraction (wt-%)) as well as the results of the detailed corrosion potential model (G: local corrosion mechanism; H: calculated parabolic rate constant of active Cl-induced oxidation (cm²/s); I: calculated parabolic rate constant of oxidation (cm²/s)J: calculated overall parabolic rate constant (cm²/s)). *77*

Figure 5.8: Scheme of the drop tube simulation including relevant CFD simulation input parameter *79*

Figure 5.9: Results of the CFD simulation. The flue gas temperature (°C) is shown in Figure a, the flue gas velocity (m/s) is presented in Figure b. *79*

Figure 5.10: Comparison of elemental composition found within the deposit probe measurements and the CFD simulations *80*

Figure 5.11: Calculated steel surface temperature (°C) on the flue gas side of the probe rings (Figure a) and calculated surface temperature of the deposit layer (°C) on the flue gas side of the probe rings (Figure b) *81*

Figure 5.12: Calculated deposition rate of chlorine (kg/m²s) (Figure a) and calculated overall deposition rate of the ash forming vapours and ash fine particles (kg/m²s) *81*

Figure 5.13: Calculated liquid salt fraction (kg/kg) (Figure a) and calculated overall parabolic rate constant $k_{p,overall}$ (cm²/s) (Figure b) *82*

Figure 5.14: Calculated parabolic rate constants for the pure oxidation (cm²/s) (Figure a) and for the active Cl-induced oxidation (cm²/s) (Figure b) *82*

Figure 5.16: Schematic view of the simulated CHP plant *84*

Figure 5.17: a.) Flue gas velocity (m/s) and b.) flue gas temperature (°C) in the symmetry plane of the simulated plant. 86

Figure 5.18: a.) Steel temperature on the boundary steel/deposit (fouling layer) (°C) and b.) surface temperature at the boundary deposit (fouling) / flue gas (°C) in the symmetry plane of the simulated plant 87

Figure 5.19: a.) Chlorine deposition rate (kg/m²s) and b.) liquid fraction of the deposit (kg/kg) on the superheater tube bundles depicted in the symmetry plane of the simulated plant..... 87

Figure 5.20: a.) Corrosion mechanism prevailing and b.) overall parabolic rate constant $k_{p,overall}$ *(cm²/s) in the symmetry plane of the simulated plant..... 88*

Figure 5.21: a.) Oxidation related part of the overall parabolic rate constant $k_{p,oxide}$ *(cm²/s) and b.) active Cl-induced oxidation related part of the overall parabolic rate constant* $k_{p,Cl}$ *(cm²/s) in the symmetry plane of the simulated plant..... 89*

Figure 5.22: Comparison of the mass loss calculated after 1000h (mm) with the detailed model (left) and with the empirical model (right). 90

Figure 8.1: Schematic view of the simulated CHP plant..... 109

Figure 8.2: Scheme of the test case..... 113

Figure 8.3: Scheme of the biomass fired drop tube reactor..... 115

Figure 8.4: Flue gas velocity profile over the length of the biomass furnace grate..... 117

Figure 8.5: Flue gas temperature profile over the length of the biomass furnace grate..... 118

Figure 8.6: Profile of major flue gas species over the length of the biomass furnace grate 118

Figure 8.7: Detailed view of the simulated corrosion probe 119

Figure 8.8: Scheme of the simulated plant..... 120

List of Tables

Table 3.1: Composition of 13CrMo4-5 (1.7335) *14*

Table 4.1: Combustion conditions during the corrosion probe measurements *29*

Table 4.2: Results of fuel analyses *31*

Table 4.3: Optimized coefficients of the empirical function [Paper I] *40*

Table 4.4: Relevant boiler information (Table adapted from [Paper II]) *46*

Table 4.5: Relevant boundary conditions for the superheater tubes (Table adapted from [Paper II]) *46*

Table 4.6: Comparison of the transferred heat by convection and the pressure loss according to the CFD simulations and the calculations based on [78] (heat transfer) and [80] (pressure loss) for SH1 (Table adapted from [Paper II]) *51*

Table 4.7: Comparison of the transferred heat by convection and the pressure loss according to the CFD simulations and the calculations based on [78] (heat transfer) and [80] (pressure loss) for SH2 (Table adapted from [Paper II]) *51*

Table 4.8: Comparison of the transferred heat by convection and the pressure loss according to the CFD simulations and the calculations based on [78] (heat transfer) and [80] (pressure loss) for SH3 (Table adapted from [Paper II]) *51*

Table 4.9: Maximum values of the calculated corrosion potential for superheater 3 ..... *52*

Table 5.1: Relevant operating conditions of the drop tube reactor and the mass loss probe *59*

Table 5.2: Results of fuel analyses [Paper III] *60*

Table 5.3: Basic data for model development as well as the empirical determined coefficients and their values *73*

Table 5.4: Logical scheme used for the determination of the dominating local corrosion mechanism *75*

Table 5.5: Release rates of the ash forming elements *79*

Table 5.6: Relevant boiler information *83*

Table 5.7: Relevant boundary conditions for the superheater tubes *84*

Table 8.1: Boundary conditions for finned walls *110*

Table 8.2: Boundary conditions at the simulation inlet *110*

Table 8.3: Boundary conditions for the superheater tubes CS1 ..... *110*

Table 8.4: Boundary conditions for the superheater tubes CS2 ..... *111*

Table 8.5: Boundary conditions for the superheater tubes CS3 ..... *112*

Table 8.6: Boundary conditions at the simulation inlet *114*

Table 8.7: Boundary conditions for the heat exchanger *114*

Table 8.8: Summary of the different CFD calculations performed *116*

Table 8.9: Boundary conditions at the different simulation inlets *117*

Table 8.10: Boundary conditions at corrosion probe *119*

Table 8.11: Boundary conditions at the simulation inlet *121*

Table 8.12: Boundary conditions for finned tube walls *122*

Table 8.13: Boundary conditions for the superheater tubes *122*

Nomenclature

Abbreviations

MSWI	municipal solid waste incinerators
CHP	combined heat and power
CFD	computational fluid dynamics
MLP	mass loss probe
SEM	scanning electron microscopy
EDX	energy dispersive X-ray
wt-%	weight percentage
vol-%	volume percentage
at-%	atomic percentage
d.b.	dry basis
w.b.	wet basis
RBU	build-up rate
CS	case study
SH	super heater
ET	evaporator tube
HTC	High-Temperature Corrosion

Symbol	**Unit**	**Description**
$\dot{N}_{cond}$	(mol/m²s)	condensation flux per area
β	(m/s)	mass transfer coefficient
c_{∞}	(mol/m³)	species concentration in the flue gas
c_{w}	(mol/m³)	saturation concentration of the species on the wall
α	(J/m²s)	heat transfer coefficient

c_p	(J/kgK)	heat capacity
ρ	(kg/m³)	density of the flue gas
v_{th}	(m/s)	thermophoretic diffusion velocity
v_{gas}	(m/s)	velocity of the fine particle in the flue gas
K_{th}	(-)	thermophoretic coefficient
T_p	(K)	temperature of the particle
∇T_{gas}	(K)	local temperature gradient prevailing in the gas phase
k	(mm/1000h)	corrosion rate
$A(T_S)$	(mm/1000h)	pre-exponential factor (empirical model)
$B(T_S)$	(J/mol)	activation energy (empirical model)
T_{FG}	(K)	flue gas temperature
T_S	(K)	steel temperature
v_{FG}	(m/s)	flue gas velocity
R	(J/molK)	gas constant
$C(v_{FG})$		linear correction factor (empirical model)
a_{1-3}, b_{1-3}, c_{1-2}		dimensionless coefficients (empirical model)
X	(cm)	oxide thickness
k_p	(cm²/s)	parabolic rate constant
t	(s)	time
$a(O_2)$		oxygen activity at the oxide interfaces
α		ratio between oxygen and metal in the oxide (MeO_α)
f_M, f_O		dimensionless correlation factors
D*(M)	(cm²/s)	metal tracer diffusion coefficient

$D^*(O)$	(cm^2/s)	oxygen tracer diffusion coefficient
$k_{p,overall}$	(cm^2/s)	overall parabolic rate constant
$k_{p,Cl}$	(cm^2/s)	part of $k_{p,overall}$ related to active Cl-induced oxidation
$k_{p,oxide}$	(cm^2/s)	part of $k_{p,overall}$ related to oxidation
ω_{Cl}	(kg/kg)	mass fraction of Cl in the deposit
$k_{0,Cl}$	(cm^2/s)	pre-exponential coefficient (detailed model)
E_{act}	(J/mol)	activation energy (J/mol)
$\bar{T}_D$	(K)	mean deposit temperature

1 Introduction and objectives

The worldwide increasing demand for energy in combination with climate related issues caused by fossil energy sources necessitates to increase the share of renewable energy sources. Thereby, the energy production from biomass fuels is indispensable besides other sources of renewable energy e.g. wind, water or sunlight.

However, ash related problems strongly influence the operation of biomass combustion plants and often result in unscheduled shut-downs and reduced economic efficiencies. Among the reduced heat transfer in the boiler section by deposit layers on the heat exchanger surfaces, also material corrosion of steel surfaces in the hot furnace, of radiative boiler walls and of convective heat exchanger tube bundles (superheaters) is of major importance. Especially the corrosion of superheaters (SH) known as high-temperature corrosion becomes important when firing biomass with a high content of chlorine, alkali metals or heavy metals, such as herbaceous fuels (e.g. straw or Miscanthus) [1], [2], [3], [4], [5], [6], [7], [8], [9], [10], [11], agricultural fuels [12] or waste wood [13], [14], [15], [16]. Furthermore, high-temperature corrosion becomes relevant for future highly efficient combined heat and power (CHP) plants, operated with enhanced steam parameters [17], even if they are fired with woody fuels.

Therefore, a lot of research has been carried out in the last decades to identify and quantify relevant influencing parameters on high-temperature corrosion occurring in plants firing biomass rich in chlorine (a good overview is given by [15], [17], [18], [19], [20]) and municipal solid waste incinerators (MSWI) (an overview can be found in [2], [20], [21], [22]). Also high-temperature corrosion in plants firing fuels with low to moderate chlorine and heavy metal contents, such as forest wood chips, bark as well as quality sorted waste wood has already been investigated (e.g. [23] and [24]).

Although a considerable amount of research has been carried out to investigate high temperature corrosion phenomena, no reliable model exists up to now to predict the local high temperature corrosion in biomass fired boilers. The absence of such a model is based on several issues. In many cases the experimental data gained in real-scale plants cannot be used for the development of a reliable corrosion model. This is caused by the fact, that it is generally not possible to vary just one parameter of interest to determine its effect on the high-temperature corrosion in biomass fired real scale plants. On the other side, considerable research has been conducted to investigate the effect of a certain species (e.g. alkali chlorides, heavy metal chlorides, sulphur oxides, etc.) or a certain parameter (e.g. flue gas or steel temperature) on high-temperature corrosion (e.g. [25], [26], [27] [28], [29]). These experiments are also not sufficient to develop a reliable model to estimate the local high-temperature corrosion potential of real-scale plants sufficiently, since they neglect important interactions of the processes involved.

The main goal of the work presented is the development of two different approaches to simulate the local high temperature corrosion of the common superheater material 13CrMo4-5 in biomass fired boilers. As already mentioned no experimental data exists so far to develop a reliable corrosion model. Therefore, online corrosion probe

measurements as well as deposit probe measurements should be performed to investigate the corrosion behaviour of the steel 13CrMo4–5 in a specially designed packed bed reactor. These test runs should serve to identify the most relevant influencing parameters and to generate reliable data for the model development.

Online corrosion probes have already been successfully applied in municipal solid waste incinerator plants [21], [22], [30] and in a biomass boiler firing forest wood chips [31]. From these measurements it is known that the most relevant parameters influencing high-temperature corrosion are the steel temperature, the flue gas temperature, the chemical compositions of the flue gas as well as the deposits, and the flue gas velocity. Although the general dependencies on those parameters obtained for the different types of fuels are comparable, some deviations exist regarding the influence of the flue gas velocity. While the measurements performed in the waste incinerators found a linear dependence on the flue gas velocity, no dependence could be found in the experiments performed in the wood chips fired boiler.

The data obtained for waste combustion environments are generally in agreement with results from material loss experiments performed in lab- and real-scale measurements [32]. However, as described earlier in general it is not possible to vary only one parameter of interest arbitrarily in a real-scale plant. Hence, the amount and range of available data regarding the variation of the parameters flue gas velocity and temperature is rather low in studies published using online corrosion probes [30], [31], [33], [34].

To avoid this issue the experimental setup used within this work enables the targeted variation of a single parameter of interest under conditions comparable to real-scale biomass fired CHP plants. Concluding, the experimental setup used enables a more detailed investigation of the influence of the single parameters of interest. Hence, the data gained in these test runs should allow the development of a clear mathematical description on these parameters.

Due to vast amount of influencing parameters, which result in different corrosion mechanisms, first of all the scope of application of the models has to be specified.

Within this work high-temperature corrosion of low alloy steels, especially the common boiler steel 13CrMo4-5, in oxidizing atmospheres in a steel temperature range between 450 °C to 550 °C should be investigated. All considerations, assumptions as well as conclusions are only valid within this defined range of application. Therefore, high-temperature corrosion phenomena occurring for example under reducing conditions, for high alloy steels as well as for temperatures below or above the range investigated, can specifically not be validated with the models developed within this work. To take the influence of different biomass fuels on the deposit formation and in further consequence on the high temperature corrosion behaviour into account two typical chemically untreated and treated woody biomasses namely, forest wood chips and waste wood A1-A2 (according to German standards) should be investigated within this work.

The models should represent approaches to model high temperature corrosion in biomass fired boiler. The goal of these approaches is not to predict actual corrosion rates, due to the high complexity of the topic. Instead, the models should enable the calculation of a so-called local corrosion potential. Hence, all results obtained with the newly developed approaches should be interpreted qualitatively.

The first and simpler approach should be an empirical model, which describes the corrosion potential in dependence of relevant influencing parameters like the flue gas temperature and surface temperature. The model should be based on the data gained within the online corrosion probe test runs.

Following, a second and more sophisticated CFD-based model should be developed. This model should consider transport processes and chemical reactions between the steel surface, surrounding deposit layer and gas phase for the most relevant high-temperature corrosion processes in biomass combustion plants. Therefore, the chemical composition and structure of the deposits as well as the corrosion products formed should be investigated carefully.

To gain the relevant input data needed, the detailed model should be linked with an existing and comprehensive CFD based deposit formation model. This deposit formation model provides the local values of e.g. flue gas temperatures and species concentrations as input values for the corrosion potential model. The coupling of the models allows for a 3D simulation of the local corrosion potential in dependence of the influencing parameters.

Finally, after a careful validation, the newly developed models should be applied to simulate the local corrosion potential of real-scale biomass fired boilers. In addition to the actual state analysis also the influences of enhanced steam temperatures as well as a change of the flow direction of the final superheater tube bundle from parallel to counter-flow on the local corrosion potential should be investigated and evaluated.

2 Theoretical background on high-temperature corrosion

High-temperature corrosion is generally denoted as chemical attack of a material, especially a metal, by gases, solid or molten salts, or molten metals, typically at temperatures above 400 °C. Thereby the corrosion process does not necessarily require a liquid electrolyte. In biomass fired plants high-temperature corrosion can be caused both by interaction with the flue gas and deposits. Thereby different types of high-temperature corrosion may be distinguished for example carburization, chlorination, nitridation, oxidation or sulphidation, depending on the corrosive agent.

The prevention and reduction of high-temperature corrosion in biomass fired furnaces and boilers is of major importance since high-temperature corrosion may significantly reduce the life-times and hence, economic efficiencies of boilers. Due to the relevance of the topic considerable research has been carried out in the last decades to identify and quantify the most influencing parameters on high-temperature corrosion. A detailed discussion of the topic can be found for example in [35], [36] or [37]. A short overview of the most important high-temperature corrosion mechanisms in biomass fired furnaces and boilers, is given in the following sections.

In general, the conditions causing high-temperature corrosion can vary significantly from plant to plant. Hence, the corrosion behaviour of each plant has to be evaluated by its own. But also within one boiler the corrosion rates as well as the dominating corrosion mechanism can vary locally as well as over time. This is because the corrosion processes depend among others on the fuel fired, the position in the plant (metal grate, superheater tubes, finned wall tubes, etc.), the local steel temperature as well as the used steel itself.

2.1 High-temperature corrosion rate laws

Basically during the chemical attack a layer made of corrosion products is formed on top of the metal. In general this layer is made of the reaction products of the metal and the corrosive agents e.g. metal oxides, metal chlorides, etc. This layer often protects the material from further damage. In further progress this can slow down the corrosion process significantly. Hence, high-temperature corrosion is in general time-dependent.

Knowledge of the rate law prevailing can give important information regarding the rate limiting process as well as the dominating corrosion mechanism. Thereby, the actual rate law strongly depends on a number of factors such as temperature, gas composition (partial pressure of corrosive agents), surface preparation- and pre-treatment of the metal, as well as the composition of the metal or alloy itself.

The knowledge of the rate equation itself is insufficient to determine the corrosion mechanism with certainty, since several mechanisms follow the same rate laws. However, knowledge of the rate equation can limit the number of possible mechanism and hence, represent an important source of information.

High-temperature corrosion processes can generally follow a linear, parabolic or paralinear rate law[1]. The different rate laws, their mathematical description and the conclusions which can be drawn from a given rate law on the corrosion mechanisms are briefly discussed in the following sections.

2.1.1 Linear rate law

A linear rate law can be formulated as

$$\frac{dx}{dt} = k_l \qquad \text{Eq. 1}$$
$$x = k_l t + C$$

Explanation: *x* …may represent the oxide layer thickness, the amount of oxygen consumed per unit area or the amount of metal transformed to oxide or such like definitions which represent the mass loss of metal or mass gain of oxide; *t* … time (arbitrary unit); k_l … linear rate constant (unit depending on definition of x and t); *C* … integration constant. However, all formulations given can easily be converted among themselves using the metal or oxide density and the metal-oxide molar ratio of the oxide layer formed.

In contrast to most other rate laws, the reaction rate is time-independent. Hence, the amount of gas or metal previously consumed has no influence on the actual corrosion rate. In the case of a linear rate law, often a surface or phase boundary process (e.g. adsorption of corrosive agents on the surface) or reaction (formation of e.g. metal oxides or metal chlorides) represent the rate limiting step. A linear rate law may also be observed if the corrosion product layer stays constant over time, due to steady state removal of e.g. oxides formed.

2.1.2 Parabolic rate law

A parabolic rate is commonly found during the oxidation of metals at high temperatures. The corresponding rate law can be expressed as

$$\frac{dx}{dt} = \frac{k_p^{'}}{x} \qquad \text{Eq. 2}$$
$$x^2 = 2k_p^{'} t + C = k_p t + C$$

Explanation: *x* … corresponds either to the thickness of the oxide layer formed or the consumed metal (in this work also called “mass loss”); k_p … parabolic rate constant; *t* … time; *C* … integration constant.

[1] For the intermediate temperature range between low and high-temperature corrosion, typically between 200 °C – 400 °C, the corrosion may also follow a logarithmic rate law. Here, the reaction is initially quite rapid, but drops off to low or negligible rates with progressing times. The corrosion mechanism and rate limiting factors in this range are still insufficiently explored and subject of present research [36].

In general, a parabolic rate law indicates that a diffusion process through a compact reaction layer or a uniform diffusion is rate limiting. In this case the high-temperature corrosion strongly depends on the diffusion coefficients of the anions and cations through the corrosion product; the concentration difference of the corrosive agents as well as the temperature prevailing. A further discussion on the topic is given in the Section 2.2.1.

2.1.3 Paralinear rate law

The linear and parabolic rate laws describe ideal processes. In contrast to these model descriptions real processes often deviate from these idealistic rate laws. This can happen because of an alteration of the rate determining process due to changes in the nature of the oxide scale or concurrently corrosion mechanisms, which follow different rate laws. Such combinations of different rate laws are commonly found during high-temperature corrosion processes in MSWI [21], [22] and can be described as follows (paralinear rate law).

$$\frac{dx}{dt} = k_l t + \frac{k_p}{x} \qquad \text{Eq. 3}$$

$$x = k_l\, t + \sqrt{k_l^2 t^2 + k_p t} + C$$

Explanation: x … corresponds either to the thickness of the oxide layer formed or the consumed metal; k_p … parabolic rate constant; k_l … linear rate constant; t … time; C … integration constant.

2.2 High-temperature corrosion mechanisms

As already mentioned, high-temperature corrosion of low alloy steels strongly depends on the gas compositions as well as the depositions formed on top of the metal. Based on these boundary conditions, the following basic corrosion mechanisms as well as combinations of these are of relevance in biomass fired boilers: oxidation of metals, active Cl-induced oxidation as well as molten salt corrosion.

In addition to the "simple" oxidation of metals, chlorine can strongly enhance high-temperature corrosion processes in particular and hence, has to be highlighted among all other corrosive species. On the one hand, chlorine containing species in the flue gas or the deposit such as Cl_2, HCl, KCl, NaCl, CaCl, ZnCl or PbCl are able to cause enhanced corrosion, a process often called active Cl-induced oxidation (see Chapter 2.2.2). On the other hand chlorine containing species may reduce the melting temperature of ash mixtures deposited on e.g. superheater tubes leading to additional high-temperature corrosion mechanisms e.g. molten salt corrosion (see Chapter 2.2.3).

Other types of high-temperature corrosion e.g. sulphidation of the steel might also influence the overall corrosion behaviour of the metal. However, these mechanisms are more common in other applications such as coal fired plants or gas turbines. Hence, insufficient research has been carried out for conditions typical for biomass fired plants so far. Nevertheless, the influence of these species on the overall high-temperature

corrosion behaviour will be discussed together with the development of the detailed model in Section 5.2.

A short summary on the most common corrosion mechanisms in biomass fired boilers is given in the following sections.

2.2.1 Oxidation of metals

Oxidation is the most common form of high-temperature corrosion in oxidizing conditions. Due to the restrictions made on the application range of the work presented, the oxidation of metals will be elucidated for the case of iron and can be expanded for iron based alloys where necessary.

From a thermodynamic point of view the formation of an iron oxide Fe_xO_y is favored if the free enthalpy of the following reaction is negative [38]:

$$\frac{2\mathrm{m}}{\mathrm{n}} Fe + O_2 = \frac{2}{\mathrm{n}} Fe_m O_n \qquad \text{Eq. 4}$$

Explanation: Fe … iron; O … oxygen, m,n stoichiometric coefficients

Generally iron and oxygen can form three different oxide scales: wustite (FeO), hematite (Fe_2O_3) and magnetite (Fe_3O_4). Below 570 °C only an inner, relatively thick layer of Fe_3O_4 followed by an outer layer of Fe_2O_3 are formed. The formation of wustite is thermodynamically limited to temperatures above 570 °C. Above this temperature, the so-called wustite point, additionally a very fast growing inner FeO layer is formed (see Figure 2.1). While magnetite generally forms a homogenous, dense scale, which protects the iron from further corrosion (resulting in a parabolic rate law), the formation of wustite barely protects the steel. The poor protection and hence, high oxidation rates are originated by the high vacancy concentration in wustite. Due to this, the cation diffusion through wustite is strongly enhanced compared to magnetite. Therefore, the wustite formation and hence, rapid scaling of iron is among other reasons responsible for the limited application range of carbon steels (application range < 500 °C) and low alloy ferritic steels, such as 13CrMO4-5 (application range < 550°C).

However, the oxidation of metals is not in any case an undesired process. For example, oxide layers made of e.g. chromium oxides enhance the corrosion resistance of high alloy steels significantly, since they represent effective diffusion barriers for anions and cations alike. However, the formation of a passivating chromium oxide layer can only be achieved in steels with a Cr content higher than 10 wt-% [40]. Due to the fact, that the work focuses on the high-temperature corrosion of low alloy steels, with a Cr content up to 1 wt-%, the formation of such a layer and the effect on the corrosion behavior will not be discussed any further.

A more detailed discussion on the oxidation of iron as well as on modelling concepts can be found in Section 5.2.1. Further literature on the oxidation of metals can be found in [35], [37], [38], [41].

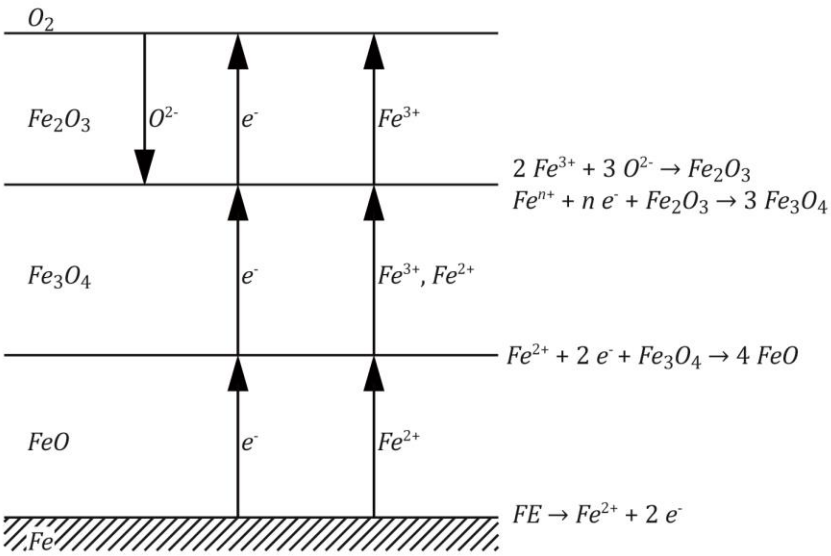

Figure 2.1: Schematic figure of the oxidation of iron for temperatures higher than 570 °C. Below this temperature the formation of wustit is disabled [39].

2.2.2 Active Cl-induced oxidation

During the combustion of biomass, alkali species (mainly K as well as Na) are partly volatilised due to the high temperatures prevailing in the fuel bed. Additionally, sulphur and chlorine and in the case of waste wood combustion, also considerable amounts of the heavy metals Pb and Zn, are released. Thereby the chlorides react in high temperature environments with the alkali metals and the heavy metals to gaseous salt species.

After their formation, the salt species travel in the flue gas, and may deposit on cold surfaces (e.g. tube walls). The deposition can occur via direct condensation or the corrosive salts may already undergo a phase transition in the flue gas and impact on the tube walls as fine particles. A more detailed description on possible deposit mechanisms can be found for example in [42] and in Section 3.2.3.

While the metals (alkali metals as well as heavy metals) and chlorine released initially form gaseous salt species at high temperatures, the released sulphur mainly forms SO_2 and partly SO_3 as soon as oxygen excess is available. In the further course these sulphur oxides may react with the chlorides to sulphates. During this sulphation reaction chlorine is released. Subsequently, the released chlorine can react with the metal and cause severe corrosion. Hence, the sulphation process represents a key reaction within the active Cl-induced oxidation corrosion mechanism. In the presence of a wet flue gas the conversion of chlorides (e.g. KCl) can be effected by the following reaction.

$$2\ KCl + SO_2 + {}^1/_2\ O_2 + H_2O \rightarrow 2\ HCl + K_2SO_4 \qquad \text{Eq. 5}$$

The sulphation process itself is kinetically limited. Therefore, depending on the sulphur excess to chlorine available and the time/temperature profile in the plant a part of the

chlorides becomes sulphated already in the flue gas. If this happens the chlorine becomes released in secure distance to the metal surface and most likely reacts with hydrogen to gaseous HCl.

The sulphation of the chlorides already in the flue gas can reduce the corrosion potential significantly, since the sulphates formed behave relatively inert at temperatures below 600 °C and hence, represent an effective protection layer. Once deposited the chlorides become sulphated. Thereby, the chlorine is released very close to the steel surface. Hence, the amount of Cl available for the corrosion process is significantly higher compared to the adsorption of HCl.

The underlying mechanisms of this heterogeneous reaction are not completely understood so far [43]. Still, reaction rates have already been empirically determined for various temperatures, gas velocities and concentration ranges ([43], [44], [45], [46]). However, the concentration of SO_2 used within these experiments generally exceeds the concentration of SO_2 in the flue gas of woody biomass fired boilers by far which makes an extrapolation of these data not meaningful.

However, the overall concept of the active chlorine induced oxidation is generally accepted. Here, the basic mechanism can be applied for alkali and heavy metal chlorides alike as well as for pure metals and alloys. As already mentioned only low alloy steels are considered within this work. Due to this restriction only the effects of active Cl-induced oxidation on iron will be discussed in detail. The theory may also be applied for the active Cl-induced oxidation of other common alloy components such as Ni or Cr [36].

The Cl_2 or HCl formed during the sulphation of chlorides can penetrate through the iron oxide layer to the metal surface. There the chlorine attacks the iron, forming iron chlorides which are generally stable at low O_2 concentrations [26].

Depending on the tube surface temperature, a certain vapour pressure of the iron chloride is given and it evaporates and diffuses towards the outer deposit layers with prevailing oxygen rich conditions, where it will be oxidized to Fe_3O_4 or Fe_2O_3. The released chlorine is again available for further reactions with the metal oxide layer. At higher wall and flue gas temperatures, the amounts of liquid melts of alkali and heavy metal salts in the layer increase. Due to the higher reactivity of liquid salts, higher corrosion rates occur (see Section 2.2.3).

The process of active Cl-induced oxidation in ash deposit layers on tube bundles is outlined in Figure 2.2. A more detailed description of the mechanism can be found in [19], [22], [47].

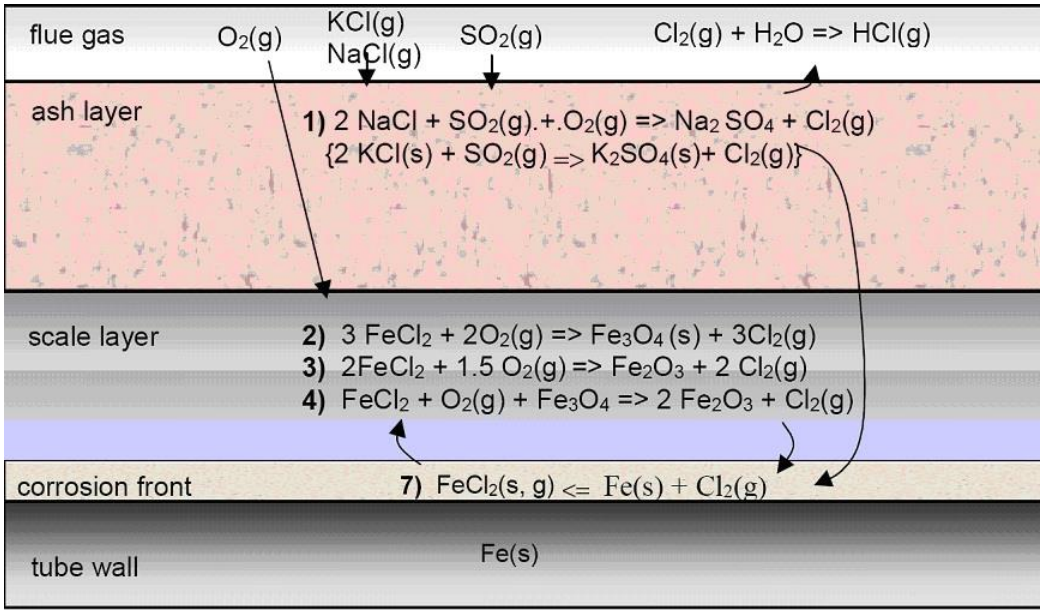

Figure 2.2: Mechanisms of chloride sulphation in deposits as well as the subsequent active Cl-induced oxidation on boiler tubes (adapted from [48])

2.2.3 Molten salt corrosion

As already mentioned in the previous section, the presence of molten phases can significantly increase the corrosion rate. If active Cl-induced oxidation is the dominating corrosion mechanism the increased attack is simply caused by the fact, that the molten or partly molten ash layer represents a liquid electrolyte in which the transport processes are significantly accelerated.

However, molten phases can also increase the corrosion rate without the presence of chlorine. Here, two types can be distinguished according to [49]:

- **hot corrosion type I**, often referred to as "high temperature hot corrosion"; in the temperature range between 800 °C – 1000 °C [2]
- **hot corrosion type II**, also called "low temperature hot corrosion", in the temperature range up to 800 °C

Due to the typical steam temperatures in biomass fired boilers (< 550 °C) as well as the restriction made on the application range of this work (< 550 °C), hot corrosion type I has basically no relevance for this work and hence, will not be further discussed. For the sake of completeness a detailed description of the corrosion mechanism can be found for example in [49].

Hot corrosion type II is basically based on a fluxing mechanism [50]. During the corrosion process positive metal ions are formed, which represent an acidic dissolution. Hence, hot corrosion requires the existence of a molten or partly molten layer. In general the melting

[2] Above ~ 1000 °C generally the oxidation of the metal becomes the dominating effect [49].

temperatures of the single sulphates K_2SO_4 or Na_2SO_4 are too high for melting to occur. Due to the heterogeneous deposit composition in biomass fired boilers, eutectics with relatively low melting points, far below 500 °C, may form [51]. Especially the presence of heavy metals can significantly reduce the melting temperature. Hence, the danger of hot corrosion is significantly higher when firing fuels with elevated heavy metal contents, such as waste wood.

Generally, there are two types of molten sulphate reactions known which cause hot corrosion. The first reaction includes the formation of pyrosulfates while the second represents the formation of alkali metal trisulfates. In both cases the protective oxide layers formed (Fe-, Ni- or Cr-oxides) react with the molten salts and additional SO_2 from the flue gas in an oxidizing atmosphere [52]. Hence, the protective layer becomes degraded which enhances the further corrosion process. A detailed discussion on the mechanism of hot corrosion can be found in [19], [36], [50], [52], [53].

2.3 Influencing factors

Summarizing the previous sections on high-temperature corrosion, the rates as well as the mechanism prevailing are influenced by a considerable number of parameters. In the following, the most important parameters are briefly summarized and additionally relevant literature is presented.

Steel: The steel composition has a strong influence on high-temperature corrosion processes. Special alloying elements such as Cr or Ni form very dense oxides, which can significantly reduce the speed of corrosion (selected further literature: [18], [36], [49]).

Steel temperature: Most high-temperature corrosion processes are limited by solid state diffusion, which is generally a temperature dependent process. Hence, a higher steel temperature most likely increases the corrosion rate. Also, chemical reactions such as sulphation of chlorides, and hence, the release rate of chlorine in the deposit layer will be enhanced at elevated temperatures (selected further literature: [11], [41], [46]).

Flue gas velocity: The flue gas velocity influences the local heat transfer and therefore, can lead to locally higher steel and deposit temperatures (also see: steel temperature). In real-scale plants the flue gas velocity is generally depending on the furnace load conditions. Hence, a higher velocity means also a higher mass flux of corrosive species, which can enhance the speed of corrosion (selected further literature: [22], [30]).

Flue gas temperature: Similar to the flue gas velocity, the flue gas temperature has an impact on the local heat flux and hence, the steel and deposit temperature. Furthermore, the flue gas temperature profile over the plant influences the flue gas chemistry (sulphation of chlorides in the flue gas) as well as the aggregate state of the ash vapours/fine particles (selected further literature: [21], [32], [42]).

Stress: Stress and strain can lead to spallation of protective oxide scales. Here, the stress can be caused by a number of factors, for example a temperature gradient, the tube

geometry, different molar volumes of metal and oxide, mechanical stress, etc. (selected further literature: [38], [54], [55])

Chemical composition of the flue gas and ash deposits: High concentrations of corrosive agents in the flue gas can significantly increase the corrosion rate. Here, typical corrosive agents are: chlorine species (HCl, Cl_2, alkali chlorides, heavy metal chlorides), oxidizing species (O_2, CO_2, H_2O) and sulphur oxides (SO_2, SO_3). While the presence of chlorine in any case increases the corrosion rate, the presence of sulphur oxides can either increase or decrease the corrosion behaviour. In coal fired plants the high concentrations of sulphur oxides in the flue gas may cause severe corrosion. In biomass fired boilers these concentrations are typically considerably lower, which reduces the danger of sulphidation of the metal significantly. As already mentioned the sulphation of alkali chlorides is kinetically limited. On the contrary, a high sulphur excess to chlorine may increase the sulphation reaction rate in the flue gas and hence, decrease the overall corrosion behaviour of the plant (selected further literature: [19], [22], [36], [56], [57]).

2.4 Existing model

Within the last years, several approaches have been developed to estimate the local high-temperature corrosion in coal and municipal solid waste combustion plants by means of CFD simulations. Most of these approaches have in common that they use simple correlations and assumptions in order to calculate the deposit build-up on the walls as a basis for the estimation of the corrosion potential [58], [59], [60]. Due to strong simplifications used for the description of the deposit build-up, the models are not able to sufficiently describe corrosion processes depending on relevant influencing parameters and therefore, are not suitable for an application in biomass combustion plants. In addition, most of the correlations used, are not or only of minor relevance for biomass fired plants. For example one approach, which was developed to calculate the corrosion potential in coal fired boilers, uses the amount of unburned fuel in the deposits (which represents a source of sulphur) as well as the local concentration of H_2S in the flue gas to estimate the local corrosion potential in the furnace duct [58]. However, in general the amount of sulphur species is significantly lower in biomass fired boilers and in addition the amount of H_2S in the convective section of a biomass fired boiler is, due to the oxidizing conditions, negligible.

More physics-based models have been proposed for active Cl-induced oxidation being the dominating corrosion mechanism [19], [26], [47], [61]. However, the development of these models is based on experimental data gained for conditions typically prevailing in municipal solid waste plants. Its common view that active Cl-induced oxidation is the dominating high-temperature corrosion mechanism in MSWI. Based on this assumption, interactions with other corrosion mechanisms such as oxidation of the steel are not considered in these models. However, since the dominating corrosion mechanisms in boilers fired with chemically untreated woody biomass are not clear yet, the applicability of these models in biomass fired boilers is uncertain. In addition, all of these models have in common that several important coefficients of the models are based on rough assumptions and estimations (e.g. diffusion coefficients of $FeCl_2$ or Cl_2, etc.).

In addition to these approaches considerable work has been done to develop numerical models for the high temperature oxidation of metals [41], [62], [63], [64] [65]. However, these approaches neglect the complex interactions between the flue gas, the chemical reactive deposit layer and the steel. Hence, these models can only represent sub-models for an overall high-temperature corrosion model in biomass fired boilers (see also Section 5.2).

Concluding, although a lot of work has been carried out so far to develop reliable high-temperature corrosion models, up to now, none of the models published is adequate to simulate the local high-temperature corrosion potential in a biomass fired boiler, due to strong simplifications or underlying boundary conditions which are typical for municipal solid waste plants.

3 Methodology

The development of the high-temperature corrosion models for low alloy boiler steels is based on the results of lab-scale test runs in a specially designed drop tube reactor. The investigated steel as well as the reactor used, including all supplementary measurement technics are presented in Section 3.1.

The high-temperature corrosion models developed are especially designed to be used together with CFD simulations of flow and heat transfer. The CFD models used to simulate the combustion of the fuel as well as the chemically reactive flow of the flue gas are presented in Section 3.2. High-temperature corrosion in biomass fired boilers is strongly influenced by ash deposits as described in the previous section. A CFD based deposit and fine dust formation model has already been developed [66]. To enable the calculation of the deposition behaviour in the convective heat exchanger section this model has been coupled with a finite cell based heat exchanger model[3] [77]. Since these two models are coupled with the detailed corrosion potential model developed within this work, both models are briefly introduced within this section.

3.1 Experimental section

3.1.1 Steel 13CrMo4-5

The material investigated was 13CrMo4-5 (material number 1.7335) which is commonly used as steel for superheater tubes in biomass fired boilers. The composition of this heat resistant ferritic steel can be found in Table 3.1.

Table 3.1: Composition of 13CrMo4-5 (1.7335)

element		C	Si	Mn	P	S	Al	Cu	Cr	Mo	Ni	Fe
min.	[wt-%]	0.10	-	0.40	-	-	-	-	0.70	0.40	-	remaining
max.	[wt-%]	0.17	0.35	0.70	0.025	0.02	0.04	0.30	1.15	0.60	0.30	remaining

3.1.2 Drop Tube reactor

The high-temperature corrosion test runs have been carried out using a combined packed bed / drop tube reactor with which well-defined conditions regarding flue gas temperature and composition, typically prevailing in biomass fired boilers, can be achieved. The reactor enables the combustion of various types of biomass fuels including pellets (made from wood or herbaceous biomasses) as well as wood chips. After a proper preparation, including chopping and sieving out bigger metal parts the reactor is able to

[3] The deposit and fine dust formation model was developed by BIOENERGY2020+ GmbH in cooperation with BIOS BIOENERGIESYSTEME GmbH and TU-Graz. The heat exchanger model was developed by BIOS BIOENERGIESYSTEME GmbH. The implementation of the heat exchanger model in the deposit formation model as well as the GUI development was done by Bioenergy2020+ GmbH in cooperation with ANSYS Inc. (Fluent), TU-Graz and BIOS BIOENERGIESYSTEME GmbH.

fire waste wood of all quality fractions. A detailed description of the setup used can be found in [Paper I]. A schematic view of the reactor is shown in Figure 3.1.

The setup applied consists of a packed bed reactor (biomass grate furnace with air staging and flue gas recirculation), an additional natural gas burner and an upper transition part to a successively heated vertical tube with isothermal conditions (the so-called drop tube). The gas burner and the biomass furnace can each be operated on their own or in combination. The electrical heating of the drop tube allows a compensation of the fluctuation of the grate furnace operation and, therefore, to achieve constant and adjustable flue gas temperatures in front of the corrosion probe. Hence, the flue gas temperature can be adjusted independently of the furnace\gas burner load and therefore, enables corrosion measurements under defined flow and temperature conditions. Finally, the flue gas is transferred via a lower transitional part to a water cooled heat exchanger before it enters the chimney. An additional water cooled pipe is installed to bypass the measurement unit during the start-up and shutdown of the reactor. Furthermore, an optical port enables the visual monitoring of the deposit or corrosion probe experiments.

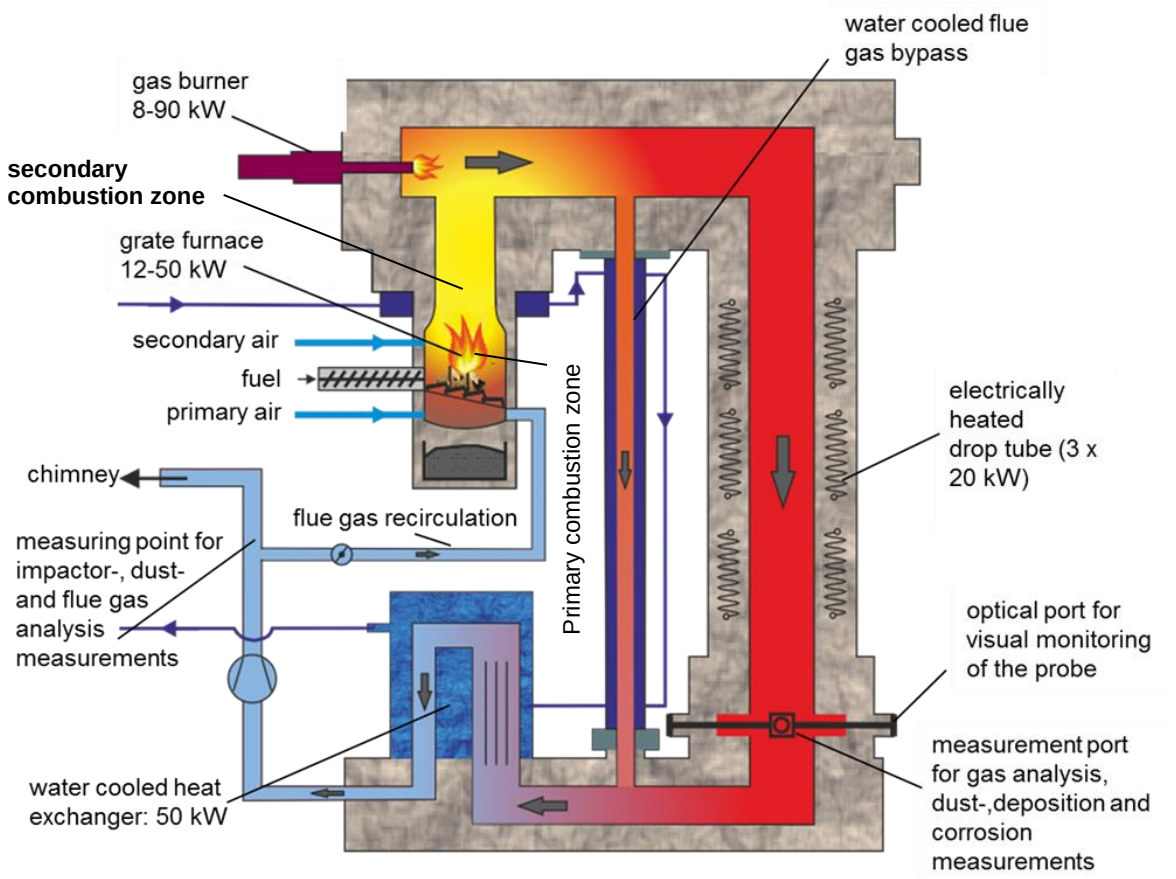

Figure 3.1: Schematic view of the combined packed bed/drop tube reactor with relevant units and measurement ports (adapted from [Paper I]).

To correct the flue gas temperature measured with the reactor internal thermocouples regarding radiation, suction pyrometer measurements according to standards of the

International Flame Research Foundation (IFRF) have been performed at the position of the measurement port (see Figure 3.1).

3.1.3 Online corrosion probe measurements

The corrosion probe provided by the company CORRMORAN GmbH (Augsburg, Germany) is based on a system which was developed at the Institute of Physics, University of Augsburg in Germany [21], [22]. The system geometry is designed to simulate a superheater tube.

The probe design consists of an air cooled support lance made from a heat resistant nickel based super alloy (Figure 3.2, left) with an air-cooled probe head (Figure 3.2, right). The probe head consists of four sample rings that are separated by ceramic rings. The sample rings can in general be made of any superheater material. In the test runs performed within this work these sample rings were made of 13CrMo4–5 and are held at a constant temperature which can be arbitrarily changed by the air cooling. When exposed to the flue gas, an ionic layer is formed which allows the measurement of a linear polarization resistance between the steel surface and the ionic layer. This resistance is directly proportional to the current corrosion attack [67]. The measured signal can be related to a corrosion rate, which describes the steel loss over time. This can be achieved by quantifying the actual mass loss of an additional ring, the so-called mass loss ring, subsequent to the test run. To determine the mass loss of steel the oxide layer formed on top of the sample ring is removed according to ASTM G1-03. A detailed description of the probe can be found in [22], [31].

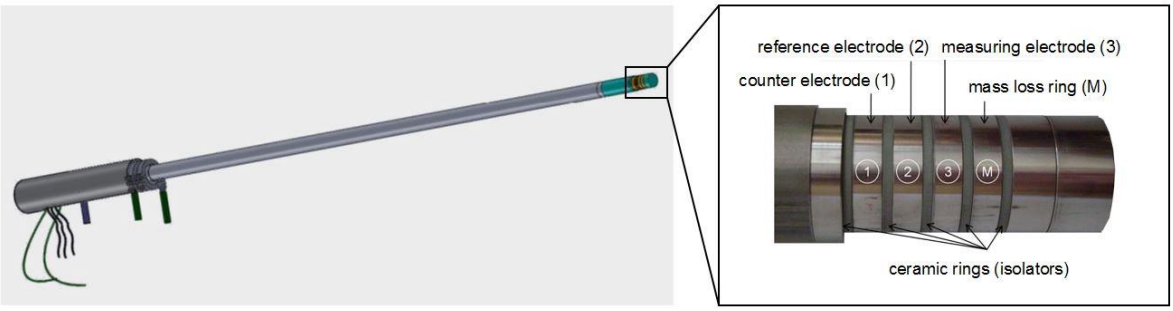

Figure 3.2: Schematic view of the corrosion probe (left) and the sensor probe head (right) with the electrodes (1–3) and the mass loss ring (M) **[69]**

It should be mentioned that the corrosion rates measured within this work give only qualitative information about the corrosion potential in dependence of relevant operating parameters. High-temperature corrosion is a strongly time-dependent process which often follows a paralinear trend (see [67] and Section 2.1.2). Therefore, the corrosion rates gained within short-term measurements generally differ from those found within long-term measurements. In addition to this time dependence a systematic measurement error the so-called “start-up” effect could be attested by Retschitzegger et al. [68]. This measurement error strongly depends on the measurement time and becomes negligible for long measurement times.

Nevertheless, the short-term online corrosion measurements still allow the investigation of the dependence on a certain parameter.

3.1.4 Mass loss probe measurements

The mass loss probe (MLP) was originally developed to correct the systematic measurement error described earlier (see Section 3.1.3).

The MLP can either be used in combination with the online corrosion probe to allow for the correction of the "start-up" error as described in full detail in [68] or it can be used solely to determine the progress of mass loss for a certain constant parameter setup.

In this work the MLP was solely used as a stand-alone system to investigate the time depend mass loss for constant flue gas parameters and steel temperatures.

The MLP is inserted into the flue gas of the drop tube reactor at the same position as the online corrosion probe (see Figure 3.1). The probe consists of a carrier-lance with five test rings on top. These rings are cooled by air similar to the online corrosion probe. The temperature of the sample rings is measured on the inside of a sample ring by a thermocouple. A PID controller regulates the amount of cooling airflow and hence, the steel temperature of the sample rings.

To gain a time-dependent mass loss, the individual test rings are removed from the probe after different times. To determine the mass loss of the test rings, the rings are weighed before being exposed to the flue gas. Subsequent to the test run, the corrosion products formed on the sample rings are removed according to ASTM G1-03 and the mass loss is determined gravimetrically. Between the extractions of the sample rings from the flue gas and removal of the corrosion products which mainly consists of iron oxides the sample rings are stored in a desiccator.

A detailed description of this probe can be found in [68].

3.1.5 Deposit probe measurements

To investigate the chemical composition, the structure of the deposit layer as well as the build-up rate (RBU), short term deposit probe measurements with a duration of 2 hours were performed. These measurements were carried out subsequent to the corrosion test runs to avoid an interaction of the corrosion respectively the mass loss and the deposit probe.

The deposit probe consists of a carrier lance with a test ring on top, which is cooled by air (see Figure 3.3) and is inserted into the flue gas at the corrosion probe measurement port (see Figure 3.1).

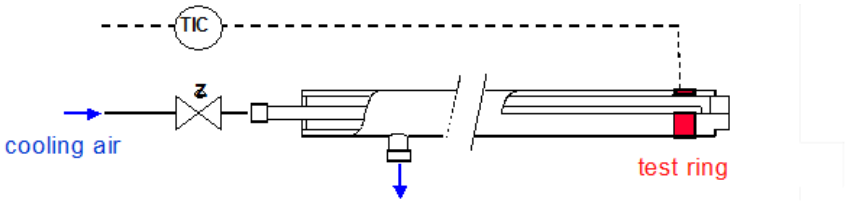

Figure 3.3: Scheme of the deposit probe **[31]**
Explanations: TIC … temperature measurement and control

The sample ring consists of a high alloy heat resisting steel (material number 1.4841) to minimize the effect of oxidation/corrosion on the RBU. All deposit probe measurements were performed with clean sample rings.

The air cooling of the probe allows the investigation of the initial deposit formation behaviour of different steal temperatures, which simulate different steam temperatures. Deposit probe measurements at different probe temperatures give an indication regarding the condensation temperature of gaseous flue gas components such as alkali or heavy metal chlorides.

To determine the RBU the mass gain of the test ring by deposit formation is determined by gravimetric measurements of the test ring before and after the exposure to the flue gas. Scanning electron microscopy (SEM) and dispersive X-ray (EDX) analyses were performed to analyse the deposits subsequently to the measurements on three different locations (windward, windward + 50° and the leeward side) of each deposit probe ring.

A more detailed description of the deposit probe measurements can be found in [31].

3.1.6 Biomass fuel and ash analyses

To investigate the composition of the biomass fuels representative samples were taken during the test run. The sample preparation was carried out according to ÖNORM CEN/TS 14780. The ash content is determined according to ÖNORM CEN/TS 14775. The determination of C, H and N is carried out according to ÖNORM CEN/TS 15104. The chlorine content is determined according to ÖNORM CEN/TS 15289. Major and minor ash forming elements were determined by multi-step pressurized digestion of the fuel with HNO_3 (65%) / HF (40%) / H_3BO_3 followed by measurement by inductively coupled plasma optical emission spectroscopy (ICP-OES) or inductively coupled plasma mass spectroscopy (ICP-MS) depending on detection limits. The moisture content of the fuel sample is determined according to ÖNORM CEN/TS 14774.

3.1.7 HCl/SO_x measurements

The determination is carried out according to VDI 3480, Sheet 1. Flue gas is sucked from an extraction point over several successively connected washing flasks with distilled water and diluted sodium hydroxide solution (enriched with H_2O_2). The dissolved anions are measured by ion-chromatography (IC). HCl/SO_x measurements were performed at the position of the corrosion probe (see Figure 3.1).

3.1.8 SEM/EDX analyses and sample preparation

SEM/EDX analyses are well-suited to gain information regarding the structure and the chemical composition of the deposit layer, the oxide layer and the corrosion front.

To investigate the deposits formed during the short term deposit probe measurements, the sample rings were first coated with a thin carbon layer to avoid an electrical charging of the sample. The samples were analyzed using a ZEISS Gemini 982 field emission scanning electron microscope equipped with a Noran Voyager X-ray analysis system (Si(Li) detector, ultra-thin window). Within the analyses the oxygen content was determined by stoichiometric calculations. The compositions of the deposit layers were determined by area scans using magnifications of 100 at representative spots of the ring sections: windward, windward + 50° and leeward.

Due to the interaction volume of the electron beam with the sample not only the deposit layer becomes analyzed, but also the underlying steel of the probe ring. Especially for thin deposit layers, as formed during short-term deposit measurements, this is an essential problem. However, the amount of Ni and Cr is negligible in the fuels used within the test runs (see Table 4.2 and Table 5.2) and the release rate of Fe from the fuel is typically low, hence, these elements were excluded from the analyses. The measured quantities of these elements are most likely components of the probe steel ring.

To gain more information regarding the corrosion mechanism, SEM/EDX analyses of cross sections of the MLP as well as the online corrosion probe sample rings were performed subsequently to each test run.

First, the ring was embedded in epoxy resin, afterwards the profile was grinded using sand papers until a smooth, plane surface was achieved. The cross sections were prepared under dry conditions without the use of a lubricant. Afterwards, the ring was coated with a thin carbon layer. Between the various steps the probe rings were stored in a desiccator. The systems used for the elemental mappings are a Zeiss Ultra 55 field emission scanning electron microscope equipped with an EDAX Pegasus X-ray analysis system. To investigate the chemical composition highly resolved spot analyses as well as elemental mappings have been carried out. Within these analyses, the oxygen content was measured and not stoichiometrically calculated to detect oxides and to achieve a clear separation between the corrosion layer and the original steel surface. The elemental mappings show the relative distribution of each element over the area investigated. Thereby, bright colors mean a high concentration whereas a weak color represents a low concentration of the element.

Since alkali chlorides are quite sensitive to heat it was ensured that the probe ring did not become too hot during the grinding process. Therefore, a reference sample with well-defined KCl content was prepared and analyzed in the same way as the corrosion probe ring. The pre-defined KCl content of this sample could be confirmed with EDX analyses. In doing so, it is assured that KCl is not removed from the corrosion probe rings during sample preparation.

An accelerating voltage of 12 kV was used for the analyses to minimize the damage on the deposits caused by the electron beam. However, because of the limited resolution of the energy-dispersive spectrometer (EDS) the exited S K-line, Pb M-line and Mo L-line are overlapping in the spectrum. Hence, these elements are hard to distinguish accurately, especially if only small amounts of these elements are present. Also the accuracy of the quantitative analyses of these elements is limited.

3.2 Basic CFD models applied

All CFD simulations within this thesis were performed with the software package ANSYS®, Fluent; Versions 14.0.0 and 15.0.7.

Due to the complexity of the chemical and physical processes involved, CFD modelling of biomass grate furnaces is still a challenging task. In addition to deposit formation and corrosion processes, also modelling of the turbulent reactive flow as well as the combustion process of the solid biomass fuels are challenging problems.

Although detailed models exist for the thermal conversion of solid biomass particles (e.g. [70]) up to now, their engineering applications are limited due to the high computational resources needed. Therefore, within this work the thermal conversion and hence, the release of combustible gases from the fuel on the grate is described by an empirical packed bed model. A more detailed description of the model can be found in Section 3.2.1

In engineering applications, usually a combination of two models is used for the simulation of turbulent combustion in the plant [71], [72]. Here turbulence is modelled with a 2-equation model (here the Realizable k-Ɛ model) whereas gas phase combustion is modelled with the so-called Eddy Dissipation model in combination with a global 3-step methane mechanism which was especially adapted and validated for biomass combustion [73]. The radiation is taken into account by the Discrete Ordinates model (DO) [74].

The benefits of this approach are low computing costs in combination with sufficiently accurate results for engineering purposes. However, as a drawback, some empirical constants of the EDM model need to be adapted depending on the application [75], [76] and, furthermore, the model is only well-working in mixing-limited situations.

3.2.1 Empirical packed bed model

The empirical packed-bed model provides the necessary boundary conditions e.g. chemical composition, temperature and velocity of the flue gas leaving the surface of the solid biomass fuel bed. This surface often represents the boundary of the simulation domain.

The model provides the required input data for the CFD simulation in form of one-dimensional profiles along the grate. Here, it considers the effects of drying and the degradation of the fuel. The formation of the most important flue gas components CH_4, CO, CO_2, H_2, H_2O, O_2 is modelled using empirical conversion factors. These empirical

correlations are based on experimental and literature data as wells as assumptions. In a final step, balancing of the mass and energy fluxes along the grate is performed. A detailed description of the model can be found in [71]. It has been developed by BIOS BIOENERGIESYSTEME GmbH in cooperation with the TU Graz.

3.2.2 Heat exchanger model

Although, the computational performance strongly increased within the last decade a detailed CFD based simulation of the convective boiler section in which the heat exchanger tubes are resolved is still impossible within a reasonable time. This is mainly caused by the large variations of geometric length scales in this boiler section. In addition, effects like vortex shedding behind tubes should be taken into account to achieve accurate simulation results. These effects and the different length scales require a highly resolved grid, which leads to unacceptable long calculation times.

To overcome the problems mentioned above, a finite cell based convective heat exchanger model has been developed by BIOS BIOENERGIESYSTEME GmbH. A detailed description of the model can be found in [77].

The heat exchanger model was applied in order to calculate the flow as well as the convective and radiant heat transfer in the superheater tube banks. The source terms for the calculation of the momentum and energy transport equations are based on literature data [78], [79], [80].

However, only data for tube banks with staggered and in-line tube arrangements and a flow perpendicular to the tube rows are available. Hence, the empirical correlations given by the literature are only valid for tube banks which are equally flown through by the flue gas. In reality, the flue gas often passes not homogeneously through the tube banks, especially after constrictions and redirections of the flue gas at the end respectively the beginning of a boiler duct.

The pressure loss is calculated based on the Reynolds number. To take an inhomogeneous flow field into account, transient 2D simulations were performed to calculate the Reynolds number and hence, flow resistance in dependence of the flow direction. Within this approach the direction of the velocity vectors inside the tube banks are considered which allows the calculation of a pressure loss which takes an inhomogeneous flow field into account [77].

A similar approach is used to calculate the heat flux. Here, the convective heat transfer is calculated based on the Nusselt-number. The dependence on the flow direction is taken similar into account as for the pressure loss. Also the radiant heat exchange between the flue gas and the heat exchanger by means of reflection, absorption and emission is taken into account. Therefore, the heat exchanger model is well-suited to calculate the heat transfer in heat exchangers passed through by flue gas with an inhomogeneous flow field.

The secondary side (steam side) of the heat exchanger is not included in the CFD simulation. Here, boundary conditions are set according to dimensioning calculations of

the boiler manufactures. The steam/water temperature increase between the inlet and the outlet of a heat exchanger bundle is considered as linear within the model. The resulting local temperature of the secondary medium is then used to calculate the Nusselt-number and in further consequence the convective heat transfer coefficient.

3.2.3 Deposit formation model

The deposit formation model considers the following relevant physical mechanism: condensation of ash forming vapours, fine dust formation, deposition of fine-dust and coarse fly ash particles and the removal of a deposit layer by erosion. In addition, the model takes the reduced heat transfer due to the growth of the deposit layer into account. Furthermore, the dependence of radiant heat exchange between the deposit surface and the flue gas on the local emissivity of the deposit layer is considered [81].

Ash forming vapours are released from the fuel bed into the gas phase during the combustion of the solid biomass. This release process depends on several parameters like the bed temperature, the oxygen content and the biomass composition. Due to these complex interactions, no model exists up to now to describe the release behaviour of the ash forming elements sufficiently.

Still a considerable amount of research has been carried out which among others led to the development of fuel indices. These indices roughly estimate the released amount of ash forming vapours with respect to the fuel composition [12]. However, up to now this approach is not accurate enough to produce reliable input data for the calculation of the deposit formation behaviour based on CFD simulations.

Hence, the release rates of the ash forming vapours are based on elemental balancing data of test runs with comparable fuel and combustion conditions. The release rates used for the simulations are presented together with the other relevant input data in the respective sections later on.

The time-dependent deposit build-up is simulated within a post-processing step after the combustion simulation. To reduce the mathematical effort to model the transport of the ash vapours, the deposit formation model considers the transport of the elements (e.g. S, Cl, K, etc.) instead of the transport of the ash forming species (e.g. KCl, K_2SO_4, etc.).

The relevant sub-models are briefly described in the following. A detailed description of the model can be found in [66].

Condensation model and fine dust formation model

Along the flue gas path-lines the flue gas is cooled down due to the heat transfer between the flue gas and the boiler walls. This temperature decrease leads to decreasing saturation pressures. If the partial pressure becomes lower than the saturation pressure of the ash vapours, they undergo a phase transition from the gaseous to the liquid or solid phase. These aerosols are commonly known as fine dust or fine particles, due to

their size which is typically smaller than 1 µm in diameter [42]. These fine particles can either be emitted with the flue gas or become deposited on the furnace and boiler walls.

If the partial pressure is still high enough to prevent the formation of aerosols, but the saturation pressure on the wall is lower than in the flow, condensation on the walls occurs.

The chemical reactions of the ash forming vapours are assumed to be basically fast compared to the local residence time of the flue gas. Hence, as an approximation, the chemical composition of the flue gas is determined by thermodynamic equilibrium calculations. The only exception is the formation of sulphates which is expected to be kinetically limited.

The sulphation of e.g. alkali chlorides by SO_2 is several orders of magnitude slower than the formation of sulphates by SO_3. Christensen et al. [82] showed that the oxidation of SO_2 to SO_3 is the rate limiting step rather than the final formation of sulphates. Based on that finding a global one step kinetic mechanism based on an Arrhenius approach was developed to determine the sulphation rate of aerosol particles in biomass fired boilers. Additionally they showed that the sulphation reaction by SO_3 is fast enough for thermodynamic equilibrium calculations to be applied.

The condensation processes of ash vapours itself is modelled based on a mass transfer approach using the analogy of mass transfer to the convective heat transfer (see Eq. 6) [83]. For the calculation of c_∞ only the gaseous components are considered, while for the calculation of c_w also liquid and solid phases at the surfaces have to be considered.

$$\dot{N}_{cond} = \beta \cdot (c_\infty - c_w)$$
$$\beta = \frac{\alpha}{c_p \cdot \rho} \qquad \text{Eq. 6}$$

Explanation: $\dot{N}_{cond}$ … condensation flux per area (mol/m²s), β … mass transfer coefficient (m/s), c_∞ … species concentration in the flue gas (mol/m³), c_w … saturation concentration of the species on the wall (mol/m³), α … heat transfer coefficient (J/m²s) , c_p … heat capacity (J/kgK), ρ … density of the flue gas (kg/m³)

Similarly to the condensation of ash vapours on furnace and cooled boiler walls, a calculation procedure is implemented to calculate the super-saturation of ash components in the flue gas to describe the nucleation of the ash vapour components as initial aerosol formation process. Here, two equilibrium calculations are carried out in each cell, one which includes solid ash phases and one which only considers gaseous ash phases. Then the rate of nucleation is calculated according to a model developed by Friedlander [84], which is based on the classical theory of nucleation. In addition to the

formation of new particles by nucleation, the deposit formation model also considers the condensation of ash vapours on the surface of existing aerosol particles.

Due to this approach several thermodynamic equilibrium calculations per cell have to be carried out, which leads to the calculation of millions of thermodynamic equilibrium calculations in each iteration step. Therefore, the In-Situ Adaptive Tabulation Algorithm (ISAT) [85] was used to store the results of the single equilibrium calculations. This procedure reduces the necessary amount of equilibrium calculations and hence, the overall calculation time significantly.

Deposit formation model of fine particles

Fick´s law for diffusion and thermophoresis is used to model the deposit formation of the fine particles (see Eq. 7). Other deposition mechanisms of fine particles such as inertial impaction, gravitational settling as well as diffusiophoresis are neglected in the model up to now. However, it is known that these mechanisms only play a minor role for the overall deposit behaviour of the fine particles [86].

$$\mathrm{v}_{th} = \frac{\nu_{gas} \cdot K_{th}}{\rho_{gas} \cdot T_p} \cdot \nabla T_{gas} \qquad \text{Eq. 7}$$

Explanation: v_{th} … thermophoretic diffusion velocity (m/s), ν_{gas} … viscosity of the flue gas (kg/ms), K_{th} … thermophoretic coefficient (-), ρ_{gas} … density of the flue gas (kg/m³), T_p … temperature of the particle (K), ∇T_{gas} … local temperature gradient prevailing in the gas phase (K/m)

Deposit formation model for coarse fly ash particles

Due to the considerable mass of the coarse fly ash particles, the dominating deposition effect is the impaction of the particles [42].

The transport of the coarse fly ash particles is modelled using a Lagrangian approach (Discrete Phase Model), which is implemented in the CFD software package ANSYS®, FLUENT 15.0.7. Once a particle impacts on a wall, either it sticks to the wall or rebounds.

Here, the sticking probability depends on the stickiness of the wall as well as of the particle itself. Two different stickiness approaches are implemented in the deposit formation model. For silica-rich particles a viscosity approach and for salt-rich particles a melting approach is taken into account [66].

In the viscosity approach, the sticking probability of silica-rich particles is determined by the ratio of a reference viscosity and the viscosity of the particle at a certain temperature. Here the reference viscosity is calculated as a function of the kinetic energy of the particle.

The sticking probability of salt-rich particles and deposit layers is calculated according to the following approach, which considers the aggregate state. The melt fraction is calculated by thermodynamic equilibrium calculations. Below 15 wt-% molten phase of the ash, the particles are not sticky (sticking probability = 0). Between 15 wt-% and 70 wt-% molten phase, the sticking probability increases linearly from 0 to 100 %. Above 70 wt-% melt fraction, the particles are assumed to stick to the wall. This approach is based on comparisons of experimental data from biomass fired boilers with thermodynamic calculations.

Generally, a mixture of salt and silica-rich material exists in biomass fired plants. Hence, the two models are combined using the mass weighted average of the stickiness probability of both models. A detailed discussion on the coarse fly ash sub-model can be found in [66].

Erosion model

Particles which hit the wall but do not stick to it bounce off. Within this process a part of their kinetic energy becomes absorbed by the boiler wall or the deposit layer on top of the steel wall if such a layer is present. If the kinetic energy of the particle is high enough, the deposit layer or the steel becomes degraded by the impaction of coarse fly ash particles. However, in the present state of model development, only the erosion of the deposit layer is considered.

Methodology for the application of the model

The deposition of coarse fly ash particles was not considered in the simulations performed within this work, since these particles are mostly formed by rather inert oxides and hence, have only a minor effect on the high-temperature corrosion processes occurring in biomass fired boilers. Due to the exclusion of the coarse fly ash particles, also the degradation of the deposit layer by erosion is not considered.

A schematic illustration which summarizes the interaction of relevant CFD sub-models is presented in Figure 3.4. The sub-models, which are needed to gain the required input data for the two high temperature corrosion models developed, are indicated by the blue and grey boxes.

As already mentioned, deposit formation is a strongly time-dependent process. Hence, the extrapolation of a short-term deposit simulation carried out on blank boiler walls (initial deposition) is not recommended. However, due to the very long calculation times only one deposit time-step could be carried out in each simulation to estimate the deposit formation behavior. To avoid this dilemma and achieve realistic boundary conditions for a steady state simulation, a basic fouling layer was assumed on the boiler walls. This approach is commonly used in heat transfer simulations since the assumed fouling layer presents the steady-state of the plant rather than the simulation of blank boiler walls. Hence, the simulation of the deposit formation on top of such a fouling layer represents a first, but sufficient approximation to the steady state deposition behavior.

The assumption of local thickness and hence, heat resistance of the basic fouling layer used within this work is based on experience values as well as measurements.

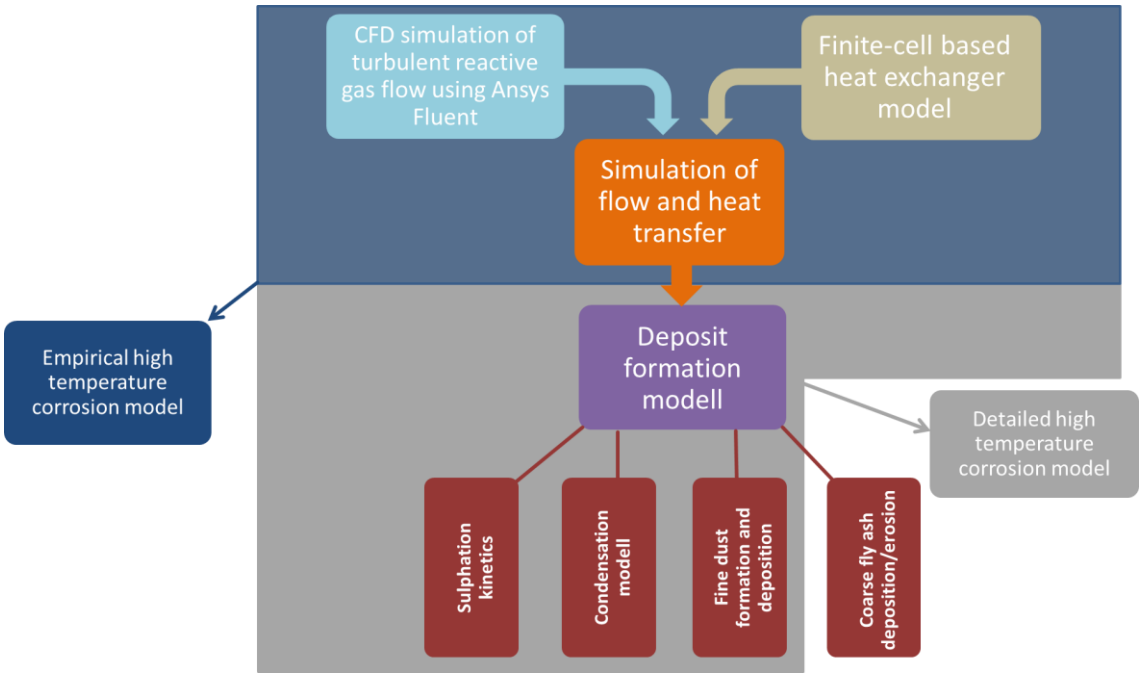

Figure 3.4: Schematic illustration of the models used within this work and their interactions.

Due to the high computational costs of the condensation and the fine dust model, only the most relevant elements and chemical compounds are considered in the simulation. Brunner et al. [86] showed that for chemically untreated woody biomass the elements Na, K, Cl, and S are the most relevant ash forming elements. Hence, only these elements are considered for the simulation of a plant firing such a fuel. These elements can form following chemical compounds: KCl, $(KCl)_2$, K_2SO_4, NaCl, $(NaCl)_2$, Na_2SO_4.

If the model is used to simulate the deposit and fine dust formation in waste wood or even municipal solid waste fired plants these elements are extended by the heavy metals Zn and Pb. In this case, also their chlorides and sulphates are taken into account. It is known that these heavy metal sulphates and chlorides have a strong influence on the melting temperature of the ash layer [51].

4 Empirical model

As already explained in the introduction of this work no sufficient data is available up to now to be used as basis for an empirical high-temperature corrosion model. Therefore, online corrosion probe measurements (see Section 3.1.3) have been carried out in a specially designed biomass fired drop tube reactor (see Section 3.1.2) to gain the necessary data for the development of a reliable empirical model. In addition to the online corrosion probe measurements also the deposits have been carefully investigated by means of short-term deposit measurements (see Section 3.1.5) as well as visual and SEM/EDX analyses (see Section 3.1.8) to gain relevant information regarding the corrosion mechanism prevailing. First, the experimental data were used to determine the most influencing parameters. Based on that data analyses an empirical model was developed which describes the experimental data sufficiently accurate. Finally, the newly developed model was applied within a CFD simulation of flow and heat transfer to estimate the local corrosion potential of a biomass fired boiler.

The relevant experimental results as well as the empirical model developed have been published in [Paper I].

4.1 Online corrosion probe test runs

As already described in detail in the introduction of this work high temperature corrosion was already extensively investigated in MSWI. From these measurements it is known that the most influencing parameters on high temperature corrosion in a MSWI are the flue gas temperature and velocity as well as the steel surface temperature [22], [21], [30]. Furthermore, it is commonly accepted that the dominating corrosion mechanism on the superheaters of a MSWI is active Cl-induced oxidation.

However, far less work has been done so far to investigate the dominating corrosion mechanism in the case of woody biomass especially for chemically untreated ones. Since the dominating corrosion mechanism is not clear following objectives should be addressed within the data gained from the test runs:

- Determination of the most influencing parameters
- Development of an empirical corrosion model
- Investigation of the dominating corrosion mechanism

To study the effect of different biomass fuels fired on deposit formation and on high-temperature corrosion, two test runs were carried out. In the first one, forest wood chips and in the second one quality sorted waste wood (A1–A2 according to German standards) was used as fuel.

4.1.1 Test run and operating conditions

The online corrosion probe test runs were performed at the coupled packed bed / drop tube reactor (see Section 3.1.2). To allow a comparison of the two test runs the same

parameter setup was investigated within the two test runs. Furthermore, comparable combustion conditions have been applied.

Within the test runs the following parameter variations have been performed: flue gas temperature (T_{FG}) between 650 °C and 880 °C, steel temperature (T_S) between 450 °C and 550 °C and flue gas velocity (v_{FG}) between 2 m/s and 8 m/s.

The flue gas temperature variations were achieved by a modification of the electrical heating power of the drop tube (see Section 3.1.2). The steel temperature was varied by a variable air cooling of the probe (see Section 3.1.3) and the flue gas velocity variations were achieved by different furnace load conditions.

The corrosion probe test run of forest wood chips lasted 1070 h. During this time the biomass furnace was 325 h in operation. The duration of the waste wood test run was 1512 h with a furnace operation time of 329 h. Due to safety reasons the furnace had to be shut down in the evenings and at weekends. To prevent chipping of the corrosion layer caused by thermal stress the drop tube was heated overnight at a constant temperature of 850 °C of the heating elements, with air streaming through the drop tube, which led to a constant probe steel temperature of about 440 °C.

The measurement technology applied for the measurement of the high-temperature corrosion rate requires a fully developed ionic layer at the corrosion front. Before this layer is fully developed, the corrosion signal strongly increases with increasing area of the ionic layer [39]. Due to this additional time-dependent effect an investigation of the dependence on other influencing parameters (e.g. T_S or T_{FG}) is not meaningful during this measurement phase. Horn et al. [87] reported that it took around 10 days to achieve a reproducible signal in similar measurements, performed in a municipal solid waste CHP plants.

Due to this technical limitation the test runs were split in two parts in which the first ~130 operating hours were used to develop the ionic layer. During that time the parameter settings were not changed. After gaining a reproducible signal from the online corrosion probe over several days, parameter variations were applied to determine their effect on high-temperature corrosion.

Subsequent to these test runs the so-called “start-up effect” (initial phase) was investigated in detail. Since this effect (duration, strength, etc.) strongly depends on the parameter setup prevailing during the initial test phase it has to be corrected to allow a quantitative comparison of the corrosion rates measured in different test runs (see [68] and [39]).

In the second phase the so-called variation phase the methodology differs for the two test series. In the case of forest wood chips, the parameter variations were all done starting from pre-defined reference conditions. The reference conditions chosen were: T_{FG} = 730 ± 10 °C, T_S = 480 ± 1 °C and v_{FG} = 2.8 ± 0.5 m/s. This parameter setup was also used to build up the ionic layer. After the parameter variations, this reference state was re-established daily before the furnace was shut down. In doing so, the reproducibility of

the reference signal was ensured on a daily basis with the drawback, that the majority of the data points are located within relatively narrow spaces of the parameter variation range.

Hence, the methodology was changed in the waste wood test run to achieve a better distributed data set. Here, only one steel temperature was investigated per day, and the flue gas temperature was slowly but steadily increased and after reaching the maximum flue gas temperature of approximately 880 °C decreased again to a temperature of around 730 °C. Meanwhile the flue gas velocity was kept constant to 3.6 ± 0.5 m/s. To ensure the reproducibility of the measurement data, the steel temperature variations were repeated at least two times. The influence of flue gas velocity was investigated subsequently to the temperature variations. Due to time restrictions, only one steel (480 °C) and flue gas (730 °C) temperature were investigated during the flue gas velocity variations.

To determine the combustion conditions during the corrosion probe test runs, balance test runs were performed. This data is of major importance since relevant processes e.g. release of volatile ash forming species, like K, strongly depend on the combustion conditions prevailing. The characteristic data of the combustion conditions can be found in Table 4.1. The fuel used within the test runs is described in detail in the following section.

Table 4.1: Combustion conditions during the corrosion probe measurements
Explanations: mv ... mean value, std ... standard deviation, w.b. ... wet basis, d.b. ...dry basis, NCV ... net calorific value, Nm³ ... m³ at 0 °C and 101325 Pa; the measurement positions can be found in Figure 3.1

		wood chips		**waste wood**	
parameter	unit	mv	std	mv	std
fuel power input related to NCV	kW	23.4		25.7	
fuel flow rate	kg/h w.b.	6.3		6.7	
temperature primary combustion zone	°C	818	15	892	17
temperature secondary combustion zone	°C	896	29	872	8
CO_2 (at chimney entry)	Vol.-% d.b.	11.1	0.9	11.8	1.1
O_2 (at chimney entry)	Vol.-% d.b.	9.5	0.9	8.7	1.2
CO (at chimney entry)	mg/Nm³ d.b. 13% O_2	13.8	0.7	18.2	41.6
SO_x (at measurement port)	mg/Nm³ d.b. 13% O_2	8.6	2.8	42.6	12.2
HCl (at measurement port)	mg/Nm³ d.b. 13% O_2	6.6	3.8	68.9	29.5
primary air flux	Nm³/h	15.4		14.5	
secondary air flux	Nm³/h	16.1		16.3	
total air flux	Nm³/h	31.5		30.9	
flue gas recirculation volume flux	Nm³/h	-		5.8	
air ratio primary combustion zone (including flue gas recirculation)		0.86		0.98	
total air ratio (including flue gas recirculation)		1.50		1.50	

4.1.2 Fuel

As already mentioned, two test runs have been carried out to investigate the influence of different fuel compositions on the high-temperature corrosion. Here, chlorine as well as the heavy metal content of the fuel is of special interest. Big differences regarding the content of these species can be typically found between chemically treated and untreated woody biomasses. Chemically untreated forest wood chips, with a rather low chlorine and heavy metal content were used as fuel in the first test run. In the second test run quality sorted waste wood (A1–A2, according to German standards), which has a significantly higher chlorine and heavy metal content, was used as fuel. The compositions of the fuels are presented in Table 4.2. The molar 2S/Cl ratios calculated based on the fuel analyses for wood chips is 6.9, and for waste wood is 1.4, which indicates a higher corrosion potential according to [12].

The fuel used in the first test run was chemically untreated forest wood chips mainly consisting of spruce. The biomass mostly consisted of logging residues, but also contained stem wood and bark as well as a low fraction of needles and fine particles. The fuel was taken from the storage of the biomass combined heat and power plant Baden (Lower Austria, Austria), which uses biomass harvested in the forests in a radius of approximately 50 km around Baden. Before the wood chips could be used in the coupled fixed bed/drop tube reactor (described in Section 3.1), the particle size had to be reduced by chopping from P63c to P45Ac according to EN 14961-1:2010. The wood chips used within the test run had the following specifications according to EN 14961-1:2010: origin… 1.1.4.4 and 1.1.4.5 (logging residues), particle… P45AC, moisture… M25, ash… A3.0, bulk density… BD200. The chemical composition of the wood chips can be found in Table 4.2. The three samples for the fuel analyses have been taken at different times over the whole test run from the fuel storage of the biomass reactor.

The fuel used in the second test run was quality sorted waste wood A1-A2 according to German standards. The biomass originates from construction demolition wood, supplied by the company “Frikus Friedrich Kraftwagentransport und Speditions-GmbH”. Prior to combustion, the waste wood was shredded until it fited into the feeding system of the drop tube reactor. Bigger metal parts were sorted out by hand to minimize the danger for a material failure in the feeding system. However, due to the shredding the fuel had a rather inhomogeneous size distribution, which is not in accordance with the EN 14961-1:2010. The other specifications according to this norm have been as follows: moisture … M25, ash … A3.0, bulk density … BD200. The chemical composition of the fuel is presented in Table 4.2. Also in this case the fuel samples have been taken at different times over the test run from the fuel storage of the biomass reactor.

A comparison with database values shows that the composition of the fuel is representative for forest wood chips respectively waste wood A1-A2 [31].

Table 4.2: Results of fuel analyses
Explanations: w.b. … wet basis; d.b. … dry basis; mean … mean value; std.-dev. … standard deviation; n … number of fuel samples

	Unit	**forest wood chips** n=3		**waste wood** n=8	
		mean	std.-dev.	mean	std.-dev.
moisture content	wt% w.b.	24.1	3.4	20.7	2.0
ash content	wt% d.b.	2.4	0.7	2.1	0.6
C	wt% d.b.	48.1	-	47.7	0.3
H	wt% d.b.	5.9	-	6.1	0.1
N	wt% d.b.	0.3	-	0.9	0.2
S	mg/kg d.b.	280	8	593	138
Cl	mg/kg d.b.	90	18	1154	798
Si	mg/kg d.b.	2122	1382	2372	948
Ca	mg/kg d.b.	6045	998	3533	1021
Mg	mg/kg d.b.	739	369	506	127
K	mg/kg d.b.	1660	147	868	71
Na	mg/kg d.b.	63	15	536	159
P	mg/kg d.b.	204	18	89	13
Al	mg/kg d.b.	446	171	593	179
Fe	mg/kg d.b.	265	77	625	516
Mn	mg/kg d.b.	108	54	91	12
Zn	mg/kg d.b.	19	1	143	51
Pb	mg/kg d.b.	1	0	35	15
2S/Cl ratio	mol/mol	6.9	0.6	1.4	0.5

4.1.3 Deposit formation

The high-temperature corrosion mechanism prevailing in biomass fired boilers is strongly influenced by the deposits formed on top of the steel surface. However, the deposit formation in biomass fired boilers is strongly time-dependent. Due to the low heat conductivity of the ash layer, the surface temperature strongly increases with increasing thickness of the layer. Therefore, the initially formed layers as well as the final deposits formed on the online corrosion probes have been carefully investigated.

Initial deposit formation

Short-term deposit probe measurements have been carried out to investigate the initial deposits formed (see Section 3.1.5). The chemical composition of the deposits has been determined by means of SEM/EDX analyses (see Section 3.1.8). Two deposit probe measurements were performed for each fuel. In the forest wood chips test run the temperatures 480 °C and 550 °C were investigated. In the case of waste wood, the

temperatures 450 °C and 550 °C were investigated, representing the lowest and highest steel temperature in the test run. The deposit samples were taken at the pre-fixed reference state which means a flue gas temperature of around 700 °C and a superficial flue gas velocity around 2.8 m/s for forest wood chips and 3.6 m/s for waste wood, respectively. The results of these analyses are shown in Figure 4.1.

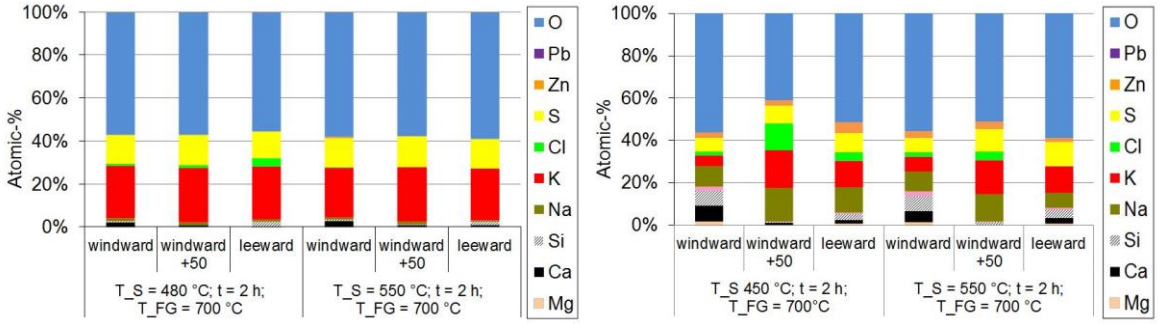

Figure 4.1: Results of the EDX-analysis of the deposits formed during the deposit probe measurements for forest wood chips (left) and waste wood (right) [Paper I]
Explanations: T_S... steel temperature, t... duration time of deposit measurement, T_FG... flue gas temperature

As one can see in Figure 4.1 (left) the deposit layer of the fuel forest wood chips mainly consists of potassium and sulphur. Based on the molar ratios measured the results suggests the presence of potassium sulphate. Chlorine, as a key species for active Cl-induced oxidation can only be found in very small amounts in the case of 480 °C steel temperature, with a slightly higher concentration on the leeward side of the probe ring. Since no chlorine can be found for 550 °C steel temperature it is concluded that the condensation temperature of the gaseous chlorides lies somewhere between 480 °C and 550 °C. Additionally, the amounts of Si, Ca and Mg, which are typical elements in the coarse fly ash [42], are rather low. Hence, the overall deposit formation is mostly caused by the deposition of fine particles, due to thermophoresis.

However, the results for waste wood considerably differ from the forest wood chips results (see Figure 4.1 right). Chlorine can be found in the deposits of both measurements, although the amount is a little bit higher for 450 °C. This indicates a higher condensation rate of chlorine containing salts for the lower temperature. Also the amounts of the typical coarse fly ash elements Si, Ca and Mg are significantly increased compared to forest wood chips. Furthermore, in contrast to the forest wood chips deposits the waste wood deposits contain a considerable amount of Zn and Na. This result was already indicated by the fuel composition (see Table 4.2).

The RBU's determined within the measurements can be compared to gain information regarding the general deposit built-up speed. For forest wood chips the RBU's measured are 2.8 g/m²h for 480 °C and 1.4 g/m²h for 550 °C. For waste wood the RBU's determined are 6.9 g/m²h for 450 °C and 7.0 g/m²h for 550 °C. Therefore, a faster deposit build-up has to be expected in the case of waste wood in the initial state of the test run.

Deposits formed on the online corrosion probes

Due to increasing surface temperatures, the long-term deposition behaviour can vary significantly from the findings obtained from short-term deposit probe measurements. To gain some information regarding this time dependence, the final deposit layers formed on the corrosion probes of both test runs have also been investigated. Figure 4.2 (left) shows the deposits on the corrosion probe formed during the test run with forest wood chips, whereas Figure 4.2 (right) shows the waste wood deposits. One can see that the amount of deposits formed on the online corrosion probes is considerably higher in the case of waste wood. This result was already indicated by the short time RBU's measured.

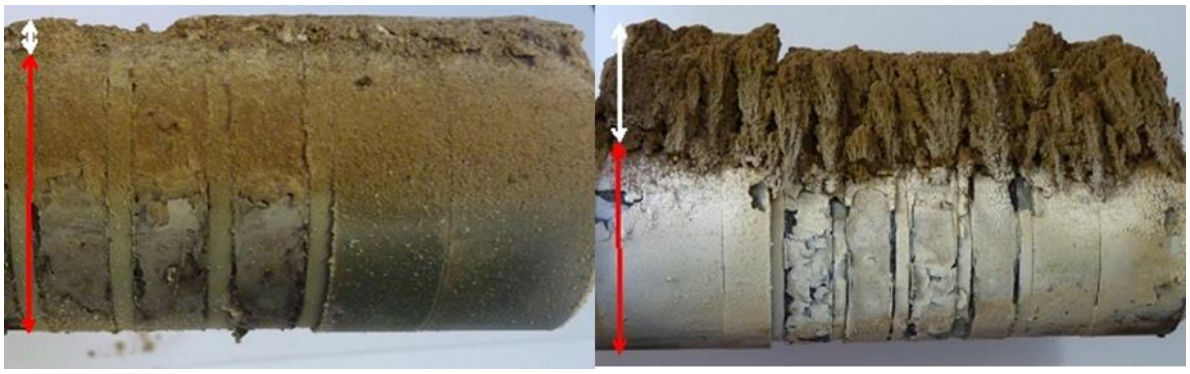

Figure 4.2: Photo of the corrosion probes after the forest wood chips test run (left) and after the waste wood test run (right) [Paper I].
Explanation: The exposure time in the case of wood chips was 325 h and 329 h in the case of waste wood, respectively. The thickness of the deposit layer is indicated by the white arrow, whereas the red arrow indicates the diameter of the probe; windward side above, leeward side below.

In addition to the different build-up velocity the two deposits also differ regarding their structure. The deposits of forest wood chips are powdery and loosely bound to the corrosion probe. No sintering occurred. The waste wood deposits on the other hand are sintered to single columns. The binding between the sintered particles is quite strong but the deposit layer has only a weak binding to the corroded probe surface. Therefore, the layer can be easily removed.

To investigate time-dependent changes in the composition of the deposit layers they have been analysed by mean of SEM/EDX (see Section 3.1.8) as well as by wet chemistry analyses (see Section 3.1.6). The results of the wet chemical analyses can be found in Figure 4.3.

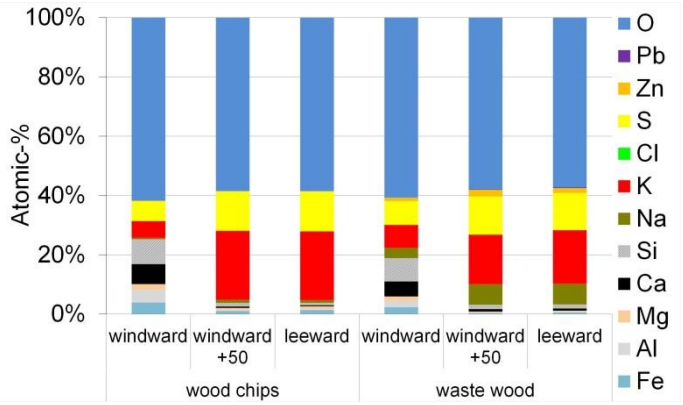

Figure 4.3: Chemical composition of the deposits found on the corrosion probes after the test runs [Paper I].

In contrast to the deposit probe measurements no chlorine could be found in the deposits of the corrosion probes. This result and its effect on the corrosion mechanism will be discussed in Section 4.1.4.

The relative amount of coarse fly ash on the windward side of the probe increased significantly compared to the short-term deposit probe measurements. This can be explained by the increasing surface temperatures over time. With increasing surface temperatures the condensation of ash vapours gets lower. The stickiness probability of coarse fly ash particles on the other hand increases with increasing particle as well as surface temperatures (see Section 3.2.3). Hence, the impaction of the coarse fly ash particles becomes more relevant.

In the case of waste wood, the considerably higher amount of coarse fly ash particles in the flue gas lead to an increased amount of coarse fly ash already in the short-term deposit probe measurements. Hence, the time-dependent effect found for wood chips could not be found in the case of waste wood. In contrast to the short-term deposit probe measurements traces of Pb can be found in the deposits of the corrosion probe. An explanation for this finding can be given by the strong deviations of the heavy metal content in the fuel (see Table 4.2) and the short measurement time of the deposit probe measurements. Also for waste wood no chlorine could be attested in the final deposits formed on the online corrosion probe.

4.1.4 SEM/EDX analyses

To investigate the chemical structure of the corrosion products and the deposit layer, SEM/EDX element mappings have been carried out on the windward, windward + 50° and leeward side of a corrosion probe ring of each test run.

The results of these analyses can be found in Figure 4.4 to Figure 4.6. The information obtained for the three different ring sides is generally the same.

The EDX analyses of the final deposit layers confirm the results of the chemical analyses already presented in Section 4.1.3. The results can be summarized as follows.

In the case of the wood chips test run the deposits mainly consist of potassium sulphate. In addition, Ca and Si oxides are embedded in this deposit layer. However, it is known that solid sulphates as well as coarse fly ash particles have only a minor influence on high-temperature corrosion [18]. The deposits formed in the waste wood test run are qualitatively comparable although the amount of coarse fly ash particles is higher.

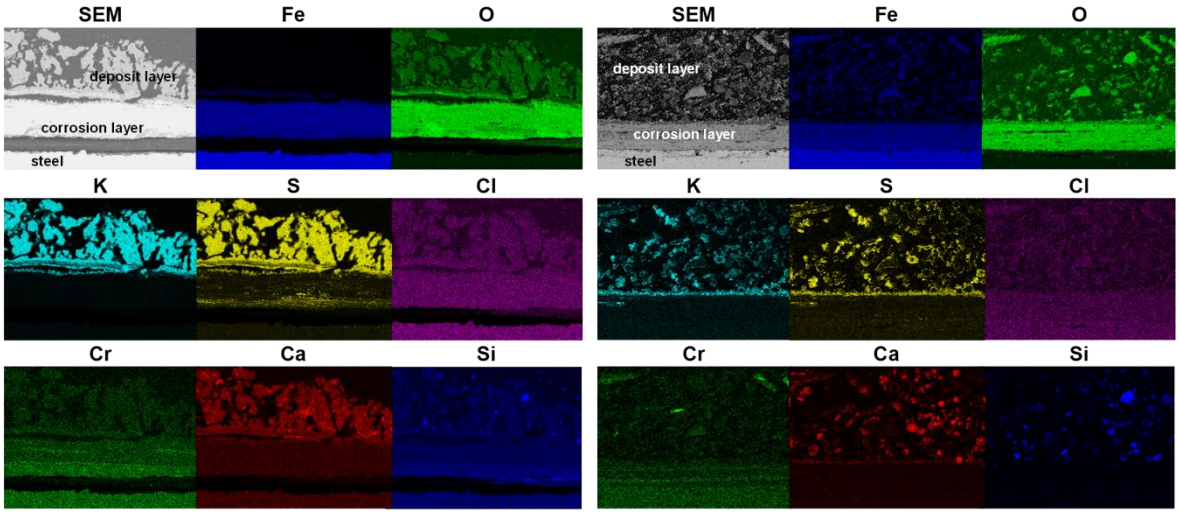

Figure 4.4: SEM/EDX element mappings through the cross section of a corrosion probe ring on the windward side. Results for forest wood chips are shown left and for waste wood right [Paper I].

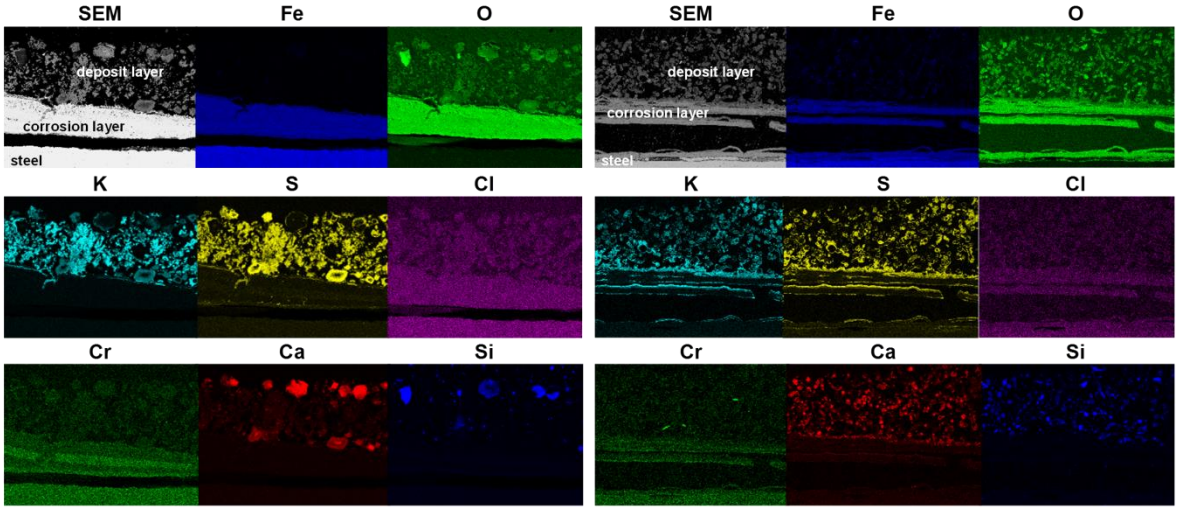

Figure 4.5: SEM/EDX element mappings through the cross section of a corrosion probe ring on the windward + 50° side. Results for forest wood chips are shown left and for waste wood right.

At the corrosion front two aspects are of special interest. The first one is the absence of chlorine in both test runs. One can only see the equally distributed background noise of the EDX analyses in the Cl mappings (see Figure 4.4 to Figure 4.6). Secondly, sulphur can be found in high concentrations at the corrosion front. This sulphur-rich layer is stronger

developed in the case of forest wood chips but it can also be found in the case of waste wood.

To gain more information regarding this layer also quantitative EDX analyses have been carried out. These analyses show that it consists of Fe, O and S. The sulphur concentration of the layer strongly varies. With highly resolved spot analyses areas solely consisting of the elements Fe and S could be detected (see Figure 4.7, zone 3). This indicates that the layer consists of a mixture of the two phases iron sulphide and iron oxide rather than of iron sulphate.

Due to the low Cr content of the steel (see Table 3.1) no protecting Cr_2O_3 layer is formed at the corrosion front (see Cr element mapping in Figure 4.4 to Figure 4.6).

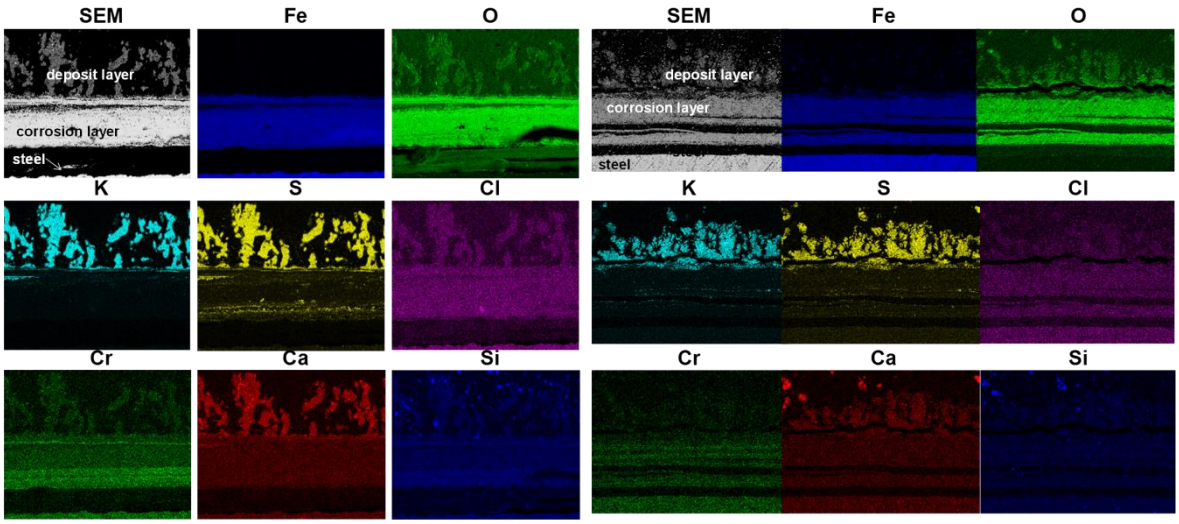

Figure 4.6: SEM/EDX element mappings through the cross section of a corrosion probe ring on the leeward side. Results for forest wood chips are shown left and for waste wood right.

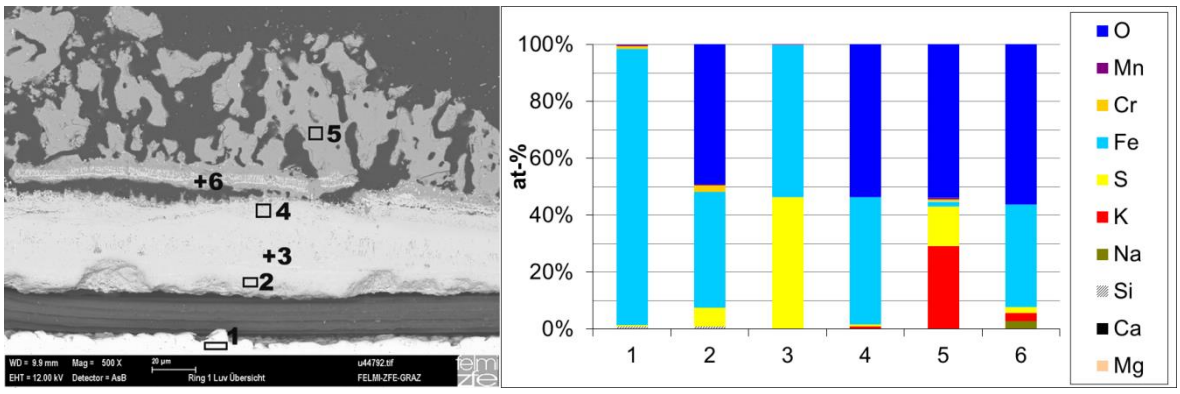

Figure 4.7: SEM image of the deposit layer and corrosion products of the wood chips corrosion probe test ring (left) and quantitative results of the EDX analysis of different zones (right).

The results for forest wood chips are in good agreement with comparable measurements carried out in a wood chips fired CHP plant [31]. Within that work also an enrichment of sulphur at the corrosion front was reported as well as the absence of chlorine throughout the layer of corrosion products.

4.2 Corrosion rates measured and empirical model development

The first goal of the work presented was the determination of the most influencing parameters. In both test runs the most influencing operating parameters have been T_S, T_{FG} and v_{FG}. Other parameters e.g. the oxygen content in the flue gas had almost no effect on the corrosion rate measured. This fact will be discussed in detail in Section 5.

All three influencing parameters have in common that they affect the corrosion rate measured immediately[4]. Exemplary measurement results of representative test days can be found in Figure 4.8 (wood chips) and Figure 4.9 (waste wood). One can also see that the influence of a certain parameter variation on the corrosion rate is well reproducible.

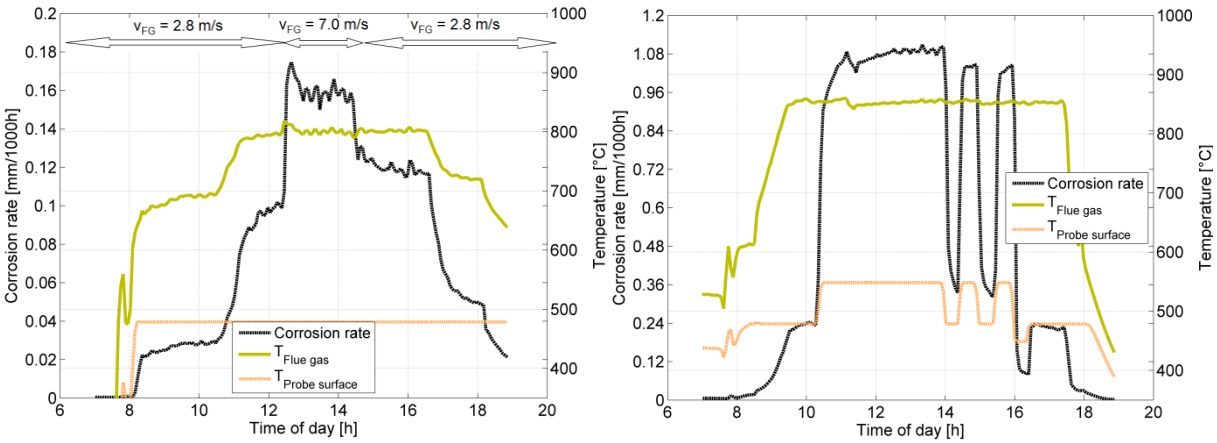

Figure 4.8: Two examples of measured corrosion rates over a testing day (wood chips test run).
Explanation: In the left figure the flue gas velocity v_{FG} was varied between 2.8 to 7.0 m/s in the right figure the flue gas velocity v_{FG} was kept constant at 2.8 m/s.

The corrosion signal measured during the combustion of forest wood chips shows an exponential dependence on the flue gas temperature (see Figure 4.11, left) as well as on the steel temperature (see Figure 4.12, left). The trend of an increased corrosion attack with an increased flue gas velocity is shown in Figure 4.13 on the left hand side.

[4] As described in detail in [22], [21] and [39], the data recording rate of the online corrosion probe and hence, time resolution is 4 minutes. Therefore, the term "immediately" technically speaking means within a timeframe of 4 minutes.

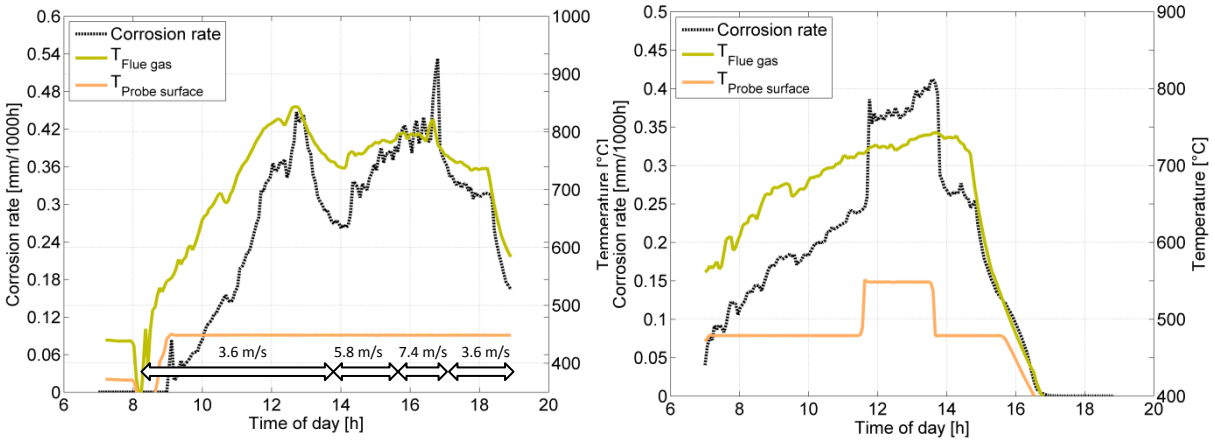

Figure 4.9: Two examples of measured corrosion rates over a testing day (waste wood test run).
Explanation: In the left figure the flue gas velocity v_{FG} was varied between 3.6 to 7.4 m/s in the right figure the flue gas velocity v_{FG} was kept constant at 3.6 m/s.

Also in the waste wood test run an exponential dependence on the flue gas temperature could be found (see Figure 4.11, right). However, the dependence on the steel temperature differs. While, for low steel temperatures (< 500 °C) the corrosion rate significantly increases with increasing steel temperatures, this dependence cannot be found for steel temperatures above 500 °C. In this temperature range the measured signal stagnates and even slightly decreases (see Figure 4.12, right). To rule out a (systematic) measurement error all variations have been performed at least two times the trend shown could be reproduced in any case. Additionally, the measured signal is more scattered than the one of the forest wood chips test run. Most certainly this finding can be explained by the strong deviations of the waste wood composition during the test run (see Table 4.2). Therefore, only mean values and standard deviations over ± 5 °C are shown in Figure 4.11 (right) and Figure 4.12 (right). Also for waste wood, a dependence on the flue gas velocity could be found (see Figure 4.13, right).

However, the influence of the flue gas velocity is moderate for both fuels (see Figure 4.13). Hence, an adequate mathematical correlation is difficult to determine, since the scattering of the measured corrosion rates for constant flue gas and steel temperatures over the whole test run are of similar orders then the influence of the flue gas velocity. Still, the influence of the flue gas velocity can be seen on the time curve of the measured data. Examples of such time curves can be found in Figure 4.10 for waste wood and in Figure 4.8 for wood chips, respectively.

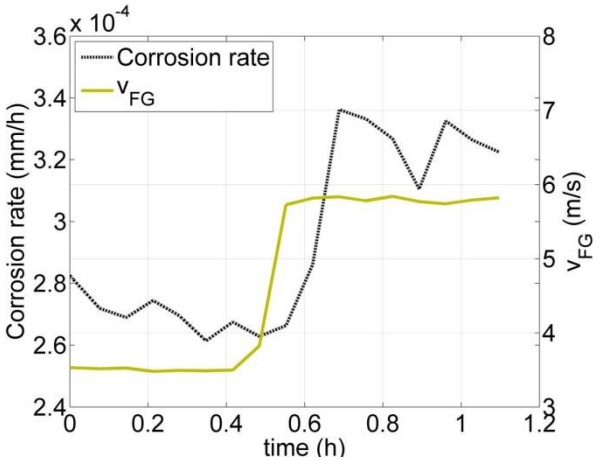

Figure 4.10: Example of a time curve of the measured corrosion rate and flue gas velocity for waste wood [Paper I].
Explanation: Steel temperature has been kept constant to 480 ± 0.5 °C; Flue gas temperature has been kept constant to 755 ± 10 °C; v_{FG} ... flue gas velocity

Based on the online corrosion probe data, an empirical function has been derived. Due to the already described dependencies found, the empirical model is a combination of an Arrhenius function, which describes the exponential dependence on the flue gas and the steel surface temperature. The dependence on the flue gas velocity is taken into account with an additional linear factor (see Eq. 8).

The coefficients of the empirical model have been determined by a stepwise approach using a least square method. First the coefficients $A(T_S)$ and $B(T_S)$ have been optimized for each steel temperature investigated (dependence on T_S; v_{FG} has been kept constant). Then the functional dependencies of the optimized parameters $A(T_S)$ and $B(T_S)$ on the steel temperature have been determined for constant flue gas velocities. Finally, the dependence on the flue gas velocity is taken into account by a linear correction of the empirical function. Due to the moderate influence and the scattered data the linear dependence is a first but sufficient assumption.

The optimized coefficients are shown in Table 4.3. In Figure 4.11 to Figure 4.13 the calculated corrosion potential using Eq. 7 is plotted as solid lines. One can see that the optimized function correlates adequately with the measured data.

In addition, the performance of the newly developed model was tested by re-calculating the time resolved corrosion signal measured within the test runs. Examples of this testing can be found in Figure 4.14 (wood chips) and Figure 4.15 (waste wood). A comparison of the measured and the calculated signal shows that the model developed is able to follow the measured signal with good accuracy. In addition, the dependencies measured for forest wood chips are in good agreement with those found in real-scale CHP plants [31].

$$k = A(T_S) \cdot \exp\left(\frac{B(T_S)}{R \cdot T_{FG}}\right) \cdot C(v_{FG})$$

$$A(T_S) = \exp(a_1 \cdot T_S^2 + a_2 \cdot T_S + a_3)$$

$$B(T_S) = b_1 \cdot T_S^2 + b_2 \cdot T_S + b_3$$

$$C(v_{FG}) = c_1 \cdot v_{FG} + c_2$$

Eq. 8

Explanation: k... corrosion rate (mm/1000h), $A(T_S)$... pre-exponential factor (mm/h), R ... gas constant (J/molK), $B(T_S)$... activation energy (J/mol), T_{FG} ... flue gas temperature (K), T_S ... steel temperature (K), v_{FG} ... flue gas velocity (m/s), $C(v_{FG})$ ...linear correction factor and $a_{1-3}, b_{1-3}, c_{1-2}$ ... coefficients

Table 4.3: Optimized coefficients of the empirical function [Paper I]

fuel	a_1	a_2	a_3	b_1	b_2	b_3	c_1	c_2
Forest wood chips	-	-0.083	73.9	-	982.0	-858364	0.07	0.81
Waste wood	0.00044	-0.707	287.4	-4.627	7375.8	-2994500	0.11	0.59

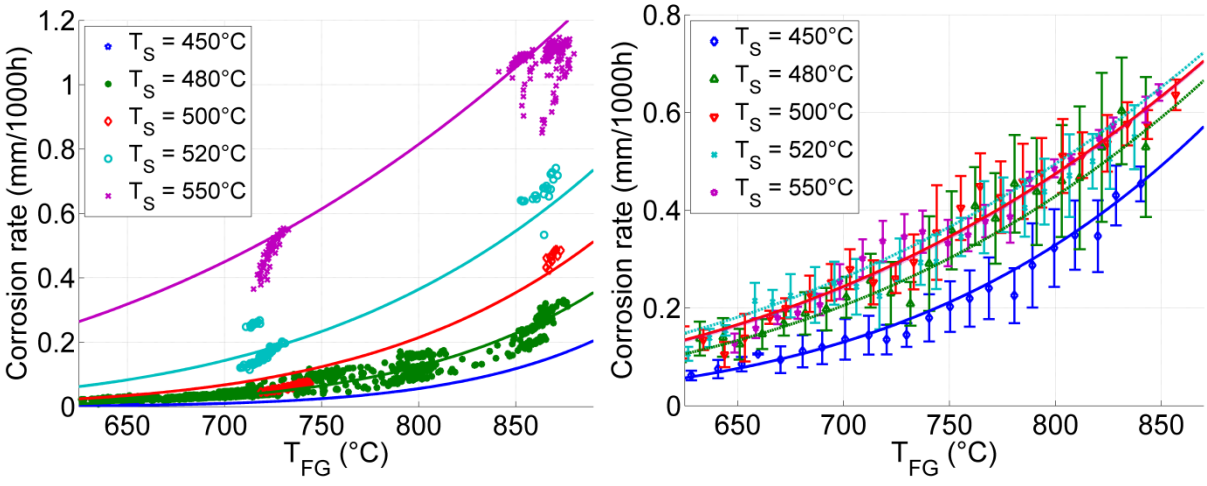

Figure 4.11: Empirical model in comparison to measurement values for forest wood chips (left) and for waste wood (right) as a function of flue gas temperature [Paper I].
Explanation: Flue gas velocity has been kept constant at 2.8 ± 0.5 m/s in the case of forest wood chips and at 3.6 ± 0.5 m/s in the case of waste wood; TS ... steel temperature, TFG ... flue gas temperature

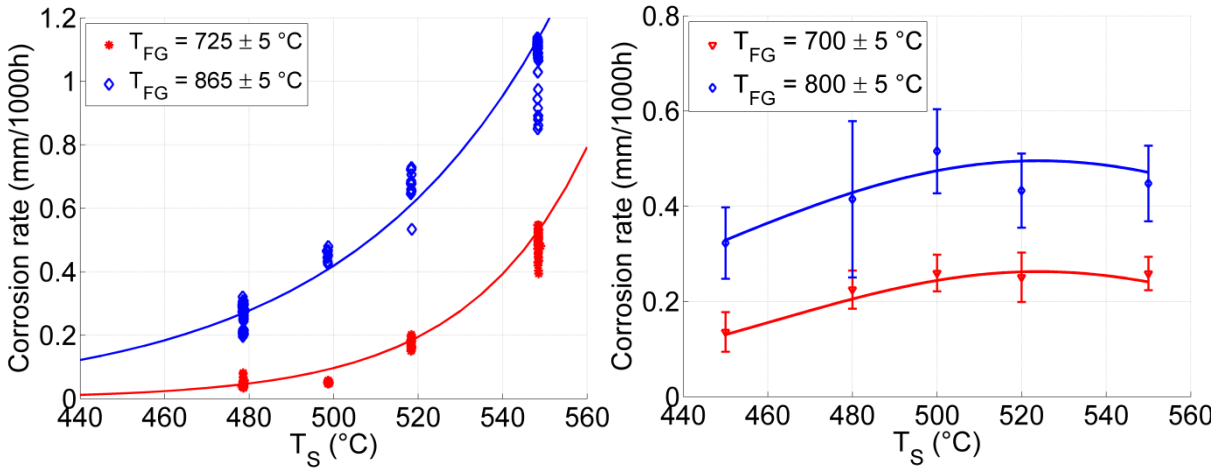

Figure 4.12: Empirical model in comparison to measurement values for forest wood chips (left) and for waste wood (right) as a function of steel temperature [Paper I].
Explanation: Flue gas velocity has been kept constant to 2.8 ± 0.5 m/s in the case of forest wood chips and to 3.6 ± 0.5 m/s in the case of waste wood; T_S ... steel temperature, T_{FG} ... flue gas temperature

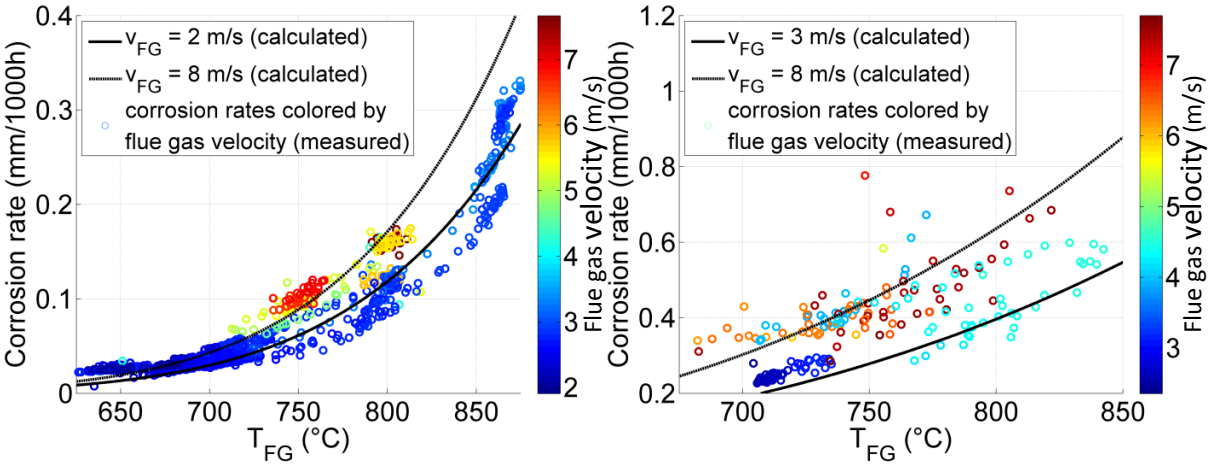

Figure 4.13: Empirical model in comparison to measurement values for forest wood chips (left) and for waste wood (right) as a function of flue gas temperature for various flue gas velocities [Paper I].
Explanation: The steel temperature has been kept constant at 480.0 ± 0.5 °C, T_{FG} ... flue gas temperature, v_{FG} … flue gas velocity

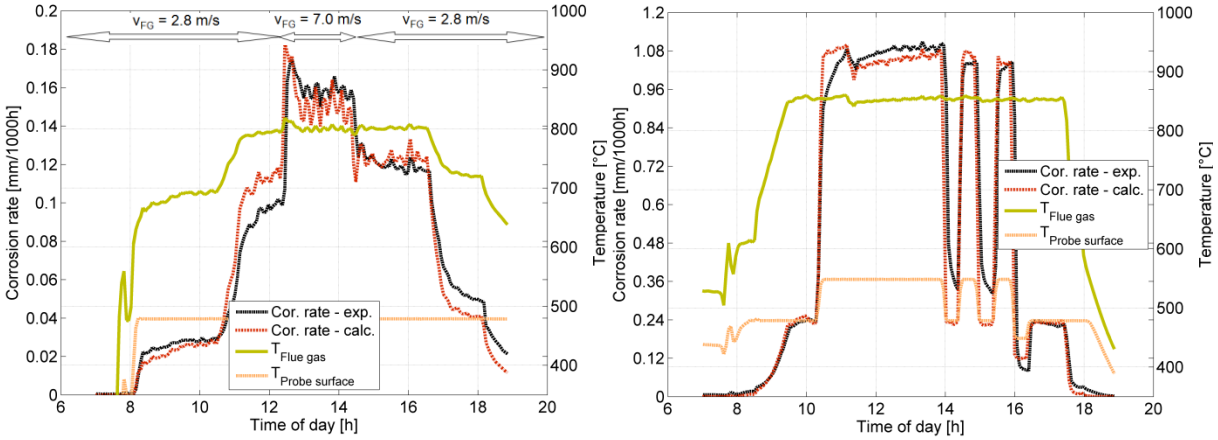

Figure 4.14: Two examples of measured corrosion rates in comparison with the calculated corrosion rate over a testing day (wood chips test run).
Explanation: In the left figure the flue gas velocity v_{FG} was varied between 2.8 to 7.0 m/s in the right figure the flue gas velocity v_{FG} was kept constant at 2.8 m/s.

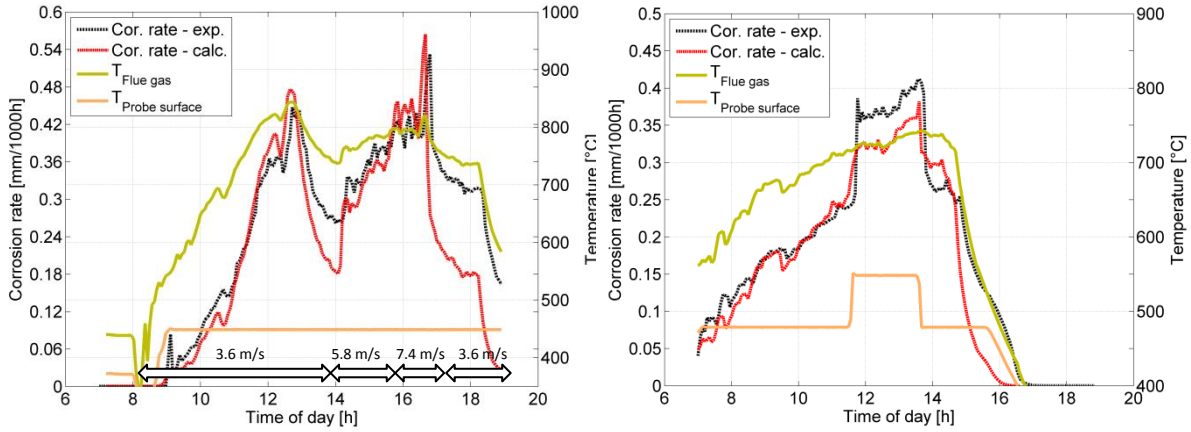

Figure 4.15: Two examples of measured corrosion rates in comparison with the calculated corrosion rate over a testing day (waste wood test run)
Explanation: In the left figure the flue gas velocity vFG was varied between 3.6 to 7.4 m/s in the right figure the flue gas velocity vFG was kept constant at 3.6 m/s.

4.3 Possible high-temperature corrosion mechanisms

The discussion on the dominating corrosion mechanisms in this section is only valid for the test runs performed within this work (short-term measurements with temperature variations). The short measurement time as well as the temperature variations may influence the deposits formed as well as the speed of chemical reactions, e.g. sulphation of deposited KCl. This is already indicated by the differences of the deposits formed on the 2h deposit probe measurements and the deposits found on the online corrosion probes subsequent to the test runs which lasted approximately 325 hours (see Section 4.1.3). Hence, the corrosion mechanisms in steady-state operated plants may deviate from the corrosion mechanisms proposed in this section. A detailed discussion on possible high-temperature corrosion mechanisms for steady-state operation can be found in Section 5.2.

Many authors (e.g. [19], [88]) reported a compact inner corrosion layer, consisting of $FeCl_2$, in the case of active Cl-induced oxidation (detailed mechanism can be found for example in [88]). In some cases an additional FeS or FeS_2 layer subsequent to the inner $FeCl_2$ layer is reported (e.g. [21], [88]).

In this work the EDX analyses confirm the presence of an iron sulphide layer. On the other hand no traces of chlorine neither in the deposit nor in the corrosion layer could be found. Based on these findings the dominating corrosion mechanism cannot be determined with certainty. However, due to the complete missing of chlorine it is suggested that the main corrosion mechanism prevailing is not active Cl-induced oxidation. It is most likely that the condensed chlorine species in the initial state of the measurement campaigns (see Section 4.1.3) become sulphated and that the supply of chlorine species cannot be maintained due to increasing surface temperatures over time.

As discussed in detail in [89], in the case of the forest wood chips test run, the main deposit component is solid potassium sulphate. It is known that solid K_2SO_4 behaves rather inert and hence, has only a minor effect on the corrosion behaviour [18] under the framework conditions investigated within this work. The only known mechanism which causes sever corrosion involving sulphates is hot corrosion (see [18], [19], [90] and Section 2.2.3). However, this mechanism can be excluded as dominating corrosion mechanism due to a missing of a molten sulphate layer. Further, the chromium content of the steel 13CrMo4-5 is too low, to form a protective chromium oxide layer. Therefore, a corrosion mechanism involving the dissolution of such a layer (as proposed in e.g. [91]) can also be excluded.

Based on this information it is suggested that the main corrosion mechanism in this case is the oxidation of the steel by oxygen in the flue gas. The formation of the iron sulphide layer can most likely be explained by the reaction of gaseous SO_2 with the steel or oxide layer [92]. However, only little is known on the effect of SO_2 on the corrosion rate in the temperature range of interest [93]. Most studies were performed under significantly higher SO_2 concentrations and temperatures [92]. The only exception is a work of Järdnäs et al. [94] who found decreasing corrosion rates in the presence of small amounts of SO_2 in the temperature range of interest. However, this work excludes any interaction with other corrosive gaseous species such as HCl, H_2O or corrosive salts e.g. alkali chlorides. Hence, extrapolations of these results to the rather complex situation prevailing in biomass fired boilers are not meaningful. This issue is further discussed later on in Section 5.2.2.

In the case of waste wood the corrosion behaviour found within the experiments differs strongly from that of forest wood chips. For the lower temperatures investigated (T_S < 480 °C, T_{FG} < 700 °C) the measured corrosive attack is much higher. This is in good agreement with the lower molar 2S/Cl ratio and the higher concentrations of heavy metals (see Section 4.1.2) in the case of waste wood. This behaviour changes with increasing temperatures since the corrosion potential of waste wood does not show the exponential dependence on the steel temperature. Therefore, it is most likely that an additional or another mechanism is responsible for the corrosion behaviour found.

A stagnating or even decreasing corrosion rate as a function of an increasing temperature is typically found in the case of hot corrosion type II (e.g. [50], [95] and [96]). Here, depending on the temperature prevailing, corrosion occurs by basic or acidic fluxing in a thin molten layer of alkali and heavy metal sulphates and/or chlorides.

In general, the melting temperatures of Na_2SO_4, K_2SO_4 as well as mixtures of these sulphates are too high for melts to occur. Nevertheless, according to [51] eutectic mixtures with very low melting temperatures can be formed in the presence of heavy metal rich sulphates. Since the amount of Zn found in the deposits is considerable, the formation of a partly molten sulphate layer could be possible. This layer could be responsible for the corrosion behaviour found.

This is also in agreement with lab-scale work of van Lith [97] in which the corrosion behaviour under conditions typically prevailing in waste wood fired boilers has been investigated. Within this work molten deposit layers were found at 500 °C.

4.4 Application range of the empirical model

To allow a broad application of the empirical model it was ensured that the chemical composition of the fuels used for the test run are representative for chemically treated and untreated woody biomasses (see Section 4.1.2). In addition it was ensured that the combustion conditions (fuel bed temperatures, air staging, etc.) during the test runs are typical for biomass fired grate combustion systems (see Section 4.1.1). Therefore, the model is well-applicable to estimate the high-temperature corrosion potential for woody biomass fired grate combustion systems with a main focus on water tube steam boilers typically operating with live steam temperatures between 450 °C and 550 °C which often use 13CrMo4-5 steel for the superheaters. However, still some restrictions on the applicability of the empirical model have to be made.

Since the empirical model is based on experimental data the application range of the model is generally limited to the temperature and velocity ranges investigated during the corrosion probe measurements (see Section 4.1.1). The empirical model does not consider the actual deposit composition formed on the steel surface. Hence, the application of the empirical model is also limited to comparable fuel compositions and combustion conditions (e.g. fuel bed temperatures, oxygen access, etc). This is essential since the model does not take transport processes or chemical reactions into account.

Additional limitations and problems arise for the application in small-scale boilers. On the one hand the return temperature in hot water boilers is around 70 °C. Due to the good heat transfer coefficient on the waterside of the boiler and the high heat conductivity of the boiler steel, the return temperature of the water is similar to the steel temperature on the flue gas/deposit side of the heat exchanger. Hence, the steel temperature in a hot water boiler is far below the lowest steel temperature investigated within the online corrosion probe test runs. High temperature corrosion phenomena are generally observed at temperatures above 200 °C to 300 °C. Due to this definition it is not expected

that high temperature corrosion occurs on the water cooled walls of small-scale water boilers.

Metallic components of a small-scale hot water boiler which have high enough surface temperatures for the application of the empirical model are the turbulators in the convective section of the boiler and the grate of the furnace. However, one has to keep in mind that it is also possible that the temperatures of these metallic parts can exceed the investigated temperature range by far (e.g. uncooled grates).

As already explained, the high-temperature corrosion model developed within this work is only valid in oxidizing conditions. Hence, the corrosion occurring on the grate or on other metallic components (e.g. temperature sensors) in the primary combustion zone, were the oxygen access is limited, cannot be evaluated with the model developed.

The turbulators on the other hand are not directly cooled by the water[5]. Hence, their temperature strongly depends on the load conditions. While the temperature range investigated is sufficient for nowadays and future water tube steam boilers, the steel temperature of the turbulators can easily exceed the highest steel temperature investigated (550°C). Above 570 °C the formation of Wüstit (FeO) during the oxidation of iron is thermodynamically favoured [98], which increases the corrosion rate significantly[6] (see Section 2.2.1). To prevent the turbulators from uncontrolled rapid oxidation typically a high alloy steel is used as material with a Cr content higher than 10 wt.-%. These steels are able to form a passivating Cr_2O_3 layer, which sufficiently suppresses a further oxidation of the material. Even if the steel temperature is, due to the load conditions, below 570 °C, the empirical model can only predict the corrosion potential of a low alloy steel, which is an uncommon material for turbulators in real scale hot water boilers.

Due to these reasons the model can hardly be applied meaningful in hot water boilers and thermal-oil boilers.

However, also in the case of CHP plants the same limitations exist. Hence, due to the low steel temperatures the model cannot be applied to estimate the high-temperature corrosion potential of evaporator grids and finned walls since their steel temperatures are typically around 300 °C. Also the corrosion of the grate or other metallic elements in the primary combustion zone cannot be validated with the model developed, due to the reducing conditions prevailing in this area.

4.5 Application of the model in a combined heat and power plant

To test the newly developed model it was applied for a CFD simulation of flow and heat transfer in a 42 MW_{th} fired CHP plant (38 MW_{th} boiler).

[5] Still they interact with the water cooled walls by means of radiation, which leads to a cooling of the turbulators.

[6] The formation of wüstit and the accompanying rapid speed of oxidation is often called “scaling” of the metal.

Selected results of the application of the model have been published in an invited article for a special issue of the international peer reviewed journal Biomass & Bioenergy [Paper II].

4.5.1 Description of the case study

Within the case study (CS), the high-temperature corrosion potential on the superheater bundles has been calculated for three different cases:

- **CS1:** Actual state analysis under full load conditions (live steam temperature of 453°C)
- **CS2:** A switch of the flow direction of the final superheater bundle from parallel to counter-flow (live steam temperature of 453 °C)
- **CS3:** Enhanced live steam temperature of 480°C

Table 4.4 provides the most relevant operating conditions of the boiler whereas Table 4.5 provides relevant information regarding the superheater tube bundles.

Table 4.4: Relevant boiler information (Table adapted from **[Paper II]**)

Fuel power input related to NCV	41.9	MW
Boiler output	37.8	MW
Flue gas mass flow	35.6	$kg \cdot s^{-1}$
saturated steam temperature	279	°C
saturated steam pressure	6300	kPa
live steam temperature	453	°C
live steam pressure	6100	kPa

Table 4.5: Relevant boundary conditions for the superheater tubes (Table adapted from **[Paper II]**)
Explanation: SH1-SH3… superheater tube bundle 1-3, ccf … cross counter flow, cpf … cross parallel flow

		SH1	**SH2**	**SH3**
Type	-	bank of in-line tubes		
Operating mode	-	ccf	ccf	cpf
Outer tube diameter	mm	38	38	38
Tube wall thickness	mm	4	4	4
Tube wall material	-	16Mo3	16Mo3	16Mo3
Heating surface	m^2	396	396	198

The original boiler uses a mixture of waste wood (A1-A2), forest wood chips and bark as fuel. Such a fuel mixture was not investigated in the test runs.

Due to the different corrosion behaviours and corrosion mechanisms found within the waste wood and the forest wood chips test run no mathematical correlation between the corrosion rates measured and the fuel composition respectively the molar 2S/Cl ratio can

be drawn. Hence, taking into account that the quality respectively the mixing ratio of the fuels can vary significantly over time, it is hardly possible to estimate the corrosion potential of the corresponding “steady state”.

To overcome this problem the corrosion potential was calculated using the two empirical functions developed for pure wood chips as well as for pure waste wood. This approach should determine at least the corrosion potential of the two boundary situations: pure wood chips as well as pure waste wood A1-A2.

The steel 16Mo3 used for the superheaters of the plant (see Table 4.5) is a low alloy heat resisting steel like 13CrMo4-5 with a low Cr and Ni content. Therefore, it should also show a comparable corrosion behaviour (see Section 4.3).

The simulation has been performed within a two-step approach. First, the flue gas flow and heat transfer of the boiler was simulated. Afterwards, the local corrosion behaviour was evaluated in a post-processing step (detailed description see Section 3.2).

The boundary conditions (e.g. flue gas temperature and composition) at the entrance of the simulation domain were taken from mass and energy balances under the assumption of complete combustion provided by the plant manufacturer.

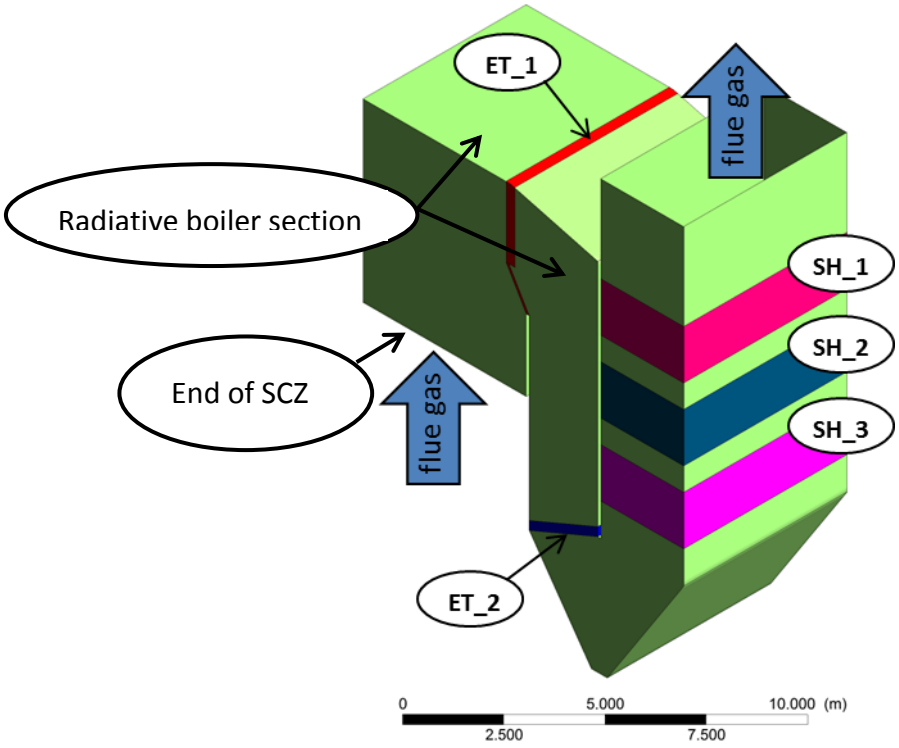

Figure 4.16: Schematic view of the simulated CHP plant
Explanation: ET_1… upper evaporator tube grid, ET_2… lower evaporator tube grid, SH_1 to SH_3… superheater tube bundles 1 to 3 (Figure adapted from **[Paper II]**)

To achieve a fully developed flow-field at the entrance to the convective boiler section, the upper part of the furnace was included in the simulation. Hence, the simulation considers the composition of a chemically not reacting, fully burnt out flue gas typical for biomass furnaces firing wood chips.

The heat loss over the finned tube walls is calculated by the saturated steam temperature and the mean heat transfer coefficient on the water side as boundary conditions. On the flue gas side the radiant heat transfer as well as the convective heat transfer are taken into account, as explained in Section 3.2.2.

To consider the reduced heat transfer due to ash deposits on the tubes a thermal resistance of 2 m^2K/kW is assumed (low fouling rate) on the finned tube walls and on the superheater tube walls.

Figure 4.16 illustrates the different sections of the biomass CHP plant considered in the CFD case study. The simulation domain comprises the upper part of the furnace section (end of secondary combustion zone), the radiative boiler section (including the two evaporator tube grids ET1 and ET2), the transition to the convective section, the ash hopper as well as the convective section with the three superheaters SH1 to SH3.

A detailed description of all relevant boundary conditions can be found in the Annex (see Section 8.1.1).

4.5.2 Results of the flow and heat transfer

Since the calculated flow fields of all three case studies investigated are qualitatively similar only the results of CS1 are presented.

The flue gas path lines colored by the flue gas temperature calculated for full load conditions are shown in Figure 4.17 on the left side, whereas the calculated flue gas velocity profiles are presented in Figure 4.17 on the right side. As described in detail in Section 3.2.2 the steam temperatures in the superheater bundles are not calculated within the simulation but represent a boundary condition of the used heat exchanger model. Hence, for the sake of completeness the steam temperatures, which were assumed as linearly increasing, are presented in Figure 4.18 (left).

As can be seen in Figure 4.17 (left) due to the deflection after the radiative boiler path the major flue gas flow passes along the outer (right) boiler wall of the superheater duct. Therefore, the flue gas flow through SH 3 is not equally distributed. This leads to enhanced flue gas velocities and flue gas temperatures on the right side of the tube bundle and therefore, locally enhanced heat transfer coefficients on the flue gas side (see Figure 4.17, right). One can also see that SH 3 homogenizes the flow distribution over the cross-section due to its flow resistance. In further consequents the flow through SH 2 is more equally distributed.

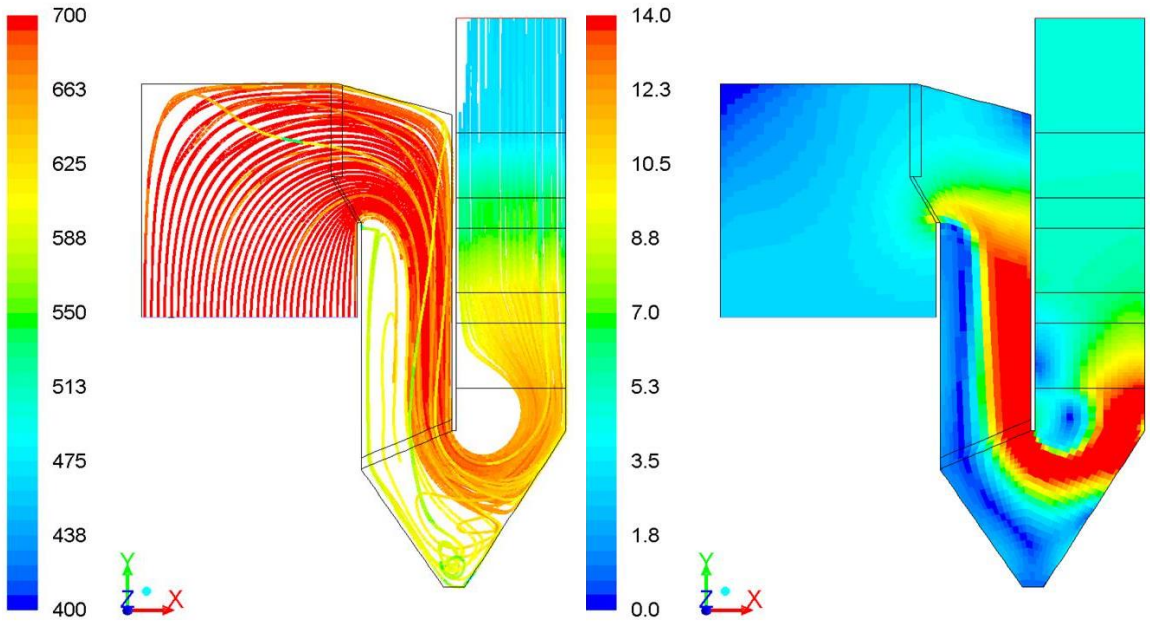

Figure 4.17: Streamlines of the flue gas colored by the temperature (°C) (left) and profiles of flue gas velocity (m/s) (right) in the symmetry plane of the simulated plant (case CS1) (Figure adapted from **[Paper II]**)

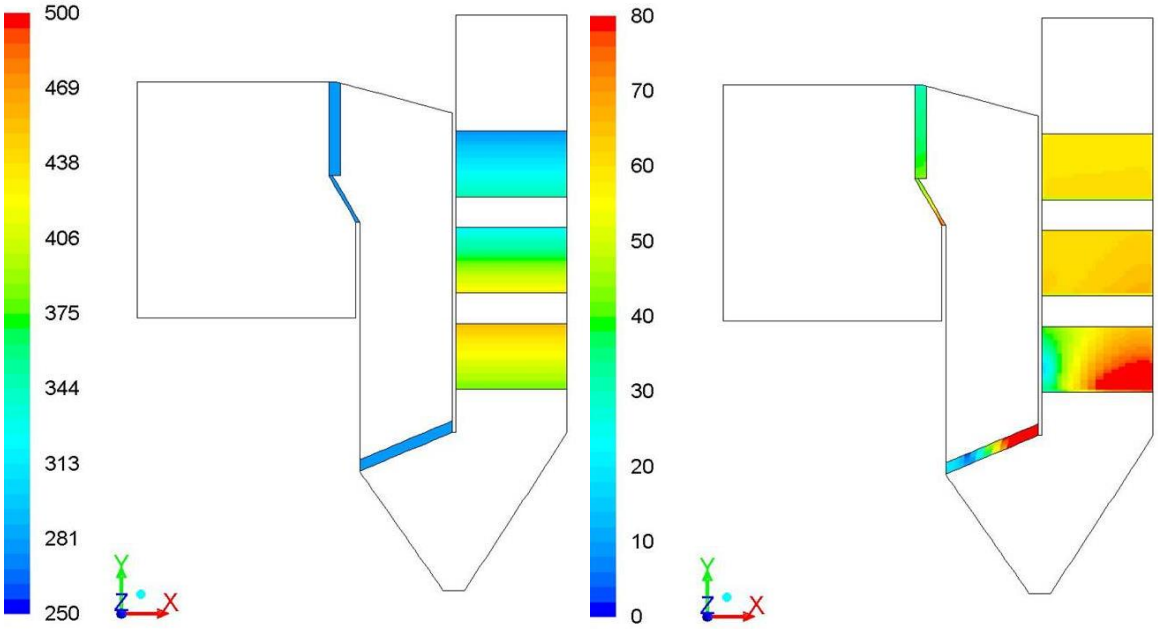

Figure 4.18: Profiles of the assumed steam temperatures (°C) (left) and the calculated total heat transfer coefficients on the flue gas side (W/m²K) (right) in the symmetry plane of the simulated plant (case CS1) (Figure adapted from **[Paper II]**)

Since the empirical model developed depends exponentially on the steel temperature, the heat exchanger model was used to calculate the local steel temperatures on the flue gas side of the superheater. The local values of steam temperature, local heat flux and the heat transfer coefficient on the flue gas side were used for this calculation. The calculated steel temperatures are presented in Figure 4.19.

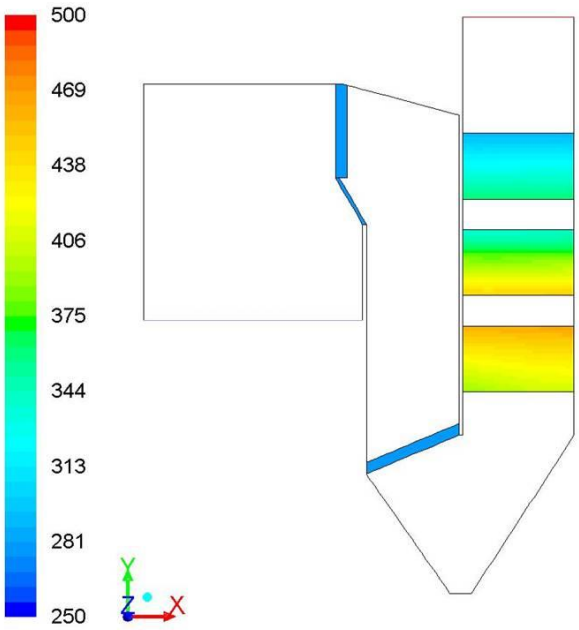

Figure 4.19: Steel temperature (°C) of the heat exchangers in the symmetry plane of the simulated plant (case CS1) (Figure adapted from **[Paper II]**)

In general an inhomogeneous flue gas flow field leads to locally enhanced flue gas velocities. This enhanced velocities increase the local heat transfer coefficient and hence, also the local steel temperature which considerably effects the local high-temperature corrosion potential.

To investigate the influence of an inhomogeneous flow field on the convective heat transfer and the pressure loss over the superheater tube bundles the results of the CFD simulation for CS1 have been compared with calculations according to the VDI heat atlas [78] Gg1 (heat transfer) and IDELCHIK - Handbook of hydraulic resistance [80] p.752 (pressure loss). The results of this comparison are shown in Table 4.6 to Table 4.8.

When the superheater bundles are homogenously passed through by the flue gas the calculated pressure losses according to the CFD simulation and the empirical calculation should be in good agreement, since the empirical correlation of [78] and [80] were developed for a homogenous gas flow perpendicular to the tube banks (see also Section 3.2.2). This is the case for the superheater bundles SH1 and SH2. One can see that there are some deviations for these two heat exchanger bundles concerning the amount of transferred heat by convection. This deviation is caused by radiation, which is not considered in the empirical correlation of [78]. Additionally one can see that there exist deviations regarding the calculated pressure loss as well as the amount of transferred

heat in the case of an inhomogeneous flow field (SH3). This is caused by the fact that the empirical correlations according to [78] have been developed for homogeneous flow fields.

Table 4.6: Comparison of the transferred heat by convection and the pressure loss according to the CFD simulations and the calculations based on **[78]** (heat transfer) and **[80]** (pressure loss) for SH1 (Table adapted from **[Paper II]**)

	Unit	**CFD**	**calculations**	**deviation (%)**
Flue gas temperature SH entry	°C	536		
Flue gas temperature SH exit	°C	469	463	1.3
Mean surface temperature	°C	366		
Transferred heat by convection	kW	3035	3205	-5.6
Pressure loss	Pa	45	46	-2.2

Table 4.7: Comparison of the transferred heat by convection and the pressure loss according to the CFD simulations and the calculations based on **[78]** (heat transfer) and **[80]** (pressure loss) for SH2 (Table adapted from **[Paper II]**)

	Unit	**CFD**	**calculations**	**deviation (%)**
Flue gas temperature SH entry	°C	610		
Flue gas temperature SH exit	°C	541	536	0.9
Mean surface temperature	°C	442		
Transferred heat by convection	kW	3087	3296	-6.3
Pressure loss	Pa	51	51	0.0

Table 4.8: Comparison of the transferred heat by convection and the pressure loss according to the CFD simulations and the calculations based on **[78]** (heat transfer) and **[80]** (pressure loss) for SH3 (Table adapted from **[Paper II]**)

	Unit	**CFD**	**calculations**	**deviation (%)**
Flue gas temperature SH entry	°C	646		
Flue gas temperature SH exit	°C	616	612	0.6
Mean surface temperature	°C	480		
Transferred heat by convection	kW	1678	1528	9.8
Pressure loss	Pa	44	40	10.0

4.5.3 Results of the empirical high-temperature corrosion model

In Section 4.4 it was argued that the application of the empirical model is limited to the parameter range investigated within the online corrosion probe test runs. Hence, only the final superheater bundle SH3 has temperatures which are high enough for the application of the newly developed model. However, since oxidation and other high temperature processes strongly depend on the steel temperature the high-temperature corrosion risk for the two superheaters SH1 and SH2 can generally be considered as low.

Due to the time dependence of most known high-temperature corrosion mechanisms and the comparable short measurement times of the online corrosion probe measurements, the calculated corrosion potential should only be interpreted qualitatively. However, the calculated potentials for several cases can be compared relatively to each other.

Since already very small leaks of the superheater tubes lead to a shut-down of the boiler, it is meaningful to compare the maximum values of the calculated corrosion potentials of the final superheater to evaluate the risk of material failure due to high-temperature corrosion (see Table 4.9). The calculated local corrosion potentials for the three different cases are presented in Figure 4.20 to Figure 4.22.

Several aspects are of special interest. As already indicated by the fuel composition (higher content of Cl, Pb, Zn; lower molar 2S/Cl ratio) the calculated high-temperature corrosion potential for pure waste wood is in any case several times higher than that of wood chips. However, the differences decrease with increasing steel temperature, as already discussed in Section 4.2.

Furthermore, the sensitivity study shows that a switch of the flow direction of the final superheater from parallel to counter-flow increases the maximum of the corrosion potential by a factor of 3.4 in the case of wood chips and by a factor of 2.3 in the case of waste wood. This finding can be explained by the combination of the highest surface temperature with an increased flue gas temperature in the first part of the superheater tube bundle which represents a disadvantageous combination of influencing parameters according to Eq. 8. An increase of the live steam temperature by ~30 °C, from 453 °C to 480 °C, leads to a maximum corrosion potential which is 7.4 times higher than that found within the actual state analysis of the plant in the case of wood chips. For waste wood the potential increases by a factor of 2.1.

Table 4.9: Maximum values of the calculated corrosion potential for superheater 3
Explanation: CS … case study; max(k) … maximum of the calculated corrosion rate

	unit	CS1	CS2	CS3
max(k) wood chips	mm/1000h	$7.4 \cdot 10^{-3}$	$2.5 \cdot 10^{-2}$	$5.5 \cdot 10^{-2}$
max(k) waste wood	mm/1000h	$1.3 \cdot 10^{-1}$	$3.0 \cdot 10^{-1}$	$2.7 \cdot 10^{-1}$

One can also see that the enhanced flue gas velocity on the right side of the superheater leads to locally enhanced steel temperatures (see Figure 4.19). Since the corrosion

potential depends exponentially on the steel temperature a homogenous flow field can reduce the overall risk of high-temperature corrosion failure considerable.

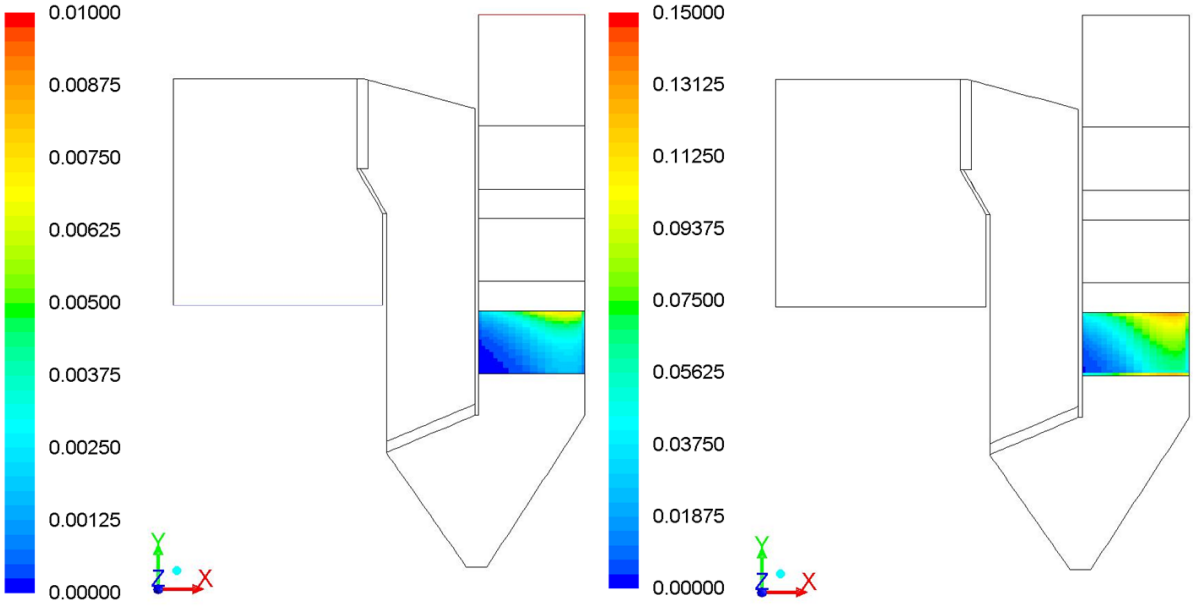

Figure 4.20: Calculated local corrosion potential (mm/1000h) of SH3 in the symmetry plane of the simulated plant under full load conditions (CS1) for wood chips **[Paper II]** (left) and waste wood (right)

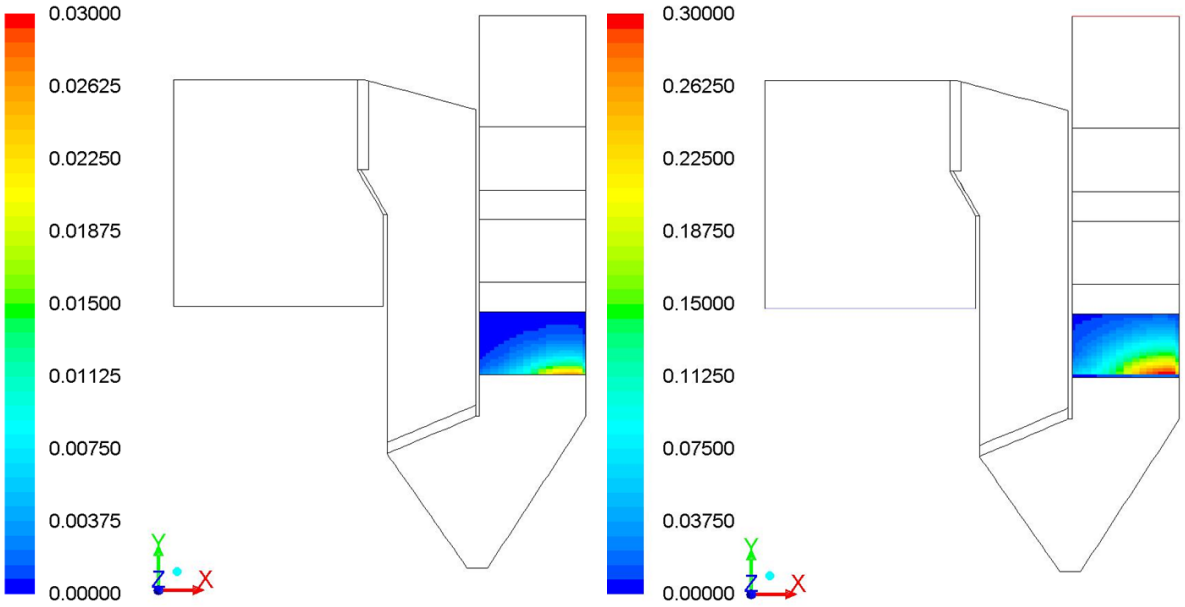

Figure 4.21: Calculated local corrosion potential (mm/1000h) of SH3 in the symmetry plane of the simulated plant for a changed flow in the final superheater (CS2) for wood chips **[Paper II]** (left) and waste wood (right)

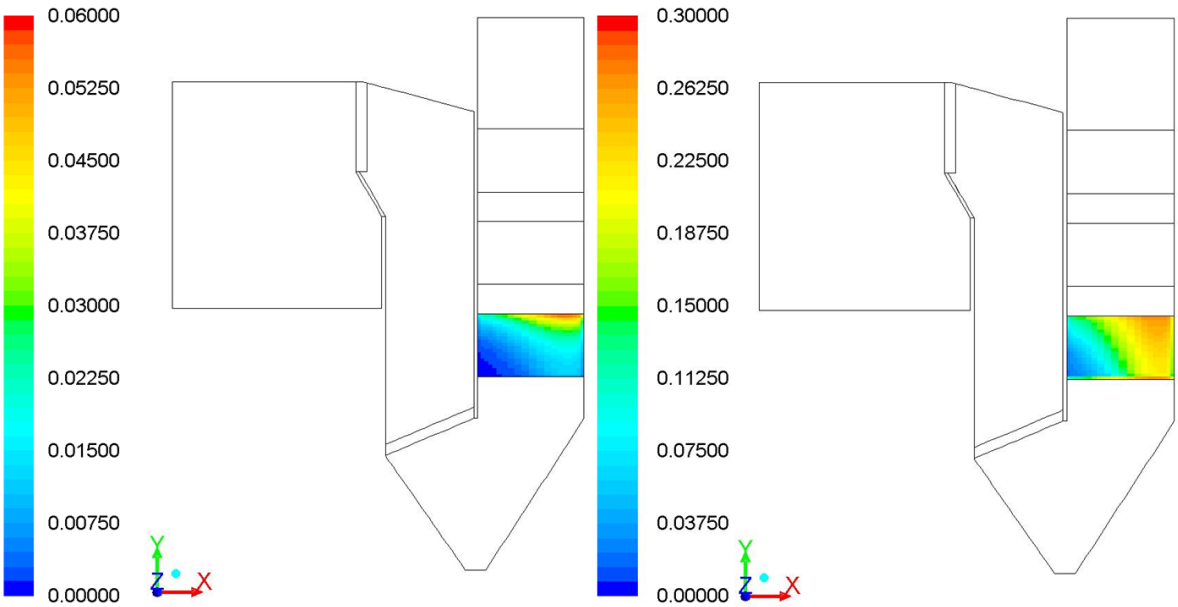

Figure 4.22: Calculated local corrosion potential (mm/1000h) of SH3 in the symmetry plane of the simulated plant for enhanced steam temperatures (from 453 °C to 480 °C) (CS3) for wood chips **[Paper II]** (left) and waste wood (right)

4.6 Summary and recommendations

To investigate the high-temperature corrosion behavior of superheater tube bundles and to gain reliable data for the development of an empirical high-temperature corrosion model, online corrosion probe measurements have been carried out in a specially designed fixed bed / drop tube reactor. The investigated low alloy boiler steel 13CrMo4-5 is commonly used as steel for superheater tubes in biomass fired heat and power plants. The experimental setup used allows the independent variation of the parameters of interest. Due to this fact, the quality of the measured correlations between the online corrosion probe signal and the influencing parameters exceeds those already published.

The corrosion probe measurements show a clear dependence on the parameters flue gas temperature and velocity as well as the steel temperature. The following variations have been carried out to investigate the influence on the corrosion behavior: flue gas temperature between 625 °C to 880 °C, steel temperature from 450 °C to 550 °C and flue gas velocity from 2 m/s to 8 m/s. Due to the experimental setup the variation of a single parameter of interest could be achieved independently from the others. The flue gas temperature variations have been accomplished by a modification of the electrical heating power of the drop tube. The steel temperatures have been varied by a variable air cooling of the probe and the flue gas velocity variations have been achieved by different furnace load conditions. Based on the experimental data gained, an empirical function which is a combination of an Arrhenius function describing the dependence on the flue gas and the steel temperature and a linear dependence on the flue gas velocity

has been developed. This empirical function is able to reproduce the corrosion potential measured sufficiently accurate.

Due to the rather short duration of the online corrosion probe test runs (~300 h) the model developed is not able to predict actual corrosion rates. However, the model allows for the comparison of different operating conditions relative to each other.

The trends and dependences found within the wood chips test runs are in good agreement with those found during a long-term measurement in a real-scale forest wood chips fired biomass steam boiler [31]. To the knowledge of the author, no comparable measurements are available so far for the fuel waste wood using a low alloy steel. Hence, no comparison can be drawn to literature data in the case of waste wood.

Some restrictions have to be made regarding the applicability of the model. Since the model is based on experimental data it is generally only valid within the parameter range investigated. Especially, for steel temperatures above 570 °C, the model is not applicable. A detailed discussion can be found in Section 4.4. The use of a Cr or Ni rich superheater material affects the corrosion behavior considerably. The empirical model developed is only valid for low alloy superheater materials such as 13CrMo4-5 or 16Mo3.

Additionally, the corrosion behavior strongly depends on the dominating corrosion mechanism. Since no traces of chlorine have been found by means of SEM/EDX as well as wet chemistry analyses it is suggested that the dominating corrosion mechanism is the oxidation of the steel by gaseous oxygen and water in the case of the wood chips. However, additional measurements have to be carried out to confirm this assumption. Due to the sintered deposit layer and the characteristic dependence on the steel temperature it is suggested that hot corrosion type II (see Chapter 2.2.3) is a relevant corrosion mechanism in the case of waste wood combustion. For the development of a detailed model which takes chemical reactions and transport mechanisms into account it is necessary to confirm these hypotheses by means of additional measurements.

Different fuels and hence, chemical compositions of the fuels can lead to different corrosion mechanisms such as active Cl-induced oxidation or corrosion by molten salts. Therefore, the application of the model is restricted to chemically untreated wood chips and quality sorted waste wood A1-A2 as fuels. To increase the validity range of the model, additional measurements with different superheater materials and different types of herbaceous fuels or agricultural residues should be performed.

The empirical model developed has been applied as a post-processing routine of a CFD simulation of flow and heat transfer in order to calculate the actual local corrosion potential of a biomass fired boiler (38 MW_{th}, 453 °C live steam temperature). By the CFD simulation the effects of an inhomogeneous flue gas flow and temperature field on the heat transfer and hence, local steel temperatures have been considered. This has been achieved by using a finite cell base heat exchanger model (see Section 3.2.2).

In reality, a combination of bark, wood chips and waste wood is fired in the simulated plant. However, due to the restrictions discussed earlier in this section the empirical

model developed is not able to estimate the corrosion potential of this fuel mix. Instead the model has been applied with the optimized parameters derived for the pure fuels wood chips and waste wood. This approach should allow for the calculation of the two extreme cases of high temperature corrosion in the plant investigated.

For both fuels, three cases have been investigated within this work. First the corrosion behavior under full load conditions has been evaluated (reference case). Additionally, the influences of enhanced steam temperatures and a switch of the direction of the steam flow through the final superheater on the high-temperature corrosion potential have been studied.

In all cases the use of waste wood leads to a considerably higher maximum corrosion potential. Furthermore, the simulations show that, independently of the fuel, an increase of the final steam temperature from 453 °C to 480 °C increases the maximum corrosion potential calculated. Moreover, a change of the flow direction of the final superheater leads to an increased danger of high-temperature corrosion failure.

Another interesting result is that a homogenous flow field in the superheaters can reduce the danger of high-temperature corrosion significantly. Here, the usage of baffles in the re-direction between the radiation and superheater duct could be very useful.

Concluding, the empirical model developed allows a comparison of the local corrosion potential of different live steam temperatures, plant geometries or interconnections of the superheater tube bundles. In addition, the model allows for a quick estimation if high-temperature corrosion is of relevance for a certain plant or not when using a low alloy steel like 13CrMo4-5 and comparable wood fuels.

Within its applicability range the empirical model developed is able to roughly estimate the local corrosion potential together with a CFD simulation of flow and heat transfer in a relatively short time and without detailed knowledge of the underlying chemical processes already in the design phase of a plant and hence is a helpful tool for boiler manufacturers.

5 Detailed model

Online corrosion probe measurements performed in a coupled biomass fixed bed / drop tube reactor represent the basis of the high-temperature corrosion models development within this work. To investigate the influence of different fuels on the corrosion behaviour two test runs have been carried out using wood chips and waste wood as fuels. The online corrosion probe was on the one hand used to gain information regarding the corrosive attack under certain conditions and on the other hand to investigate the deposit and corrosion layer formed on the probe in order to gain information regarding the corrosion mechanism prevailing.

As described in Section 4.1.4 no traces of chlorine could be found in the deposit and in the corrosion layer of the corrosion probe sample rings, neither by means of SEM/EDX analyses nor by wet chemical analysis. Therefore, it was suggested that another mechanism rather than active Cl-induced oxidation is the main corrosion mechanism prevailing.

In the case of forest wood chips also no molten phases, which would be the basis for hot corrosion type II could be attested. Furthermore, the amounts of HCl and SO_x in the flue gas were very low (see Table 4.1) which minimizes the danger of enhanced corrosion by these gaseous species. Therefore, it was concluded that the main corrosion mechanism prevailing is the oxidation of the steel by gaseous O_2 or H_2O.

The oxidation of iron by gaseous O_2 or H_2O is generally controlled by solid state diffusion of O^{-2} or Fe^{+2} ions [41]. The temperature of the online corrosion probe is controlled via the steel temperature on the inward, air-cooled side of the sample rings (see Section 3.1.3). Due to the good heat conductivity of 13CrMo4-5 (38 W/mK at 20°C) the temperature gradient over the sample rings is negligible. Therefore, the outer surface temperature is approximately the same as the steel temperature on the inside. Hence, the oxidation rate should be nearly independent of flue gas temperature and velocity. This is in contrast to the findings of the online corrosion probe test runs, which showed an exponential dependence on the flue gas temperature and a linear dependence on the flue gas velocity (see Section 4.2). To clarify whether the oxidation of the steel is the main corrosion mechanism prevailing two additional test runs have been carried out using a newly developed mass loss probe (MLP) [68].

5.1 Mass loss probe test runs

The test runs were carried out in the same coupled biomass packed bed / drop tube reactor as the online corrosion probe test runs. The mass loss by corrosion / oxidation was determined after the test runs by removing the corrosion products according to ASTM G1-03 and subsequent gravimetrical determination of the mass loss. Retschitzegger et al. [68] have already performed a test run with the MLP under a constant parameter setup to investigate the initial phase of the high-temperature corrosion process using forest wood chips as fuel. Retschitzegger et al. applied a constant parameter setup in their test run: T_{FG} = 745 ± 13 °C; T_S = 480 ± 1 °C and v_{FG} = 2.7 ± 0.1 m/s.

In the first additional test run the same parameter setup was applied, but natural gas was used as fuel instead of wood chips. The additional test run was performed to confirm that the oxidation by O_2 or H_2O is the main corrosion mechanism prevailing when firing wood chips. Since natural gas is basically free of Cl and S it is assumed that high-temperature corrosion occurring in this case is solely caused by the oxidation of the steel by gaseous O_2 or H_2O. In the case of oxidation being the main corrosion mechanism in wood chips fired boilers, this test run and the MLP test run of Retschitzegger et al. should show a comparable corrosion behaviour.

In the second test run again forest wood chips have been used as fuel. The flue gas temperature and velocity have been increased compared to the other two test runs. If oxidation is the dominating corrosion mechanism the results of this test run should also be comparable to the other two MLP test runs performed in the fixed bed reactor.

In addition, the mass loss of 13CrMo4-5 by oxidation was also investigated in a muffle furnace to get a reference value for the mass loss over time by oxidation in air environment.

5.1.1 Test run and operating conditions

Within this work two MLP test runs have been carried out to identify the dominating corrosion mechanism prevailing when using 13CrMo4-5 as a boiler steel and chemically untreated wood chips as fuel in the steel temperature range between 450 °C to 550 °C.

The results of the two MLP test runs were compared to experimental data obtained from Retschitzegger et al. [68]. In the test run of Retschitzegger et al. [68] the MLP was used in combination with an online corrosion probe to correct the systematic measurement error of the online corrosion probe (see Section 3.1.3). In this test run also chemically untreated wood chips have been used as fuel. Within the test run the influence of temperature variations on the high-temperature corrosion rate of 13CrMo4-5 was investigated. However, only the results of the mass loss probe were used for comparison in this work.

The test run of Retschitzegger et al. was divided in two parts. Following, constant parameter setup was applied in the first part of the test run: T_{FG} = 745 ± 13 °C; T_S = 480 ± 1 °C and v_{FG} = 2.7 ± 0.1 m/s. In the second phase, the so-called variation phase, the flue gas temperature was varied between 740 °C and 865 °C by the electrical heating of the drop tube. For each flue gas temperature investigated the probe surface temperature was varied between 400 °C and 550 °C. Relevant operating data and combustion conditions of the test run are summarized in Table 5.1. A detailed description of the methodology and the obtained results can be found in [68].

In the first additional MLP test run the drop tube reactor was operated using natural gas as fuel. Solely the MLP was used to investigate the time-dependent corrosion behaviour. To make the two test runs comparable the same constant parameter set as in the first part of the one of Retschitzegger et al. [68] was used.

Since the combustion of natural gas is basically free of dust emissions, 54 mg/Nm³ (related to 13% O_2 and d.b.) of powdery $Ca(OH)_2$ were injected into the flue gas. The powder injected had the following particle size distribution: D10% = 1.1 µm, D50% = 5 µm, D90% = 15 µm. Due to this measure the dust concentrations and, therefore, deposit build-up and the heat transfer on the MLP probe should become comparable for the two test runs. In the temperature range and under the conditions prevailing it is assumed that $Ca(OH)_2$ forms an inert deposit layer due to the absence of a liquid phase. To ensure this SEM/EDX measurements of the probe ring cross section have been performed (see Section 5.1.4).

In the second test run again forest wood chips have been used as fuel but the flue gas temperature and velocity have been increased compared to the other two test runs. The parameter setup in the second test run was: T_{FG} = 905 ± 13 °C; T_S = 480 ± 1 °C and v_{FG} = 3.6 ± 0.1 m/s. The most relevant operating conditions of the drop tube reactor are presented in Table 5.1.

Table 5.1: Relevant operating conditions of the drop tube reactor and the mass loss probe *Explanations:* Nm³ … m³ at 0 °C and 101 325 Pa; gaseous components measured at the chimney; T_{FG} … flue gas temperature at measurement port; v_{FG} … flue gas velocity at entrance of measurement port; T_S … probe surface temperature; d.b. … dry basis; w.b. … wet basis;

		Retschitzegger et al. [68]	**gas burner**	**wood chips elevated v_{FG} and T_{FG}**
parameter	unit	mean ± stdv	mean ± stdv	mean ± stdv
fuel power input	kW	23.2 ± 2.1	22.6 ± 0.2	24.0 ± 1.9
O_2	vol.% d.b.	8.6 ±1.6	13.1 ± 0.8	10.3 ± 0.9
CO_2	vol.% d.b.	12.0 ±1.6	7.4 ± 0.8	9.9 ± 0.9
CO	mg/Nm^3 d.b.	3.1 ± 2.1	0.2 ± 0.1	10.8 ± 5.1
H_2O	vol.% w.b.	15.4	7.7	11.6
T_{FG}	°C	745 ± 13	734 ± 4	905 ± 13
v_{FG}	m/s	2.7 ± 0.1	2.8 ± 0.1	3.6 ± 0.1
T_S	°C	480 ± 0.1	480 ± 0.1	480 ± 0.1

In addition, the mass loss of 13CrMo4-5 by oxidation was investigated using a Carbolite AAF 11/18 muffle furnace to get a reference value for the mass loss over time by oxidation in an air environment. The oxide formation and hence, mass loss of steel was determined by ASTEM G1-03 and subsequent gravimetric measurement as descripted in Section 2.3. The muffle furnace was operated at a constant temperature of 480 °C during the test run (duration: 400 hours). The water content varied between 1-2 vol-% w.b. depending on the weather conditions and hence humidity of the surrounding air.

Ambient air circulation occurred due to natural convection via a small chimney in the muffle furnace.

5.1.1 Fuel

Two fuel samples have been taken over the test run with wood chips to investigate the fuel composition. The obtained fuel composition is given in Table 5.2.

Table 5.2: Results of fuel analyses **[Paper III]**
Explanations: w.b. … wet basis; d.b. … dry basis; std.-dev. … standard deviation; mean … mean value; n = number of samples taken; data from Retschitzegger et al. is adapted from **[68]**

		wood chips Retschitzegger et al. n=4		**wood chips** elevated flue gas velocity/temperature n=2	
		mean	std-dev	sample 1	sample 2
moisture content	wt% w.b.	31.6	3.9	28.4	33.2
ash content	wt% d.b.	2.7	1.2	1.4	1.9
C	wt% d.b.	48.1	0.4	49.8	49.7
H	wt% d.b.	6.0	0.1	6.0	6.0
N	wt% d.b.	0.3	0.1	0.2	0.1
S	mg/kg d.b.	262	70	144	198
Cl	mg/kg d.b.	117	71	52	58
Si	mg/kg d.b.	3654	3009	408	840
Ca	mg/kg d.b.	4723	1207	3590	5340
Mg	mg/kg d.b.	614	193	451	372
K	mg/kg d.b.	1875	449	1360	1250
Na	mg/kg d.b.	128	92	34	41
P	mg/kg d.b.	242	71	129	172
Al	mg/kg d.b.	615	424	126	241
Fe	mg/kg d.b.	313	237	72	143
Mn	mg/kg d.b.	88	26	46	160
Zn	mg/kg d.b.	15	5	12	14
Pb	mg/kg d.b.	4	5	3	4
2S/Cl ratio	mol/mol	7.6	2.7	6.1	7.5

The fuel used in the test runs was chemically untreated forest wood chips mainly consisting of spruce (mainly logging residues including bark, with a low fraction of stem wood as well as fine particles and needles). The biomass originated from a local supplier close to Graz, Austria and was harvested within a radius of approximately 50 km around

Graz. The fuel had following specifications according to EN 14964-1:2010: origin … 1.1.4.4 and 1.1.4.5; particle … P45Ac; moisture … M35; ash … A2.0; bulk density …. BD200.

The analyses confirm that the fuel used in the biomass fired test run is comparable to the fuel used by Retschitzegger et al. [68]. Furthermore the fuel is comparable to that of the wood chips online corrosion probe test run performed within this work (see Table 4.2).

5.1.2 Mass loss over time

The mass loss over time of the steel obtained with the two drop tube reactor test runs, the muffle furnace experiments and the findings of Retschitzegger et al. are presented in Figure 5.1.

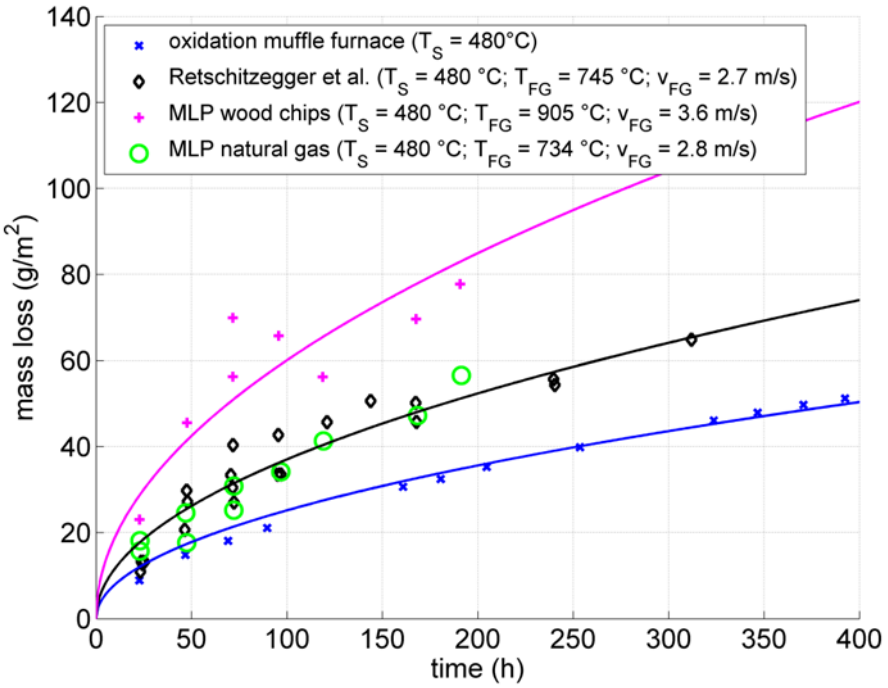

Figure 5.1: Mass loss for various test runs as a function of time **[Paper III]**.
Explanation: MLP … mass loss probe; T_S … steel surface temperature; T_{FG} … flue gas temperature

One can clearly see that the mass loss in the muffle furnace is the smallest. In the MLP test runs the same parameter setup: T_S = 480 °C, T_{FG} ~ 740 °C and v_{FG} ~ 2.8 m/s leads to the same mass loss over time for wood chips and natural gas. Finally the test run with the fuel wood chips and elevated flue gas temperatures and velocities produces significantly higher mass losses. The findings are discussed in detail in the following sections.

5.1.3 Deposit formation

The chemical composition of deposits formed on a superheater tube is able to influence the corrosion behaviour significantly. However, the corrosion behaviour is also determined by the structure and porosity as well as the aggregate state of the deposits.

While, a molten layer can cause different or additional corrosion mechanisms such as hot corrosion, the porosity as well as the heat conductivity of the deposits influence the heat transfer and hence, temperature of the deposit layer. This is important since relevant chemical reactions such as sulphation of alkali chlorides strongly depend on the temperature.

Pictures of the deposit formed on the MLP during the various test runs are shown in Figure 5.2. One can see that the deposit on the windward side is visually comparable regarding shape and thickness for all three test runs, although the duration of the test run of Retschitzegger et al. was approximately 2.5 times longer than those of the two MLP test runs performed within this work. This can most certainly be explained by the fact that the deposits formed on the windward side of the probe are all powdery and loosely bound to the MLP and no sintering occurred. Therefore, the deposits can easily be degraded by the flue gas flow as well as during the changing procedure of the mass loss probe rings.

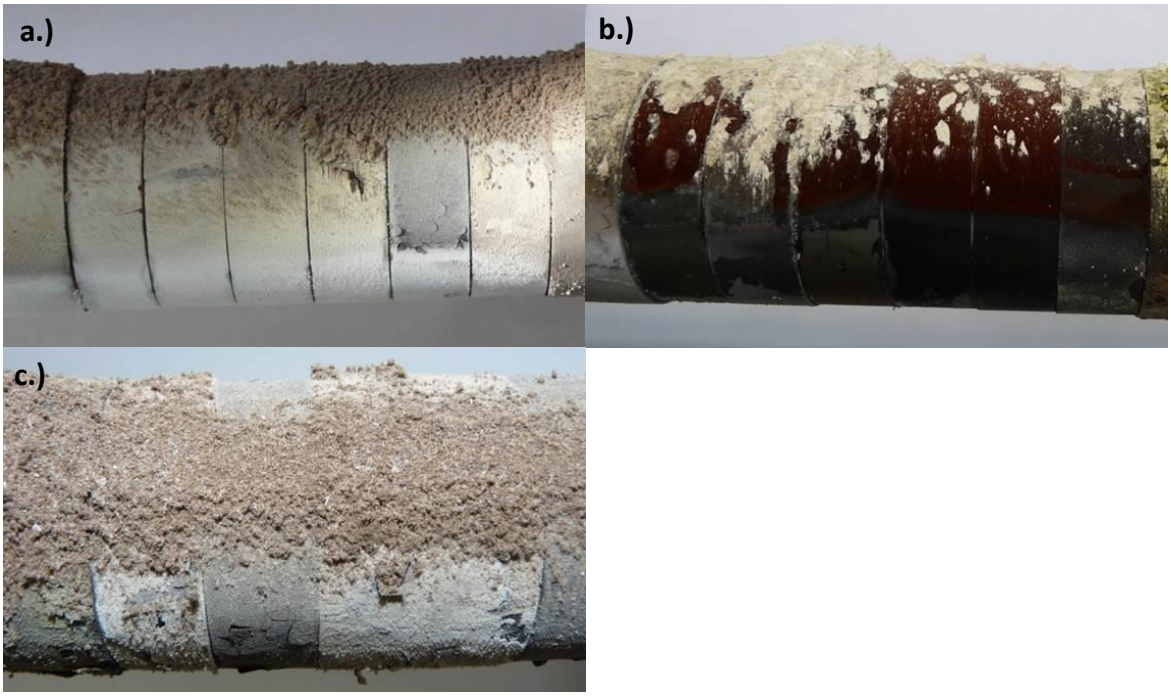

Figure 5.2: Photos of the MLP after the test runs **[Paper III]**
Explanation: a.) wood chips; setup: T_{FG} ~ 740 °C; T_S = 400-550 °C; v_{FG} ~ 2.7 m/s; maximum duration = 480 h; profile view; b.) gas burner; setup: T_{FG} ~ 730 °C; T_S = 480 °C; v_{FG} ~ 2.8 m/s; maximum duration = 192 h; profile view; c.) wood chips; setup: T_{FG} ~ 900 °C; T_S = 480 °C; v_{FG} ~ 3.6 m/s; maximum duration = 191 h; top view;

In the case of the wood chips test runs, the leeward side of the probe is covered with a thin layer consisting of condensed ash vapours. This layer is missing in the case of the gas burner test run, due to the missing ash forming vapours in the flue gas.

Additionally the $Ca(OH)_2$ injected into the flue gas during the natural gas test run does not form the same evenly distributed layer in contrast to the two wood chips test runs.

However, since the deposits formed on the MLP are thin it is expected that this has only a weak influence on the overall corrosion behaviour.

5.1.4 SEM/EDX analyses

The corrosion products as well as the deposit layer have been analysed by means of SEM/EDX analyses to gain relevant information regarding the chemical composition as well as the structure of these layers. Since no relevant differences between the windward and windward +50° side could be detected in earlier measurements (see Section 4.1.4 as well as [31] and [68]), only the leeward as well as the windward side of the probe rings have been analysed. The results of these analyses are presented in **Figure 5.3** and Figure 5.4.

The deposits formed in the test run of Retschitzegger et al. consisted mainly of K_2SO_4 (see Figure 5.3, left and Figure 5.4, left). In addition Si and Ca oxides originating from coarse fly ash particles could be found. No traces of chlorine could be detected neither in combination with potassium nor with iron which is often reported in the case of active Cl-induced oxidation being the main corrosion mechanism [19], [88]. Therefore, one can only see the equally distributed background noise of the EDX analysis in the Cl mappings. Sulphur can be found in two combinations. In the deposit, sulphur coexists in combination with potassium and oxygen, which indicates the presence of K_2SO_4. At the corrosion front, sulphur can be found in combination with iron. These findings are in good agreement with the analyses of the wood chips online corrosion probe ring (see Figure 4.4).

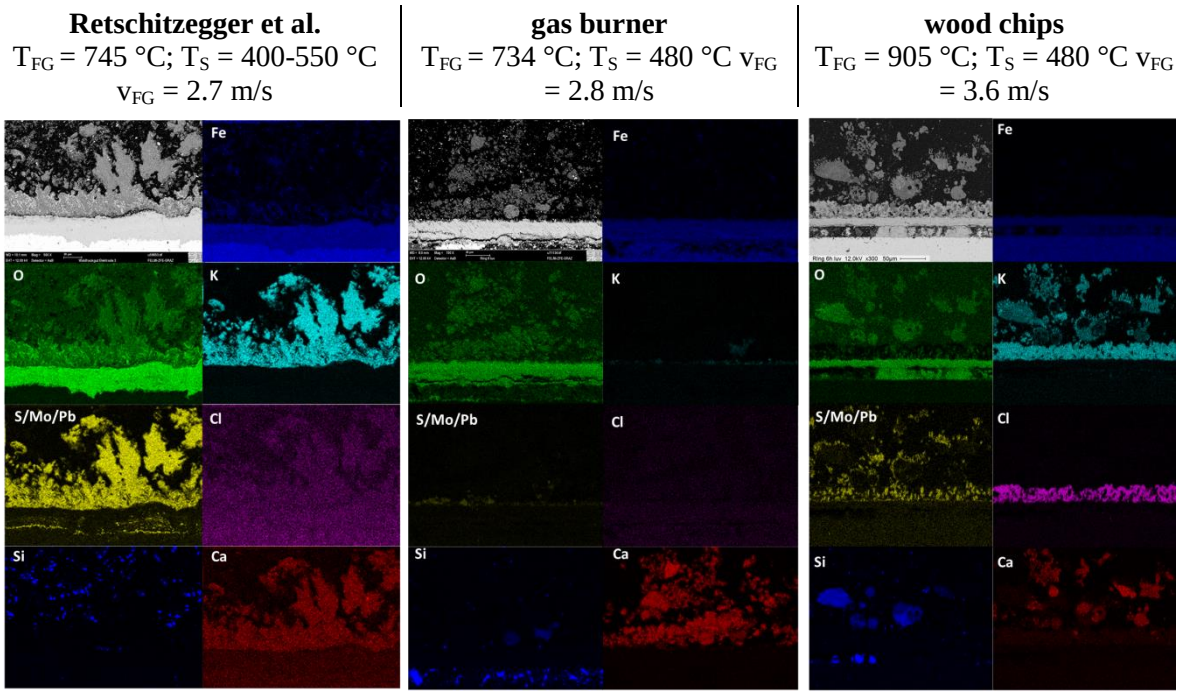

Figure 5.3: EDX elemental mappings of the deposit and corrosion layer on the windward side of the MLP sample rings for the test runs: Retschitzegger et al. (left), gas burner (middle) and wood chips at elevated temperatures and velocities (right) **[Paper III]**.

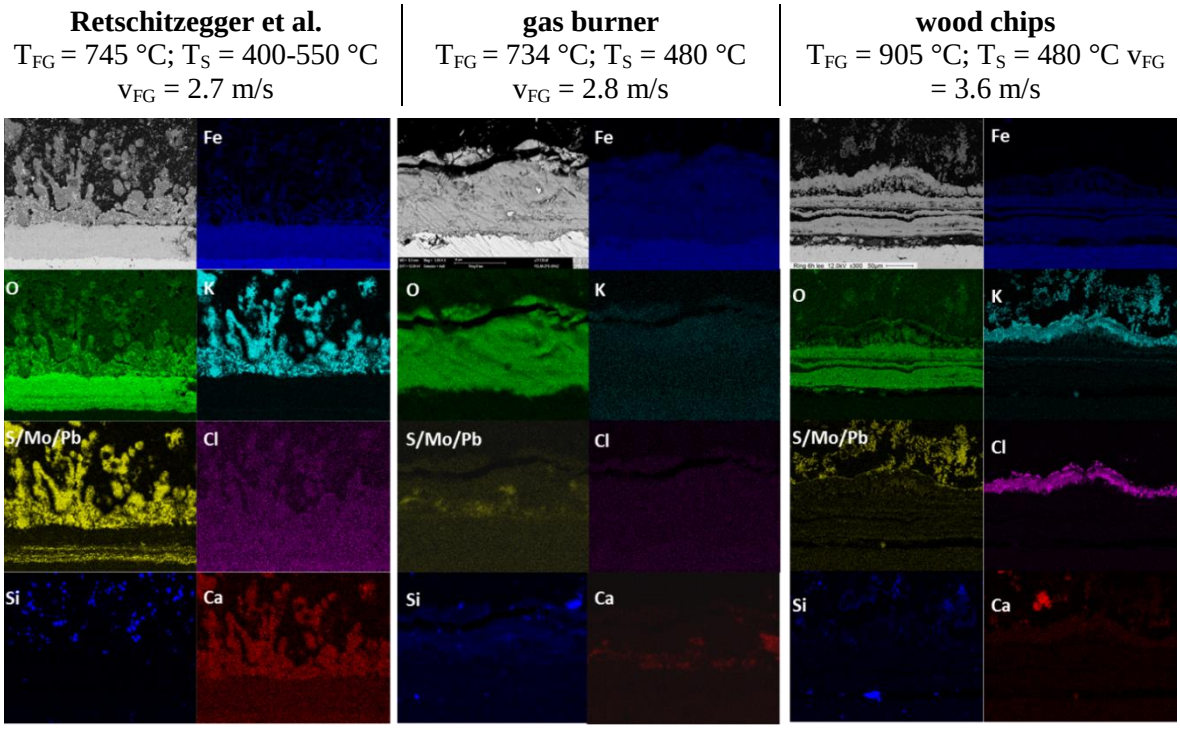

Figure 5.4: EDX elemental mappings of the deposit and corrosion layer on the leeward side of the MLP sample rings for the test runs: Retschitzegger et al. (left), gas burner (middle) and wood chips at elevated temperatures and velocities (right).

In the case of the gas burner test run (see Figure 5.3, middle and Figure 5.4, middle) the only dust source available is the injected $Ca(OH)_2$. Here, one can see in Figure 5.2 that the coarse fly ash respectively the $Ca(OH)_2$ is solely located on the windward ± 50 ° side of the MLP. Hence, only traces (lower 1 at-%) of Ca can be found on the leeward side of the sample ring. The Si spots most likely originate from the sandpaper used for the grinding process.

As described in Section 3.1.8 an acceleration voltage of 12 kV has been used for the SEM/EDX analyses. The low acceleration voltage makes a correct quantitative analysis of the elements S, Mo and Pb hardly possible. Especially when only traces (< 1 at-%) of the elements are present, as in the current case. However, the bright spots in the S/Mo/Pb mapping most likely originate from Mo since Mo is part of the steel 13CrMo4-5 (see Table 3.1). Further, the elements S and Pb are not or only in traces present in the flue gas of the gas burner test run.

The results of the test run with wood chips at elevated flue gas temperature and velocity are presented in Figure 5.3 on the right side. Similar to the test run of Retschitzegger et al. Si and Ca can only be found in local spots. Additionally one can see that the outer deposit layer mainly consist of K_2SO_4. However, the inner deposit layer is clearly consisting of KCl. These findings and their impact on the corrosion mechanism are discussed in detail in Section 5.2.

5.2 Corrosion mechanism and model development

5.2.1 Oxidation of the steel 13CrMo4-5 in air environment

In the last decades, considerable research has been done to investigate the oxidation of iron and low alloy steels including the effects of temperature and gas compositions on the oxidation rate as well as detailed investigations regarding the transport mechanisms prevailing (e.g. [41], [64], [99], [100], [101], [102], [103], [104], [105], [106], [107], [108]). According to [101] both iron and carbon steels show a parabolic oxidation behaviour. In addition, a general rule exists for iron based alloys containing chromium whereby materials containing less than 2 wt-% Cr show a similar oxidation behaviour [37]. This rule applies for 13CrMo4-5 and was also found during the oxidation in the muffle furnace as can be seen in Figure 5.1. Hence, it is assumed that the oxidation mechanism in the case of 13CrMo4-5 is comparable to that of iron. Therefore, also the theoretical models developed for the oxidation of iron are assumed to be applicable as a first approximation for the oxidation of low alloy steels such as 13CrMo4-5.

A model, which describes the growth of an oxide layer on a metal surface, is the theory of Wagner [63]. This model gives a quantitative relationship between the parabolic rate constant of thermal oxidation and the self-diffusion coefficients of the ions in the oxide. The oxide thickness calculated can be converted to a corresponding mass loss of the steel using the densities of iron oxide and iron.

$$X^2 = k_p \cdot t$$

$$k_p = \int_{a(O_2)_I}^{a(O_2)_{II}} \left(\alpha \frac{D^*(M)}{f_M} + \frac{D^*(O)}{f_O} \right) d\left[\ln a(O_2)\right] \qquad \text{Eq. 9}$$

Explanation: X … Oxide thickness (cm); k_p … parabolic rate constant (cm²/s); t … time (s); $a(O_2)$ … oxygen activity at the inner *(I)* and outer *(II)* interface of the oxide layer; α … ratio between oxygen and metal in the oxide (MeO_α); f_M, f_O … dimensionless correlation factor; $D^*(M)$, $D^*(O)$ … tracer diffusion coefficients of the metal and oxygen in the oxide (cm²/s)

The stability ranges of the oxides and thus integral boundaries $a(O_2)_I$ and $a(O_2)_{II}$ can be determined by means of chemical equilibrium calculations [37]. The model is generally well applicable to describe the growth of the iron oxide layers FeO, Fe_2O_3 and Fe_3O_4 on iron [41].

FeO is only stable for temperatures ≥ 570 °C. Since the application of 13CrMo4-5 is limited to temperatures < 560 °C the formation of FeO can be neglected in the detailed corrosion potential model.

In the relevant temperature range of high-temperature corrosion in biomass fired boilers the oxidation of iron produces a relatively thin Fe_2O_3 (hematite) layer on top of a thicker Fe_3O_4 (magnetite) layer [109]. Due to the fact that the Fe_2O_3 layer appears only as a thin film in the relevant temperature range it is only of minor technical interest. Therefore,

only insufficient experimental tracer diffusion data for Fe and O in Fe_2O_3 exists for temperatures < 700 °C [41], [64], [99], [107]. Hence, as a first approximation the oxidation of 13CrMo4-5 is solely described by the formation of Fe_3O_4.

The stability ranges for the formation of Fe_3O_4 in the temperature range of interest are presented in Figure 5.5.

In Fe_3O_4, the tracer diffusion of O is several orders of magnitude lower than that of Fe [110]. For that reason it is an adequate simplification to neglect the oxygen diffusion in Eq. 9. The diffusion mechanism of Fe in Fe_3O_4 strongly depends on the oxygen activity prevailing. The diffusion occurs by a vacancy mechanism at high oxygen activities and by an interstitial mechanism at low oxygen activities [103]. These transport mechanisms are experimentally validated in a wide temperature range from 500 to 1400 °C [111]. The tracer diffusion coefficient of Fe in Fe_3O_4 can be calculated according to Eq. 10 [103].

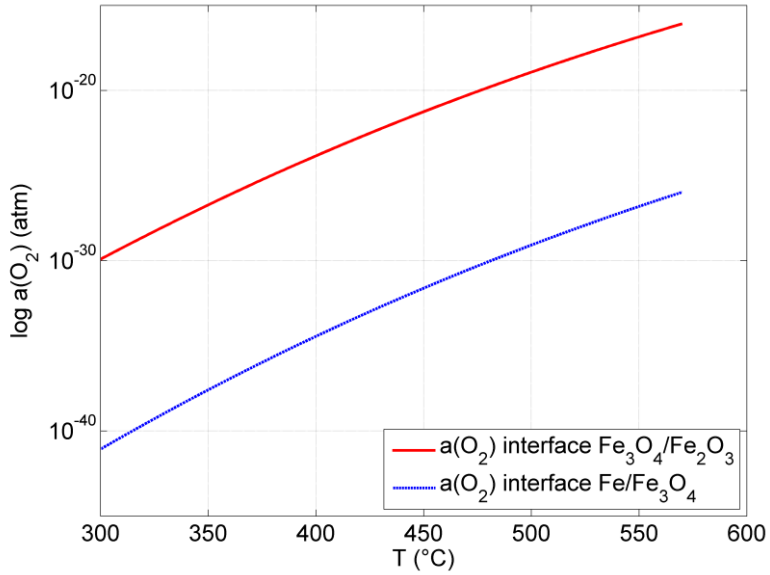

Figure 5.5: O_2 activities at the Fe_3O_4 oxide interfaces as a function of temperature.

$$D^*(Fe\ \ in\ Fe_3O_4) = \underbrace{D_v^\circ \exp\left(\frac{-E_v}{RT}\right) a_{O_2}^{2/3}}_{vacancy\ diffusion} + \underbrace{D_i^\circ \exp\left(\frac{-E_i}{RT}\right) a_{O_2}^{-2/3}}_{inerstitid\ diffusion} \qquad \text{Eq. 10}$$

Explanation: $D°_{[v]}$ = 4.45·10^{-11} (cm/s); $D°_{[i]}$ = 7.9433·10^{7} (cm/s); E_v = -1.39·10^{6} (J/mol); E_i = 6.13·10^{6} (J/mol); $a_{O2} = P_{O2} / P°_{O2}$; $P°_{O2}$ = 1 (atm); R = 8.314 (J/molK)

Since, as already discussed, the formation of the magnetite layer, which is the dominating oxide in the temperature range of interest, is limited by the outward diffusion of iron ions [41], [110], the rate of iron oxide formation below 570 °C hardly depends on the oxygen content of the flue gas. This was also experimentally validated for various carbon steels at 500 °C for oxygen pressures between 0.013 atm and 0.92 atm [112].

5.2.2 Influence of corrosive gases (HCl, SO_x)

The concentrations of the corrosive gaseous species HCl and SO_x in the flue gas are typically low for chemically untreated woody biomass fuels. During the test run performed within this work the concentration of both species was below 10 ppm (see Table 4.1). To the knowledge of the author only little experimental research has been carried out to investigate the influence of such low concentrations on the high-temperature corrosion behavior of iron or low alloy steels.

On the other hand, considerable research has been carried out for HCl concentrations between 250 and 1000 ppmv which are typical concentrations in MSWI (e.g. [26], [113], [114]). In these studies the severity of the corrosion is directly proportional to the concentration of HCl in the gas atmosphere.

Hence, due to the comparably very low HCl concentrations in the test runs performed within this work, it is assumed that the influence of HCl on the overall corrosion behavior is of minor importance. As a result of this assumption and the lack of additional experimental data the effect of HCl on the high-temperature corrosion rate of the steel 13CrMo4-5 will not be considered in the development of the detailed model.

The influence of SO_2 on the corrosion rate is a little more complex. In general for SO_2 concentrations higher than ~1 vol-% and temperatures above 500 °C a general dependence of the corrosion rate on the temperature as well as on the SO_2 concentration could be found within several experimental investigations [93], [115], [116]. Here, the corrosion rate increases with both parameters.

However, these concentrations exceed those of the test runs of this work by far. Also these experiments have in common that they neglect the influence of the ash chemistry (e.g. sulphation reactions) on the corrosion rate. Hence, the results of these lab-scale test runs are not well-suited to draw conclusions for the complex ash chemistry in biomass fired boilers.

On the other hand, recent studies of the Swedish High-Temperature Corrosion (HTC) center showed an inhibiting effect of traces of SO_2 on the corrosion rate [57], [94] of iron. The gaseous atmospheres used within this works were pure oxygen an oxygen-SO_2 mixtures with SO_2 concentrations between 1 and 1000 ppmv. The tests have been carried out in the temperature range between 500 °C to 600 °C and lasted 24 hours. Here, the inhibiting effect decreases with increasing temperatures and becomes negligible around 600 °C, while it increases with increasing SO_2 concentrations. Still, even a very small SO_2 concentration of 1 ppm decreased the corrosion rate in the experiments considerably.

Up to now, an approved and generally accepted mechanism as well as a mathematical description of this effect is still missing to the knowledge of the author. In addition, these works also exclude any interaction with other corrosive gaseous species such as HCl, H_2O or corrosive salts e.g. alkali chlorides. Hence, extrapolations of these results to the rather complex situation prevailing in biomass fired boilers are not meaningful.

In addition, the concentrations of HCl and SO_x in the gas phase are negligible in the case of the natural gas test run. However, the time-dependent mass losses of the MLP rings during of the gas burner test run and the one from Retschitzegger et al. are similar. Based on this observation, it is concluded that the influence of these species can be neglected as a first approximation.

Therefore, the influence of HCl and SO_x in the flue gas will not be considered in the detailed high-temperature corrosion model developed within this work. However, the actual interaction pathways of these species with the metal respectively the oxide layer are still insufficiently understood so far. If new experimental results or modelling approaches are available they ought to be considered in future versions of the model developed.

5.2.3 Influence of water vapor on high-temperature corrosion

As shown in Figure 5.1 the mass loss of the two MLP test runs (parameter setup: T_S = 480°C, T_{FG} ~ 740 °C and v_{FG} ~ 2.8 m/s) is significantly higher than that gained from the muffle furnace.

The negligible temperature gradient over the sample steel ring in the case of the MLP test runs is not accountable for this difference as already discussed earlier. Also the different oxygen content cannot be accounted for this difference, as explained in Section 5.2.1. Another difference between the experiments in the muffle furnace and the drop tube reactor is the different water content of the gas environment (see Section 5.1.1).

A quite recent study of the HTC center shows a strong dependence of the oxidation rate of pure iron on the water content in the surrounding atmosphere [117]. The temperature range investigated was between 400 °C to 600 °C. The atmospheres used within this work were: O_2 = 5 vol-%, H_2O = 40 vol-%, N_2 = 55 vol-% and O_2 = 5 vol-%, H_2O = 0 vol-%, N_2 = 95 vol-%.

The measured increase of the oxidation rate, between the two gas atmospheres investigated, thereby strongly depended on the temperature prevailing. It hardly had an effect at 400 °C, while it increased the parabolic rate constant at 600 °C by a factor of 2.5. In [117] it is argued that the presence of the water vapor leads to the formation of hematite whiskers. Further it is argued that these whiskers have a high density of grain boundaries. Due to this, grain boundary diffusion most likely becomes the dominating transport mechanism, which results in a faster transport of the iron cations and in further consequence in increased oxidation rates. Although, the amount of water vapor in the gas atmosphere used in [117] is considerably higher than those of the MLP test runs performed within this work, the basic mechanism proposed in [117] should generally be transferable to the work presented.

Hence, it is proposed that the enhanced water vapor content in the flue gas is responsible for the higher oxidation rates of 13CrMo4-5 in the MLP test runs compared to the oxidation rates determined in the muffle furnace.

Therefore, as a first approximation, the parabolic growth kinetics of Fe_3O_4 obtained with the theory of Wagner is corrected by an empirical factor to take the influence of a wet atmosphere into account. Due to the present lack of experimental data, the dimensionless coefficient (A_{H2O}) is chosen in that way, that the calculated parabolic rate constant of Wagner (k_p) for dry conditions, fits the parabolic rate constant determined within the MLP test runs ($k_{p,wet}$) (T_S = 480°C, T_{FG} ~ 740 °C and v_{FG} ~ 2.8 m/s).

$$k_{p,wet} = A_{H2O} \cdot k_p \qquad \text{Eq. 11}$$

Explanation: $k_{p,wet}$ … parabolic oxide growth rate in an atmosphere containing H_2O between 8 – 14 vol-% (cm²/s); A_{H2O} … empirically determined correction coefficient; *kp* … parabolic rate constant in a dry atmosphere according to the theory of Wagner (see Eq. 9) (cm²/s)

5.2.4 Influence of KCl on high-temperature corrosion

As discussed in the last section, the differences between the muffle furnace test run and the two MLP test run in the drop tube reactor can most probably be explained with the different water content in the gas environment. However, the water and oxygen contents in the flue gas of the different MLP test runs are of the same order (Table 5.1). Therefore, a different O_2 and H_2O content of the flue gas cannot be responsible for the higher mass losses obtained in the case of the MLP test run with elevated flue gas temperatures and velocities. An increased steel temperature caused by the increased heat flux can be excluded as reason for the higher mass loss as already discussed. Therefore, it can only be explained by a significant speed-up of a process in the deposit layer.

In order to investigate the chemical composition and structure of the initially formed deposit layer short term deposit probe measurements have been carried out (see Section 4.1.3). By means of SEM/EDX analyses it could be shown that the initial layer formed consists mainly of K_2SO_4 and small amounts of typical coarse fly ash builders (Si, Ca, Mg). For a steel temperature of 480 °C also small amount of chlorine could be found, while chlorine is missing in the case of 550 °C probe temperature.

This indicates on the one hand that the deposits are mainly formed by condensed ash vapors rather than coarse fly ash particles. On the other hand this finding confirms that the condensation temperature of the gaseous chlorides lies somewhere between 480 °C and 550 °C. This result is in good agreement with results obtained from chemical equilibrium calculations.

As already mentioned in Section 4.1.4 no traces of chlorine could be found neither in the final deposit nor in the final corrosion layer of the online corrosion probe test runs performed as well as in the test run of Retschitzegger et al [68].

In Section 4.3 and it was argued that the condensed chlorine species in the initial state of the measurement campaigns get sulphated and that the supply of chlorine species cannot be maintained due to increasing surface temperatures over time. Hence, the question

arises why a solid layer of KCl could be found by means of SEM/EDX analyses in the case of the MLP test runs with elevated flue gas temperatures and velocities?

The existence of the KCl layer in the MLP test run with elevated flue gas temperatures and velocities is assumed to be the result of two factors.

Due to the higher temperature gradient and flue gas velocity the condensation of gaseous KCl should be enhanced in the case of the MLP test run with elevated flue gas temperatures and velocities. Furthermore, in the test run of Retschitzegger et al. steel temperature variations up to 550 °C have been performed after the initial phase (see Section 5.1) whereas the MLP with elevated flue gas conditions was operated at a constant steel temperature of 480 °C. Hence, at least the temperature of the inner ash layer, near to the steel surface, was below the evaporation temperature of KCl.

Since the condensation temperature of KCl under the conditions prevailing lies somewhere between 480 and 550 °C, it is most likely that the condensed KCl became evaporated during the temperature variations performed in the online corrosion probe test run.

Many authors (e.g. [22], [19], [88]) reported a compact inner corrosion layer, consisting of $FeCl_2$, in the case of active Cl-induced oxidation. Although no $FeCl_2$ could be found at the corrosion front, the presence of KCl and the significantly increased mass loss in the case of the enhanced flue gas temperatures and velocities lead to the assumption that active Cl-induced oxidation is an additional corrosion mechanism prevailing. Based on the short term deposit measurements, the same measurement duration and the similar flue gas compositions, it is also most likely that a KCl layer also existed in case of the MLP test run of Retschitzegger et al. before it got evaporated during the parameter variations.

However, active Cl-induced oxidation can be ruled out as corrosion mechanism in the case of the natural gas MLP test run. Since the corresponding MLP test run shows the same corrosion behavior as the one with wood chips and the same parameter setup, it is concluded that the influence of active Cl-induced oxidation strongly increases with increasing deposit temperature. The mean deposit temperature on the other hand is due to the low heat conductivity of the ash layer [81] strongly influenced by the local heat flux and hence, also the flue gas temperature and velocity. Therefore, the sulphation process necessary to release the Cl from the KCl strongly becomes enhanced with increasing flue gas temperature and velocity [44], [45]. The released chlorine is then able to enhance the high-temperature corrosion considerable (see Figure 5.1).

5.2.5 Overall corrosion mechanism and detailed high-temperature corrosion model

Based on the findings presented it is suggested that the overall high temperature corrosion results from a combination of the two well-known mechanisms oxidation and active Cl-induced oxidation. From literature it is known that the oxidation of the steel is mainly influenced by the steel temperature and follows parabolic kinetics [41]. Due to this it is concluded, that the oxidation of the steel is similar in all three MLP test runs. Hence,

the increased mass loss, found in the test run with the elevated temperatures, is presumably solely caused by an increased share of active Cl-induced oxidation.

The combined mechanism proposed is only possible as long as a source of chlorine, e.g. KCl, is available in the deposits. As already discussed, it is most certain that already deposited KCl evaporates at higher temperatures and the condensation of new KCl may be suppressed. In this case the high temperature corrosion should be dominated by the oxidation of the metal.

The dependence on the Cl concentration in the deposit layer is taken into account in the overall corrosion model. Due to the lack of experimental data a linear dependence on the Cl mass fraction in the deposit layer is assumed. In addition, an Arrhenius dependence on the mean deposit temperature is used, taking into account that the sulphation rate of alkali chlorides generally follows an Arrhenius law [44], [45]. Based on these assumptions, the following basic high-temperature corrosion model was formulated:

$$k_{p,overall} = \underbrace{A_{H2O}}_{\text{influence of } H_2O} \cdot \overbrace{k_p}^{\text{oxidation in dry atmosphere}} + \underbrace{\omega_{Cl} \cdot k_{0,Cl} \cdot \exp\left(\frac{-E_{act}}{R \cdot \overline{T_D}}\right)}_{\text{active Cl-induced oxidation } (k_{p,Cl})} \qquad \text{Eq. 12}$$

Explanation: $k_{p,overall}$ …overall parabolic rate constant (cm²/s); A_{H2O} … empirical H_2O correction coefficient (-); k_p … parabolic rate constant according to the theory of Wagner (cm²/s); ω_{Cl} … mass fraction of Cl in the deposit (kg/kg); $k_{0,Cl}$ … pre-exponential coefficient (cm²/s); E_{act} … activation energy (J/mol) ; R … universal gas constant (J/molK) ; $\overline{T_D}$ … mean deposit temperature (K)

The mass fraction of Cl in the deposits of the test run with elevated parameter setup has been determined by quantitative SEM/EDX analyses. Here, the final (longest lasting) mass loss probe ring was analyzed (see also Section 5.1.4). In these measurements, a chlorine content of 5 wt-% could be found. The two parameters E_{act} and $k_{0,Cl}$ have been determined within an Arrhenius plot (see Figure 5.6). Here, it is assumed that the additional mass loss of the MLP test run with elevated temperatures (red cross in Figure 5.6) is solely caused by active Cl-induced oxidation, as explained earlier. Hence, the value of $k_{p,Cl}$ results from a subtraction of the two parabolic rate constants determined for the two MLP test runs (see Figure 5.1). For the second point (blue cross in Figure 5.6), which is based on the MLP test run of Retschitzegger et al., it is assumed that the effect of active Cl-induced corrosion is negligible as already explained earlier. However, since the logarithm of zero is not defined, a finite value of $k_{p,Cl}$ had to be assigned also in this case. In doing so it is assumed that the effect of active Cl-induced oxidation is 1/100th of the one of the test run with elevated parameter setup, and hence, is negligible. It should be mentioned that the setting of 1/100th is arbitrarily chosen. However, the assumption of a smaller value (e.g. 1/1000th) has, due to the logarithmic scale a significant impact on the slope of the line fit presented in Figure 5.6 and results in a pre-exponential coefficient which is of the order 10^{43} cm^2/s. Such a high coefficient leads to vast (unrealistic high)

corrosion potentials already for temperatures which are slightly higher, than those prevailing during the test run with elevated temperatures. Hence, is very important to conduct at least one more test run and get a third point in the Arrhenius plot, to reduce the big uncertainty of the current state.

The mean deposit temperatures of the two MLP test runs using wood chips as fuel have been determined within a CFD simulation. For this simulation a fouling layer of 2 mm thickness and a thermal conductivity of 0.5 W/mK was assumed[7], based on the experimental data gained from the test runs (see Section 5.1). A detailed description of the CFD simulation can be found in the Annex (see Section 8.1.3). The determined coefficients as well as the underlying measurement and simulation data are summarized in Table 5.3.

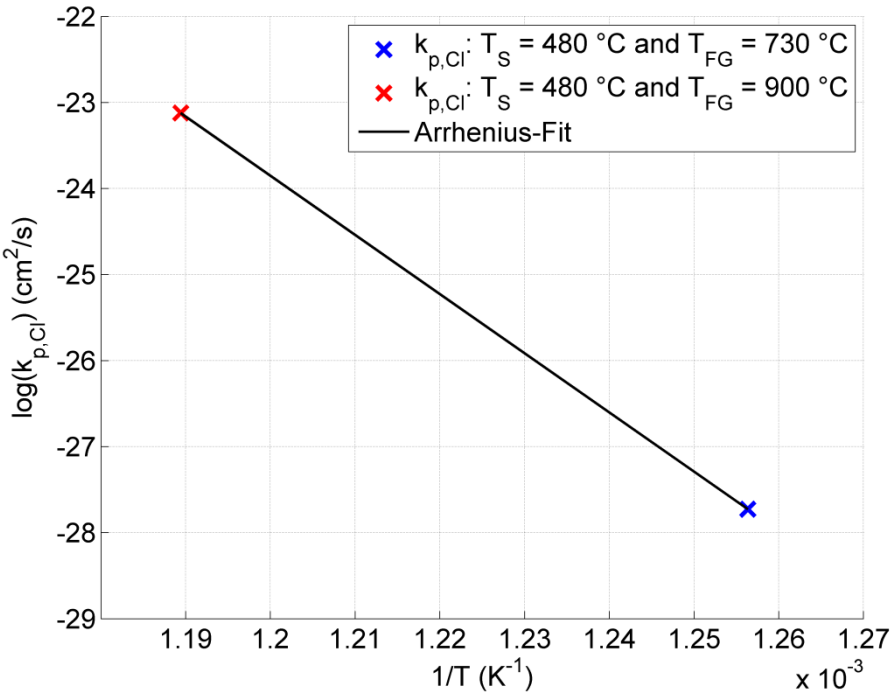

Figure 5.6: Arrhenius plot of $k_{p,Cl}$ as a function of the reciprocal mean deposit temperature

[7] According to the published final BIOASH report [82] a thermal conductivity of 0.5 W/mK represents a good approximation for not sintered (porous) ash layers over a wide temperature range. During the MLP test runs the mass loss over the whole sample ring is determined. Due to the absence of a spatial resolution of the mass loss a mean temperature over the whole sample ring is a sufficient approximation. The actual ash layers found on the corrosion probe (see Figure 4.2) as well as the MLP (see Figure 5.2) are quite evenly distributed over the sample rings. The enhanced deposit build-up at the stagnation point on the probes has only a small extension. Therefore, since the heat conduction in the steel tube is much higher than in the deposit layer, a homogeneous thickness of the layer of 2 mm was applied as a reasonable assumption for the determination of the mean deposit temperature.

Table 5.3: Basic data for model development as well as the empirical determined coefficients and their values

	Name	Unit	Value
ω_{Cl}	measured Cl mass fraction	kg/kg	0.05
$\mathcal{T}_D$	mean deposit temperature for wood chips test run (T_S = 480 °C; T_{FG} ~ 740 °C)	°C	522
$\mathcal{T}_D$	mean deposit temperature for wood chips test run (T_S = 480 °C; T_{FG} ~ 900 °C)	°C	568
A_{H2O}	empirical H_2O correction coefficient	-	13.1
$k_{0,Cl}$	pre-exponential coefficient	cm²/s	$3.16 \cdot 10^{25}$
E_{act}	activation energy	J/mol	$5.72 \cdot 10^{5}$

These results are in reasonable agreement with earlier work of Salmenoja [118]. This work proposes a lower threshold temperature for active Cl-induced oxidation to occur. Thereby, the threshold value is based on the assumption that the volatilization of the metal chlorides significantly contributes to the corrosion mechanism. Two characteristic vapor pressures are of special interest according to [119] and [120].

- vapor pressure of 10^{-6} bar: above this value volatilization of the component can generally contribute to the corrosion mechanism. The corresponding temperature at which the vapor pressure is 10^{-6} bar is called T_6 temperature [119], [120].
- vapor pressure of 10^{-4} bar: above this value volatilization of the species can be assumed as the dominant corrosion mechanisms. Similar to the T_6 temperature, the temperature at which the vapor pressure is 10^{-4} bar is called T_4 temperature [119], [120].

In [118] thermodynamic equilibrium calculations have been carried out to determine the vapor pressure of $FeCl_2$ for various temperatures under reducing conditions. Thereby the T_6 temperature for $FeCl_2$ and hence, lower threshold temperature for active Cl-induced oxidation in low alloy steels and iron was calculated to be around 418 °C, slightly depending on the oxygen content. Below that value active Cl-induced oxidation is not possible according to [118]. The T_4 temperature was calculated to be 529 °C. At this temperature the vapor pressure becomes high enough for active Cl-induced oxidation to be the dominating corrosion mechanism.

In addition, Salmenoja [118] determined the T_4 and T_6 temperatures experimentally. Thereby, they found a T_6 temperature of around 460 °C and a T_4 temperature between 530 °C and 560 °C. Although, the experimentally determined values are higher than the ones predicted by thermodynamic equilibrium calculations, the ranges of both approaches are in good agreement.

Hence, the work of Salmenoja confirms, that active Cl-induced oxidation is generally possible for a steel temperature of 480 °C. On the other hand, the work neglects the possibility that the sulphation of chlorides is the rate limiting step in the mechanism. The measurements performed within this work lead to the conclusion that for the rather low SO_2 concentrations, typically prevailing in the flue gas of woody biomass fired boilers, the sulphation of the chlorides might be indeed the rate determining step within the active Cl-induced oxidation mechanism.

It should be pointed out that in future additional measurements have to be carried out to validate the detailed model presented in Eq. 12. Especially the assumed dependencies on the water concentration of the flue gas and the Cl content in the deposits should be validated experimentally. Also the data density to determine the two coefficients $k_{0,Cl}$ and E_{act} should be increased by additional test runs. Furthermore, the time-dependent deposit growth and hence, varying mean deposit temperature and chlorine content should be taken into account in future versions.

For these reasons the detailed model has to be considered as rough first approach to model the high temperature corrosion in biomass fired boilers. Furthermore, the mass loss calculated with the basic model developed can only be interpreted on a qualitative basis and should help to understand the influences of relevant parameters on the local corrosion process.

With the explanation of a combined corrosion mechanism consisting of oxidation and active Cl-induced oxidation the dependence on the flue gas temperature and velocity, reported in Section 4.2 becomes plausible. Both parameters considerably influence the heat flux and hence, the temperature profile in the deposit layer, which in further progress leads to a significant speed up of the overall corrosion process.

5.3 Implementation of the detailed corrosion model in the coupled heat exchanger/deposit formation model

The composition and the state of aggregation of the deposit layer are directly related to the high-temperature corrosion mechanisms prevailing. To evaluate the local corrosion potential in a biomass fired boiler detailed knowledge of the local deposit composition and state of aggregation is essential.

Therefore, the detailed corrosion model was implemented in a coupled heat exchanger/deposit formation model [77], [66]. As already described earlier this model is able to simulate the deposit formation in biomass fired boilers, including the furnace and radiative boiler section as well as the convective boiler section with superheater tube bundles (as given in large steam boilers).

The detailed model developed is able to estimate the local corrosion potential in the form of a parabolic rate constant for the corrosion mechanisms oxidation and active Cl-induced oxidation (see Section 5.2). However, due to the application range of the steel 13CrMo4-5 the calculation of the parabolic rate constant is limited to temperatures below 570 °C. The corrosion induced by molten salts is also not taken into account within this first

version of the detailed corrosion model. However, this corrosion mechanism is of relevance in waste incinerators and biomass plants firing waste wood or chlorine rich herbaceous fuels (see Section 4.3, as well as [Paper I], [19], [51], [97]).

The deposit formation model is able to determine the aggregate state of the deposit by means of chemical equilibrium calculations and hence, the position of local molten deposits. Although the actual corrosion potential for this corrosion mechanism cannot be calculated with the detailed model so far, it is of interest to know which kind of corrosion is of relevance for a plant under certain operating conditions.

Therefore, the type of high-temperature corrosion locally prevailing is determined by the following approach:

Table 5.4: Logical scheme used for the determination of the dominating local corrosion mechanism

Cl content in deposit	**liquid fraction in deposit**	**steel temperature**	**local corrosion mechanism**	**assigned value**	**k_p**
= 0	= 0	< 570 °C	oxidation	0	calculated using Eq. 12
= 0	= 0	≥ 570 °C	oxidation + FeO formation	-1	not calculated
> 0	= 0	< 570 °C	oxidation + active Cl-induced oxidation	-2	calculated using Eq. 12
= 0	> 0	independent of T	molten salt corrosion	-3	not calculated
> 0	> 0	independent of T	Molten salt corrosion + active Cl-induced oxidation	-4	not calculated

This approach has two levels of detail. The first one allows for an evaluation which corrosion mechanisms are of relevance for a plant under certain conditions. The second one allows the calculation of a local high-temperature corrosion potential, if the local corrosion mechanism prevailing can be described with the model developed. Therefore, above 570°C and for molten phases, the parabolic rate constant is set to the fixed value of -1e30. This should indicate that in general, the local rate constant would have a value larger than zero but cannot be calculated due to the temperature or the corrosion mechanism prevailing.

To illustrate the modeling approach an exemplary result of a calculation of the local corrosion mechanism as well as the parabolic rate constant can be found in Figure 5.7. The simple test case shown comprises the simulation of a heat exchanger tube bundle, with clean steal surfaces (no ash deposits), through which a fully burnt flue gas is passing. A detailed description of the test case as well as the relevant boundary conditions can be found in the Annnex (see Section 8.1.2). The heat exchanger is operated in co-current mode. The flue gas temperature at the entry of the simulation is 860 °C, while the flue gas velocity is 6 m/s. In the simulation the formation and deposition of fine dust as well as the direct condensation of the ash forming vapours is considered. Within the test case, the following chemical composition of the flue gas is taken into account: O_2 = 0.093 kg/kg;

CO_2 = 0.149 kg/kg; H_2O = 0.086 kg/kg; Na = $2.55 \cdot 10^{-07}$ kg/kg; K = $6.46 \cdot 10^{-06}$ kg/kg; Cl = $8.00 \cdot 10^{-07}$ kg/kg; S = $2.49 \cdot 10^{-06}$ kg/kg; N_2 = remaining. The radiative and convective heat flux is calculated with the heat exchanger model. The trend of the flue gas temperature resulting from this calculation is shown in Figure 5.7a. For the heat exchanger model a linear increase of the steam temperature in the heat exchanger bundle from 400 °C to 580 °C is assumed, which leads to the steel temperatures presented in Figure 5.7b. The mass of ash deposited after 2 hours is shown in Figure 5.7c, whereas the mass of Cl deposited is shown in Figure 5.7d. The resulting mass fraction of Cl is shown in Figure 5.7e. One can see that condensation of Cl does only occur for steel temperatures below 500 °C and no liquid phase is present throughout the heat exchanger (see Figure 5.7f). Therefore, three different local corrosion mechanisms take place on the heat exchanger bundle in the test case investigated (see Figure 5.7g).

Up to now the parabolic rate constant for the two mechanisms active Cl-induced oxidation (see Figure 5.7h) and oxidation (see Figure 5.7i) can be estimated with the detailed high-temperature corrosion potential model. The resulting overall rate constant according to Eq. 12 is shown in Figure 5.7j. In the case of steel temperatures higher than 570°C (represented by the purple color in Figure 5.7g) the parabolic rate constant is not calculated. Although no rate constant is calculated, one has to expect a high local corrosion potential due to the strongly enhanced oxidation rate of iron above 570 °C (see Section 5.2.1). Figure 5.7j shows continuously increasing corrosion rates with increasing steel temperatures, although no Cl is deposited at temperatures above 500°C. As discussed earlier, it is assumed that the influence of Cl-induced oxidation strongly depends on the deposit temperature. However, in the test case only the deposit formation during the first two hours was simulated, which leads to rather low deposit temperatures. Hence, the effect of Cl-induced oxidation is negligible and the oxidation of the steel is the dominating effect even though chlorine is present on the cold parts of the heat exchanger.

This approach has the benefit that it allows for a quick overview of relevant local corrosion mechanism illustrated in one figure. Moreover, due to the modular approach, the model can be easily modified regarding additional corrosion mechanisms or improved coefficients resulting from new experimental data.

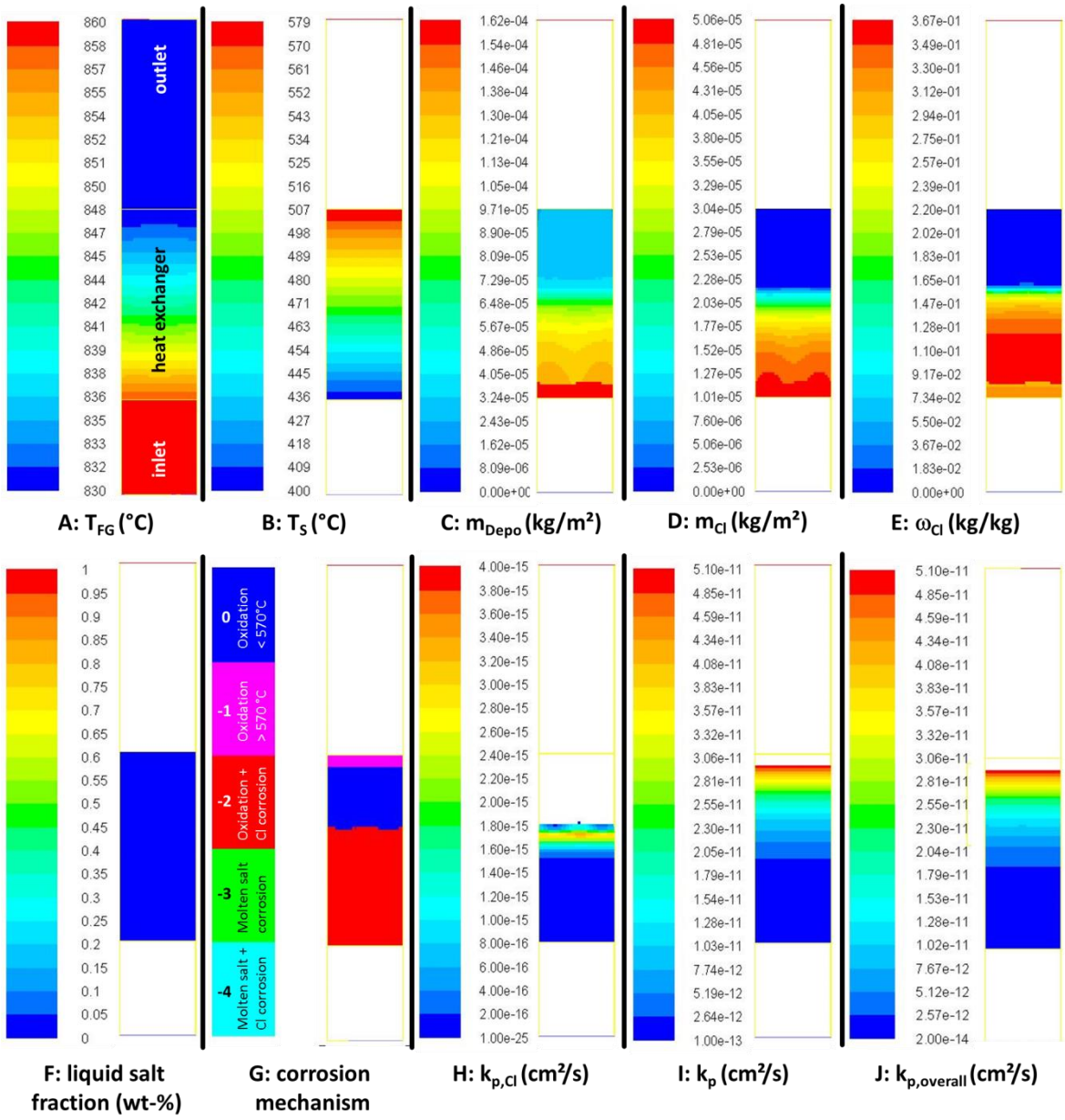

Figure 5.7: Exemplary results of the coupled heat exchanger/deposit formation/detailed corrosion potential model. The figure shows the most relevant parameters (A: flue gas temperature (°C); B: steel temperature (°C); C: mass of ash deposition (kg/m²); D: mass of Cl deposition (kg/m²); E: mass fraction of chlorine (kg/kg); F: liquid salt fraction (wt-%)) as well as the results of the detailed corrosion potential model (G: local corrosion mechanism; H: calculated parabolic rate constant of active Cl-induced oxidation (cm²/s); I: calculated parabolic rate constant of oxidation (cm²/s)J: calculated overall parabolic rate constant (cm²/s)).

5.4 Comparison of selected results from the detailed high-temperature corrosion model with experimental data

The ash deposit formation on heat exchanger surfaces in biomass fired boilers is generally time-dependent. This was also found within the experimental work of this thesis (see Section 4.1.3). However, due to the complexity of the underlying processes the CFD simulation of the deposit formation is computationally very expensive (see Section 3.2.3). Therefore, up to now it is only possible to simulate the deposit formation of one time step within reasonable calculation time. Since a rate of deposit formation is calculated, which can be integrated over an arbitrary time, the deposit formation is assumed to follow a linear trend over this time step. Due to the time dependence of the ash deposition, the time step investigated should not be too long to avoid systematic errors. Hence, it is generally not recommended to extrapolate the results of such a one-time step simulation from the initial to the steady state.

Due to this, all CFD simulations of deposit growth performed within this work represent a rather strong simplification to the reality. Furthermore, they are not suitable to thoroughly validate the newly developed model by comparing simulation results with the experimental data, after a rather long time of several hundred hours (e.g. 200 h or 300 h), which have been typical times of corrosion test runs performed within this work.

However, the initial deposit formation in the first two hours is, due to the thin ash layer formed during this time, nearly time independent. Hence, the short-term deposit measurements are well-suited for a comparison of the predicted and the measured deposit formation under a given parameter setup.

To allow a comparison of the deposit probe measurements and the CFD simulation, the same combustion conditions as for the reference state of the online corrosion probe test run with wood chips have been chosen as boundary conditions for the simulation. This means a fuel power input of 23 kW (related to NCV) and a total air ration of 1.5 (see Section 4.1.1 and Table 4.1). A scheme of the drop tube reactor and the relevant mass fluxes of the combustion simulation can be found in Figure 5.8.

The simulation has been performed within a two-step approach. Firstly, the flue gas flow and the heat transfer in the drop tube reactor were simulated using the models described in Section 3.2. Then, the local deposit and corrosion behaviour was evaluated in a post-processing step using the coupled heat exchanger/deposit formation model (see Section 3.2.3) in combination with the newly developed corrosion potential model (see Section 5.2). The release rates of the ash forming vapours, which are necessary boundary conditions for the simulation of the deposit formation, were taken from the balancing test run performed during the wood chips online corrosion probe test run (see [89] and Table 5.5).

A detailed description of the relevant simulation boundary conditions can be found in the Annex (see Section 8.1.3).

Table 5.5: Release rates of the ash forming elements

	K	Na	S	Cl
release rates	18 %	5 %	90 %	98 %

Based on this release rates, the primary air and fuel mass fluxes, the concentrations of ash forming elements at the fuel bed (CFD inlet) have been set to: Na = $2.06 \cdot 10^{-06}$ kg/kg; K = $6.28 \cdot 10^{-05}$ kg/kg; Cl = $1.89 \cdot 10^{-05}$ kg/kg; S (as "passive" SO_2) = $1.08 \cdot 10^{-04}$ kg/kg.

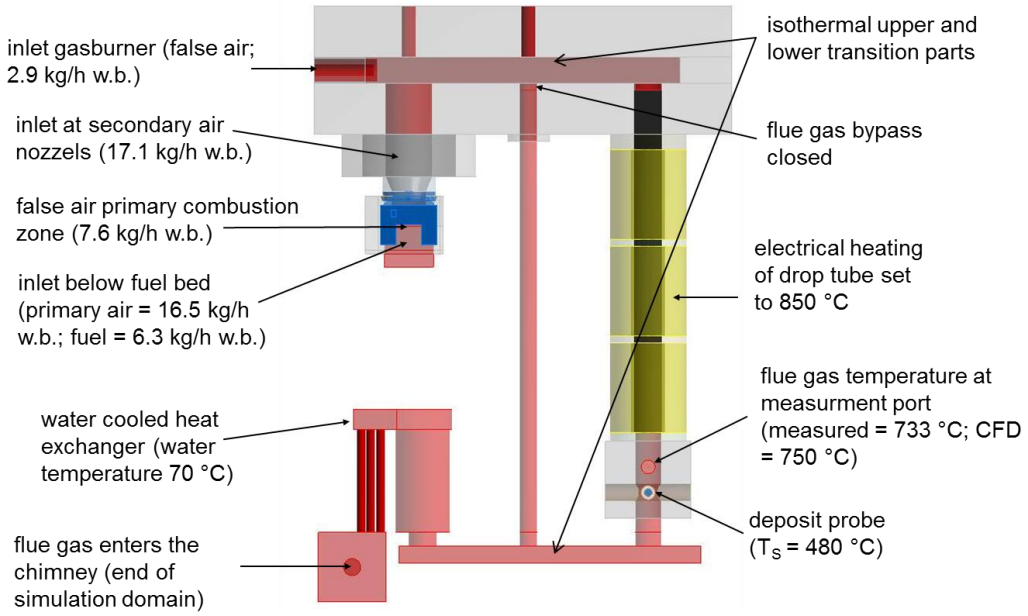

Figure 5.8: Scheme of the drop tube simulation including relevant CFD simulation input parameter

The calculated flue gas temperature at the position of the thermocouple as well as the flue gas velocity at the entrance of the measurement box are in reasonable agreement with the measurements (see Figure 5.9 and Section 4.1.1).

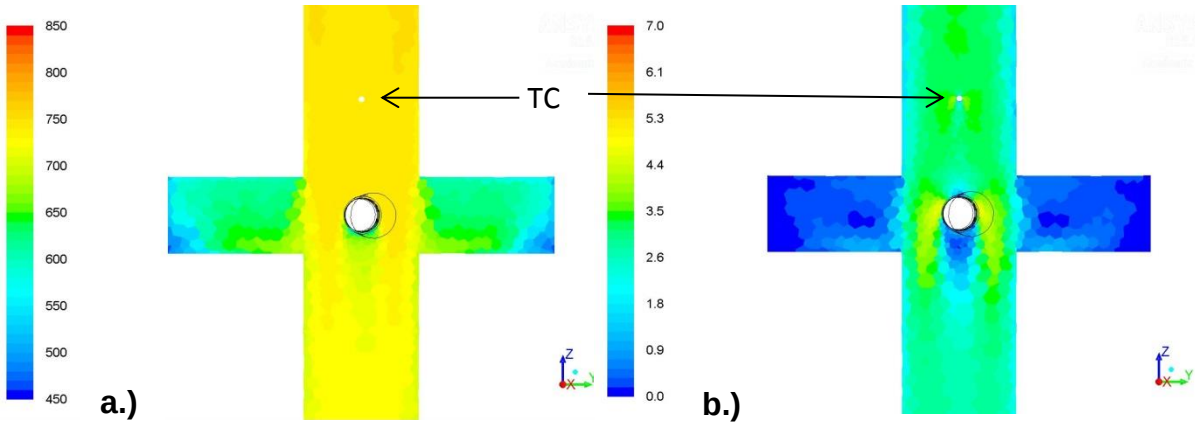

Figure 5.9: Results of the CFD simulation. The flue gas temperature (°C) is shown in Figure a, the flue gas velocity (m/s) is presented in Figure b.
Explanation: TC … thermocouple

A built-up rate of 2.8 g/m²h was measured during the deposit probe experiments (see Chapter 4.1.3). The CFD simulation yielded a rate of 0.4 g/m²h and hence, showed deviations from the measurements. When comparing these two results one has to keep in mind that only one deposit probe measurement has been carried out for this parameter setup. Generally, this measurements show rather strong variations (see [31] and [81]) due to the inhomogeneous biomass and the fluctuating combustion conditions due to control measures. Therefore, some deviations between simulation and experiment have to be expected. The mean (mass weighted average over the whole sample ring) chemical compositions of the deposits formed are in good agreement as can be seen in Figure 5.10.

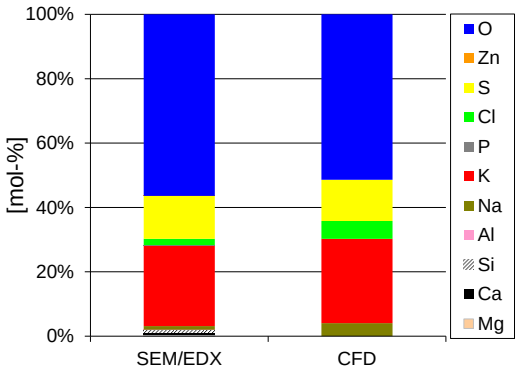

Figure 5.10: Comparison of elemental composition found within the deposit probe measurements and the CFD simulations
Explanation: Measurement time 2 h; elemental contribution represents the mean value over the whole sample ring

As already mentioned, this simulation results for the initial phase of the test run should not be extrapolated to 300 h operation time, due to the time-dependence of the deposit formation. However, the local high temperature corrosion potential, after 300 h, which represents the typical duration of the test runs performed within this work, is of special interest. To take the reduced heat transfer and hence the increased surface temperatures of the ash layer into account, the deposit formation was calculated under the assumption of a basic deposit layer. Again, the reference state of the online corrosion test run with wood chips was simulated, which means T_S of 480 °C, v_{FG} around 3 m/s and T_{FG} around 730 °C. A detailed list of all parameters is given in the Annex.

The role of chlorine for the overall corrosion mechanism during the short-term online corrosion probe measurements was quite unclear. Hence, on the one hand, this simulation should clarify if Cl is still deposited under these boundary conditions or not. On the other hand, the detailed model should be applied to determine the dominating corrosion process as well as the local corrosion potential, which can be qualitatively compared with the experimental results gained within this work.

The steel surface temperature on the flue gas side is presented in Figure 5.11a, and the surface temperature of the ash layer is presented in Figure 5.11b. One can see that the assumed fouling layer enhances the surface temperature significantly.

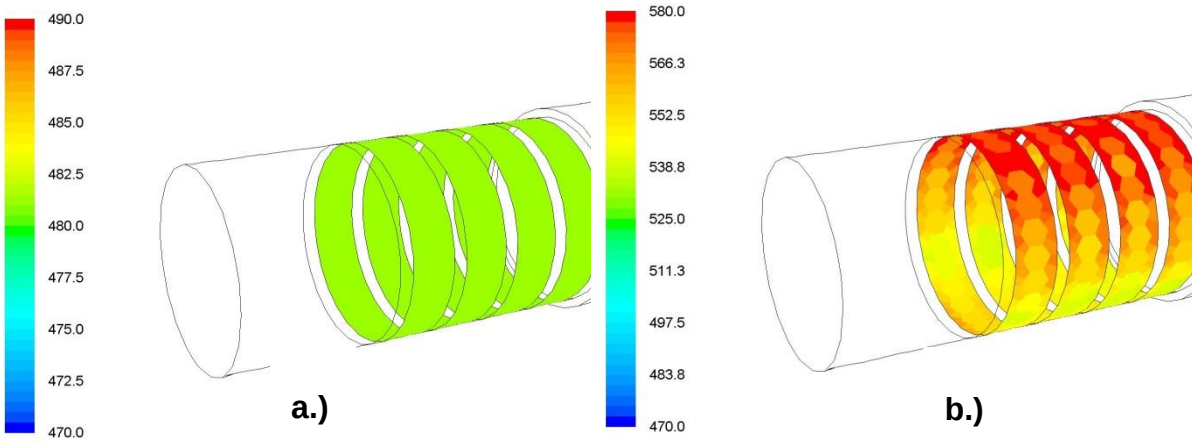

Figure 5.11: Calculated steel surface temperature (°C) on the flue gas side of the probe rings (Figure a) and calculated surface temperature of the deposit layer (°C) on the flue gas side of the probe rings (Figure b)

Due to the high surface temperatures, almost no chlorine is deposited anymore (see Figure 5.12a). Here, the build-up rate of chlorine is a factor of 10^4 smaller than the overall deposit build-up rate and hence, negligible.

These results support the explanatory approach proposed earlier in this work (see Section 4.3). Due to the temperature variations, the already deposited chlorine becomes most likely evaporated during the test runs with high steel temperatures and the supply of chlorine cannot be maintained further on, due to the high deposit surface temperatures, caused by the already deposited ash particles.

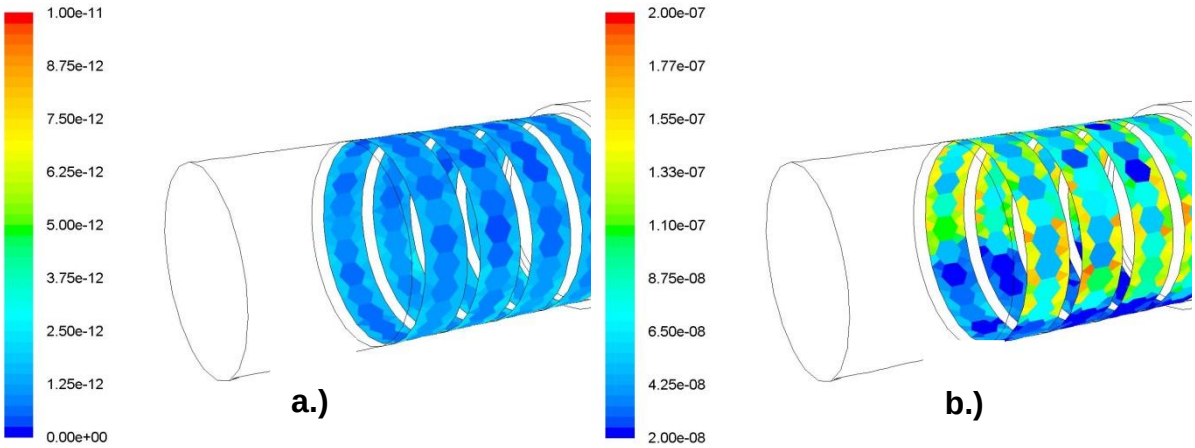

Figure 5.12: Calculated deposition rate of chlorine (kg/m²s) (Figure a) and calculated overall deposition rate (kg/m²s) (Figure b)

Furthermore, the overall deposit growth is 0.33 mg/m²h and hence, reduced compared to the initial build-up on the clean probe (0.40 mg/m²h). This result is plausible, since due to the high surface temperatures, the condensation of the alkali chlorides is suppressed.

The simulation predicts the absence of a liquid phase (see Figure 5.16a). This was also found in the online corrosion probe test runs (see Section 4.1.3).

Moreover, one can see in Figure 5.16b that the model predicts a rather uniform corrosion potential over the sample rings. This can be explained by the fact that the oxidation of the steel is the dominating corrosion mechanism (see Figure 5.17) and the steel temperature is constant over the sample rings (see Figure 5.11a).

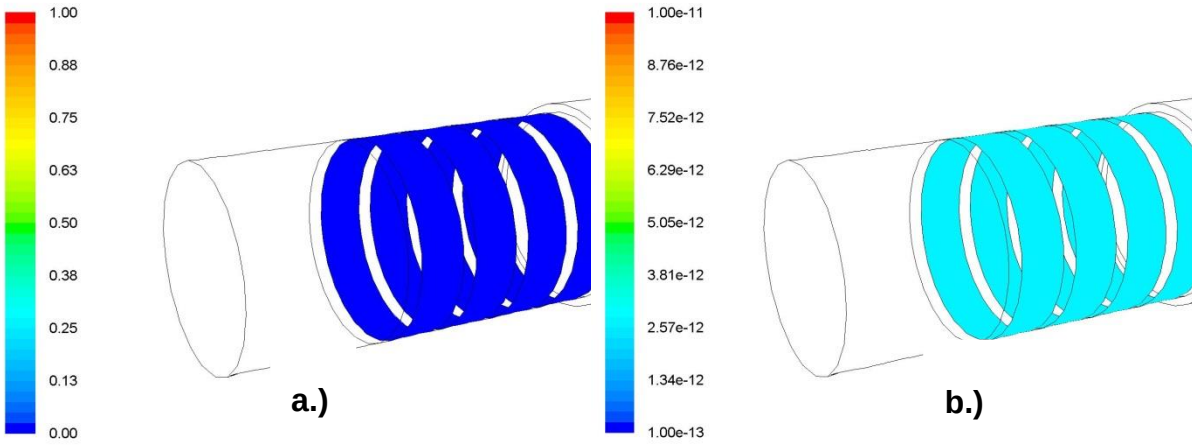

Figure 5.13: Calculated liquid salt fraction (kg/kg) (Figure a) and calculated overall parabolic rate constant $k_{p,overall}$ (cm^2/s) (Figure b)

The online corrosion test run as well as the simulation agree that no more chlorine should be deposited in the final stage of the test run. Due to this, the share of active-Cl induce corrosion on the overall corrosion mechanism is negligible (see Figure 5.14). This is in good agreement with the MLP test run performed by Retschitzegger et al. which was carried out under comparable, but not identical, boundary conditions (see Section 5.1.2).

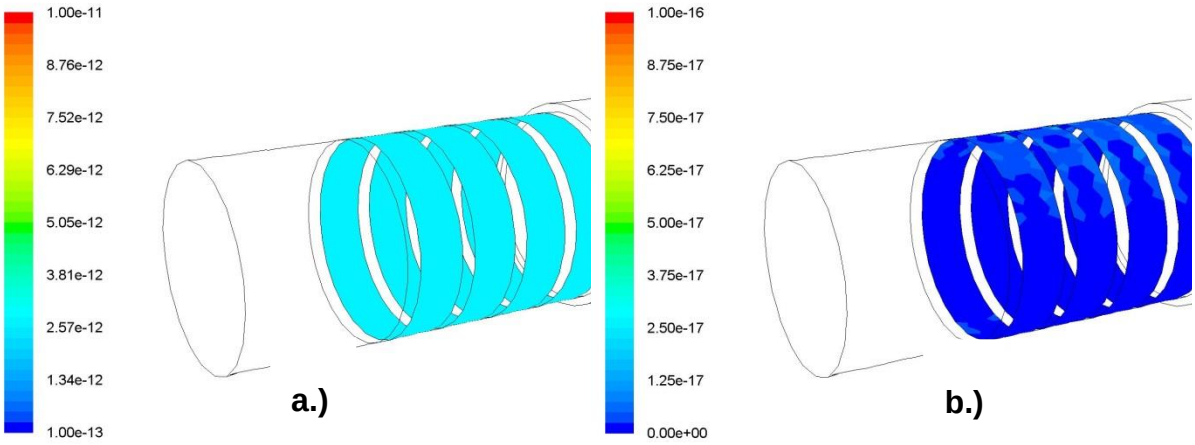

Figure 5.14: Calculated parabolic rate constants for the pure oxidation (cm^2/s) (Figure a) and for the active Cl-induced oxidation (cm^2/s) (Figure b)

Also the parabolic rate constant determined in the test run of Retschitzegger et al. (presented in Figure 5.1; 2.76·10-12 cm²/s) is in good agreement with the average overall parabolic rate constant $k_{p,overall}$ calculated by the CFD simulation (see Figure 5.13b; 2.78·10-12 cm²/s).

5.5 Application of the model

5.5.1 Description of the case study

The detailed model developed has been applied within a CFD simulation of flue gas flow and heat transfer to estimate the local corrosion potential of a forest wood chips fired water tube steam boiler. As already explained in Section 3.2.3, with the CFD based deposit formation model applied, it is not possible up to now to calculate the time-dependent growth of the deposit layer over a longer exposition time due to the calculation times which are too long for practical applications. However, the thickness of a deposit layer on the superheater tubes generally varies due to cleaning cycles alternating with a continuous growth of the deposit layer. Based on this saw tooth behaviour of deposit thickness over time, it is possible to define a "virtual" quasi-steady state deposit layer, which is given by the average thickness of the deposit layer over one cleaning cycle. This procedure is commonly used as a sufficient approximation to calculate the average steady-state heat transfer of a boiler. Based on this assumed basic deposit layer, one can carry out a CFD simulation to determine the elemental distribution of the local ash deposits. Using this information, the detailed corrosion model can be applied to calculate the local quasi-steady state corrosion potential. However, one has to keep in mind, that this represents a rather strong simplification. Future work should be conducted on this problem and investigate the time-dependent deposit growth in more detail.

The most relevant operation data of the plant can be found in Table 5.6, whereas Table 5.7 provides the most important information regarding the superheaters of the plant. A detailed list of all relevant parameters can be found in the Annex (see Section 8.1.4).

The boundary conditions (e.g. flue gas temperature and composition) at the entrance of the simulation domain were taken from mass and energy balances under the assumption of complete combustion provided by the plant manufacturer.

Table 5.6: Relevant boiler information

Fuel power input related to NCV	13.1	MW
Boiler output	10.7	MW
Flue gas mass flow	11.1	$kg \cdot s^{-1}$
Saturation steam temperature	271	°C
Saturation steam pressure	5600	kPa
Live steam temperature	475	°C
Live steam pressure	5400	kPa

Table 5.7: Relevant boundary conditions for the superheater tubes
Explanation: SH1, SH2… superheater tube bundles, ccf … cross counter flow, cpf … cross parallel flow

		SH1	SH2
Type	-	bank of in-line tubes	
Operating mode	-	ccf	cpf
Outer tube diameter	mm	38	38
Tube wall thickness	mm	4	4
Tube wall material	-	16Mo3	13CrMo4-5
Heating surface	m^2	140	66

Figure 5.15 illustrates the different sections of the biomass CHP plant considered in the CFD case study. To achieve a fully developed flow field at the entrance to the convective boiler section, the upper transition part from the furnace to the radiative duct, as well as the radiative duct itself were included in the simulation. Therefore, the simulation domain comprises the transition from the furnace duct to the radiative boiler section, the radiative boiler section, the transition to the convective section, the two ash hoppers as well as the convective section with the two superheater bundles SH1 to SH2 as well as the evaporator tube banks ET.

The heat loss over the finned tube walls is calculated by the saturated steam temperature and the mean heat transfer coefficient on the water side as boundary conditions.

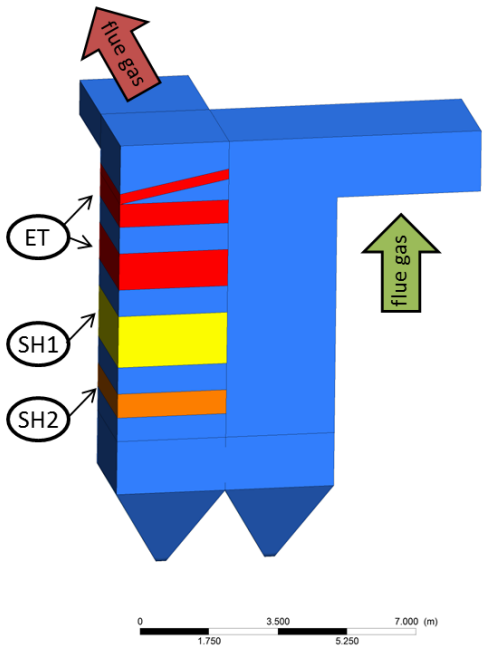

Figure 5.15: Schematic view of the simulated CHP plant
Explanation: ET … evaporators; SH1 … first superheater grid; SH2 … second and final superheater grid

To consider the reduced heat transfer due to the an assumed mean ash deposit layer on the heat exchanger surfaces a thermal resistance of 8 m²K/kW (4 mm fouling layer with a thermal conductivity of 0.5 W/mK) is assumed on the finned tube walls respectively 5 m²K/kW (2.5mm fouling layer with a thermal conductivity of 0.5 W/mK) on the superheater tube walls. The fouling layers have been chosen in that way, that the entrance temperature of the flue gas in the final superheater fits the data given by the plant manufacturer best.

In contrast to the computationally cheap empirical model the detailed corrosion model needs additional information from a deposit formation model (see Section 5.2). Therefore, the simulations were performed in a three-step approach. Firstly, the flue gas flow and heat transfer in the boiler was simulated. Thereby, the flow as well as the convective and radiant heat transfer in the superheater tube banks as well as the evaporator grids were calculated with the heat exchanger model described in Section 3.2.2. Then, the formation of aerosols and deposits was calculated in a post-processing step. Finally, the local corrosion behaviour was evaluated.

A necessary boundary condition for the application of the deposit formation model is the concentration of condensing ash forming species as well as the concentration of SO_2 at the entrance to the simulation domain. Since no model is able to estimate the released amounts from the fuel into the flue gas sufficiently accurate, the values for the simulations have been taken from an experimental balancing test run of a comparable forest wood chips firing grate furnace. The measured release rates of the relevant ash forming elements were: K = 24.1 wt.-%, Na = 37.5 wt.-%, S = 82.8 wt.-%, Cl = 97.9 wt.-%. A detailed description of these test runs including the fuel composition can be found in [31]. According to this experimental data and the specifications from the plant manufacturer the following gas composition was used as boundary condition for the simulation[8]: O_2 = 0.065 kg/kg, CO_2 = 0.111 kg/kg, H_2O = 0.123 kg/kg, SO_2 = $3.6 \cdot 10^{-5}$ kg/kg, Na = $3.97 \cdot 10^{-6}$ kg/kg, K = $3.74 \cdot 10^{-5}$ kg/kg, Cl = $9.49 \cdot 10^{-6}$ kg/kg.

5.5.2 Simulation results

The calculated flue gas velocities are presented in Figure 5.16a, whereas the calculated flue gas path lines coloured by the flue gas temperature are shown in Figure 5.16b.

Due to the sharp deflection and the strong change of the cross-section at the entrance of the radiative boiler duct, the flue gas passes along the inner (left) wall of the radiative duct, as can be seen in Figure 5.16a. The flue gas flow does not even cover half of the duct diameter. This leads to decreased efficiencies. The problem might be solved using baffles at the entrance of the duct. Further on after the entrance to the superheater duct the flue gas hits the outer (left) wall of the superheater duct. Therefore, the flow through SH2 is not even distributed. This leads to enhanced flue gas velocities and flue gas

[8] For the sake of completeness the concentrations of the ash forming vapours are also given in ppmv: K = 26.3 ppmv, Na = 4.8 ppmv, Cl = 7.4 ppmv, SO2 = 15.4 ppmv.

temperatures on the left side of the tube bundle and therefore, locally enhanced surface temperatures on the deposit layer (see Figure 5.17b).

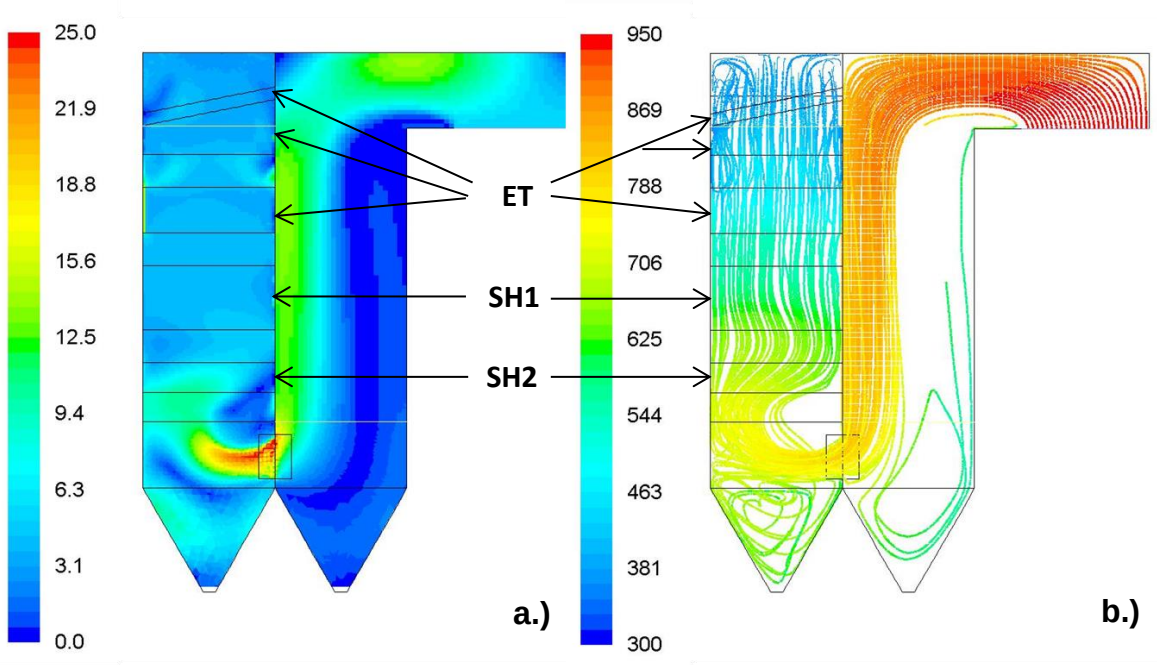

Figure 5.16: a.) Flue gas velocity (m/s) and b.) flue gas temperature (°C) in the symmetry plane of the simulated plant.
Explanation: SH … superheater, ET … evaporator

One can also see that SH2 homogenizes the flow distribution over the cross-section of the boiler pass. Due to this fact SH1 is more equally passed through by the flue gas as SH2. The outer steel surface temperature (boundary between the steel and the deposit layer), which is a relevant parameter for the high-temperature corrosion model (see Eq. 12) is presented in Figure 5.17a. One can also notice that the assumed fouling layer enhances the surface temperature (deposit/flue gas) considerably.

In Figure 5.18a one can see that chlorine is deposited throughout the superheaters SH1 and SH2 in the case investigated. Due to the fact that the outer steel temperature of the evaporator tubes is considerably below the validation range of the model (see Figure 5.17a) only the corrosion behaviour of the superheater bundles is calculated within this work.

As already explained earlier in this section, the concentrations of the ash forming vapours in the simulation are comparable to the wood chips test runs performed. During the wood chips test run, no molten phase could be allocated in the deposits, whereby flue gas temperature variations up to 900 °C and steel surface temperatures variations up to 550 °C have been performed. In the final and therefore hottest superheater SH2 the flue gas temperatures are around 700 °C (see Figure 5.16b) and the highest steam temperature is 475 °C (see Figure 5.17), which is far below the highest temperature variations investigated during the experimental test runs. Hence, it is plausible that the simulation

predicts the absence of a molten phase under the boundary conditions prevailing (see Figure 5.18b).

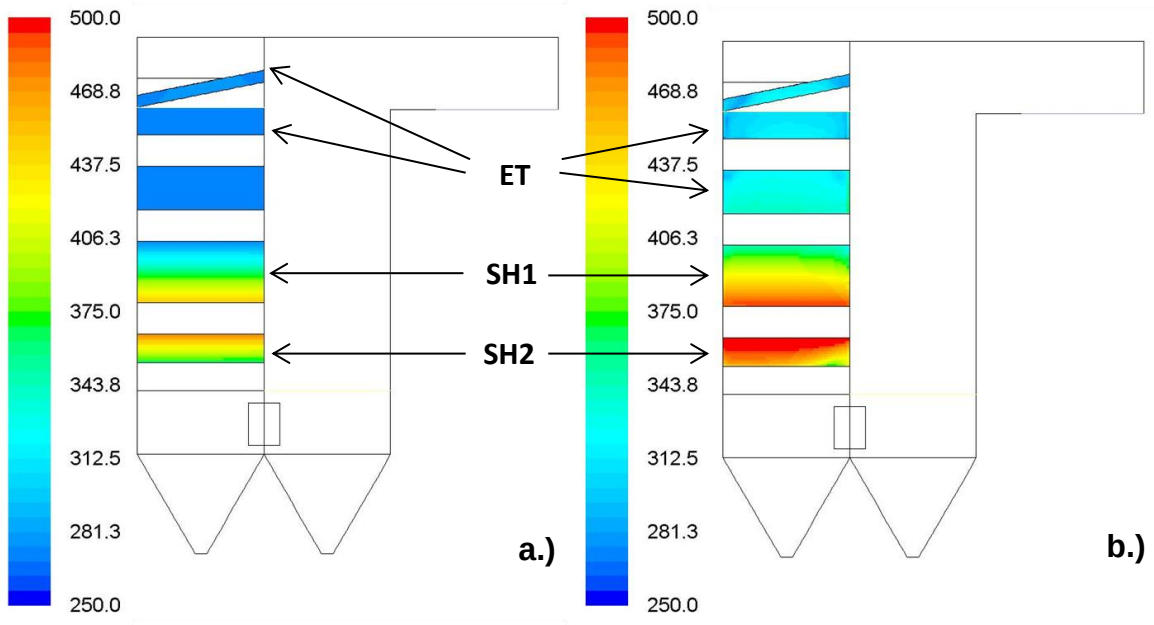

Figure 5.17: a.) Steel temperature on the boundary steel/deposit (fouling layer) (°C) and b.) surface temperature at the boundary deposit (fouling) / flue gas (°C) in the symmetry plane of the simulated plant
Explanation: SH … superheater, ET … evaporator

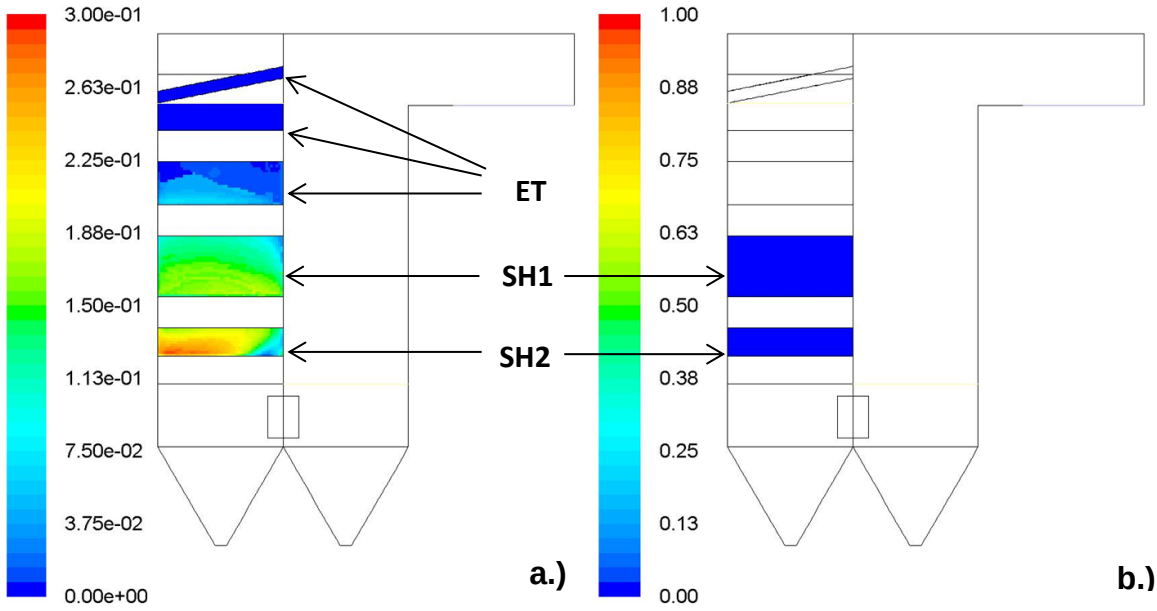

Figure 5.18: a.) Chlorine deposition rate (kg/m²s) and b.) liquid fraction of the deposit (kg/kg) on the superheater tube bundles depicted in the symmetry plane of the simulated plant
Explanation: SH … superheater, ET … evaporator

Due to presence of chlorine, the absence of a molten phase and steel temperatures below 570 °C, the corrosion mechanism prevailing is a combination of oxidation and chlorine induced active oxidation of the low alloy steel, as can be seen in Figure 5.19a. This result is in agreement with the measurements performed within this work. The calculated overall high temperature corrosion potential (overall parabolic rate constant) is shown in Figure 5.19b.

According to Eq. 12 the fractions of the rates of the two corrosion mechanisms oxidation and chlorine induced oxidation can be calculated to gain information regarding the most dominant corrosion mechanism. The local rate constant for the oxidation of the steel by oxygen and water is presented in Figure 5.20a, the one of the active Cl-induced oxidation can be found in Figure 5.20b. One can clearly see that the oxidation of the steel is several orders of magnitude faster than the active oxidation by chlorine for the parameter setup investigated. It should be mentioned that the behaviour may vary within one cleaning cycle of the real boiler, since the influence of the Cl-induced oxidation strongly depends on the deposit temperature.

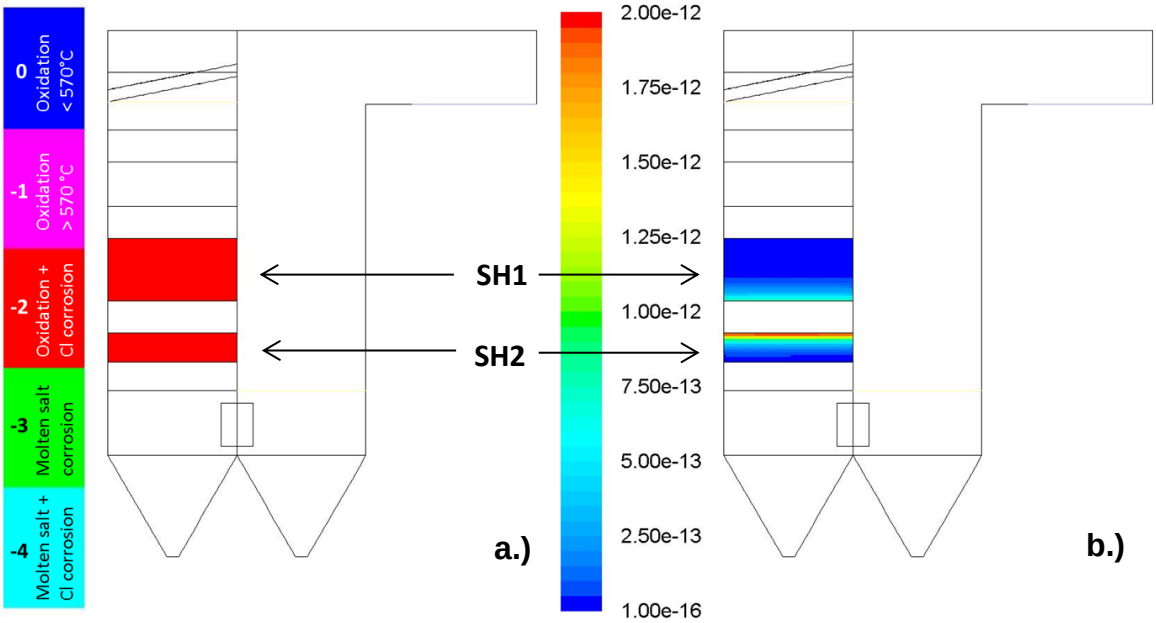

Figure 5.19: a.) Corrosion mechanism prevailing and b.) overall parabolic rate constant $k_{p,overall}$ (cm²/s) in the symmetry plane of the simulated plant.
Explanation: SH … superheater

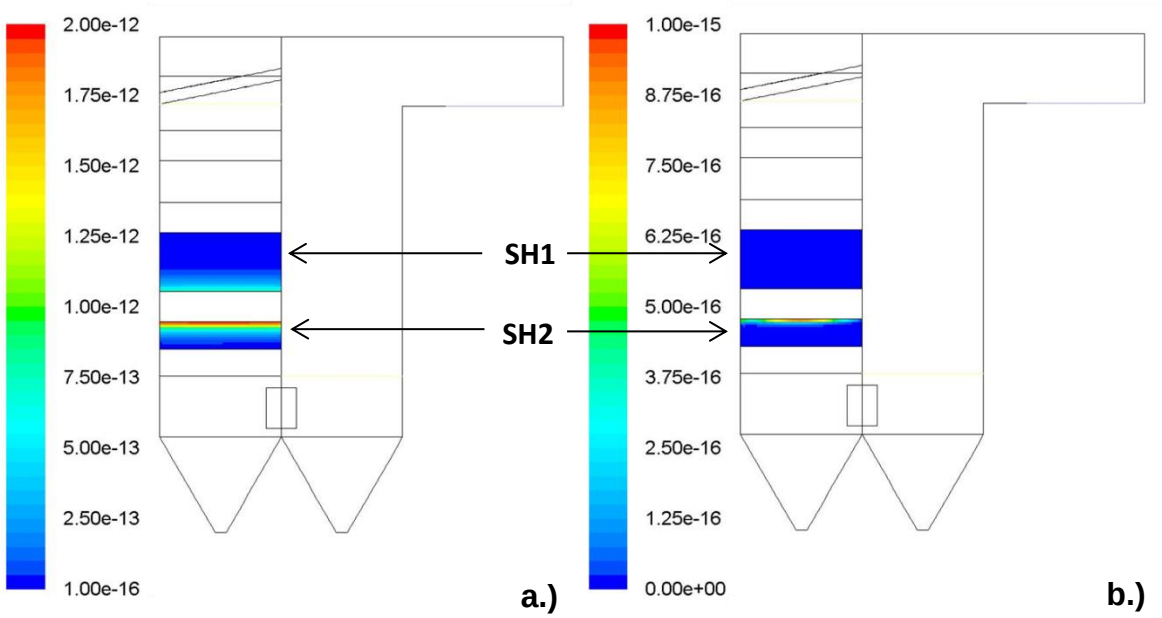

Figure 5.20: a.) Oxidation related part of the overall parabolic rate constant $k_{p,oxide}$ (cm²/s) and b.) active Cl-induced oxidation related part of the overall parabolic rate constant $k_{p,Cl}$ (cm²/s) in the symmetry plane of the simulated plant.
Explanation: SH … superheater

To compare the two models developed, the empirical model developed was also applied for the same case study with the same parameter setup (gas compositions, heat fluxes, etc.).

The empirical model was developed based on short-term measurements without the consideration of the time-dependence of the corrosion process. Hence, the corrosion potential (mm/1000h) calculated by the empirical model represents a steady-state potential. The detailed model on the other hand is time-dependent, as already discussed earlier. Hence, the results of the two models can only be compared qualitatively. As already mentioned, the case study was carried out under the assumption of an average deposit layer to approximately calculate the steady state heat transfer and rate of deposit formation (as well as the local chemical composition of the ash deposits). Due to this assumption, it is possible to calculate a parabolic rate constant, according to Eq. 12, which can be used to calculate the material loss for an arbitrary time frame. In doing so, the material loss of steel after 1000h is calculated with both models. The results are presented in Figure 5.21.

Both models show qualitatively a comparable corrosion potential with the highest corrosion potential being at the exit of the final superheater (SH2). While high-temperature corrosion might also be of relevance at the entrance of SH1, it only plays a minor role for the rest of the CHP plant.

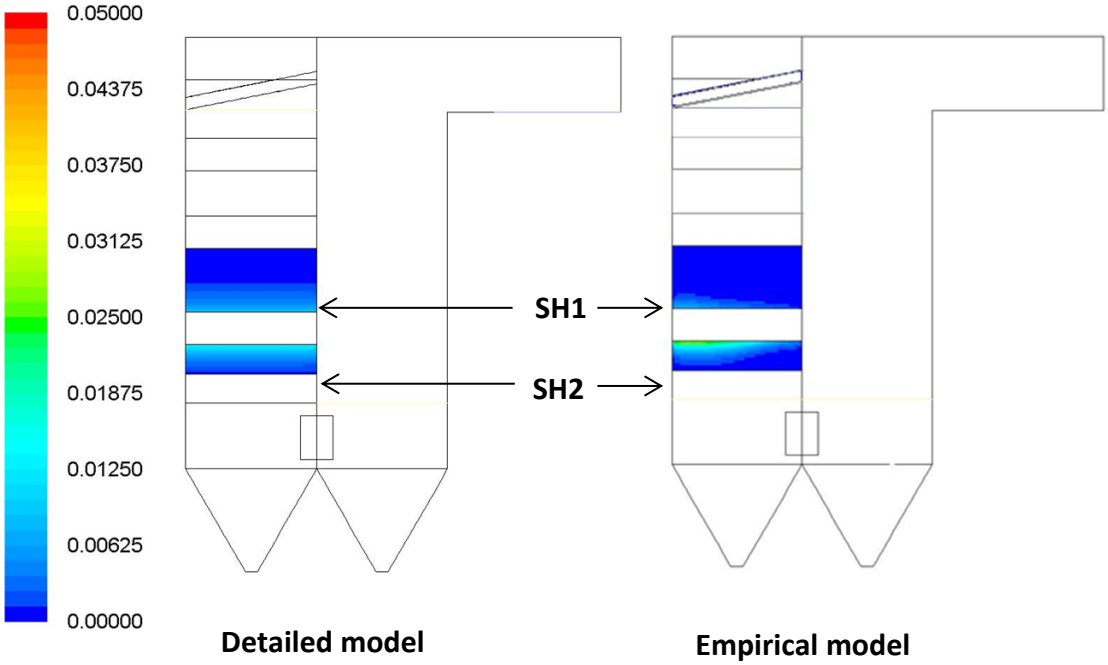

Figure 5.21: Comparison of the mass loss calculated after 1000h (mm) with the detailed model (left) and with the empirical model (right).
Explanation: SH … superheater

5.6 Summary and recommendations

For chemically untreated woody biomass the online corrosion probe measurements performed did not clarify with certainty the high-temperature corrosion mechanisms prevailing on low alloy steel like 13CrMo4-5 superheater tubes. Hence, additional measurements have been carried out to identify the most dominant corrosion mechanism prevailing.

These additional measurements lead to the conclusion that two corrosion mechanisms prevail in the temperature range of interest. While the oxidation of the steel by gaseous O_2 and H_2O solely depends on the steel temperature, the share of active Cl-induced oxidation on the overall corrosion rate depends on the deposited mass of chlorine as well as on the deposit temperature.

Based on these results a detailed corrosion model has been developed which takes the diffusion processes occurring during the oxidation of low alloy steel into account. Furthermore, the sulphation of alkali chlorides in the deposits was identified as key reaction for the active Cl-induced oxidation. Hence, the reaction kinetics of this corrosion mechanism is determined by the amount of chlorine in the deposits as well as the mean deposit temperature. Here, the deposit temperature controls the reaction rate, which is known to follow an Arrhenius equation.

Due to uncertainties regarding the dependence on the flue gas water content as well as the low data density for the optimization of the coefficients E_{act} and $k_{0,Cl}$ the model developed is not able to predict actual corrosion rates. In addition the theory of Wagner

was developed to describe the oxide formation on pure metals. Hence, the usage for low alloy steel represents an approximation, although, steels with a Cr content lower than 2 wt-% generally show a similar corrosion behavior than pure iron (see Section 5.2.1). The results have to be interpreted qualitatively as corrosion potential and the model allows for the comparison of the influence of different operating conditions relative to each other.

While the empirical corrosion model developed is only valid for similar fuel compositions and combustion conditions as in the test runs, the detailed model is free of these limitations. Here, different fuel compositions lead to a different deposit build-up, which directly influences the local corrosion mechanism. Furthermore, the detailed model not only estimates the local corrosion potential, it also gives relevant information regarding the dominating corrosion mechanisms.

Up to now it is not possible to estimate a rate constant for all corrosion mechanisms relevant in biomass fired boilers. For example the model is able, to estimate, were hot corrosion type II will most probably occur, but it gives no information regarding the corrosion rate. However, from literature it is known that this type of corrosion can cause severe problems, which indeed is an useful information.

An additional drawback of the detailed model developed is the high computational effort and hence calculation time needed to calculate the deposit formation, which represents necessary input data for the corrosion simulation. For example, the CFD case study in which the detailed corrosion model was applied (see Section 5.5) had around 900 000 cells and needed around 700 hours (> 4 weeks) to converge[9]. Furthermore, the model is vulnerable to convergence problems, which additionally can increase the calculation time.

Comparisons of the calculated corrosion potential and deposit formation are in reasonable agreement with results obtained from the test runs. Hence, the detailed model was applied within a CFD simulation of flow and heat transfer to calculate the local corrosion potential of a biomass fired CHP plant (13.1 MW_{th}, 475 °C live steam temperature). The results obtained have been compared with those of the empirical model. On the first sight both models show a comparable corrosion potential, with a maximum at the exit of the final superheater. The detailed model additionally shows that the dominating mechanism is the oxidation of the steel by gaseous O_2 and H_2O. Due to the fact, that this mechanism is solely influenced by the steel temperature the inhomogeneous flow field has in contrast to the empirical model only an negligible effect on the estimated corrosion potential. However, this behavior can change if the deposit temperature as well as the chlorine content rises and hence, the active Cl-induced oxidation becomes the dominating mechanism.

[9] Using 4 cores of a HP Blade-System (ProLiant BL460c Gen8): CPU … Intel(R) Xeon(R) CPU E5-2667 v2 @ 3.30GHz; 32 GB RAM; the CPU'S are internal coupled with a Infiniband-Switch (40GB/s)

Finally, due to the modular approach, the detailed model is very flexible regarding modifications based on new experimental results obtained in the future.

6 Overall summary and conclusions

The goal of the work presented was the development of two approaches to model high temperature corrosion in biomass fired boilers. The first approach is an empirical one, the second one is a more sophisticated approach which also takes transport processes and chemical reactions into account.

Firstly, online corrosion probe test runs in a specially designed fixed bed / drop tube reactor have been carried out to investigate the most relevant parameters and their effects on the high-temperature corrosion processes occurring in biomass fired boilers (see Section 4.1). To take the influence of different fuel compositions into account test runs have been carried out with forest wood chips and waste wood A1-A2 (according to German standards). These fuels represent typical chemically moderately treated and untreated woody biomass.

The test runs showed that the most influencing parameters are the flue gas temperature, the steel surface temperature as well as the flue gas velocity. Based on the experimental data gained, an empirical corrosion model was derived. The model consists of an Arrhenius equation which describes the dependence on the flue gas as well as the steel surface temperature, whereas a linear correction term takes the influence of the flue gas velocity into account. The model developed fits the experimental data sufficiently (see Section 4.2).

Due to the rather short duration of the online corrosion probe test runs (~300 h) the model developed is not able to predict actual corrosion rates. Instead the model can be used to calculate a local corrosion potential. The model is well suited to identify areas which have a high risk regarding corrosion failures. Moreover, the model can be used to compare the local corrosion potential of different operating conditions and plant geometries.

While for both fuels the corrosion rate measured showed an exponential dependence on the flue gas temperature and a linear dependence on the flue gas velocity, the dependence on the steel temperature differs. Here, an exponential dependence was found for wood chips, while the measured signal showed a stagnating or even decreasing behaviour in the case of waste wood for steel temperatures above 500 °C (see Section 4.2).

The different dependencies on the steel temperature are most certainly related to different corrosion mechanism prevailing (see Section 4.3). In the case of waste wood, the measured corrosion rates stagnate or even slightly decrease with increasing steel temperatures. Since also molten phases could be found in the deposit probe measurements, it is suggested that hot corrosion type II represents a relevant corrosion mechanism in this case. For wood chips it is suggested, that the oxidation of the steel represents a relevant corrosion mechanism. However, the role of chlorine for the high temperature corrosion process is not clear, since no chlorine could be detected neither in the deposits nor at the corrosion front of the corrosion probe. However, the exponential

dependence on the flue gas temperature measured can hardly be explained with the oxidation being the only corrosion mechanism. Since the mechanism had to be clear prior to the development of the detailed model, additional test runs had to be carried out, to clarify which corrosion mechanisms are of relevance when firing wood chips. These measurements and their results are discussed later on in this summary and in Section 5.1.

Due to the empirical approach the application range of the model is limited. In general, the model is only valid for comparable fuel and combustion conditions within the parameter ranges investigated (flue gas temperature variations between 650 °C and 880 °C; steel temperature variations between 450 °C and 550 °C; flue gas velocity variations between 2 m/s to 8 m/s). The steel used within the test runs was 13CrMo4-5. Hence, the application of the model is limited to estimate the local high-temperature corrosion potential of this or similar ferritic low alloy steels like 16Mo3. Furthermore, the model developed can only by applied meaningfully to estimate the corrosion potential of biomass fired water tube steam boilers. A detailed discussion of the limitations can be found in Section 4.4.

The empirical model has been applied to simulate the high-temperature corrosion potential of a 42 MW_{th} fired CHP plant (38 MW_{th} boiler). In addition to an actual state analysis of the plant under full load conditions, two other cases have been investigated. In one case the live steam temperature of the plant has been increased from 453 °C to 480 °C in the second case the flow direction of the final superheater have been switched from parallel to counter-flow.

Both variations of the operating conditions lead to significantly higher maximum corrosion potentials than the actual state of the boiler. In the case study the optimized coefficients for the pure fuels wood chips and waste wood have been applied. A comparison of the predicted maximum corrosion potential shows that the use of pure waste wood increases the danger of a material failure due to high-temperature corrosion significantly. Furthermore, the case study showed that an inhomogeneous flow field has a negative effect on the maximum corrosion potential prevailing due to locally enhanced flue gas velocities and temperatures. A detailed discussion of these findings can be found in Section 4.5.

Concluding the empirical model developed is well suited to predict the local corrosion potential in biomass fired water tube steam boilers, based on the local values of influencing parameters: steel temperature, flue gas temperature and flue gas velocity. Additionally, the empirical model has the advantage that it is computationally inexpensive. Furthermore, no detailed knowledge regarding the underlying chemical and physical processes is necessary, which makes the model a very useful tool for a quick estimation if high temperature corrosion is of relevance in a biomass fired steam boiler under the framework conditions defined.

The second approach to model high temperature corrosion should take chemical reactions as well as transport processes into account. Since the online corrosion probe measurements did not clarify with certainty which corrosion mechanism is dominating,

additional measurements have been carried out in the drop tube reactor. Retschitzegger et al. used a newly developed mass loss probe to determine the time-dependent mass loss for the parameter setup (T_S = 480 °C, T_{FG} ~ 740 °C and v_{FG} ~ 3 m/s) and wood chips as fuel. Additionally, the probe was used to determine the time-dependent mass loss for the parameter setup (T_S = 480 °C, T_{FG} ~ 900 °C and v_{FG} ~ 3.3 m/s) for the same fuel. The results of these two test runs have been compared with a third test run using the probe for the same parameter setup as Retschsitzeger et al. (T_S = 480 °C, T_{FG} ~ 740 °C; and v_{FG} ~ 3 m/s), but natural gas instead of wood chips as fuel. Since this gas is basically free of the corrosive species SO_x and HCl, this test run represents a reference value for the case of oxidation being the dominating corrosion mechanism. Additionally, the oxidation behaviour of the steel 13CrMo4-5 under air was investigated using a muffle furnace (see Section 5.1).

The data gained in these experiments was used to determine the dominating corrosion mechanism as well as to gain time-dependent mass losses for the development of the detailed model (see Section 5.2). The data lead to the conclusion that two corrosion mechanisms namely the oxidation of the steel by gaseous O_2 and H_2O and active Cl-induced oxidation are the dominating corrosion mechanisms for the fuel wood chips in the steel temperature range investigated. Furthermore, it was shown, that the share of the two mechanisms on the overall corrosion behaviour strongly depends on the deposit temperature (see Section 5.2.4).

Based on these observations a second approach has been developed. The detailed model allows the prediction of the local corrosion mechanism as well as the calculation of a parabolic rate constant of the local corrosion potential. The approach which determines the local corrosion mechanism can be found in Section 5.3. However, while the model is able to estimate the likeliest high-temperature corrosion mechanism locally prevailing, up to now it is not possible for all corrosion mechanisms to calculate a local corrosion potential. Hence, the rate constant can only be calculated for the oxidation of the steel as well as for active Cl-induced oxidation. However, due to the modular approach other high-temperature corrosion mechanisms can be implemented easily in the existing code in future.

The newly developed model requires input data from a deposit formation model. Necessary input data are the local fraction of chlorine in the deposits formed, the aggregate state of the deposits as well as the mean deposit temperature. Due to the coupling of the model developed with the deposit formation model, the model is computational very expensive. Hence, the additional information regarding the local corrosion mechanism has the drawback of long calculation times.

Furthermore, the detailed model has been applied in a simulation of the corrosion potential of the online corrosion probe test runs. The obtained results are in reasonable agreement with the experimental data (see Section 5.4).

The model was applied to simulate the high-temperature corrosion potential of a real-scale biomass fired CHP plant (see Section 5.5). The simulation has been carried out for

actual state full load conditions of the plant, using wood chips as fuel. To allow a comparison and a better evaluation of the two models developed, the local corrosion potential of the plant was also simulated using the empirical model.

The results of both models are in good agreement. Both predict the maximum of the corrosion potential at the exit of the final superheater, where the highest steel temperatures prevailed. However, small differences between the two models exist. While the inhomogeneous flow field has a considerable effect on the corrosion potential predicted by the empirical model, it hardly plays a role in the detailed model. This is caused by the fact, that the dominating corrosion mechanism is the oxidation of the steel, according to the detailed model. However, the oxidation is solely influenced by the steel temperature, which is mostly determined by the local steam temperature, due to the high heat transfer coefficient on the steam side as well as the high heat conductivity of the steel. However, the share of active Cl-induced oxidation would strongly increase with increasing deposit temperature. Hence, the local corrosion potential estimated by the detailed model is, in contrast to the one of the empirical model, time-dependent.

Concluding, both models developed are well applicable to estimate the local corrosion potential of low alloy steels in biomass fired boilers within CFD simulations of flow and heat transfer. The models can be applied for typical combustion conditions, fuels and steam parameters prevailing in current and future biomass fired boilers. Here it could be shown that the results of both models are qualitatively in good agreement. However, both models have their advantages and disadvantages:

- The empirical model is very fast, but it has the drawback that it provides no information regarding the local corrosion mechanisms prevailing. Furthermore, it has rather strong limitations regarding its application range.
- The detailed model supplies information regarding the local corrosion mechanisms and provides a deeper understanding of relevant influencing parameters. As a drawback the model is very time-consuming. Also some parameters of the model need additional measurements to increase their accuracy. Further at the moment it is not possible to calculate a local corrosion potential (rate constant) for all possible corrosion mechanisms (e.g. molten salt corrosion or oxidation above 570 °C).

Although some unsolved problems exist, it is concluded that both models developed are an important first step towards a reliable prediction of the local high-temperature corrosion potential in biomass fired boilers by means of CFD simulations. Due to the reasonable agreement of the calculated corrosion potentials with experimental data as well as the good applicability of the models within CFD simulations of flow and heat transfer the models developed represent a useful tool for plant manufacturers and engineers already at the present stage of development.

7 Outlook

Although the two models developed have been tested and applied successfully, there are some issues and improvements left which could not be addressed within this work.

Firstly, the empirical model developed is solely valid to estimate the corrosion behaviour of low alloy steels like 13CrMo4-5 or 16Mo3. Also comparable fuel compositions and combustion conditions as used within the test runs of this work are necessary to make the model applicable. Hence, future works should also investigate the high-temperature corrosion behaviour of steels with higher Cr contents such as P91 or 1.4541. Also test runs should be performed to gain additional information or even to develop a mathematical description of the corrosion behaviour in dependence of the fuel composition. For this purpose forest wood chips could be systematically doped with the corrosive species S and Cl or the heavy metals Zn and Pb.

Further test runs should also be carried out to increase the reliability of the detailed model developed as discussed in detail in Section 5.2. Here, especially the dependencies on the flue gas water content as well as the coefficients for the active Cl-induced oxidation (E_{act}, $k_{0,Cl}$) should be carefully validated and modified where necessary. Also, an additional test run using the gas burner in combination with elevated flue gas temperatures and velocities (same parameter setup as used for the MLP test run) should be performed. This test run could prove if the influence of the heat flux is negligible, as proposed within this work.

Another improvement concerns the deposit formation model with which the detailed corrosion model is coupled. In the deposit formation model the sulphation of the solid alkali chlorides deposited and hence, depletion of chlorine source, is not taken into account up to now. Due to interactions and catalytic reactions with the oxide layer, the reaction kinetics differs from the sulphation reaction of gaseous or solid alkali metals in the flue gas. Experimental work on this topic is ongoing [43], [121]. The results should be implemented into to the existing model as soon as reliable experimental data is available for conditions prevailing in biomass fired boilers.

Do to this issue and the long calculation times the detailed model developed is not able to predict the progress of high-temperature corrosion. Hence, the detailed model is only able to estimate the corrosion behaviour of the initial or a quasi-steady state, like within the case studies performed and described in this work. Although the estimated fouling layer has been proven to be reliable for the calculation of the flue gas flow and heat transfer, it would be preferable to investigate the corrosion behaviour of a plant from the very beginning to the steady state. This procedure would most certainly enhance the understanding of high-temperature corrosion occurring in biomass fired boilers significantly.

Bibliography

[1] T. Blomberg, “Correlation of the corrosion rates of steels in a straw fired boiler with the thermodynamically predicted trend of KOH(g) in the flue gases,” *Biomass and Bioenergy,* vol. 39, no. 0, pp. 489-493, 2012.

[2] F. J. Frandsen, “Utilizing biomass and waste for power production - a decade of contributing to the understanding, interpretation and analysis of deposits and corrosion products,” *Fuel,* vol. 84, no. 10, pp. 1277-1294, 2005.

[3] S. B. Hansen, P. A. Jensen, F. J. Frandsen, H. Wu, B. Sander, J. Wadenbäck and P. Glarborg, “Deposit probe measurements in danish grate and pulverized fuel biomass power boilers,” in *Proceedings Impacts of Fuel Quality on Power Production and Environment*, 2012, Palo Alto, CA: Electric Power Research Institute (EPRI), 2013.

[4] L. A. Hansen, H. P. Nielsen, F. J. Frandsen, K. Dam-Johansen, S. Hoerlyck and A. Karlsson, “Influence of deposit formation on corrosion at a straw-fired boiler,” *Fuel Processing Technology,* vol. 64, no. 3, pp. 189-209, 2000.

[5] O. H. Larsen and N. Henrisken, “Ash Deposition and High Temperature Corrosion at Combustion of Aggressive Fuels,” in *Int. Conf. on Power Plant Chemical Technology*, 1997.

[6] S. C. v. Lith, F. J. Frandsen, M. Montgomery, T. Vilhelmsen and S. A. Jensen, “Lab-scale Investigation of Deposit-induced Chlorine Corrosion of Superheater Materials under Simulated Biomass-firing Conditions. Part 1: Exposure at 560 °C ,” *Energy & Fuels,* vol. 23, no. 7, pp. 3457-3468, 2009.

[7] H. P. Michelsen, F. Frandsen, K. Dam-Johansen and O. H. Larsen, “Deposition and high temperature corrosion in a 10 MW straw fired boiler,” *Fuel Processing Technology,* vol. 54, no. 3, pp. 95-108, 1998.

[8] M. Montgomery, S. A. Jensen, U. Borg, O. Biede and T. Vilhelmsen, “Experiences with high temperature corrosion at straw-firing power plants in Denmark,” *Materials and Corrosion,* vol. 62, no. 7, pp. 593-605, 2011.

[9] M. Montgomery, A. Karlsson and O. H. Larsen, “Corrosion Investigations at Masnedø Combined Heat and Power Plant Part VI,” 2001.

[10] H. Nielsen, L. Baxter, G. Sclippab, C. Morey, F. Frandsen and K. Dam-Johansen, “Deposition of potassium salts on heat transfer surfaces in straw-fired boilers: a pilot-scale study,” *Fuel,* vol. 79, no. 2, pp. 131-139, 2000.

[11] I. Obernberger and T. Brunner, “Deposition und Korrosion in Biomassefeuerungen,” in *Tagungsband zum VDI-Seminar 430504 "Beläge und Korrosion in Großfeuerungsanlagen"*, 2004.

[12] P. Sommersacher, T. Brunner and I. Obernberger, “Fuel Indexes: A Novel Method for the Evaluation of Relevant Combustion Properties of New Biomass Fuels,” *Energy & Fuels,* Vols. -, p. 11, 2011.

[13] Y. Alipour, “High temperature corrosion in a biomass-fired power boiler - Reducing furnace wall corrosion in a waste wood-fired power plant with advanced steam data,” 2013.

[14] D. Bankiewicz, “Corrosion behaviour of boiler tube materials during combustion of fuels containing Zn and Pb,” 2012.

[15] W. B. A. Sharp, “Superheater corrosion in biomass boilers: Today’s Science and Technology,” Oak Ridge National Laboratory, ORNL/TM-2011/399, 2010, 2010.

[16] W. Sharp, L. Douglas and J. R. Keiser, “Energy from Biomass - Lessons from European Boilers,” 2011.

[17] R. W. Bryers, “Fireside slagging, fouling, and high-temperature corrosion of heat-transfer surface due to impurities in steam-raising fuels,” *Progress in Energy and Combustion Science,* vol. 22, no. 1, pp. 29-120, 1996.

[18] R. A. Antunes and M. C. L. de Oliveira, “Corrosion in biomass combustion: A materials selection analysis and its interaction with corrosion mechanisms and mitigation strategies,” *Corrosion Science ,* vol. 76, no. 0, pp. 6-26, 2013.

[19] H. Nielsen, F. Frandsen, K. Dam-Johansen and L. Baxter, “The implications of chlorine-associated corrosion on the operation of biomass-fired boilers,” *Progress in energy and combustion science,* vol. 26, no. 3, pp. 283-298, 2000.

[20] C. Schroer and J. Konys, “Rauchgasseitige Hochtemperatur-Korrosion in Müllverbrennungsanlagen - Ergebnisse und Bewertung einer Literaturrecherche,” Forschungszentrum Karlsruhe; Technik und Umwelt, Wissenschaftliche Berichte FZKA 6695, Karlsruhe, Germany, 2002.

[21] B. Waldmann, “PhD-thesis: Korrosion in Anlagen zur thermischen Abfallverwertung : elektrochemische Korrosionserfassung und Modellbildung,” Augsburg, Germany, 2007.

[22] S. Maisch, “Identifikation und Quantifizierung von korrosionsrevlevanten Parametern in Müllverbrennungsanlagen mittels Charakterisierung der deponierten

Partikel und elektrochemischer Online-Messungen," 2011.

[23] P. Henderson, P. Szakálos, R. Pettersson, C. Andersson and J. Högberg, "Reducing superheater corrosion in wood-fired boilers," *Materials and Corrosion,* vol. 57, no. 2, pp. 128-134, 2006.

[24] A. Nafari and A. Nylund, "Field study on superheater tubes in the loop seal of a wood fired CFB plant," *Materials and Corrosion,* vol. 55, no. 12, pp. 909-920, 2004.

[25] Y. Li, M. Spiegel and S. Shimada, "Corrosion behaviour of various model alloys with NaCl–KCl coating," *Materials Chemistry and Physics,* vol. 93, p. 217–223, 2005.

[26] H. Grabke, E. Reese and M. Spiegel, "The effects of chlorides, hydrogen chloride, and sulfur dioxide in the oxidation of steels below deposits," *Corrosion Science,* vol. 37, no. 7, pp. 1023-1043, 1995.

[27] J. Lehmusto, D. Lindberg, P. Yrjas, B.-J. Skrifvars and M. Hupa, "The role of potassium in high temperature corrosion of superheater steels," in *Proceedings Impacts of Fuel Quality on Power Production and Environment*, 2012, Palo Alto, CA: Electric Power Research Institute (EPRI), 2013..

[28] M. Uusitalo, P. Vuoristo and T. Mäntylä, "High temperature corrosion of coatings and boiler steels below chlorine-containing salt deposits," *Corrosion Science,* vol. 46, no. 6, pp. 1311-1331, 2004.

[29] T. Jonsson, N. Folkeson, J.-E. Svensson, L.-G. Johansson and M. Halvarsson, "An ESEM in situ investigation of initial stages of the KCl induced high temperature corrosion of a Fe2.25Cr1Mo steel at 400°C," *Corrosion Science,* vol. 53, no. 6, pp. 2233-2246, 2011.

[30] F. Haider, S. Horn, B. Waldmann and R. Warnecke, "Quantifizierung des Korrosionsdiagramms auf der Basis von Messungen mit der Augsburger Korrosionssonde," in *VDI-Wissensforum, Beläge und Korrosion*, 2008.

[31] S. Retschitzegger, T. Brunner, I. Obernberger and B. Waldmann, "Assessment of Online Corrosion Measurements in Combination with Fuel Analyses and Aerosol and Deposit Measurements in a Biomass Combined Heat and Power Plant," *Energy & Fuels,* vol. 27, no. 10, pp. 5670-5683, 2013.

[32] Y. Kawahara, "Evaluation of high-temperature corrosion life using temperature gradient corrosion test with thermal cycle component in waste combustion environments," *Materials and Corrosion,* vol. 57, no. 1, pp. 60-72, 2006.

[33] S. Maisch, B. Waldmann, R. Warnecke, R. Haider and S. Horn, "Quantifizierte Korrosionsgeschwindigkeit in Abhängigkeit der Rohrwand- und

Rauchgastemperatur," in *VDI-Fachkonferenz - Feuerung und Kessel - Beläge und Korrosion - in Großfeuerungen*, 2010.

[34] S. Maisch, R. Warnecke, B. Waldmann, F. Haider and S. Horn, "Validierung des Korrosionsdiagramms und Einfluss der Strömung auf die Korrosionssgeschwindigket," in *VDI-Fachkonferenz - Feuerung und Kessel - Beläge und Korrosion - in Großfeuerungen*, 2009.

[35] P. Gellings and K. Tostmann, Korrosion und Korrosionsschutz von Metallen: eine Einführung, München, Germany: Carl Hanser Verlag; ISBN: 3-446-12594-9, 1981.

[36] P. Kofstad, High Temperature Corrosion, Essex, UK: ELSEVIER APPLIED SCIENCE PUBLISHERS LTD: ISBN 1 85166 154 9, 1988.

[37] M. Schütze, "Fundamentals of High Temperature Corrosion," in *Corrosion and Environmental Degradation*, Weinheim, Germany, Wiley VCH; ISBN: 9783527299713, 2000, pp. 67-130.

[38] M. Schütze, Protective oxide scales and their breakdown, D. Holmes, Ed., West Sussex, UK: John Wiley & Sons; ISBN: 0-471-95904 9, 1997.

[39] C. Bernsteiner, "Master thesis: Online-Monitoring von Korrosionsvorgängen in Biomasse-befeuerten Anlagen," TU Graz, Graz, Austria, 2013.

[40] E. Werner, S. Kalpakjian and S. Schmid, Werkstofftechnik, vol. 5, Munich, Germany: Pearson Studium; ISBN: 978-3868940060., 2011.

[41] A. Atkinson, "Transport processes during the growth of oxide films at elevated temperature," *Rev. Mod. Phys.,* vol. 57, pp. 437-470, 1985.

[42] T. Brunner, Aerosols and coarse fly ashes in fixed-bed biomass combustion: Formation, characterisation and emissions, Graz, Austria: Medienfabrik Graz, Austria. ISBN: 3-9501980-3-2, 2006.

[43] F. Haider, S. Horn, Z. Haque, M. Bauer, S. Maisch and R. Warnecke, "Bestimmung kinetischer Daten zur Sulfatierung von Chloriden," in *VDI-Fachkonferenz - Feuerung und Kessel - Beläge und Korrosion - in Großfeuerungen*, 2010.

[44] L. Boonsongsup, K. Iisa and W. J. Frederick, "Kinetics of the Sulfation of NaCl at Combustion Conditions," *Industrial & Engineering Chemistry Research,* vol. 36, no. 10, pp. 4212-4216, 1997.

[45] H. Matsuda, S. Ozawa, K. Naruse, K. Ito, Y. Kojima and T.Yanase, "Kinetics of HCl emission from inorganic chlorides in simulated municipal wastes incineration conditions," *Chemical Engineering Science,* vol. 60, p. 545 – 552, 2005.

[46] L. Sengeloev, T. Hansen, C. Bartolomé, H. Wu, K. Pedersen, F. Frandsen, A. Jensen and P. Glarborg, “Sulphation of condensed potassium chloride by SO2,” *Energy & Fuels,* vol. 27, pp. 3283 - 3289, 2013.

[47] C. P. O’Hagan, B. O’Brien, F. Griffin, B. Hooper, S. Leen and R. Monaghan, “Porosity-Based Corrosion Model for Alkali Halide Ash Deposits during Biomass Co-firing,” *Energy & Fuels,* vol. 29, pp. 3082-3095, 2015.

[48] R. Riedl, J. Dahl, I. Oberberger and M. Nardoslawsky, “Corrosion in fire tube boilers of biomass combastion plants,” *Proceedings of the China international corrosion control conference '99,* Vols. -, pp. 1-5, 1999.

[49] R. Bürgel, H. J. Maier and T. Niendorf, Handbuch Hochtemperatur-Werkstofftechnik, 4 ed., Wiesbaden, Germany: Vieweg+Teubner; ISBN 978-3-8348-1388-6, 2011.

[50] R. A. Rapp, “Hot corrosion of materials: a fluxing mechanism?,” *Corrosion Science ,* vol. 44, no. 2, pp. 209-221, 2002.

[51] M. Spiegel, “Salt melt induced corrosion of metallic materials in waste incineration plants,” *Materials and Corrosion,* vol. 50 (7), no. 7, pp. 373-393, 1999.

[52] D. O. Albina, “Theory and experience on corrosion of waterwall and superheater tubes of waste-to-energy facilities,” 2005.

[53] Y. S. Zhang and R. A. Rapp, “Solubilities of alpha-Fe2O3 and Fe3O4 in Fused Na2SO4 at 1200 K,” *Journal of The Electrochemical Society,* vol. 132, no. 10, pp. 2498-2501, 1985.

[54] T. Mitchell, D. Voss and E. Butler, “The observation of stress effects during the high temperature oxidation of iron,” *Journal of Matrials Sicence,* vol. 17, pp. 1825-1833, 1982.

[55] H. Evans, “Stress effects in high temperature oxidation of metals,” *International Materials Reviews,* vol. 40, pp. 1-40, 1995.

[56] L. G. Johansson, J. E. Svensson, E. S., J. Pettersson, C. Pettersson, N. Folkeson, H. Asteman, T. Jonsson and M. Halvarsson, “Critical Corrosion Phenomena on Superheaters in Biomass and Waste-Fired Boilers,” in *Proceedings of Sino-Swedish Structural Materials Symposium 2007*, Göteborg, 2007.

[57] T. Jonsson, A. Järdnäs, J.-E. Svensson, L.-G. Johansson and M. Halvarsson, “The Effect of Traces of SO2 on Iron Oxidation: A Microstructural Study,” *Oxidation of Metals,* vol. 67, no. 3-4, pp. 193-213, 2007.

[58] T. M. Linjewile, J. Valentine, K. Davis, N. Harding and W. M. Cox, “Prediction and real-time monitoring techniques for corrosion characterisation,” *Materials at high temperature,* vol. 20, no. 1/2, 2003.

[59] K. A. Davis, T. M. Linjewile, J. Valentine, D. Swensen and S. D., “A Multi-point Corrosion Monitoring System Applied in a 1300 MW Coal-fired Boiler,” *Anti-Corrosion Methods and Materials,* vol. 51, no. 5, pp. 321 -330, 2004.

[60] R. Warnecke, S. Horn and M. Weghaus, “Feuerungsimulation zur Aufdeckung korrosiver Chloride,” in *VDI-Fachkonferenz - Feuerung und Kessel - Beläge und Korrosion - in Großfeuerungen*, Oberhausen, Germany, 12.-13. June, 2008.

[61] F. H. Stott and C. Y. Shih, “The influence of HCl on the oxidation of iron at elevated temperatures,” *Materials and Corrosion,* vol. 51, pp. 277-286, 2000.

[62] J. Nesbitt, “Numberical modeling of high-temperature corrosion processes,” *Oxidation of metals,* vol. 44, no. 1/2, pp. 309-338, 1995.

[63] C. Wagner, “Beitrag zur Theorie des Anlaufvorgangs,” *Zeitschrift für Physikalische Chemie,* vol. B41, pp. 25-42, 1933.

[64] S. Hallstroem, L. Höglund and J. Agren, “Modelling of iron diffusion in the iron oxides magnetite and hematite with variable stoichimetry,” *Acta Materialia,* vol. 59, pp. 53-60, 2011.

[65] G. Yurek, J. Hirth and R. Rapp, “The formation of two-phase layered scales on pure metals,” *Oxidation of Metals,* vol. 8, no. 5, pp. 265-281, 1974.

[66] K. Schulze, R. Scharler and I. Obernberger, “Development of an advanced CFD model for ash deposit and aerosol formation in biomass fired boilers,” in *Proceedings of the international conference:9th INFUB (European Conference on industrial furnaces and boilers)*, Estoril, Portugal, 2011.

[67] P. Gellings and K. Tostmann, Korrosion und Korrosionsschutz von Metallen: eine Einführung, München, Germany: Carl Hanser Verlag; ISBN: 3446125949, 1981.

[68] S. Retschitzegger, T. Gruber, T. Brunner and I. Obernberger, “Short term online corrosion measurements in biomass fired boilers. Part 1: Application of a newly developed mass loss probe,” *Fuel Processing Technologies,* 2015, doi:10.1016/j.fuproc.2015.03.026.

[69] C. Deuerling and B. Waldmann, “Innovative Messtechnik zur kombinierten Korrosions- und Materialforschung im Kraftwerksbereich,” in *Proceedings of the 43. Kraftwerkstechnisches Kolloquium*, Dresden, Germany, 2011.

[70] R. Mehrabian, S. Zahirović, R. Scharler, I. Obernberger, S. Kleditzsch, S. Wirtz, V. Scherer, H. Lu and L. L. Baxter, “A CFD model for thermal conversion of thermally thick biomass particles,” *Fuel Processing Technology,* vol. 95, no. 0, pp. 96-108, 2012.

[71] R. Scharler, “Entwicklung und Optimierung von Biomasse-Rostfeuernungen durch CFD-Analyse,” PhD Thesis, Graz University of Technology, 2001.

[72] A. Brink, “Eddy Break-Up based models for industrial diffusion flames with complex gas phase chemistry,” PhD Thesis, Abo Akademi University, 1998.

[73] B. F. Magnussen and B. H. Hjertager, “On mathematical modeling of turbulent combustion with special emphasis on soot formation and combustion,” in *the 16th Symp. (Int.) on Combustion*, Pittsburgh, 1976.

[74] T. F. Smith, Z. F. Shen and J. N. Friedman, “Evaluation of Coefficients for the Weighted Sum of Gray Gases Model,” *Journal of Heat Transfer,* vol. 104, no. 4, pp. 602-608, 1982.

[75] R. Scharler, T. Fleckl and I. Obernberger, “Modification of a Magnussen Constant of the Eddy Dissipation Model for biomass grate furnaces by means of hot gas in-situ FT-IR absorption spectroscopy,” *Progress in Computational Fluid dynamics,* vol. 3, no. 2-4, pp. 102-111, 2003.

[76] S. Yaxin, C. Chen and A. Su, “Simulation of High Temperature Air Combustion with modified Eddy-Break-Up combustion model,” *Energy Procedia,* vol. 14, pp. 127-132, 2012.

[77] R. Scharler, M. Forstner, M. Braun, T. Brunner and I. Obernberger, “Advanced CFD analysis of large fixed bed biomass boilers with special focus on the convective section,” in *In: ETA-Florence & WIP Munich, editor. Proceedings of the 2nd World Conference and Exhibition on Biomass for Energy, Industry and Climate Protection*, Rome, Italy, 2004.

[78] V.-G. V. u. Chemieingenieurwesen, VDI-Wärmeatlas, 10 ed., H. Martin, Ed., Heidelberg, Germany: Springer; ISBN: 978-3-642-19980-, 2006.

[79] A. Zukauskas and R. Ulinskas, High-performance single-phase heat exchangers, Washington DC, USA: Hemisphere Publishing Corporation. ISBN: 0891167153, 1989.

[80] I. Idelchik, Handbook of hydraulic resistance, vol. 3, New York, USA: Begell House. ISBN: 1-56700-074-6., 1996.

[81] EU-project-no.SES-CT-2003-502679, “BIOASH – Ash and aerosol related problems in

biomass comubstion and co-firing. Publishable final activity report," Project coordinator: Ingwald Obernberger, TU Graz, Graz, Austria, 2007.

[82] K. A. Christensen, M. Stenholm and H. Livbjerg, "The formation of submicron aerosol particles, HCl and SO2 in straw-fired boilers," *Journal of Aerosol Science,* vol. 29, no. 4, pp. 421-444, 1998.

[83] H. Baehr and K. Stephan, Wärme- und Stoffübertragung 2nd. Edition, Berlin, Germany: Springer, 1996.

[84] S. Friedlander, Smoke, dust and haze, New York, USA: John Wiley & Sons, ISBN 0-471-01468-0., 1977.

[85] S. Pope, "Computationally efficient implementation of combustion chemistry using in situ adaptive tabulation," *Combustion Theory and Modelling,* vol. 1, no. 1, pp. 41-63, 1997.

[86] T. Brunner, G. Bärnthaler and O. I, "Evaluation of parameters determining PM emissions and their chemical composition in modern residential biomass heating appliances," in *In: Proc. of the int. Conf. World BIOENERGY 2008, Swedish Bioenergy Association (Ed.), Stockholm, Sweden. ISBN 978-91-977624-0-3,*, Jönköping, Sweden, 2008.

[87] S. Horn, F. Haider, B. Waldmann and R. Warnecke, "Quantifizierte Betrachtung des Stoffübergangs in Belägen und Korrosionsschichten zur Beschreibung der Korrosionsgeschwindigkeit," in *VDI - Korrosionstagung*, 2008.

[88] H.-H. Reichel and U. Schirmer, "Waste incineration plants in the FRG: Construction, materials, investigation on cases of corrosion," *Materials and Corrosion,* vol. 40, no. 3, pp. 135-141, 1989.

[89] T. Gruber, K. Schulze, R. Scharler, B. Waldmann, F. Haider and I. Obernberger, "Development of an empirical model to describe the local high temperature corrosion risk of 13CrMo4-5 steel in biomass CHP plants regarding the fuel wood chips," in *Proceedings Impacts of Fuel Quality on Power Production and Environment*, Puchberg, Austria, 2012, Palo Alto, CA: Electric Power Research Institute (EPRI), 2013.

[90] A. J. B. Cutler and E. Raask, "External Corrosion in coal fired Boilers: Assessment from laboratory data," *Corrosion Science,* vol. 21, pp. 789-800, 1981.

[91] J. Pettersson, H. Asteman, J.-E. Svensson and L.-G. Johansson, "KCl Induced Corrosion of a 304-type Austenitic Stainless Steel at 600°C; The Role of Potassium," *Oxidation of Metals,* vol. 64, pp. 23-41, 2005.

[92] F. Gesmundo, D. Young and S. Roy, “The High Temperature Corrosion of Metals in Sulfidizing-Oxidizing Environments: A Critical Review,” *High Temperature Materials and Processes,* vol. 8, pp. 149-190, 2011.

[93] D. Young and S. Watson, “High-temperature corrosion in mixed gas environments,” *Oxidation of metals,* vol. 44, no. 1, pp. 239-264, 1995.

[94] A. Järdnäs, J.-E. Svensson and L.-G. Johansson, “The Inhibitive Effect of Traces of SO2 on the Oxidation of Iron,” *Oxidation of Metals,* vol. 60, no. 5-6, pp. 427-445, 2003.

[95] S. Bose, “Chapter 5 - High-Temperature Corrosion,” in *High Temperature Coatings*, S. Bose, Ed., Burlington, Butterworth-Heinemann; ISBN: 978-0-7506-8252-7, 2007, pp. 53-70.

[96] Y. Zhang and W. Wu, “Summary of studies on hot corrosion of iron-based alloys by sodium sulfate in O2/SO2/SO3 environment.,” *Journal de Physique IV,* vol. 03 (C9), pp. 319-326, 1993.

[97] S. van Lith, C. Buchardt and F. J. Frandsen, “Lab-Scale Investigation of the Potential for Corrosion of Deposits,” 2007.

[98] E. Macherauch and H. W. Zoch, Praktikum Werkstoffkunde, Wiesbaden, Germany: Springer; ISBN: 987-3-8348-0343-6, 2011, p. 586.

[99] A. Atkinson and R. Taylor, “Diffusion of 55Fe in Fe2O3 single crystals,” *Journal of Physics and Chemistry of Solids ,* vol. 46, no. 4, pp. 469-475, 1985.

[100] D. Caplan and M. Cohen, “Scaling of iron at 500 °C,” *Corrosion Science,* vol. 3, no. 3, pp. 139 - 143, 1963.

[101] R. Chen and W. Yuen, “Review of the High-Temperature Oxidation of Iron and Carbon Steels in Air or Oxygen,” *Oxidation of Metals,* vol. 59, no. 5-6, pp. 433-468, 2003.

[102] A. C. S. Sabioni, A. M. Huntz, A. M. J. M. Daniel and W. A. A. Macedo, “Measurement of iron self-diffusion in hematite single crystals by secondary ion-mass spectrometry (SIMS) and comparison with cation self-diffusion in corundum-structure oxides,” *Philosophical Magazine,* vol. 85, no. 31, pp. 3643-3658, 2005.

[103] R. Dieckmann and H. Schmalzried, “Defects and Cation Diffusion in Magnetite (I),” *Berichte der Bunsengesellschaft für physikalische Chemie,* vol. 81, no. 3, pp. 344-347, 1977.

[104] R. Dieckmann and H. Schmalzried, “Defects and Cation Diffusion in Magnetite (II),” *Berichte der Bunsengesellschaft für physikalische Chemie,* vol. 81, no. 3, pp. 414-419, 1977.

[105] R. Dieckmann and H. Schmalzried, “Defects and Cation Diffusion in Magnetite (IV),” *Berichte der Bunsengesellschaft für physikalische Chemie,* vol. 86, no. 3, pp. 112-118, 1982.

[106] R. Dieckmann, “Point defects and transport in non-stoichiometric oxides: Solved and unsolved problems,” *Journal of Physics and Chemistry of Solids ,* vol. 59, no. 4, pp. 507-525, 1998.

[107] K. Reddy and A. Cooper, “Oxygen Diffusion in MgO and \alpha-Fe2O3,” *Journal of the American Ceramic Society,* vol. 66, no. 9, pp. 664-666, 1983.

[108] A. G. Crouch and J. Robertson, “Creep and oxygen diffusion in magnetite,” *Acta metall. mater.,* vol. 38, no. 12, pp. 2567-2572, 1990.

[109] N. Birks, G. Meier and F. Pettit, Introduction to High Temperature Oxidation of Metals, Cambridge, England: Cambridge University Press; ISBN-13 978-0-521-48042-0, 2006.

[110] J. Van Orman and K. Crispin, “Diffusion in Oxides,” *Reviews in Mineralogy & Geochemistry,* vol. 72, pp. 757-825, 2010.

[111] A. Atkinson, M. O'Dwyer and R. Taylor, “55Fe diffusion in magnetite crystals at 500 ° C and its relevance to oxidation of iron,” *Journal of Materials Science,* vol. 18, no. 8, pp. 2371-2379, 1983.

[112] W. Boggs and R. Kachik, “The oxidation of iron-carbon alloys at 500 °C,” *Journal of the electrochemical society,* vol. 116, pp. 424-430, 1969.

[113] H. Asteman and M. Spiegel, “Investigation of the HCl (g) attack on pre-oxidized pure Fe, Cr, Ni and commercial 304 steel at 400°C,” *Corrosion Science,* vol. 49, p. 3626–3637, 2007.

[114] H. J. Grabke, M. Spiegel and A. Zahs, “Chloridation and oxidation of iron, chromium, nickel and their alloys in chloridizing and oxidizing atmospheres at 400±700°C,” *Corrosion Science,* vol. 42, pp. 1093 - 1122, 2000.

[115] A. Holt and P. Kofstad, “High temperature corrosion of iron in O2+ 4% SO2/SO3 at 500-800°C,” *Materials Science and Engineering: A ,* vol. A120, no. 0, pp. 101-104, 1989.

[116] J. Gilewicz-Wolter, “Study of iron oxdiation in sulfur dioxide atmospheres by means of the 35S Radioistiope,” *Oxidation of metals,* vol. 11, no. 2, pp. 81 - 91, 1977.

[117] B. Pujilaksono, T. Jonsson, M. Halvarsson, J.-E. Svensson and L.-G. Johansson, “Oxidation of iron at 400 - 600 °C in dry and wet O2,” *Corrosion Science ,* vol. 52, no. 5, pp. 1560-1569, 2010.

[118] K. Salmenoja, “PhD-thesis: Field and laboratory studies on chlorine-induced superheater corrosion in boilers fired with biofuels,” Abo Akademi, Abo, Finnland, 2000.

[119] M. J. McNallan, “High-Temperature Corrosion in Halogen Environments,” *Material Performance,* vol. 33, no. 9, pp. 54-57, 1994.

[120] P. L. Daniel and R. A. Rapp, “Halogen Corrosion of Metals,” in *Advances in Corrosion Science and Technology*, M. G. Fontana and R. W. Staehlc, Eds., New York, USA: Plenum Press, 1976, pp. 55 - 171.

[121] T. Stegmüller, “Master Thesis: Untersuchung der Sulfatierung von Natriumchlorid,” Universität Augsburg, Augsburg, Germany, 2011.

[122] T. Gruber, K. Schulze, R. Scharler and I. Obernberger, “Investigation of the corrosion behaviour of 13CrMo4-5 for biomass fired boilers with coupled online corrosion and deposit probe measurements,” *Fuel ,* vol. 144, no. 0, pp. 15-24, 2015.

[123] T. Gruber, R. Scharler and I. Obernberger, “Application of an empirical model in CFD simulations to predict the local high temperature corrosion potential in biomass fired boilers,” *Biomass & Bioenergy,* vol. 79, pp. 145-154, 2015.

[124] J. Neilson and A. Gilchrist, “Erosion by a stream of solid particles,” *Wear,* vol. 11, no. 2, pp. 111-122, 1968.

8 ANNEX

8.1 Boundary Conditions of the CFD case studies

8.1.1 Case study 1: Application of the empirical high-temperature corrosion model (see Section 4.5)

In the first case study performed within this work a biomass fired CHP plant with a water tube steam boiler was simulated to test and demonstrate the usability of the newly developed empirical model. Within the case study following different load conditions as well as steam temperatures and interconnections of the superheater tube bundles have been investigated:

- **CS1:** Actual state analysis under full load conditions (live steam temperature of 453°C)
- **CS2:** A switch of the flow direction of the final superheater bundle from parallel to counter-flow (live steam temperature of 453 °C)
- **CS3:** Enhanced live steam temperature of 480°C

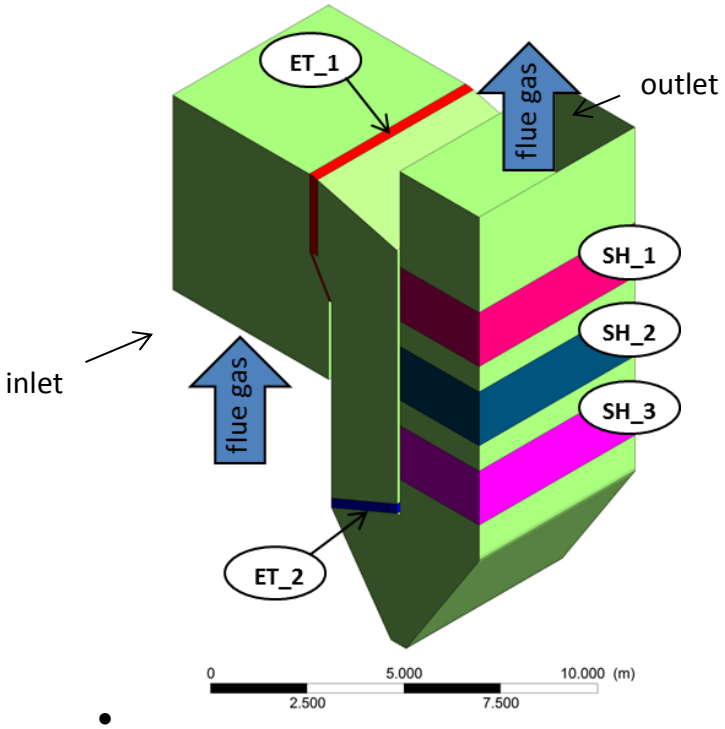

Figure 8.1: Schematic view of the simulated CHP plant
Explanation: ET_1… upper evaporator tube grid, ET_2… lower evaporator tube grid, SH_1 to SH_3… superheater tube bundles 1 to 3 (Figure adapted from **[Paper II]**)

The case study is described in detail in Section 4.5.1. The boundary conditions used for the simulations are summarized in the following tables. The gas compositions as well as the boundary conditions for the finned tube walls are similar for all three cases investigated. Since the simulation has been carried out under the assumption of a fully

combusted flue gas no chemical reactions have been considered. On the flue gas side the radiant heat transfer as well as the convective heat transfer are taken into account, as explained in Section 3.2. The heat transfer as well as the pressure loss in the superheater tube bundles and the evaporator tube grids are calculated using the heat exchanger model described in Section 3.2.2. The heat transfer of the steam side of the finned walls is calculated via convection using the saturated steam temperature and the mean heat transfer coefficient on the water side as boundary conditions. The settings are presented in Table 8.1.

Table 8.1: Boundary conditions for finned walls

	unit	**Finned walls**
Thermal conductivity of the steel	W/mK	50
Steel thickness	mm	4.5
Thermal conductivity of the fouling layer	W/mK	0.5
Fouling layer thickness	mm	1
Heat transfer coefficient (waterside)	W/m°K	10608
Free stream temperature	°C	278.9
Internal Emissivity		0.8

Table 8.2: Boundary conditions at the simulation inlet

Name	**unit**	**CS1/CS2**	**CS3**
Mass flow rate	kg/s	35.8	34.5
Flue gas temperature	°C	706.9	742
CO_2	kg/kg	0.208	0.208
O_2	kg/kg	0.033	0.033
H_2O	kg/kg	0.111	0.111
Ar	kg/kg	0.011	0.011
N_2	kg/kg	rest	rest

Table 8.3: Boundary conditions for the superheater tubes **CS1**
Explanation: SH1-SH3… superheater tube bundle 1-3, ET1-ET2… evaporator tube grids, ccf … cross counter flow, cpf … cross parallel flow

	unit	**ET1**	**ET2**	**SH3**	**SH2**	**SH1**
				staggered tubes		
Operation Mode		cpf	cpf	cpf	ccf	ccf
Tube wall material		St 35.8	St 35.8	15 Mo 3	15 Mo 3	15 Mo 3
Outside tube diameter	mm	51	51	38	38	38
Tube wall thickness	mm	4.5	4.5	4	4	4
Transverse tube pitch	mm	300	300	200	100	100
Longitudinal tube pitch	mm	300	300	90	90	90
Width flue gas duct	mm	5700	5700	5700	5700	5700
Height flue gas duct	mm	3500	2500	3000	3000	3000
Number of tubes per row width (transversal)		18	18	28	56	56

Number of tubes in gas flow direction		3	3	20	20	20
Thermal conductivity of the steel	W/mK	50	50	41	42	44
Heating surface	m²	30.3	21.6	197.9	395.7	395.7
Fouling layer thickness of tubes on flue gas side	mm	1	1	1	1	1
Thermal conductivity of fouling layer on flue gas side	W/mK	0.5	0.5	0.5	0.5	0.5
Heat transfer coefficient (waterside)	W/m°K	17290	17290	1252	763	860
Water/steam temperature inlet	°C	278.9	278.9	381.9	318.9	277.9
Water/steam temperature outlet	°C	278.9	278.9	452.9	431.9	348.9
Nusselt first row/Nussel core		0.8	0.8	0.8	0.8	0.8
Clean surface emissivity on flue gas side		0.8	0.8	0.8	0.8	0.8

Table 8.4: Boundary conditions for the superheater tubes **CS2**
Explanation: SH1-SH3… superheater tube bundle 1-3, ET1-ET2… evaporator tube grids, ccf … cross counter flow, cpf … cross parallel flow

	unit	**ET1**	**ET2**	**SH3**	**SH2**	**SH1**
				staggered tubes		
Operation Mode		cpf	cpf	ccf	ccf	ccf
Tube wall material		St 35.8	St 35.8	15 Mo 3	15 Mo 3	15 Mo 3
Outside tube diameter	mm	51	51	38	38	38
Tube wall thickness	mm	4.5	4.5	4	4	4
Transverse tube pitch	mm	300	300	200	100	100
Longitudinal tube pitch	mm	300	300	90	90	90
Width flue gas duct	mm	5700	5700	5700	5700	5700
Height flue gas duct	mm	3500	2500	3000	3000	3000
Number of tubes per row width (transversal)		18	18	28	56	56
Number of tubes in gas flow direction		3	3	20	20	20
Thermal conductivity of the steel	W/mK	50	50	41	42	44
Heating surface	m²	30.3	21.6	197.9	395.7	395.7
Fouling layer thickness of tubes on flue gas side	mm	1	1	1	1	1
Thermal conductivity of fouling layer on flue gas side	W/mK	0.5	0.5	0.5	0.5	0.5
Heat transfer coefficient (waterside)	W/m²K	17290	17290	1252	763	860
Water/steam temperature inlet	°C	278.9	278.9	381.9	318.9	278.9
Water/steam temperature outlet	°C	278.9	278.9	452.9	431.9	348.9
Nusselt first row/Nussel core		0.8	0.8	0.8	0.8	0.8
Clean surface emissivity on flue gas side		0.8	0.8	0.8	0.8	0.8

Table 8.5: Boundary conditions for the superheater tubes **CS3**
Explanation: SH1-SH3… superheater tube bundle 1-3, ET1-ET2… evaporator tube grids, ccf … cross counter flow, cpf … cross parallel flow

	unit	ET1	ET2	SH3	SH2	SH1
				staggered tubes		
Operation Mode		cpf	cpf	cpf	ccf	ccf
Tube wall material		St 35.8	St 35.8	15 Mo 3	15 Mo 3	15 Mo 3
Outside tube diameter	mm	51	51	38	38	38
Tube wall thickness	mm	4.5	4.5	4	4	4
Transverse tube pitch	mm	300	300	200	100	100
Longitudinal tube pitch	mm	300	300	90	90	90
Width flue gas duct	mm	5700	5700	5700	5700	5700
Height flue gas duct	mm	3500	2500	3000	3000	3000
Number of tubes per row width (transversal)		18	18	28	56	56
Number of tubes in gas flow direction		3	3	20	20	20
Thermal conductivity of the steel	W/mK	50	50	40	42	44
Heating surface	m²	30.3	21.6	197.9	395.7	395.7
Fouling layer thickness of tubes on flue gas side	mm	1	1	1	1	1
Thermal conductivity of fouling layer on flue gas side	W/mK	0.5	0.5	0.5	0.5	0.5
Heat transfer coefficient (waterside)	W/m²K	19774	18676	1242	781	858
Water/steam temperature inlet	°C	278.9	278.9	410.3	312.8	278.9
Water/steam temperature outlet	°C	278.9	278.9	480.3	430.0	353.2
Nusselt first row/Nussel core		0.8	0.8	0.8	0.8	0.8
Clean surface emissivity on flue gas side		0.8	0.8	0.8	0.8	0.8

8.1.2 Case study 2: Test case to demonstrate the detailed corrosion model (see Section 5.3)

To illustrate the approach of the detailed corrosion model a simple test case was used, which solely comprises an inlet section, a heat exchanger and an outlet section. The boundary conditions chosen do not represent conditions prevailing in a current biomass fired boiler. However, the boundary conditions are chosen such that all relevant features of the detailed model can be explained in one test case. The test case is illustrated in Figure 8.2.

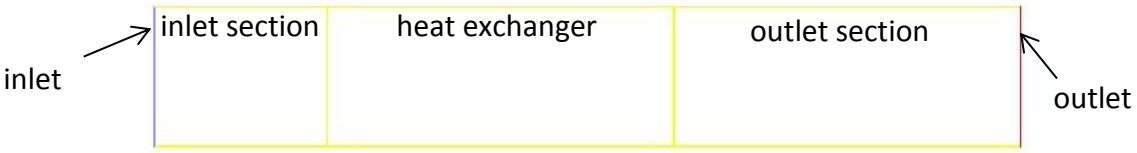

Figure 8.2: Scheme of the test case

The radiative and convective heat flux in the heat exchanger is calculated with the heat exchanger model. The simulation was conducted with clean heat exchanger surfaces (no ash deposits). The heat exchanger is operated in cross parallel mode. The boundary conditions used for the heat exchanger are presented in Table 8.7.

The simulation was carried out for a fully combusted flue gas (no combustion reactions have been considered) to keep the simulation as simple and fast as possible, which is a necessary criterion for a test case. As another consequence of this need for simplicity, the depth (length in the z-coordinate) of the simulation was set to 0.01 m (with zero flux boundary conditions at the simulation boundaries normal to the z-coordinate) to keep the amount of cells as low as possible. Furthermore, the gas phase sulphation reaction of Christensen et al. (see Section 3.2.3 and [82]) was deactivated for the test case. Therefore, sulphur is able to form sulphates according to the local chemical equilibrium prevailing without kinetic limitations. In the simulation the formation and deposition of fine dust as well as the direct condensation of the ash forming vapours is considered. The ash forming elements are K, Na, S and Cl which are able to form following fine dust species: KCl, $(KCl)_2$, K_2SO_4, NaCl, $(NaCl)_2$, Na_2SO_4. The composition of the flue gas as well as the other relevant boundary conditions at the inlet can be found in Table 8.6. A time-step of 2 hours was used for the simulation.

Table 8.6: Boundary conditions at the simulation inlet

Name	**unit**	
Velocity magnitude	m/s	6
Flue gas temperature	°C	860
CO_2	kg/kg	0.149
O_2	kg/kg	0.093
H_2O	kg/kg	0.086
Na	kg/kg	$2.55 \cdot 10^{-7}$
K	kg/kg	$6.46 \cdot 10^{-6}$
Cl	kg/kg	$8.00 \cdot 10^{-7}$
S	kg/kg	$2.49 \cdot 10^{-6}$
SO_2	kg/kg	0.000
N_2	kg/kg	rest

Table 8.7: Boundary conditions for the heat exchanger

	unit	**heat exchanger**
		staggered tubes
		cross parallel flow
Outside tube diameter	mm	38
Tube wall thickness	mm	5
Transverse tube pitch	mm	100
Longitudinal tube pitch	mm	100
Width flue gas duct	mm	400
Height flue gas duct	mm	2500
Number of tubes per row width (transversal)		3
Number of tubes in gas flow direction		24
Thermal conductivity of the steel	W/mK	45
Heating surface	m^2	0.033
Fouling layer thickness of tubes on flue gas side	mm	-
Thermal conductivity of fouling layer on flue gas side	W/mK	-
Heat transfer coefficient (waterside)	W/m^2K	20000
Water/steam temperature inlet	°C	400
Water/steam temperature outlet	°C	580
Nusselt first row/Nussel core		0.9
Clean surface emissivity on flue gas side		0.8

8.1.3 Case study 3: Simulation of the drop tube reactor (see Section 5.4)

CFD simulations of the drop tube reactor have been carried out on the one hand to determine the mean temperatures of the deposited ash layer on top of the MLP and on the other hand to compare the results of the detailed corrosion model with the experimental data.

Four variations have been considered in these simulations, which are based on the same combustion calculation. The boundary conditions of the combustion simulation are based on the balancing test run performed for the wood chips fired online corrosion probe test run described in Section 4.1.1. The main results of this balancing test run can be found in Table 4.1. The boundary conditions at the simulation inlets can be found in Table 8.9. The differences of the four variations are summarized in Table 8.8.

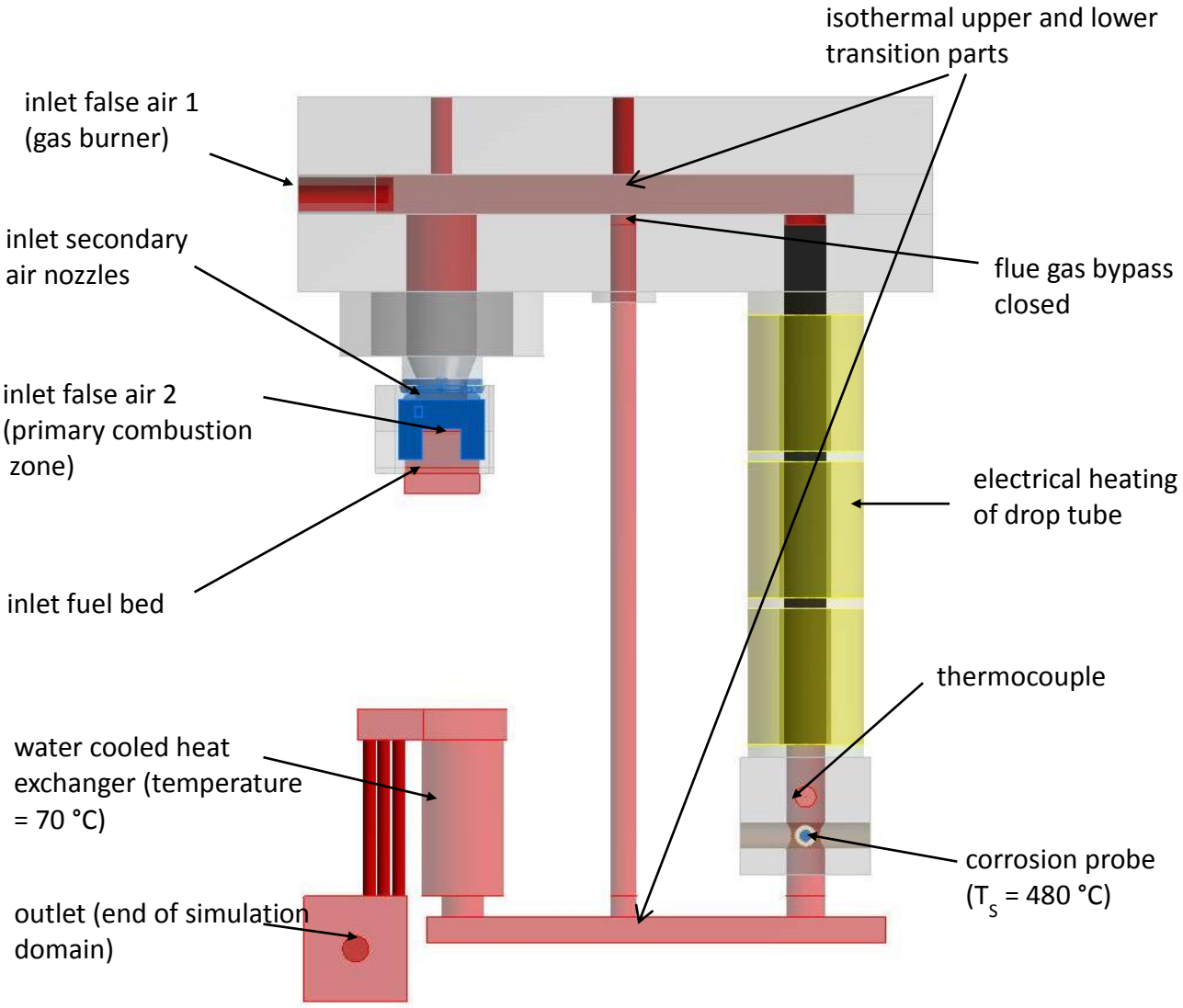

Figure 8.3: Scheme of the biomass fired drop tube reactor

Table 8.8: Summary of the different CFD calculations performed

	case 1	**case 2**	**case 3**	**case 4**
Purpose of simulation	Determine mean deposit temperature for MLP test run at reference temperature (see Section 5.1)	Determine mean deposit temperature for MLP test run with elevated flue gas temperatures (see Section 5.1)	Investigate the initial deposit formation	Investigate the deposit formation + corrosion behaviour after several hundred hours
Probe temperature	480 °C	480 °C	480 °C	480 °C
Wall temperature heating elements	850 °C	1050 °C	850 °C	850 °C
Fouling layer on corrosion probe	yes	yes	no	yes
Detailed corrosion/ deposit formation model applied	no	no	yes	yes

The combustion calculation was carried out using the models described in Section 3.2. The flue gas temperature and velocity profiles as well as the profiles of the gaseous species presented in Figure 8.4 to Figure 8.6 were calculated with the empirical packed bed model described in Section 3.2.1.

For the case 3 and case 4 the coupled deposit formation model and the detailed high-temperature corrosion model have been applied subsequent to the combustion simulation. In doing so the fine dust formation and fine dust deposition as well as the direct wall condensation have been calculated by the deposit formation model. The mass fractions of the elements K, Na, S and Cl (see Table 8.9) are based on release rates determined by mean of the balancing test run performed during the wood chips online corrosion probe test run (see [89] and Table 5.5). The formation of sulphates is kinetically limited (see Section 3.2.3). Hence, the whole amount of sulphur released from the fuel is considered as "passive" (SO_2) at the entrance of the simulation domain.

The corrosion probe is in full detail taken into account in the CFD simulations performed. A scheme of the probe can be found in Figure 8.7. A detailed list of the relevant boundary conditions for the simulation of the probe can be found in Table 8.10.

The porosity as well as the chemical composition of the ash layer have a considerably influence on the thermal conductivity of the ash layer. Due to their time-dependence, the determination of both values at a certain point of time, as boundary conditions for the CFD simulation, is not meaningful. Instead, a thermal conductivity of 0.5 W/mK is used for the basic fouling layer, which represents a good approximation for not sintered (porous) ash layers over a wide temperature range as could be shown by [81]. According to the actual final ash layers found on the corrosion probe (see Figure 4.2) as well as the MLP (see Figure 5.2) the enhanced deposit build-up at the stagnation point on the probes has only a small extension. Therefore, since the heat conduction in the steel tube is much higher than in the deposit layer, a homogeneous thickness of the layer of 2 mm was applied as a reasonable assumption for the determination of the mean deposit

temperature for case 1 and case2 as well as the simulation of the deposit formation after several hundred hours (case 4).

Table 8.9: Boundary conditions at the different simulation inlets
Explanation: pcz … primary combustion zone

name	**unit**	**fuel bed**	**secondary air nozzles**	**false air 1 (gas burner)**	**false air 2 (pcz)**
Velocity magnitude	m/s	see Figure 8.4	3.64	0.21	1.2
Flue gas temperature	°C	see Figure 8.5	25	25	25
Mass flux	kg/s	0.0062	0.0047	0.0008	0.0021
CO_2	kg/kg	see Figure 8.6	0.00	0.00	0.00
O_2	kg/kg	see Figure 8.6	0.23	0.23	0.23
H_2O	kg/kg	see Figure 8.6	0.01	0.01	0.01
CO	kg/kg	see Figure 8.6	0.00	0.00	0.00
H_2	kg/kg	see Figure 8.6	0.00	0.00	0.00
CH_4	kg/kg	see Figure 8.6	0.00	0.00	0.00
Na	kg/kg	$2.10 \cdot 10^{-6}$	0.00	0.00	0.00
K	kg/kg	$6.28 \cdot 10^{-5}$	0.00	0.00	0.00
Cl	kg/kg	$1.85 \cdot 10^{-5}$	0.00	0.00	0.00
S	kg/kg	0.00	0.00	0.00	0.00
SO_2	kg/kg	$1.08 \cdot 10^{-4}$	0.00	0.00	0.00
N_2	kg/kg	rest	rest	rest	rest

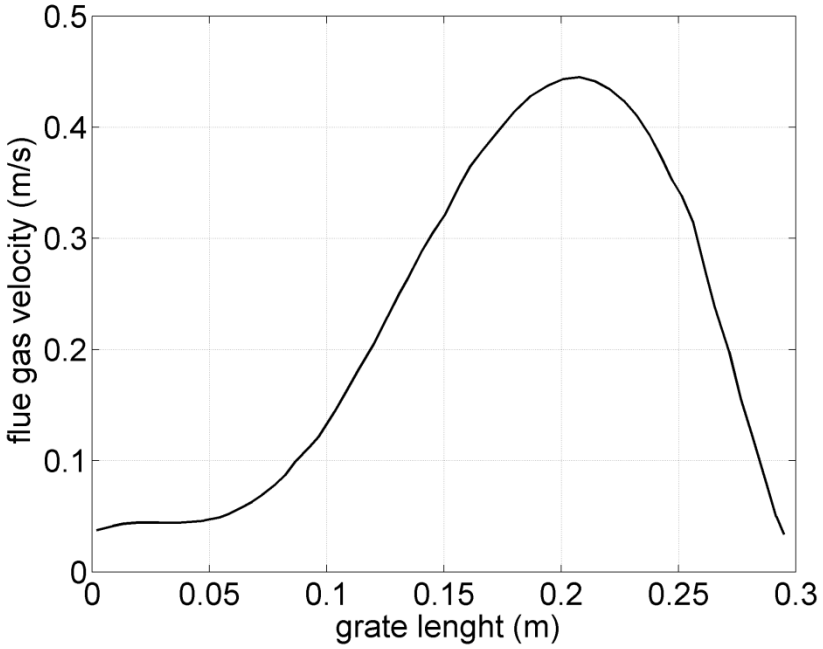

Figure 8.4: Flue gas velocity profile over the length of the biomass furnace grate

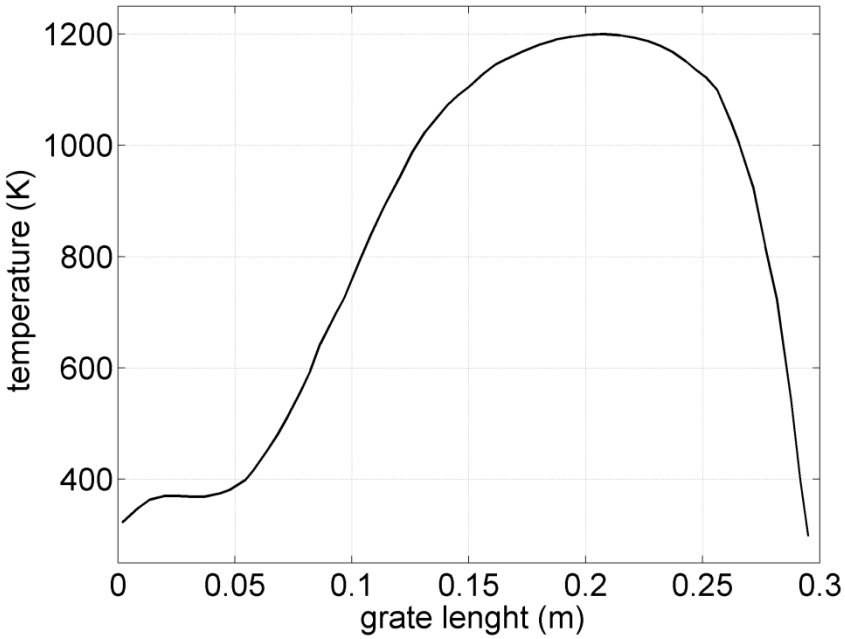

Figure 8.5: Flue gas temperature profile over the length of the biomass furnace grate

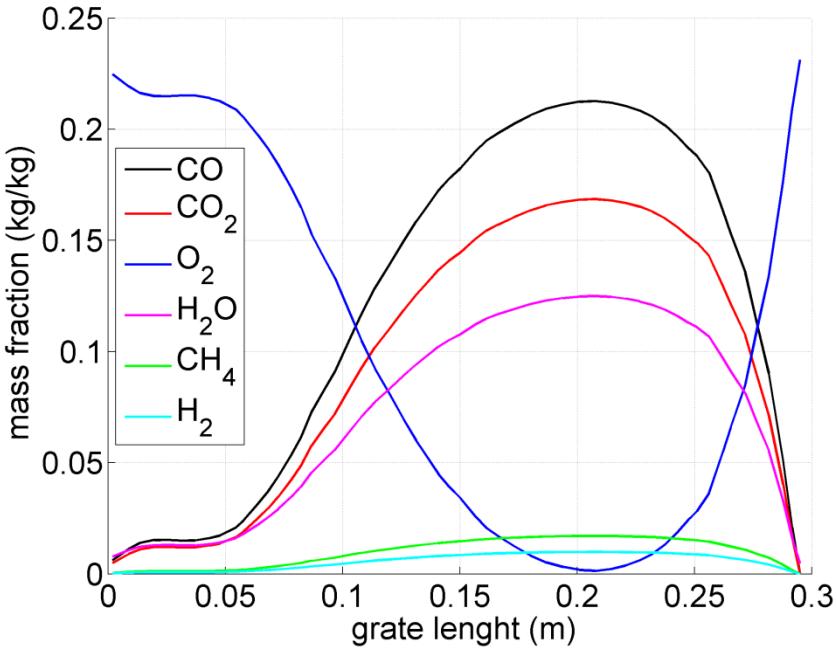

Figure 8.6: Profile of major flue gas species over the length of the biomass furnace grate

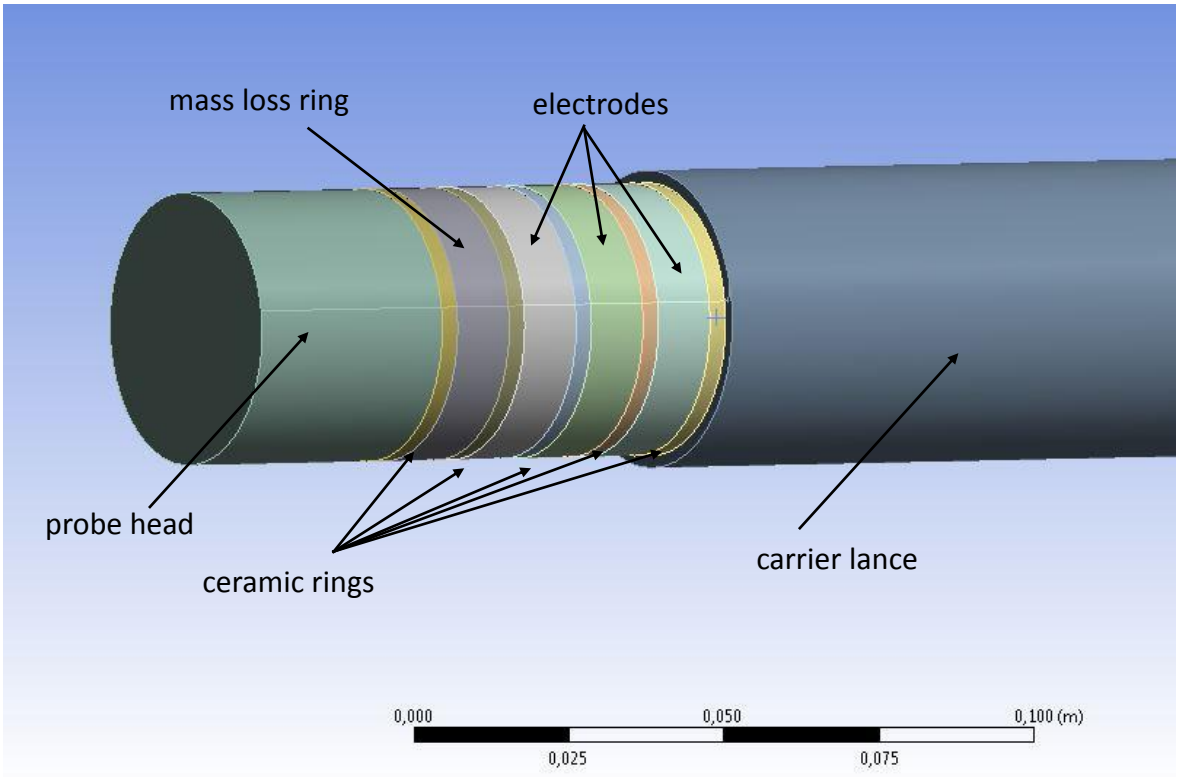

Figure 8.7: Detailed view of the simulated corrosion probe

Table 8.10: Boundary conditions at corrosion probe
Explanation: * … a fouling layer was only applied in the cases 1, 2 and 4 (see Table 8.8)

name	unit	Probe head	Ceramic rings	Mass loss ring	electrodes	Carrier lance
Material	-	Inconel 625	Ceramic	13CrMo4-5	13CrMo4-5	Inconel 625
Thermal conductivity	W/mK	16.5	2.3	45	45	16.5
Wall temperature at the probe inside	°C	uncooled solid	480	480	480	480
Fouling layer thickness*	mm	2	2	2	2	2
Thermal conductivity of the fouling layer*	W/mK	0.5	0.5	0.5	0.5	0.5

8.1.4 Case study 4: Application of the detailed model (see Section 5.5)

In the final CFD case study performed within this work a second wood chips fired plant with a water tube steam boiler was simulated to test and evaluate the applicability of the newly developed detailed high-temperature corrosion model. Figure 8.8 illustrates the plant investigated.

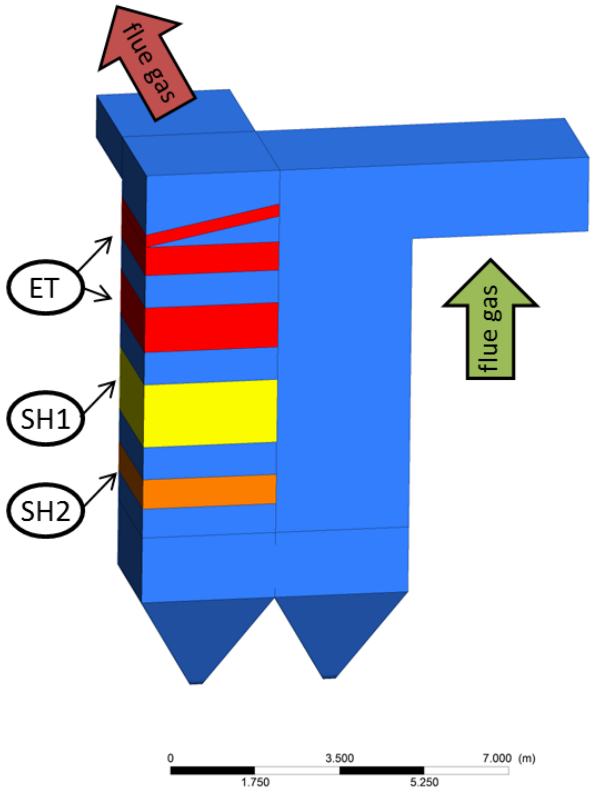

Figure 8.8: Scheme of the simulated plant
Explanation: ET … evaporators; SH1 … first superheater grid; SH2 … second and final superheater grid

The boundary conditions (e.g. flue gas temperature and composition) at the entrance of the simulation domain were taken from mass and energy balances provided by the plant manufacturer under the assumption of complete combustion. The boundary conditions at the simulation inlet can be found in Concerning ash deposit formation, the formation of fine dust, the deposition of fine dust as well as the direct wall condensation of the ash forming vapours were considered. The walls of the furnace ducts are lined using chamotte bricks. Due to this measure, the flue gas temperature at the end of the furnace duct (beginning of the simulation domain) is still quite high (950 °C). In further consequence, the residence time at high temperatures is still high enough to reach chemical equilibrium of gas phase sulphation. Hence, the whole amount of sulphur released from the fuel is considered as "passive" (SO_2) at the entrance of the simulation domain. The ash forming elements are K, Na, S and Cl which are able to form the following fine dust species: KCl, $(KCl)_2$, K_2SO_4, NaCl, $(NaCl)_2$, Na_2SO_4. The composition of

the flue gas as well as the other relevant boundary conditions at the inlet can be found in Table 8.6.

Table 8.11.

Concerning ash deposit formation, the formation of fine dust, the deposition of fine dust as well as the direct wall condensation of the ash forming vapours were considered. The walls of the furnace ducts are lined using chamotte bricks. Due to this measure, the flue gas temperature at the end of the furnace duct (beginning of the simulation domain) is still quite high (950 °C). In further consequence, the residence time at high temperatures is still high enough to reach chemical equilibrium of gas phase sulphation. Hence, the whole amount of sulphur released from the fuel is considered as "passive" (SO_2) at the entrance of the simulation domain. The ash forming elements are K, Na, S and Cl which are able to form the following fine dust species: KCl, $(KCl)_2$, K_2SO_4, NaCl, $(NaCl)_2$, Na_2SO_4. The composition of the flue gas as well as the other relevant boundary conditions at the inlet can be found in Table 8.6.

Table 8.11: Boundary conditions at the simulation inlet

Name	**unit**	
Velocity magnitude	m/s	5.37
Flue gas temperature	°C	950
CO_2	kg/kg	0.111
O_2	kg/kg	0.065
H_2O	kg/kg	0.123
Na	kg/kg	$3.97 \cdot 10^{-6}$
K	kg/kg	$3.74 \cdot 10^{-5}$
Cl	kg/kg	$9.49 \cdot 10^{-6}$
S	kg/kg	0.000
SO_2	kg/kg	$3.60 \cdot 10^{-5}$
N_2	kg/kg	rest

To basic fouling layer is taken into account to approximately allow the calculation of the deposit formation (chemical composition) as well as the high-temperature corrosion potential of the steady-state (a detailed discussion can be found in 5.5.1). The values for this layer can be found in Table 8.12 and Table 8.13.

The heat loss over the finned walls is calculated by the saturated steam temperature and the mean heat transfer coefficient as boundary conditions on the water side. The boundary conditions can be found in Table 8.12

Table 8.12: Boundary conditions for finned tube walls

	unit	Finned tube walls
Thermal conductivity of the steel	W/mK	50
Steel thickness	mm	3.2
Thermal conductivity of the fouling layer	W/mK	0.5
Fouling layer thickness	mm	4
Heat transfer coefficient (waterside)	W/m°K	1250
Free stream temperature	°C	271
Internal emissivity		0.6

Table 8.13: Boundary conditions for the superheater tubes
Explanation: SH1-SH3… superheater tube bundle 1-2, ET, ccf … cross counter flow, cpf … cross parallel flow

	unit	ET	SH1	SH2
		bank of staggered tubes		
		cpf	cpf	ccf
Tube wall material		St 35.8	16Mo3	13CrMo4-5
Outside tube diameter	mm	38	38	38
Tube wall thickness	mm	4	4	4
Transverse tube pitch	mm	100	100	100
Longitudinal tube pitch	mm	65	90	90
Width flue gas duct	mm	2800	2800	2800
Height flue gas duct	mm	3048	1300	570
Number of tubes per row width (transversal)		28	28	28
Number of tubes in gas flow direction		30	15	7
Thermal conductivity of the steel	W/mK	50	45	45
Heating surface	m²	281	140	66
Fouling layer thickness of tubes on flue gas side	mm	2.5	2.5	2.5
Thermal conductivity of fouling layer on flue gas side	W/mK	0.5	0.5	0.5
Heat transfer coefficient (waterside)	W/m²K	16000	1000	1200
Water/steam temperature inlet	°C	271	271	357
Water/steam temperature outlet	°C	271	450	475
Nusselt first row/Nussel core		0.8	0.8	0.8
Clean surface emissivity on flue gas side		0.6	0.6	0.6

8.2 Scientific journal papers

Paper I

Fuel 144 (2015) 15–24

Contents lists available at ScienceDirect

Fuel

journal homepage: www.elsevier.com/locate/fuel

Investigation of the corrosion behaviour of 13CrMo4–5 for biomass fired boilers with coupled online corrosion and deposit probe measurements

Thomas Gruber [a,b,*], Kai Schulze [a], Robert Scharler [a,b,c], Ingwald Obernberger [b,c]

[a] BIOENERGY 2020+ GmbH, Inffeldgasse 21b, 8010 Graz, Austria
[b] Institute for Process and Particle Engineering, Graz University of Technology, Inffeldgasse 13, 8010 Graz, Austria
[c] BIOS BIOENERGIESYSTEME GmbH, Inffeldgasse 21b, 8010 Graz, Austria

HIGHLIGHTS

- Online corrosion probe measurements were applied.
- Deposit probe measurements were applied.
- A fixed bed/drop tube reactor was used for the measurements.
- An empirical corrosion model was developed.
- Possible corrosion mechanisms are discussed.

ARTICLE INFO

Article history:
Received 18 September 2014
Received in revised form 20 November 2014
Accepted 24 November 2014
Available online 5 December 2014

Keywords:
Biomass combustion
High-temperature corrosion
Online corrosion measurement
Empirical corrosion model
Deposit formation

ABSTRACT

High-temperature corrosion in biomass fired boilers is still an insufficiently explored phenomenon which causes unscheduled plant shutdowns and hence, economical problems. To investigate the high-temperature corrosion and deposit formation behaviour of superheater tube bundles, online corrosion probe as well as deposit probe measurements have been carried out in a specially designed fixed bed/drop tube reactor in order to simulate a superheater boiler tube under well-controlled conditions. The investigated boiler steel 13CrMo4–5 is commonly used as steel for superheater tube bundles in biomass fired boilers. Forest wood chips and quality sorted waste wood (A1–A2 according to German standards) as relevant fuels have been selected to investigate the influence on the deposit formation and corrosion behaviour. The following influencing parameter variations have been performed during the test campaigns: flue gas temperature between 650 and 880 °C, steel temperature between 450 and 550 °C and flue gas velocity between 2 and 8 m/s. One focus of the work presented is the detailed investigation of the structure and the chemical composition of the deposits formed as well as of the corrosion products. A further goal of the work presented was the development of an empirical model which can be used within CFD simulations of flow and heat transfer to calculate and evaluate the local corrosion potential of biomass fired plants already at the planning stage. The corrosion probe measurements show a clear dependency on the parameters investigated and the empirical function developed reproduces the measured corrosion behaviour sufficiently accurate. Since the additional calculation time within the CFD simulation is negligible the model represents a helpful tool for plant designers to estimate whether high-temperature corrosion is of relevance for a certain plant or not, when using fuels with similar compositions and the steel 13CrMo4–5.

1. Introduction

Ash related problems have a strong influence on the operation of biomass combustion plants, resulting in unscheduled outages and reduced economic efficiencies. Among these problems, material corrosion of steel surfaces in the hot furnace, of radiative boiler walls and of convective heat exchanger tube bundles (superheaters) is of major importance. This is especially of interest when firing biomass fuels with high contents of chlorine and alkali metals (e.g. waste wood as well as agricultural and herbaceous fuels like straw and Miscanthus). Also corrosion is of relevance for conventional wood fuels (e.g. forest wood chips and bark) in more

* Corresponding author at: BIOENERGY 2020+ GmbH, Inffeldgasse 21b, 8010 Graz, Austria. Tel.: +43 (0) 316 873 9228; fax: +43 (0) 316 8739202.
E-mail address: thomas.gruber@bioenergy2020.eu (T. Gruber).

http://dx.doi.org/10.1016/j.fuel.2014.11.071
0016-2361/

efficient future biomass combined heat and power (CHP) plants with increased steam parameters. Therefore, a lot of research has been done in the last decades to identify and quantify the most influencing parameters on high-temperature corrosion occurring in biomass fired boilers (an overview is given by [1,2]).

High-temperature corrosion has already been extensively investigated in plants firing biomass rich in chlorine such as straw (e.g. [3–6]) and, furthermore, in municipal solid waste incinerators (an overview is given by [3,7–9]). Also the corrosion processes occurring in plants firing fuels with low to moderate chlorine contents, such as forest wood chips and bark as well as quality sorted waste wood have already been investigated (e.g. [10,11]). However, in measurements in real-scale biomass plants it is often not possible to vary just one parameter of interest to determine its effect on the high-temperature corrosion.

In addition, a wide range of experimental data exist, where the effect of deposits of certain species (e.g. KCl or NaCl) are investigated and possible corrosion reaction mechanisms are proposed (e.g. [12–15]). Nevertheless, these experiments are also not sufficient to predict the high-temperature corrosion behaviour of real-scale plants accurately, due to the interaction and the high complexity of the processes involved.

2. Objectives

The aim of the work presented was the detailed investigation of the high-temperature corrosion processes occurring in the superheater section of biomass fired CHP plants. Therefore, online corrosion probe measurements (see Section 3.2) as well as deposit probe measurements (see Section 3.3) were performed to investigate the corrosion behaviour of the steel 13CrMo4–5 in a specially designed packed bed reactor. To study the effect of different biomass fuels fired on deposit formation and on high-temperature corrosion, two test campaigns were carried out. In the first one, forest wood chips and in the second one quality sorted waste wood (A1–A2 according to German standards) was used as fuel.

Online corrosion probes have already been successfully applied in municipal solid waste incinerator plants [8,9,16] and in a biomass boiler firing wood chips [17]. From these measurements it is known that the most relevant parameters influencing high-temperature corrosion are the steel temperature, the flue gas temperature, the chemical compositions of the flue gas as well as the deposits, and the flue gas velocity. For waste combustion environments these findings are in accordance with results from material loss lab- and real-scale measurements [18]. However, as already mentioned in general it is not possible to vary just one parameter of interest arbitrarily in real-scale plants. Therefore, the range and the amount of available data regarding the variation of the parameters flue gas temperatures and velocities is rather low in studies already published [16,17,19,20] using online corrosion probes.

On the contrary the experimental setup used within this work enables the arbitrary variation of a single parameter of interest under conditions comparable to real-scale biomass fired CHP plants. Therefore, the dependence on the influencing parameters can be studied in more detail which allows the development of a clear mathematical description on these parameters. The empirical model can be used within CFD simulations of flow and heat transfer to calculate the local high-temperature corrosion potential as a function of the parameters investigated.

3. Methodology

The corrosion probe test campaign took place at the specially designed packed bed/drop tube reactor of BIOENERGY 2020+ GmbH (see Section 3.1). The boiler steel investigated was 13CrMo4–5. The composition of this heat resistant ferritic steel can be found in Table 1. To investigate the effect of different fuel compositions, especially regarding increased chlorine and heavy metal contents, two test campaigns with typical treated and untreated woody biomass fuels were carried out. Forest wood chips, with a rather low chlorine and heavy metal content, and quality sorted waste wood (A1–A2), which shows significantly higher chlorine and heavy metal contents, were used as fuels. The compositions of the fuels are presented in Table 2. The molar 2S/Cl ratios calculated based on the fuel analyses for the fuel wood chips is 6.9, whereas the ratio of the waste wood used is 1.4, which indicates a higher corrosion potential according to [21].

The following parameter variations were performed during the test campaigns: flue gas temperature variation between 650 and 880 °C, steel temperature variations between 450 and 550 °C and flue gas velocity variations between 2 and 8 m/s. The flue gas temperature variations were achieved by a variation of the electrical heating power of the drop tube (see Section 3.1), the variations of the steel temperature were established by variable air cooling of the probe (see Section 3.2) and the flue gas velocity was varied by an increase of the furnace load.

The duration of the corrosion probe test campaign of forest wood chips was 1070 h in which the biomass furnace was 325 h in operation. The test campaign of waste wood lasted 1512 h with a furnace operation time of 329 h. Due to safety reasons the furnace had to be shut down in the evenings and at weekends. To prevent chipping of the corrosion layer caused by thermal stress the drop tube was heated overnight at a constant temperature of 850 °C of the heating elements, with air streaming through the drop tube, which led to a constant probe steel temperature of about 440 °C.

The corrosion probe applied needs a fully developed ionic layer at the corrosion front to achieve a stable corrosion signal. Horn et al. [22] reported that it took around 10 days to achieve a stable layer structure in similar measurements, performed in municipal solid waste CHP plants. Therefore, both test campaigns were split in two parts in which the first ≈130 operating hours were used to develop an ionic layer. During that time the parameter settings were not changed. After gaining a reproducible signal from the online corrosion probe over several days, parameter variations were applied to determine the effects on high-temperature corrosion. Here, the methodology differs for the two test campaigns. For forest wood chips, the parameter variations were all done starting from pre-defined reference conditions, which mean a flue gas temperature of 710 ± 10 °C, a steel temperature of 480 ± 1 °C and a flue gas velocity of 2.8 ± 0.5 m/s, which were also used to build up the ionic layer. After the parameter variations, this reference state was re-established before the furnace was shut down. In doing so, the reproducibility of the reference signal was ensured on a daily basis with the drawback, that the majority of the data points are located within relatively narrow spaces of the parameter variation range. To achieve a better distributed data set the procedure was changed for waste wood. Here, only one steel temperature was investigated per day, and the flue gas temperature was slowly but steadily increased and after reaching the maximum flue gas temperature of approximately 880 °C decreased again to a temperature of around 710 °C. Meanwhile the flue gas velocity was kept constant to 3.6 ± 0.5 m/s. To ensure the reproducibility, all steel temperature variations were repeated at least two times. Flue gas velocity variations were performed subsequent to the temperature variations. To determine the combustion conditions during the corrosion probe test campaigns, balance test runs were performed. The characteristic data of the combustion conditions can be found in Table 3.

Table 1
Chemical composition of the steel 13CrMo4–5.

	C	Si	Mn	P	S	N	Cu	Cr	Mo	Fe
Min [weight-%]	0.08	–	0.40	–	–	–	–	0.70	0.40	Remaining
Max [weight-%]	0.18	0.35	1.00	0.03	0.01	0.01	0.30	1.15	0.60	Remaining

Table 2
Chemical composition of the fuels investigated. *Explanations:* mv . . .mean value, std . . .standard deviation, w.b. . . .wet basis, d.b. . . .dry basis; wt.% . . .weight percent; number of samples: forest wood chips = 3; waste wood = 8; for forest wood chips the concentrations of the elements C, H and N have only been determined from one representative sample.

	Unit	Forest wood chips		Waste wood A1–A2	
		mv	std	mv	std
Moisture content	wt.% w.b.	24.1	3.4	20.7	2.0
Ash content	wt.% d.b.	2.4	0.7	2.1	0.6
Ash content corrected	wt.% d.b.	1.9	0.6	1.8	0.6
C	wt.% d.b.	48.1	–	47.7	0.3
H	wt.% d.b.	5.9	–	6.1	0.1
N	wt.% d.b.	0.3	–	0.9	0.2
S	mg/kg d.b.	280	8	593	138
Cl	mg/kg d.b.	90	18	1154	798
Si	mg/kg d.b.	2122	1382	2372	948
Ca	mg/kg d.b.	6045	998	3533	1021
Mg	mg/kg d.b.	739	369	506	127
K	mg/kg d.b.	1660	147	868	71
Na	mg/kg d.b.	63	15	536	159
P	mg/kg d.b.	204	18	89	13
Al	mg/kg d.b.	446	171	593	179
Fe	mg/kg d.b.	265	77	625	516
Mn	mg/kg d.b.	108	54	91	12
Zn	mg/kg d.b.	19	1	143	51
Pb	mg/kg d.b.	1	0	35	15
Molar 2S/Cl ratio	mol/mol	6.9	0.6	1.4	0.5

Table 3
Combustion conditions during the corrosion probe measurements *Explanations:* mv . . .mean value, std . . .standard deviation, w.b. . . .wet basis, d.b. . . .dry basis, NCV . . .net calorific value, Nm^3 . . .m^3 at 0 °C and 101325 Pa.

Parameter	Forest wood chips		Waste wood		
	mv	std	mv	std	Unit
Fuel power input related to NCV	23.4		25.7		kW
Fuel flow rate	6.3		6.7		kg/h w.b.
Temperature primary combustion zone	818	15	892	17	°C
Temperature secondary combustion zone	896	29	872	8	°C
CO_2	11.1	0.9	11.8	1.1	Vol.-% d.b.
CO	13.8	0.7	18.2	41.6	mg/Nm^3 d.b. 13% O_2
O_2	9.5	0.9	8.7	1.2	Vol.-% d.b.
SO_x	8.6	2.8	42.6	12.2	mg/Nm^3 d.b. 13% O_2
HCl	6.6	3.8	68.9	29.5	mg/Nm^3 d.b. 13% O_2
Primary air flux	15.4		14.5		Nm^3/h
Secondary air flux	16.1		16.3		Nm^3/h
Total air flux	31.5		30.9		Nm^3/h
Flue gas recirculation volume flux	–		5.8		Nm^3/h
Air ratio primary combustion zone (Including flue gas recirculation)	0.86		0.98		
Total air ratio (Including flue gas recirculation)	1.5		1.5		

3.1. Biomass reactor

The corrosion probe test campaigns were carried out using a combined packed bed/drop tube reactor (Fig. 1), with which conditions regarding flue gas temperature, composition and velocity as well as temperatures at the steel surface, typically prevailing in biomass combustion plants can be achieved. The used setup consists of a packed bed reactor (biomass grate furnace equipped with air staging and flue gas recirculation), which is connected via an upper transition part to a heated vertical tube with isothermal conditions (the so-called drop tube) which is followed by the measurement port. With the heating elements of the drop tube (60 kW electrical input power) flue gas temperatures of 900 °C can be achieved at the measurement port at the reference load operation mode of the reactor. An additional water cooled pipe is installed to bypass the measurement unit during the startup and shutdown of the reactor. The drop tube has a length, which is sufficient to achieve a fully developed flow at the entrance of the measurement

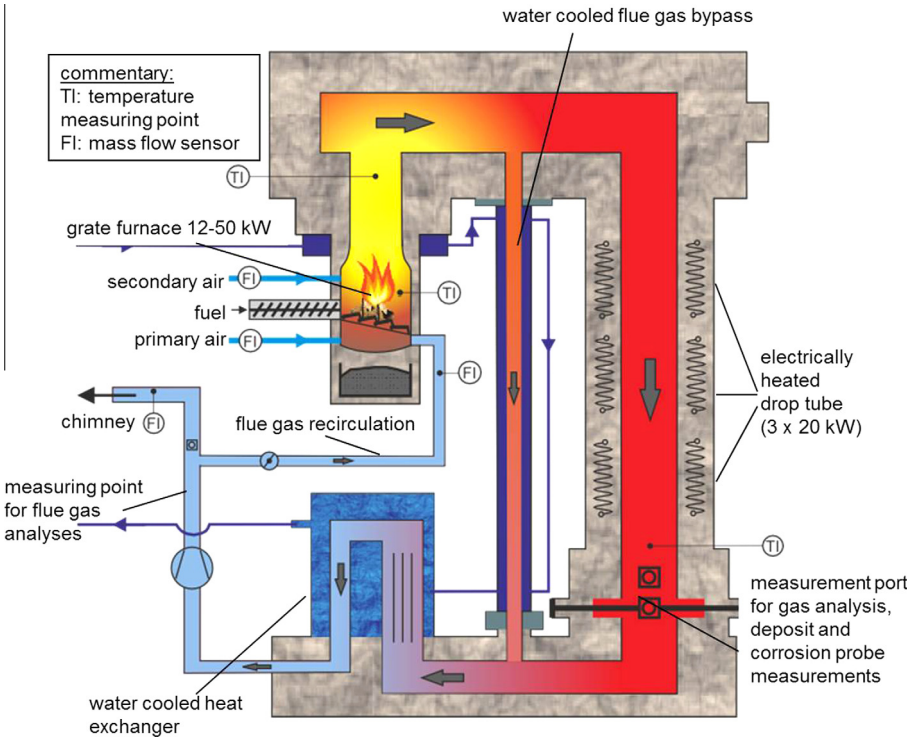

Fig. 1. Schematic view of the combined packed bed/drop tube reactor with relevant units and measurement ports.

port, which is equipped with a corrosion and/or a deposit probe. Therefore, the reactor enables corrosion measurements under defined flow and temperature conditions with a flue gas typical for fixed bed combustion systems. Finally, the flue gas is transferred via a lower transitional part to a water cooled heat exchanger before it enters the chimney. An additional port is installed before the entrance to the chimney to allow flue gas analysis.

3.2. Online high-temperature corrosion probe measurements

The corrosion probe provided by the company CORRMORAN GmbH (Augsburg, Germany) is based on a system which was developed at the Institute of Physics, University of Augsburg in Germany. The system is especially designed to simulate high-temperature corrosion occurring on superheater tubes. The probe design consists of an air cooled support lance made from a heat resistant nickel based super alloy (Fig. 2 left) with an air-cooled probe head (Fig. 2 right). The probe head itself is composed of four sample rings that are separated by ceramic rings. These sample rings, made of 13CrMo4–5, are held at a constant temperature which can be arbitrarily changed by the air cooling. When exposed to the flue gas, an ionic layer is formed which allows the measurement of a linear polarization resistance between the steel surface and the ionic layer. This resistance is directly proportional to the current corrosion attack [24]. The measured signal can be related to a corrosion rate, which describes the steel loss over time, subsequent to the test campaign by quantifying the actual loss of weight of an additional ring, the so-called mass loss ring, over the whole test campaign. A detailed description of the probe can be found in [8,17].

It should be mentioned that the corrosion rates measured within this work give only qualitative information about the corrosion potential in dependence of relevant operating parameters. High-temperature corrosion is a strongly time-dependent process which often follows a paralinear trend [24]. Therefore, the corrosion rates gained within short-term measurements generally differ from those found within long-term measurements. Nevertheless, the short-term online corrosion measurements still allow the investigation of the dependence on a certain parameter. The steel temperatures investigated were 450, 480, 500, 520 and 550 °C.

3.3. Deposit probe measurements

To gain more information about the chemical composition, the build-up rate (RBU) and the structure of the deposit layer, deposit probe measurements were performed. These measurements were

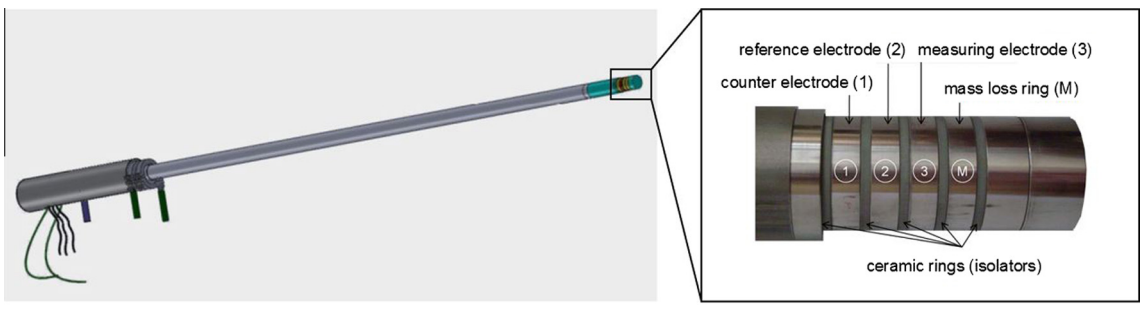

Fig. 2. Schematic view of the corrosion probe (left) and the sensor probe head (right) with the electrodes (1–3) and the mass loss ring (M) [23].

carried out subsequent to the corrosion probe test campaigns to avoid an interaction of the corrosion and the deposit probe. The deposit probe consists of a carrier lance with a test ring on top, which is cooled by air and is inserted into the flue gas at the position of the corrosion probe (see Fig. 1). The air cooling of the probe allows the investigation of arbitrary constant ring temperatures to simulate different steam temperatures. Deposit probe measurements at different probe temperatures give an indication regarding the condensation temperature of gaseous flue gas components such as KCl or NaCl. The mass gain of the test ring is determined by gravimetric measurements of the test ring before and after the exposure to the flue gas. A more detailed description of the deposit probe measurement can be found in [17]. Scanning electron microscopy (SEM) and energy dispersive X-ray (EDX) analyses were performed to analyse the deposits subsequently to the measurements on three different locations (windward, windward + 50° and the leeward side) of each deposit probe ring. For each fuel two deposit probe measurements were performed. In case of forest wood chips the temperatures investigated were 480 °C and 550 °C. For waste wood, the temperatures 450 °C and 550 °C were investigated, representing the highest and lowest steel temperature investigated during the test campaign. All deposit samples were taken at a flue gas temperature of around 700 °C and a superficial flue gas velocity of 2.8 m/s for forest wood chips and 3.6 m/s for waste wood, respectively. The sampling time was two hours in each case and the measurements were conducted with clean probe rings made of the steel 1.4841.

3.4. SEM/EDX- analyses and sample preparation

To investigate the chemical composition of the deposit layer by means of SEM/EDX- analyses, the deposit probe rings were first coated with a thin carbon layer to avoid an electrical charging of the sample. The samples were analyzed using a ZEISS Gemini 982 field emission scanning electron microscope equipped with a Noran Voyager X-ray analysis system (Si(Li) detector, ultra-thin window). The oxygen content was determined by stoichiometric calculations. The compositions of the deposit layers were determined by area scans using magnifications of 100 at representative spots of the ring sections: windward, windward + 50 and leeward. Because of the interaction volume of the electron beam with the sample not only the deposit layer becomes analyzed, but also the underlying steel of the probe ring. Especially for thin deposit layers, as formed during short-term deposit measurements, this is an essential problem. Due to the fact that the amount of Ni and Cr is negligible in both fuels and the release rate of Fe from the fuel is typically low, these elements were excluded from the analyses. The measured quantities of these elements are most likely components of the probe steel ring.

To gain more information regarding the corrosion mechanism, SEM/EDX analyses of the corrosion probe rings were performed subsequently to the test runs. To investigate the elemental distribution through the tube crosscut, first the ring was embedded in epoxy resin, afterwards the profile was grinded using sand papers with decreasing grain sizes until a smooth, plane surface was achieved. The cross sections were prepared under dry conditions without the use of a lubricant. Afterwards, the ring was coated with a thin carbon layer. Between the various steps the probe rings were stored in a desiccator. Elemental mappings were performed at a magnification of 400 to analyse the chemical composition of the corrosion layer. The systems used for the mappings are a Zeiss Ultra 55 field emission scanning electron microscope equipped with an EDAX Pegasus X-ray analysis system. These elemental mappings show the distribution of each element over the area investigated (bright colours mean a high concentration, weak colours a low concentration). Within these mappings the oxygen content was measured and not stoichiometrically calculated to detect oxides and to achieve a clear separation between the corrosion layer and the original steel surface. Since alkali chlorides are quite sensitive to heat it was ensured that the probe ring did not become too hot during the grinding process. Therefore, a reference sample with well-defined KCl content was prepared and analysed in the same way as the corrosion probe ring. The pre-defined KCl content of this sample could be confirmed with EDX analyses. In doing so, it is assured that KCl is not removed from the corrosion probe rings during sample preparation.

3.5. Fuel and ash analyses

To investigate the fuel composition, representative samples of the fuels were prepared. The moisture content of the fuel sample is determined according to CEN/TS 14774. Fuel sample preparation is carried out according to CEN/TS 14780. The ash content is determined according to CEN/TS 14775. Additionally, the corrected ash content were calculated by a reduction of the ash content by the amounts of carbonates in the ash. These carbonates are formed during the ashing process, which occurs at a constant temperature of 550 °C. In fixed bed biomass furnaces carbonates do typically not occur due to the high temperatures prevailing. The determination of C, H and N is carried out according to CEN/TS 15104. The chlorine content is determined according to CEN/TS 15289. Major and minor ash forming elements are determined by multi-step pressurized digestion of the fuel with HNO_3 (65%)/HF (40%)/H_3BO_3 followed by inductively coupled plasma optical emission spectroscopy (ICP-OES) or inductively coupled plasma mass spectroscopy (ICP-MS) depending on detection limits.

3.6. HCl/SO_x measurements

The determination is carried out according to VDI 3480, Sheet 1. Flue gas is sucked from an extraction point over several successively connected washing flasks with distilled water and diluted sodium hydroxide solution (enriched with H_2O_2). The dissolved anions are measured by ion-chromatography (IC). HCl/SO_x measurements were performed three times during the test run (conditions can be found in Table 3) at the position of the corrosion probe (see Fig. 1).

4. Results and discussion

4.1. Deposit formation

4.1.1. Deposit probe measurements

The chemical composition of the deposits has been determined by means of SEM/EDX analyses (see Section 3.4). The findings are presented in Fig. 3. The deposit layer of the fuel forest wood chips (see Fig. 3 left) mainly consists of potassium and sulphur which indicates the presence of potassium sulphate based on the molar ratios measured. Chlorine can only be found in very small amounts in the case of 480 °C steel temperature, with a slightly higher concentration on the leeward side of the probe ring. This indicates that the condensation temperature of the gaseous chlorides lies somewhere between 480 °C and 550 °C. Furthermore, the amounts of Si, Ca and Mg, which are typical elements in the course fly ash, are rather low.

The composition of the waste wood deposits differs strongly from the results obtained for forest wood chips (see Fig. 3 right). Here, chlorine can be found in both deposits, although the amount of chlorine is a little bit higher for 480 °C, indicating a higher condensation rate of chlorine containing salts for this temperature. One can also see, that the amount of the typical elements of the

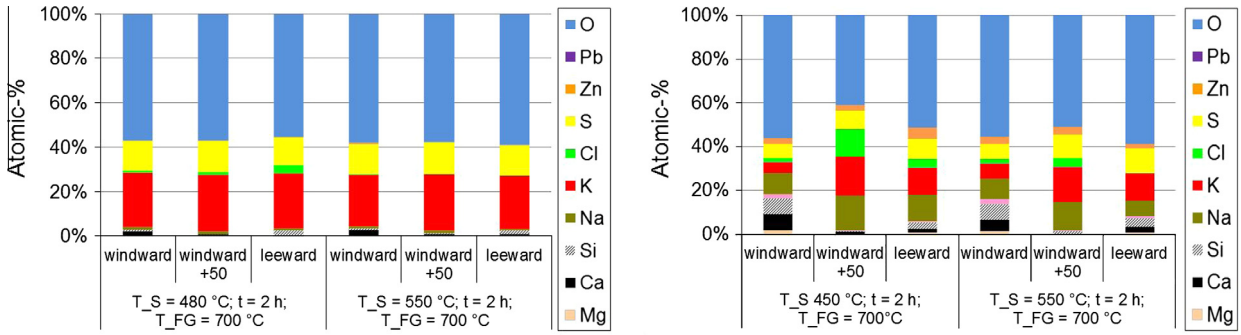

Fig. 3. Results of the EDX-analysis of the deposits formed during the deposit probe measurements for forest wood chips (left) and waste wood (right) *Explanations:* T_S . . .steel temperature, *t* . . .duration time of deposit measurement, T_FG . . .flue gas temperature.

coarse fly ash is increased compared to forest wood chips. Furthermore, in contrast to the forest wood chips deposits the waste wood deposits contain a considerable amount of Zn and Na.

For forest wood chips the RBU's measured are 2.8 g/m² h for 480 °C and 1.4 g/m² h for 550 °C. For waste wood values of 6.9 g/m² h for 450 °C and 7.0 g/m² h for 550 °C have been found. Therefore, a faster deposit build-up has to be expected in the case of waste wood in the initial state of the test campaign.

4.1.2. Deposits formed on the corrosion probes

One has to keep in mind that the long-term deposition behaviour can vary from the findings obtained from short-term deposit probe measurements due to increased surface temperatures. Therefore, the final deposit layers formed on the corrosion probes of both test campaigns have also been investigated. Fig. 4 shows the deposits on the corrosion probe formed during the test campaign with forest wood chips, whereas Fig. 5 shows the waste wood deposits. The deposit formation on the deposit probe is much faster in the case of waste wood. This result has already been indicated by the short time RBU's measured. Furthermore, the two deposits differ regarding their structure. The deposits of forest wood chips are powdery and loosely bound to the corrosion probe and no sintering occurred. On the contrary, the waste wood deposits are sintered to single columns where the binding within the particles is quite strong but the sintered deposit layer has only a weak binding to the corroded probe surface and therefore, can be easily removed.

To investigate time dependent changes in the composition between the short-term deposit probe measurements and the deposits on the corrosion probes, the deposits of the corrosion probes have been analysed according to Section 3.5. The results

Fig. 4. Photo of the corrosion probe after the forest wood chips test campaign (exposure time 325 h). *Explanation:* the thickness of the deposit layer is indicated by the white arrow, whereas the red arrow indicates the diameter of the probe; windward side above, leeward side below. (For interpretation of the references to colour in this figure legend, the reader is referred to the web version of this article.)

Fig. 5. Photo of the corrosion probe after the waste wood test campaign (exposure time 329 h). *Explanation:* the thickness of the deposit layer is indicated by the white arrow, whereas the red arrow indicates the diameter of the probe; windward side above, leeward side below. (For interpretation of the references to colour in this figure legend, the reader is referred to the web version of this article.)

of the chemical analyses can be found in Fig. 6. In contrast to the deposit probe measurements no chlorine could be found in the deposits of the corrosion probes. This result and it's effect on the corrosion mechanism will be discussed in detail in Section 4.4. Furthermore, in the case of forest wood chips, the relative amount of coarse fly ash on the windward side significantly increased compared to the short-term deposit probe measurements. A plausible explanation can be given by the growing deposit layer, which results in increased surface temperatures. Hence, condensation of aerosols becomes limited and impaction of coarse fly ash particles becomes the dominating process. This effect is not distinctive in the case of waste wood due to the higher amount of coarse fly ash particles in the flue gas. In contrast to the short-term deposit probe measurements traces of Pb can be found in the deposits of the corrosion probe. An explanation could be

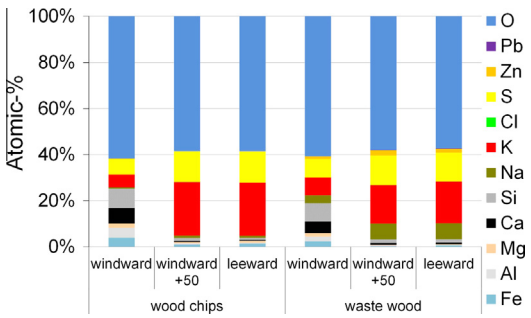

Fig. 6. Chemical composition of the deposits found on the corrosion probe after the test campaign.

given by the strong deviations of the heavy metal content in the case of waste wood (see Table 2) and the rather short measurement time of the deposit probe measurements. A further difference in the chemical composition between the deposits of the deposit probe and the corrosion probe is the missing of chlorine in the deposits of the corrosion probe.

4.2. SEM/EDX analyses of the corrosion probe rings

To determine the chemical structure over the ring profile of the corrosion products and the deposit layer, SEM/EDX element mappings have been carried out on the windward, windward + 50 and leeward side of a corrosion probe ring. The findings of these analyses are presented in Fig. 7. Since the general information obtained for the various ring sides is the same, only the mappings of the windward side are presented. The composition of the deposit layer has already been determined with chemical analyses (see Section 4.1.2). The findings of the EDX analyses presented confirm the results of the chemical analyses. At the corrosion front two aspects are of special interest. The first one is the absence of chlorine for all EDX mappings. Therefore, one can only see the equally distributed background noise of the EDX analyses in the Cl mappings (see Fig. 7). The second one is the enrichment of sulphur at the corrosion front. This layer is stronger developed in the case of forest wood chips but one can also find this layer in the case of waste wood. Quantitative EDX analyses of this layer showed that it consists of Fe, O and S, with strong variations regarding the sulphur concentration. Highly resolved spot analyses show areas where the layer consists solely of Fe and S indicating the presence of FeS or FeS_2. Therefore, it is concluded that the layer consists of a mixture of the two phases iron sulphide and iron oxide rather than iron sulphate. Due to the low Cr content of the steel (see Table 1) no protecting Cr_2O_3 layer is formed at the corrosion front (see Cr element mapping in Fig. 7).

The results for forest wood chips are in good agreement with comparable measurements carried out in a wood chips fired CHP plant [17]. Within that work also an enrichment of sulphur at the corrosion front was reported as well as the absence of chlorine.

4.3. Corrosion probe measurements

The corrosion signal measured during the combustion of forest wood chips (see Section 3.2) shows an exponential dependence on the flue gas temperature (see Fig. 8, left) as well as on the steel

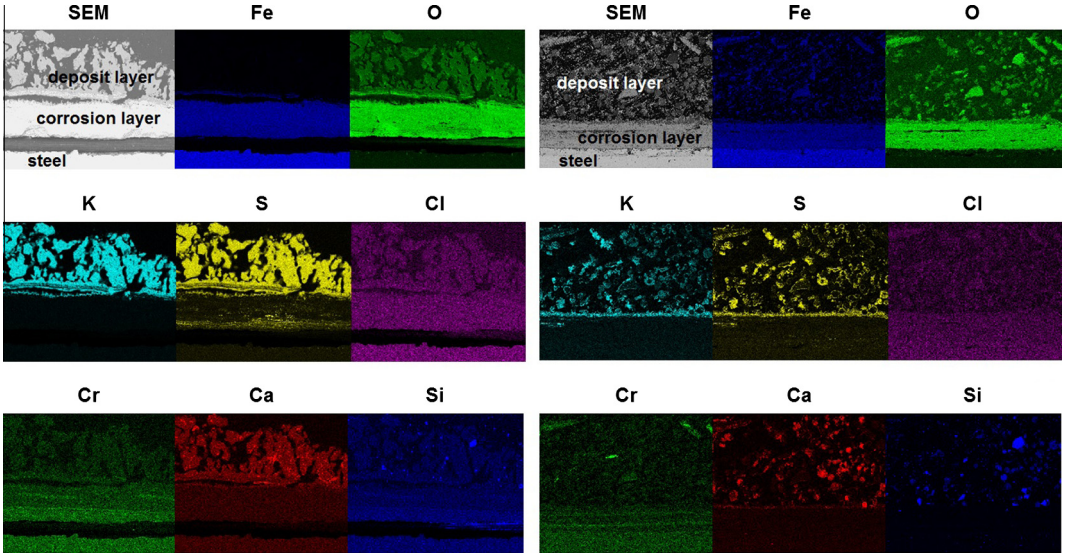

Fig. 7. SEM/EDX element mappings through the cross section of a corrosion probe ring on the windward side. Results for forest wood chips are shown left and for waste wood right.

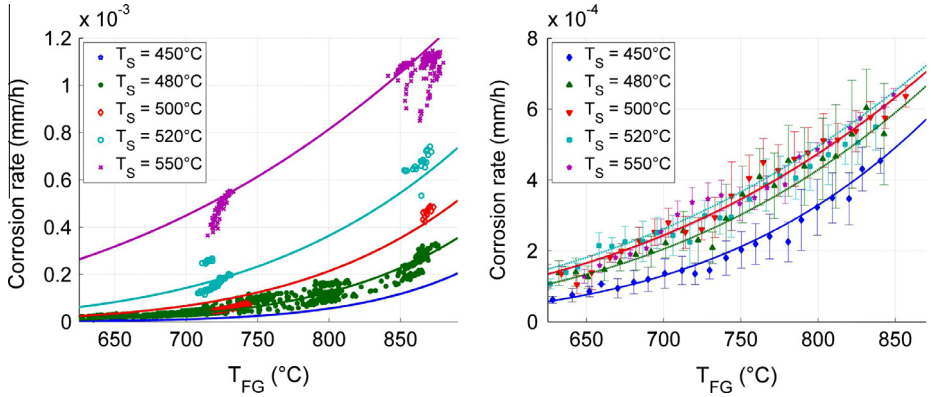

Fig. 8. Empirical model in comparison to measurement values for forest wood chips [25] (left) and for waste wood (right) as a function of flue gas temperature *Explanation:* flue gas velocity has been kept constant to 2.8 ± 0.5 m/s in the case of forest wood chips and to 3.6 ± 0.5 m/s in the case of waste wood; T_S . . .steel temperature, T_{FG} . . .flue gas temperature.

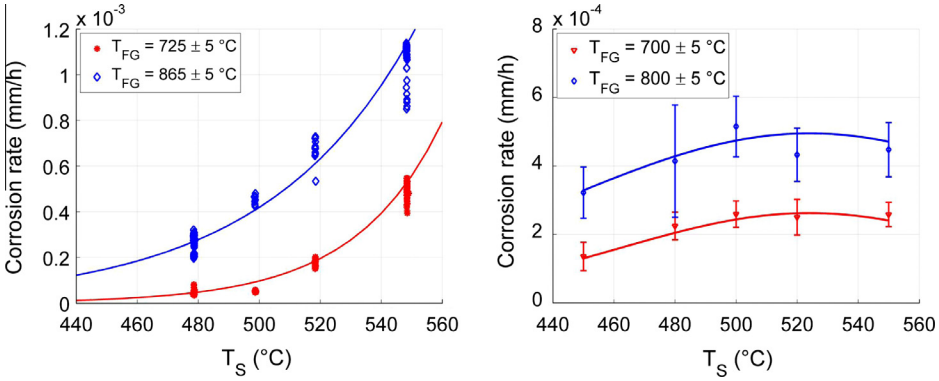

Fig. 9. Empirical model in comparison to measurement values for forest wood chips [25] (left) and for waste wood (right) as a function of the steel temperature *Explanation:* flue gas velocity has been kept constant to 2.8 ± 0.5 m/s in the case of forest wood chips and to 3.6 ± 0.5 m/s in the case of waste wood; T_S . . .steel temperature, T_{FG} . . .flue gas temperature.

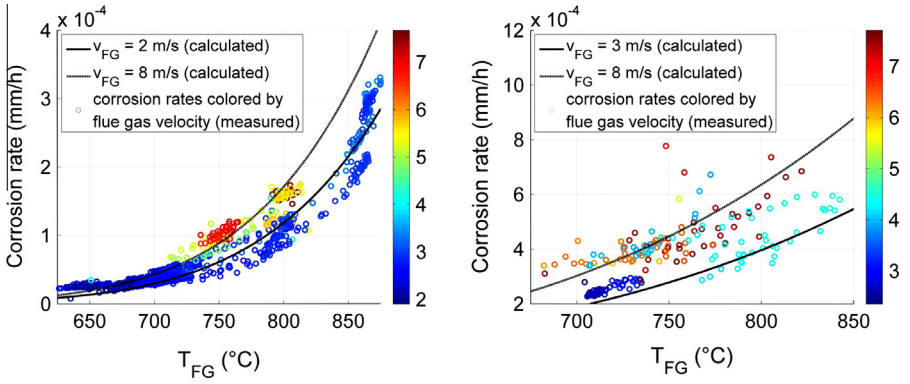

Fig. 10. Empirical model in comparison to measurement values for forest wood chips [25] (left) and for waste wood (right) as a function of the flues gas temperature for various flue gas velocities. *Explanation:* steel temperature has been kept constant to 480 ± 0.5 °C; T_{FG} . . .steel temperature, v_{FG} . . .flue gas velocity.

temperature (see Fig. 9, left). The trend of an increased corrosion attack with an increased flue gas velocity is shown in Fig. 10 on the left hand side.

An exponential dependence on the flue gas temperature could also be found in the case of the waste wood test campaign (see Fig. 8, right). But instead of an exponential increase with increasing steel temperatures the measured signal stagnates and even slightly decreases when reaching temperatures above 500 °C (see Fig. 9, right). The steel temperature variations have been performed at least two times and the trend shown could be reproduced. However, the measured signal is more scattered than those found within the forest wood chips test campaign. A plausible explanation for that could be given by the strong deviations of the waste wood composition during the test campaign (see Table 2). Therefore, only mean values and standard deviations over ±5 °C are shown in Fig. 8 (right) and Fig. 9 (right). Also in this case a dependence on the flue gas velocity could be found. The trend is shown in Fig. 10 on the right hand side.

The dependence on the flue gas velocity is moderate for both fuels. A precise determination of this dependence is difficult, since the scattering of the measured corrosion rate for constant flue gas and steel temperatures over the whole test campaign is of similar order. Nevertheless, the dependence on the flue gas velocity can be seen on the time curve of the measured data. An example of such a time curve for waste wood is shown in Fig. 11.

Based on the experimental data, an empirical function has been derived. The empirical model developed is a combination of an Arrhenius function which describes the dependence on the steel surface and the flue gas temperature and an additional linear factor

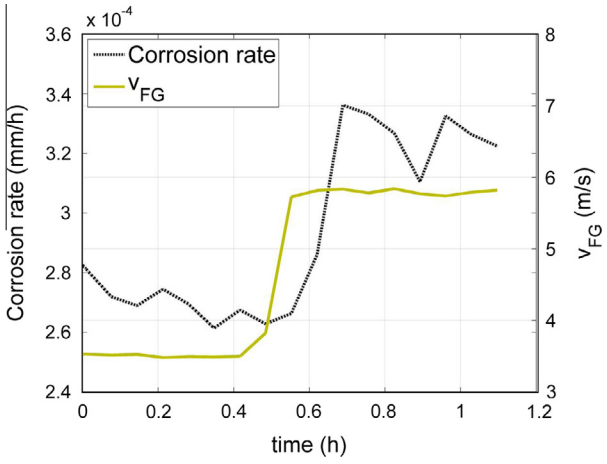

Fig. 11. Example of a time curve of the measured corrosion rate and flue gas velocity for waste wood. *Explanation:* steel temperature has been kept constant to 480 ± 0.5 °C; flue gas temperature has been kept constant to 755 ± 10 °C; v_{FG} . . .flue gas velocity.

which describes the dependence on the flue gas velocity. The coefficients of the empirical model (see Eq. 1) have been determined within a stepwise approach using a least square method. First the coefficients E_{activ} and A for each steel temperature and constant flue gas velocities have been optimized. Then the functional dependencies of these optimized parameters on the steel temperature

Table 4
Optimized coefficients of the empirical function.

Fuel	a_1	a_2	a_3	b_1	b_2	b_3	c_1	c_2
Forest wood chips	–	−0.083	73.9	–	982.0	−858364	0.07	0.81
Waste wood	0.00044	−0.707	287.4	−4.627	7375.8	−2994500	0.11	0.59

have been determined for constant flue gas velocities. In a last step, the dependence on the flue gas velocity is assumed to be a linear correction of the empirical function. Due to the moderate influence and the scattered data the linear dependence is a first but sufficient assumption.

The optimized coefficients are shown in Table 4. In Figs. 8–10 the calculated corrosion potential using Eq. (1) is plotted as solid lines. One can see that the optimized function correlates adequately with the measured data.

$$k = A(T_S) \cdot exp\left(\frac{E_{activ}(T_S)}{R \cdot T_{FG}}\right) \cdot \frac{C(v_{FG})}{1000} \quad (1)$$

$$A(T_S) = exp\left(a_1 \cdot T_S^2 + a_2 \cdot T_S + a_3\right)$$
$$E_{activ}(T_S) = b_1 \cdot T_S^2 + b_2 \cdot T_S + b_3$$
$$C(v_{FG}) = c_1 \cdot v_{FG} + c_2$$

with: k...corrosion rate (mm/h), $A(T_S)$ ...pre-exponential factor (mm/h), R ...gas constant (J/mol K), E_{activ} (T_S) ...activation energy (J/mol), T_{FG} ...flue gas temperature (K), T_S ...steel temperature (K), v_{FG} ...flue gas velocity (m/s), $C(v_{FG})$ linear correction factor and a_{1-3}, b_{1-3}, c_{1-2} ...coefficients.

The dependencies measured for forest wood chips are in good agreement with those found in real-scale CHP plants [17].

4.4. Corrosion mechanism

Many authors (e.g. [2,26]) reported a compact inner corrosion layer, consisting of $FeCl_2$, in the case of active Cl-induced oxidation (detailed mechanism can be found for example in [26]). In some cases an additional FeS or FeS_2 layer subsequent to the inner $FeCl_2$ layer is reported (e.g. [9,26]). In this work the EDX analyses confirm the presence of an iron sulphide layer, but due to the absence of chlorine in the deposition as well as in the corrosion layer, it is concluded that the main corrosion mechanism prevailing is not active Cl-induced oxidation. It is most likely that the condensed chlorine species in the initial state of the measurement campaigns (see Section 4.1.1) get sulphated and that the supply of chlorine species cannot be maintained due to increasing surface temperatures over time. Therefore, chlorine might be involved in the initial stage of the corrosion process, but no evidence for active Cl-induced oxidation can be found after ≈300 operating hours. Since the measured corrosion signal gained during the parameter variations was reproducible, it is concluded that chlorine has no or only a negligible effect on the corrosion rate throughout the time parameter variations have been performed.

In the case of the forest wood chips test campaign solid potassium sulphate is the main component of the deposit. Usually solid potassium sulphate has only a minor effect on the corrosion behaviour [1]. The only known mechanism involving sulphates is hot corrosion [1,2,27] which can be excluded as corrosion mechanism due to a missing molten sulphate layer. Since the chromium content of the steel 13CrMo4–5 is too low to form a protective chromium oxide layer (see Section 4.2), a corrosion mechanism involving the dissolution of such a layer (as proposed in e.g. [28]) can also be excluded. Therefore, it is suggested that the main corrosion mechanism in this case is the oxidation of the steel by oxygen in the flue gas. The formation of the iron sulphide layer can most likely be explained by the reaction of gaseous SO_2 with the steel or oxide layer [29].

The measured corrosion signals in the case of waste wood differ strongly from those of forest wood chips. For low temperatures ($T_S \leqslant 480$ °C, $T_{FG} \leqslant 700$ °C) the measured corrosive attack is much higher. This is in good agreement with the lower molar 2S/Cl ratio and the higher concentration of heavy metals (see Section 3) in the case of waste wood. This behaviour changes with increasing temperatures since the corrosion potential of waste wood does not show the exponential dependence on the steel temperature. Therefore, it is most likely that an additional or another mechanism is responsible for the corrosion behaviour found. A stagnating or even decreasing corrosion rate as a function of an increasing temperature is typically found in the case of hot corrosion type II (e.g. [30–32]). Thereby, depending on the temperature prevailing, the corrosion occurs by basic or acidic fluxing in a thin molten layer of alkali and heavy metal sulphates and/or chlorides. In general, the melting temperatures of Na_2SO_4, K_2SO_4 as well as mixtures of these sulphates are too high for melts to occur. Nevertheless, according to [33] eutectic mixtures with very low melting temperatures can be formed in the presence of heavy metal rich sulphates. Since the amount of Zn found in the deposits is considerable, the formation of a partly molten sulphate layer could be possible. This layer could be responsible for the corrosion behaviour found. This is also in agreement with lab-scale work of van Lith [34] in which the corrosion behaviour under conditions typically prevailing in waste wood fired boilers has been investigated. Within this work molten deposit layers were found at 500 °C.

5. Summary and conclusions

To investigate the high-temperature corrosion and deposit formation behaviour of superheater tube bundles, online corrosion probe and deposit probe measurements have been carried out in a specially designed fixed bed/drop tube reactor. The investigated boiler steel 13CrMo4–5 is commonly used as steel for superheater tubes in biomass fired heat and power plants. Forest wood chips and quality sorted waste wood (A1–A2 according to German standards) have been used as fuels to investigate the influence of different fuels on the deposit formation and corrosion behaviour. The reactor used allows an independent variation of a single parameter of interest. Therefore, the quality of the measured correlations between the corrosion probe signal and the influencing parameters exceeds those already published. The corrosion probe measurements show a clear dependence on the parameters flue gas temperature and velocity as well as steel temperature. Following, variations have been carried out to investigate the influence on the corrosion behaviour: flue gas temperature between 650 and 880 °C, steel temperature from 450 to 550 °C and flue gas velocity from 2 to 8 m/s. Based on the experimental data gained, an empirical function has been developed which is a combination of an Arrhenius function which describes the dependence on the flue gas and the steel temperature and a linear dependence on the flue gas velocity. This empirical function is able to reproduce the corrosion potential measured sufficiently accurate.

Therefore, the empirical model developed allows plant designers and operators a quick estimation if high-temperature corrosion is of relevance for a certain parameter setup or not, when using the

steel 13CrMo4–5 and comparable flue gas compositions within the parameter range investigated. Furthermore, the model is able to roughly estimate the local corrosion potential together with a CFD simulation of flow and heat transfer in a relatively short time and without detailed knowledge of the underlying chemical processes. It can be used by boiler manufacturers as a helpful tool in the design phase of a plant.

For forest wood chips an exponential dependence on the flue gas as well as on the steel temperature was found. This is in good agreement with long-term corrosion measurements performed in a large-scale biomass grate combustion plant [17]. Analyses of the deposits formed on the probe as well as subsequent SEM/EDX investigations of the corrosion probe rings show that the deposit layer mainly consists of potassium sulphate. Furthermore, no chlorine could be found neither in the deposit layer nor at the corrosion front. Therefore, it is suggested that the main corrosion mechanism prevailing is the oxidation of the steel by oxygen in the flue gas.

The corrosion probe signals obtained for waste wood show a different behaviour. Here, the measured corrosive attack does not increase exponentially with the increasing steel temperature. Also in this case no chlorine could be found in the deposit layer or at the corrosion front. The temperature behaviour found is typical for hot corrosion type II. Since the content of Zn in the deposit is clearly enriched compared to forest wood chips, the formation of a low melting eutectic is possible. This is also in agreement with the sintered deposit layer found on the corrosion probe.

Acknowledgments

The financial support by the Austrian Ministry for Transport, Innovation and Technology (BMVIT) (programme: ModSim: project number: 828703) as well as of the companies BIOS BIOENERGIESYSTEME GmbH, KWB Kraft und Wärme aus Biomasse GesmbH, POLYTECHNIK Luft- und Feuerungstechnik GmbH and Josef Bertsch GmbH & Co. is gratefully acknowledged. The online corrosion probe measurements were performed in cooperation with CORRMORAN GmbH, Germany.

References

[1] Antunes RA, de Oliveira MCL. Corrosion in biomass combustion: a materials selection analysis and its interaction with corrosion mechanisms and mitigation strategies. Corrosion Sci 2013;76:6–26.
[2] Nielsen HP, Frandsen FJ, Dam-Johansen K, Baxter LL. The implications of chlorine-associated corrosion on the operation of biomass-fired boilers. Progr Energy Combust Sci 2000;26:283–98.
[3] Frandsen FJ. Utilizing biomass and waste for power production – a decade of contributing to the understanding, interpretation and analyses of deposits and corrosion products. Fuel 2005;84:1277–94.
[4] Obernberger I, Brunner T. Depositionen und Korrosion in Biomassefeuerungen. Tagungsband zur VDI-Fachkonferenz: Beläge und Korrosion in Großfeuerungsanlagen, Göttingen, Germany, 2004. Düsseldorf, Germany: VDI-Wissensforum GmbH; 2004.
[5] Montgomery M, Jensen SA, Borg U, Biede O, Vilhelmsen T. Experiences with high temperature corrosion at straw-firing power plants in Denmark. Mater Corrosion 2011;62:593–605.
[6] Hansen L, Nielsen H, Frandsen F, Dam-Johansen K, Karlsson A. Influence of deposit formation on corrosion at a strawfired boiler. Fuel Process Technol 2000;64:189–209.
[7] Schroer C, Konys J. Rauchgasseitige Hochtemperatur-Korrosion in Müllverbrennungsanlagen – Ergebnisse und Bewertung einer Literaturrecherche. Wissenschaftliche Berichte FZKA 6695. Forschungszentrum Karlsruhe GmbH, Karlsruhe, Germany; 2002.
[8] Maisch S. Identifikation und Quantifizierung von Korrosionsrelevanten Parametern in Müllverbrennungsanlagen mittels Charakterisierung der deponierten Partikel und elektrochemischer Online-Messungen. PhD thesis, University of Augsburg, Augsburg, Germany; 2011.
[9] Waldmann B. Korrosion in Anlagen zur thermischen Abfallverwertung: Elektrochemische Korrosionserfassung und Modellbildung. PhD thesis, University of Augsburg, Augsburg, Germany; 2007.
[10] Henderson P, Szakalos P, Pettersson R, Andersson C, Hogberg J. Reducing superheater corrosion in wood-fired boilers. Mater Corrosion 2006;57:128–34.
[11] Nafari A, Nylund A. Field study on superheater tubes in the loop seal of a wood fired CFB plan. Mater Corrosion 2004;55:909–20.
[12] Li YS, Spiegel M, Shimada S. Corrosion behaviour of various model alloys with NaCl–KCl coating. Mater Chem Phys 2005;93:217–23.
[13] Grabke HJ, Reese E, Spiegel M. The effects of chlorides, hydrogen chloride, and sulfur dioxide in the oxidation of steels below deposits. Corrosion Sci 1995;37:1023–43.
[14] Lehmusto J, Lindberg D, Yrjas P, Skrifvars BJ, Hupa M. The role of potassium in high temperature corrosion of superheater steels. In: Proceedings: impacts of fuel quality on power production and environment, Puchberg, Austria, September 23–27, 2012. Palo Alto, CA: Electric Power Research Institute (EPRI); 2013.
[15] Uusitalo MA, Vuoristo PMJ, Mäntylä TA. High temperature corrosion of coatings and boiler steels below chlorine-containing salt deposits. Corrosion Sci 2004;46:1311–31.
[16] Haider F, Horn S, Waldmann B, Warnecke R. Quantifizierung des Korrosionsdiagramms auf der Basis von Messungen mit der Augsburger Korrosionssonde. Tagungsband zur VDI-Fachkonferenz: Beläge und Korrosion in Großfeuerungsanlagen, Oberhausen, Germany, 2008. Düsseldorf, Germany: VDI-Wissensforum GmbH; 2008.
[17] Retschitzegger S, Brunner T, Obernberger I, Waldmann B. Assessment of online corrosion measurements in combination with fuel analyses and aerosol and deposit measurements in a biomass combined heat and power plant. Energy Fuels 2013;27:5670–83.
[18] Kawahara Y. Evaluation of high-temperature corrosion life using temperature gradient corrosion test with thermal cycle component in waste combustion environments. Mater Corrosion 2006;57:60–73.
[19] Maisch S, Warnecke R, Waldmann B, Haider R, Horn S. Validierung des Korrosionsdiagramms und Einfluss der Strömung auf die Korrosionssgeschwindigkeit. Tagungsband zur VDI-Fachkonferenz: Beläge und Korrosion in Großfeuerungsanlagen, Stuttgart, Germany, 2009. Düsseldorf, Germany: VDI-Wissensforum GmbH; 2009.
[20] Maisch S, Waldmann B, Warnecke R, Haider R, Horn S. Quantifizierte Korrosionsgeschwindigkeit in Abhängigkeit der Rohrwand- und Rauchgastemperatur. Tagungsband zur VDI-Fachkonferenz: Beläge und Korrosion in Großfeuerungsanlagen, Frankfurt, Germany, 2010. Düsseldorf, Germany: VDI-Wissensforum GmbH; 2010.
[21] Sommersacher P, Brunner T, Obernberger I. Fuel indexes: a novel method for the evaluation of relevant combustion properties of new biomass fuels. Energy Fuels 2012;26:380–90.
[22] Horn S, Haider F, Waldmann B, Warnecke R. Quantifizierte Betrachtung des Stoffbergangs in Belgen und Korrosionsschichten zur Beschreibung der Korrosionsgeschwindigkeit. Tagungsband zur VDI-Fachkonferenz: Beläge und Korrosion in Großfeuerungsanlagen, Oberhausen, Germany, 2008. Düsseldorf, Germany: VDI-Wissensforum GmbH; 2008.
[23] Deuerling C, Waldmann B. Innovative Messtechnik zur kombinierten Korrosions- und Materialforschung im Kraftwerksbereich. In: Proceedings of the 43. Kraftwerkstechnisches Kolloquium, Dresden, Germany, 2011.
[24] Gellings PJ, Tostmann KH. Korrosion und Korrosionsschutz von Metallen: eine Einführung. Carl Hanser Verlag, München, Germany; 1981. ISBN: 3-446-12594-9.
[25] Gruber T, Scharler R, Obernberger I. Application of an empirical model in CFD simulations to predict the local high temperature corrosion potential in biomass fired boilers. In: Proceedings 22nd European biomass conference and exhibition, Hamburg, Germany, June 2014. ISBN: 978-88-89407-52-3; 2014. p. 402–8, ETA Florence (Ed.), Italy.
[26] Reichel H, Schirmer U. Waste incineration plants in the FRG: construction, materials, investigation on cases of corrosion. Mater Corrosion 1989;40:135–41.
[27] Cutler AJB, Raask E. External corrosion in coal fired boilers: assessment from laboratory data. Corrosion Sci 1981;21:789–800.
[28] Pettersson J, Asteman H, Svensson JE, Johansson LG. KCl induced corrosion of a 304-type austenitic stainless steel at 600 °C; the role of potassium. Oxidat Metals 2005;64:23–41.
[29] Gesmundo F, Young DJ, Roy SK. The high temperature corrosion of metals in sulfidizing–oxidizing environments: a critical review. High Temperat Mater Processes 1989;8:149–89.
[30] Sudhangshu B. High-temperature corrosion. Burlington (USA): Butterworth-Heinemann; 2007. ISBN: 978-0-7506-8252-7.
[31] Rapp RA. Hot corrosion of materials: a fluxing mechanism? Corrosion Sci 2002;44:209–21.
[32] Zhang Y, Wu W. Summary of studies on hot corrosion of iron-based alloys by sodium sulfate in $O_2/SO_2/SO_3$ environment. J Phys IV 1993;3:319–25.
[33] Spiegel M. Salt melt induced corrosion of metallic materials in waste incineration plants. Mater Corrosion 1999;50:373–93.
[34] van Lith S, Buchardt C, Frandsen FJ. Final report (D20) for SES6-CT-2003-502679: ash and aerosol related problems in biomass combustion and co-firing (BIOASH), task 2.3: lab-scale investigation of the potential for corrosion of deposits. CHEC Research Centre, Technical University of Denmark, Denmark; 2007.

Paper II

Available online at www.sciencedirect.com

ScienceDirect

http://www.elsevier.com/locate/biombioe

Application of an empirical model in CFD simulations to predict the local high temperature corrosion potential in biomass fired boilers

Thomas Gruber [a,*], Robert Scharler [a,b,c], Ingwald Obernberger [b,c]

[a] BIOENERGY 2020+ GmbH, Inffeldgasse 21b, 8010 Graz, Austria
[b] Institute for Process and Particle Engineering, Graz University of Technology, Inffeldgasse 13, 8010 Graz, Austria
[c] Bios Bioenergiesysteme GmbH, Inffeldgasse 21b, 8010 Graz, Austria

ARTICLE INFO

Article history:
Received 17 July 2014
Received in revised form
19 February 2015
Accepted 20 February 2015
Available online 18 March 2015

Keywords:
Biomass combustion
Combined heat and power generation (CHP)
Corrosion
Model
Wood chips

ABSTRACT

To gain reliable data for the development of an empirical model for the prediction of the local high temperature corrosion potential in biomass fired boilers, online corrosion probe measurements have been carried out. The measurements have been performed in a specially designed fixed bed/drop tube reactor in order to simulate a superheater boiler tube under well-controlled conditions. The investigated boiler steel 13CrMo4-5 is commonly used as steel for superheater tube bundles in biomass fired boilers. Within the test runs the flue gas temperature at the corrosion probe has been varied between 625 °C and 880 °C, while the steel temperature has been varied between 450 °C and 550 °C to simulate typical current and future live steam temperatures of biomass fired steam boilers. To investigate the dependence on the flue gas velocity, variations from 2 $m \cdot s^{-1}$ to 8 $m \cdot s^{-1}$ have been considered. The empirical model developed fits the measured data sufficiently well. Therefore, the model has been applied within a Computational Fluid Dynamics (CFD) simulation of flue gas flow and heat transfer to estimate the local corrosion potential of a wood chips fired 38 MW steam boiler. Additionally to the actual state analysis two further simulations have been carried out to investigate the influence of enhanced steam temperatures and a change of the flow direction of the final superheater tube bundle from parallel to counter-flow on the local corrosion potential.

1. Introduction

High temperature corrosion processes have a strong influence on the operation of biomass fired boilers and result in unscheduled outages and reduced economic efficiencies. Still, the high temperature corrosion of superheaters in biomass combustion plants is insufficiently explored so far. A wide range of experimental data exists, where the effect of deposits of certain species, such as NaCl or KCl or the influence of single parameters such as flue gas temperature or steel temperature has been investigated (e.g. Refs. [1–5]). These experiments are not sufficient to describe the high temperature corrosion processes in real-scale plants accurately, due to the interaction and the high complexity of the processes involved. High temperature corrosion in real scale biomass fired plants

* *Corresponding author*. Tel.: +43 0 316 873 9228; fax: +43 0 316 873 9202.
E-mail address: thomas.gruber@bioenergy2020.eu (T. Gruber).
http://dx.doi.org/10.1016/j.biombioe.2015.02.024
0961-9534/

has been investigated by several authors (e.g. Refs. [6–9]). Measurements in real scale plants generally have the drawback that it is not possible to vary parameters of interest arbitrarily. For these reasons no experimental data are available so far which are sufficient to develop a reliable simulation tool to calculate the local corrosion potential in biomass fired plants.

2. Objectives

The aim of the work presented is the application of a newly developed empirical model [10] together with a CFD simulation of flow and heat transfer to calculate the local high temperature corrosion potential in a biomass fired steam boiler. In addition to the actual state analysis the influences of enhanced steam temperatures as well as a change of the flow direction of the final superheater tube bundle from parallel to counter-flow on the local corrosion potential is investigated within this work.

3. Methodology

To enhance the readability of the work the basic principles of the experimental approach as well as the model development already presented in Ref. [10] are summarized in the sections 3.1–3.4 as detailed as necessary.

3.1. *Combined biomass fired packed bed/electrically heated drop tube reactor*

The experiments have been carried out using a combined packed bed/drop tube reactor, with which well-defined conditions regarding flue gas temperature and composition, typically prevailing in biomass fired boilers, can be achieved. A schematic view of the reactor can be found in Fig. 1. The setup applied consists of a packed bed reactor (biomass grate furnace with air staging and flue gas recirculation), an upper transition part to a successively heated vertical tube with isothermal conditions (the so-called drop tube). The drop tube has an electrical input power of 60 kW and allows the control of the flue gas temperature between 625 °C and 900 °C. The power input of the drop tube allows a compensation of the fluctuation of the grate furnace operation and, therefore, to achieve constant and adjustable flue gas temperatures in front of the corrosion probe. The drop tube has a length, which is sufficient to get a fully developed flow at the entrance to the measurement port, which is equipped with the corrosion probe. Therefore, the reactor enables corrosion measurements under defined flow and temperature conditions with a flue gas composition typical for fixed bed combustion systems. Finally, the flue gas is transferred via a lower transitional part to a water cooled heat exchanger before it enters the chimney. A detailed description of the setup used can be found in Ref. [10].

The experimental setup allows variations of the parameters of interest independently from each other. The flue gas temperature is varied by the electrical heating of the drop tube, the flue gas velocity is varied by the furnace load conditions, whereas the steel temperature is varied by the air cooling of the probe.

3.2. *Online corrosion probe measurement*

The online corrosion probe measurement technique applied within the test runs was developed and provided by Corrmoran GmbH, Augsburg, Germany. It is especially designed to simulate the high temperature corrosion occurring on superheater tubes. The corrosion probe is inserted into the flue gas at the measuring port below the electrically heated drop tube. It consists of a temperature controlled sensor placed on the top of an air cooled carrier lance. When exposed to the flue gas, a layer consisting of deposits and corrosion products is formed on the sensor surface. This layer represents an electrolyte and allows the measurement of a linear polarization resistance, which is proportional to the instantaneous corrosion rate. The factor describing the relation between the linear polarization resistance and the corrosion rate is determined subsequently to the test run by a gravimetric measurement of a mass loss ring. A detailed description of the probe can be found in Refs. [11] and [12].

The corrosion probe used has already been successfully applied in waste incinerators [11,13] as well as biomass fired boilers [12].

It should be mentioned that the corrosion rates measured within this work give only qualitative information about the corrosion potential in dependence of relevant operating parameters. High temperature corrosion is a strongly time-dependent process which often follows a parabolic or para-linear trend [14]. Therefore, the corrosion rates gained within short-term measurements generally differ from those found within long-term measurements. Nevertheless, short-term online corrosion measurements still allow the investigation of the dependence on a certain parameter.

3.3. *Corrosion probe test campaign*

The fuel used in the test campaign was chemically untreated forest wood chips mainly consisting of spruce (lat. *picea abies*). The biomass mostly consists of logging residues, but also contains stem wood and bark as well as a low fraction of needles and fine particles. A photo of the fuel is given in Fig. 2. The fuel was taken from the storage of the biomass combined heat and power plant Baden (Lower Austria, Austria), which uses biomass harvested in the forests in a radius of approximately 50 km around Baden. Before the wood chips could be used in the coupled fixed bed/drop tube reactor, descripted in Section 3.1, the particle size had to be reduced by chopping from $P63^{c}$ to $P45A^{c}$ according to EN 14961-1:2010. The resized wood chips were stored for 1–7 weeks, depending on their time of usage, in several 1 m^3 plastic big bags before they were fired in the biomass reactor. The wood chips used within the test campaign had following specifications according to EN 14961-1:2010: origin … 1.1.4.4 and 1.1.4.5 (logging residues), particle … $P45A^{C}$, moisture … M25, ash … A3.0, bulk density … BD200. The chemical composition of the wood chips can be found in Table 1. The three samples for the fuel analyses have been taken at different times over the whole test campaign from the fuel storage of the biomass reactor.

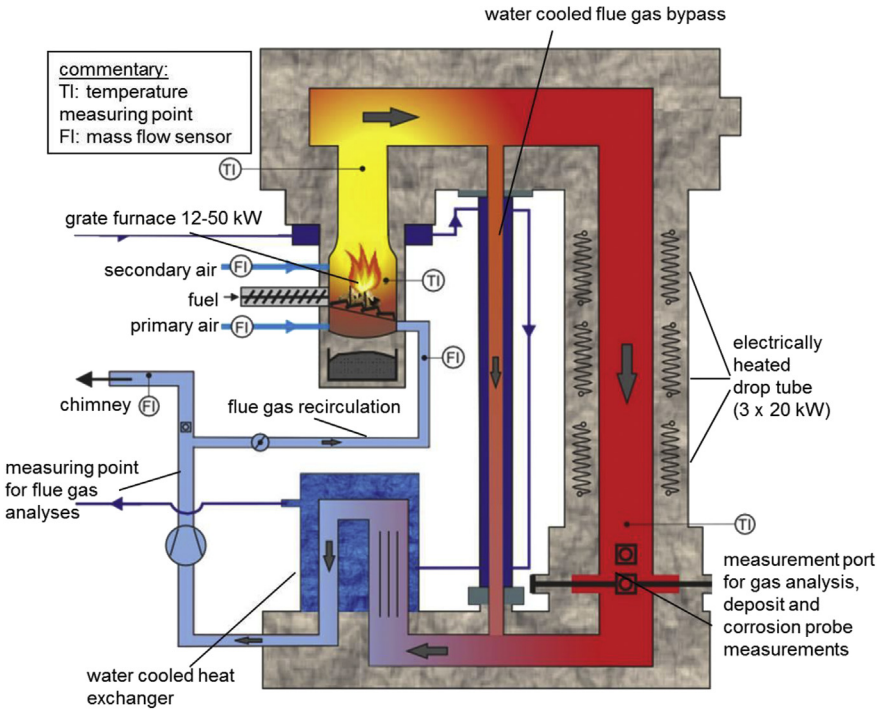

Fig. 1 – Schematic view of the combined packed bed/drop tube reactor with relevant units and measurement ports [10].

A detailed description of the test campaign methodology and boundary conditions can be found in Ref. [10]. Nevertheless, the most important parameters are listed in Tables 2 and 3.

The investigated boiler steel 13CrMo4-5 is commonly used as steel for superheater tubes in biomass fired heat and power plants. The operating duration of the biomass reactor was 325 h. After a startup time which was used to achieve a reproducible signal, the parameter variations listed in Table 2 have been performed.

Fig. 2 – Picture of the biomass fuel used for the test runs.

3.4. *Model development*

Origin of the model development was a sensitivity analysis of relevant influencing parameters. Based on this analysis, the parameters of the model function (see section 4.2) were

Table 1 – Chemical composition of the fuel investigated. Explanation: mean … mean value, std-dev … standard deviation, w.b. … wet basis, d.b. … dry basis; number of samples = 3; the concentrations of the elements C, H and N have only been determined from one representative sample.

	Mean	Std-dev	Unit
Moisture content	0.241	0.036	Mass fraction w.b.
Ash content	0.024	0.007	Mass fraction d.b.
C	0.481	–	Mass fraction d.b.
H	0.059	–	Mass fraction d.b.
N	0.003	–	Mass fraction d.b.
S	280	8	$mg \cdot kg^{-1}$ d.b.
Cl	90	18	$mg \cdot kg^{-1}$ d.b.
Si	2122	1382	$mg \cdot kg^{-1}$ d.b.
Ca	6045	998	$mg \cdot kg^{-1}$ d.b.
Mg	739	369	$mg \cdot kg^{-1}$ d.b.
K	1660	147	$mg \cdot kg^{-1}$ d.b.
Na	63	15	$mg \cdot kg^{-1}$ d.b.
P	204	18	$mg \cdot kg^{-1}$ d.b.
Al	446	171	$mg \cdot kg^{-1}$ d.b.
Fe	265	77	$mg \cdot kg^{-1}$ d.b.
Mn	108	54	$mg \cdot kg^{-1}$ d.b.
Zn	19	1	$mg \cdot kg^{-1}$ d.b.
Pb	1	0	$mg \cdot kg^{-1}$ d.b.
Molar 2S/Cl ratio	6.9	0.6	$mol \cdot mol^{-1}$

Table 2 – Range of parameter variations performed.

	Unit	Min	Max
Steel temperature	°C	450	550
Flue gas temperature	°C	625	880
Flue gas velocity	$m \cdot s^{-1}$	2	8

determined by a stepwise minimization of the quadratic errors for all influencing parameters.

3.5. CFD models used and heat exchanger model

Following models have been used in the CFD simulation: Realizable k-ε model with enhanced wall functions (turbulence) and the Discrete Ordinates model (radiation).

In the last decade the computational performance strongly increased. A detailed CFD simulation of the convective boiler section with a resolution of the heat exchanger tubes is still impossible within a reasonable time due to the large variations of geometric length scales and transient flow phenomena like vortex shedding behind tubes. Therefore, a finite cell based convective heat exchanger model has been developed by BIOS BIOENERGIESYSTEME GmbH, Graz, Austria in order to investigate the whole boiler by means of CFD simulations. A detailed description of the model can be found in Ref. [15].

The heat exchanger model was applied in order to calculate the flow as well as the convective and radiant heat transfer in the superheater tube banks. The calculation of the source terms for momentum and energy transport equations is based on literature data [16–18]. These data are available for tube banks of staggered and in-line arrangement and flow perpendicular to the individual tube rows. Transient 2D simulations were performed to calculate the flow resistance for flow directions other than the literature values. Thus, the dependence of flow resistance on the flow angle within a tube bank can correctly be accounted for [15].

For these reasons the heat exchanger model is well suited to calculate the heat transfer in heat exchangers passed through by flue gas with an inhomogeneous flow field.

3.6. Case study description

To test and verify the model developed, it has been applied for a CFD simulation of flow and heat transfer in a 42 MW_{th} wood chips fired CHP plant. The high temperature corrosion potential on the superheater bundles has been calculated for three different cases:

- **CS1**: Actual state analysis under full load conditions (live steam temperature of 453 °C)
- **CS2**: A switch of the flow direction of the final superheater bundle from parallel to counter-flow (live steam temperature of 453 °C)
- **CS3**: Enhanced live steam temperature of 480 °C

Table 4 – Relevant boiler information.

Fuel power input related to NCV	41.9	MW
Boiler output	37.8	MW
Flue gas mass flow	35.6	$kg \cdot s^{-1}$
Saturated steam temperature	279	°C
Saturated steam pressure	6300	kPa
Live steam temperature	453	°C
Live steam pressure	6100	kPa

Table 4 provides the most relevant operating conditions of the boiler; whereas Table 5 provides relevant information regarding the superheater tube bundles.

The steel 16Mo3 used for the superheaters of the plant is a low alloy heat resisting steel like 13CrMo4-5 with a low Cr and Ni content and, therefore, should show a comparable corrosion behavior.

The simulation has been performed within a two-step approach. First, the flue gas flow and heat transfer of the boiler was simulated. Afterwards, the local corrosion behavior was evaluated in a post-processing step.

The boundary conditions (e.g. flue gas temperature and composition) at the entrance of the simulation domain were taken from mass and energy balances under the assumption of complete combustion provided by the plant manufacturer.

To achieve a fully developed flow-field at the entrance to the convective boiler section, the upper part of the furnace was included in the simulation. Hence, the simulation considers the composition of a chemically not reacting flue gas typical for biomass furnaces firing wood chips.

Furthermore, a linear increase of the steam temperature within the superheater tube bundles was assumed.

The heat loss over the finned tube walls is calculated by the saturated steam temperature and the mean heat transfer coefficient on the water side as boundary conditions.

To consider the reduced heat transfer due to ash deposits on the tubes a thermal resistance of 2 $m^2\,K \cdot kW^{-1}$ is assumed (low fouling rate) on the finned tube walls and the superheater tube walls.

Fig. 3 illustrates the different sections of the biomass CHP plant considered in the CFD case study. The simulation domain comprises the upper part of the furnace section, the radiative boiler section (including the two evaporator tube grids ET1 and ET2), the transition to the convective section,

Table 3 – Flue gas composition during the online corrosion probe measurements. Explanation: mean … mean value over the balancing time, std-dev … standard deviation over the balancing time.

	Mean	Std-dev	Unit
CO_2	11.1	0.9	Vol.-% dry flue gas
O_2	9.5	0.9	Vol.-% dry flue gas
CO	13.8	0.7	$mg \cdot m^{-3}$ (at 0 °C and 101 325 Pa, dry flue gas, 13 Vol.-% O_2)
SO_2	8.6	2.8	$mg \cdot m^{-3}$ (at 0 °C and 101 325 Pa, dry flue gas, 13 Vol.-% O_2)
HCl	6.6	3.8	$mg \cdot m^{-3}$ (at 0 °C and 101,325 Pa, dry flue gas, 13 Vol.-% O_2)

Table 5 – Relevant boundary conditions for the superheater tubes. Explanation: SH1–SH3 … superheater tube bundle 1–3, ccf … cross counter flow, cpf … cross parallel flow.

		SH1	SH2	SH3
Type	–	Bank of in-line tubes		
Operating mode	–	ccf	ccf	cpf
Outer tube diameter	mm	38	38	38
Tube wall thickness	mm	4	4	4
Tube wall material	–	16Mo3	16Mo3	16Mo3
Heating surface	m^2	396	396	198

the ash hopper as well as the convective section with the three superheaters SH1 to SH3.

4. Result and discussion

4.1. *Selected results of corrosion probe measurements*

The online corrosion measurements for the fuel forest wood chips showed an exponential dependence on the flue gas temperature as well as on the steel temperature (see Figs. 4 and 5). This result is in good agreement with long-term corrosion probe measurements performed at a CHP plant fired with forest wood chips [12]. Furthermore, a weaker, linear dependence could be found on the flue gas velocity (see Fig. 6). The experimental data were recorded over a period of several days and were well reproducible. Due to these facts, these short-term corrosion measurements at the test rig seem well applicable to develop an empirical function, which can be used to calculate the local high temperature corrosion potential of real-scale biomass firing plants. A more detailed description of these results can be found in Ref. [10].

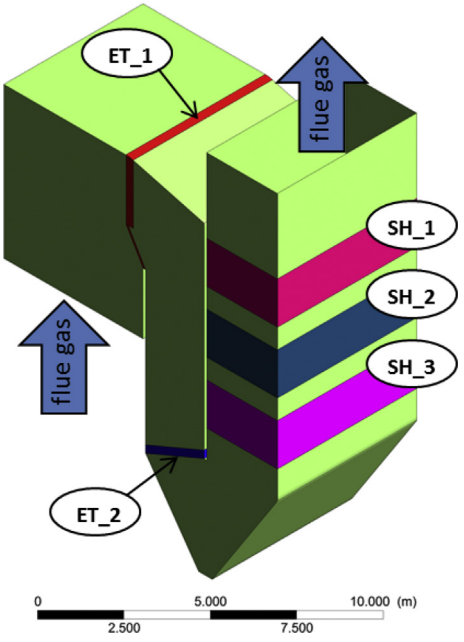

Fig. 3 – Schematic view of the simulated CHP plant. Explanation: ET_1 … upper evaporator tube grid, ET_2 … lower evaporator tube grid, SH_1 to SH_3 … superheater tube bundles 1 to 3.

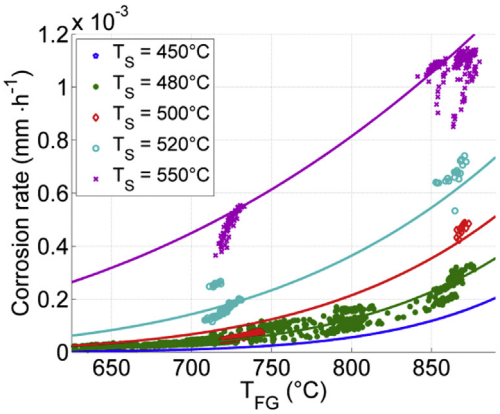

Fig. 4 – Plot of the measured corrosion rates (markers) and the empirical function developed (lines) as a function of the flue gas temperature for several steel temperatures [10]. Explanation: T_S … steel temperature; T_{FG} … flue gas temperature; the flue gas velocity has been kept constant to 2.8 ± 0.5 m·s^{-1}.

4.2. *Empirical corrosion model*

The model developed consists of an Arrhenius function, which describes the dependence on the flue gas and steel temperature, the influence of the flue gas velocity is taken into account by a linear function. The quality of the empirical model is shown in Figs. 4–6, where the measured data are compared with the function developed. The optimized coefficients of the empirical function are listed in Table 6.

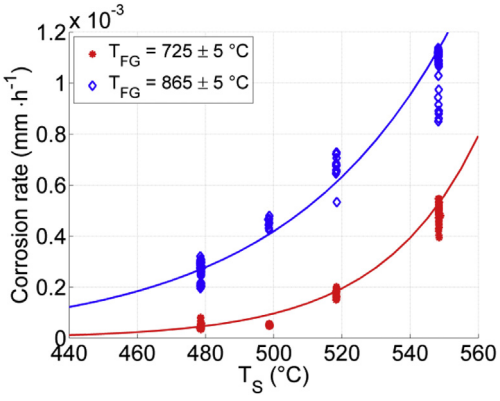

Fig. 5 – Plot of the measured corrosion rates (markers) and the empirical function developed (lines) as a function of the steel temperatures for several flue gas temperatures [10]. Explanation: T_{FG} … flue gas temperature; T_S … steel temperature; the flue gas velocity has been kept constant to 2.8 ± 0.5 m·s^{-1}.

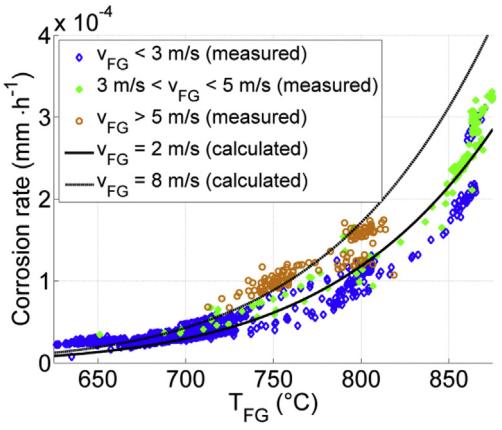

Fig. 6 – Trend of measured corrosion rates as a function of flue gas velocity and temperature (markers) in comparison to the values of the empirical function (lines) developed [10]. Explanation: v_{FG} … flue gas velocity; T_{FG} … flue gas temperature; the steel temperature has been kept constant at 480 ± 0.5 °C.

$$CorrRate = A(T_S)\cdot\exp\left(\frac{B(T_S)}{R\cdot T_{FG}}\right)\cdot\frac{C(v_{FG})}{1000} \quad (1)$$

$$A(T_S) = \exp(a_1\cdot T_S + a_2) \quad (2)$$

$$B(T_S) = b_1\cdot T_S + b_2 \quad (3)$$

$$C(v_{FG}) = c_1\cdot v_{FG} + c_2 \quad (4)$$

with: CorrRate … corrosion rate (mm·h^{-1}), $A(T_S)$ … max. corrosion rate (mm·h^{-1}), $B(T_S)$ … activation energy (J·mol^{-1}), T_{FG} … flue gas temperature (K), T_S … steel temperature (K), v_{FG} … flue gas velocity (m·s^{-1}), R … gas constant (J·mol^{-1}·K^{-1}), a_{1-2},b_{1-2},c_{1-2} … coefficients.

4.3. *Application range of the empirical model*

Generally, the empirical function developed is valid within the parameter range of the corrosion probe measurements (see Table 2) and can be applied for comparable corrosion mechanisms.

As discussed in detail in Ref. [10] no chlorine or traces of a molten layer could be found neither in the deposit nor the corrosion layer of the corrosion probe by means of SEM/EDX analyses. Therefore, it is suggested that the main corrosion mechanism prevailing is the oxidation of the low alloy steel by molecular oxygen.

Hence, for other corrosion mechanisms such as active Cl induced oxidation or corrosion by molten sulfates, the model is not validated.

Table 6 – Optimized coefficients of the empirical model [10].

a_1	a_2	b_1	b_2	c_1	c_2
−0.083	73.9	982	−858,364	0.07	0.81

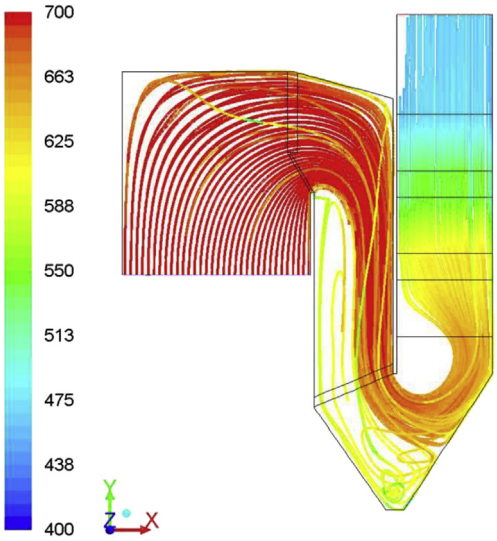

Fig. 7 – Streamlines of the flue gas colored by the temperature (°C) in the symmetry plan of the simulated plant (case CS1).

4.4. *Results of the CFD simulations of flow and heat transfer*

Since the calculated flow fields of CS2 and CS3 are qualitatively similar to the one of CS1 only results of CS1 are presented within this work.

The calculated flue gas path lines colored by the flue gas temperature for full load conditions are shown in Fig. 7, whereas the calculated flue gas velocities are presented in Fig. 8. The linearly increasing steam temperatures in the superheater bundles (boundary conditions) are presented in Fig. 9.

One can see that the flue gas passes along the right boiler wall of the superheater duct. Therefore, superheater 3 is not

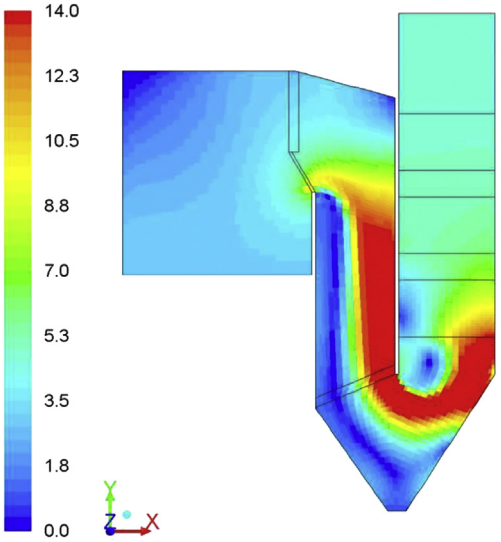

Fig. 8 – Flue gas velocity (m·s^{-1}) in the symmetry plan of the simulated plant (case CS1).

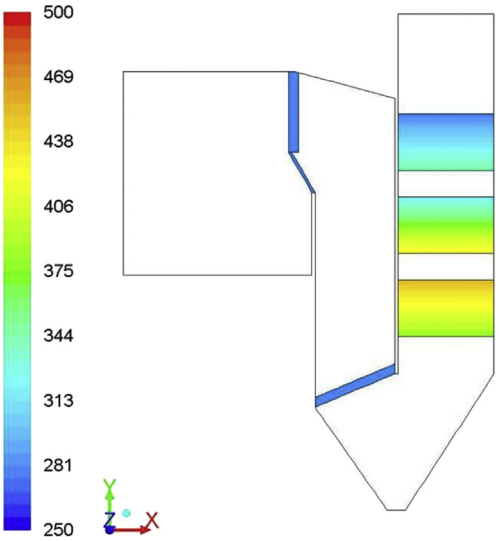

Fig. 9 – Plot of the linearly increasing steam temperatures (°C) in the symmetry plan of the simulated plant (case CS1).

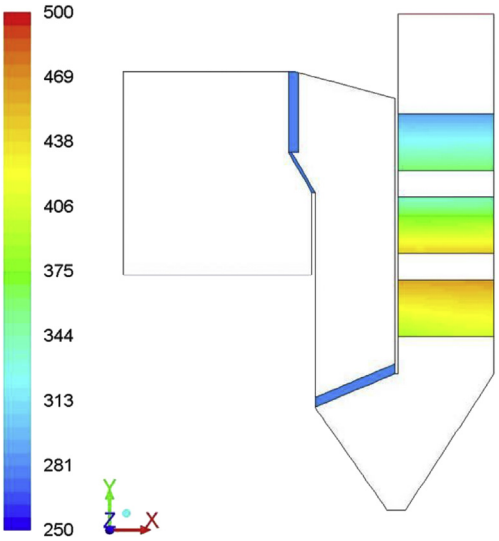

Fig. 11 – Steel temperature (°C) of the heat exchangers in the symmetry plan of the simulated plant (case CS1).

equally passed through by the flue gas. This leads to enhanced flue gas velocities and flue gas temperatures on the right side of the tube bundle and therefore, locally enhanced heat transfer coefficients on the flue gas side (see Fig. 10). Furthermore, it can be seen that superheater 3 homogenizes the flow distribution over the cross-section before the flue gas enters the superheater bundle 2.

The empirical model developed strongly depends on the local steel temperature. To calculate the local steel temperatures, the heat exchanger model uses the local values of steam temperature, local heat flux and the heat transfer coefficient on the flue gas side. Therefore, the calculated steel temperatures in this work take the effects of an inhomogeneous flow field into account. The calculated steel temperatures of the heat exchangers are shown in Fig. 11.

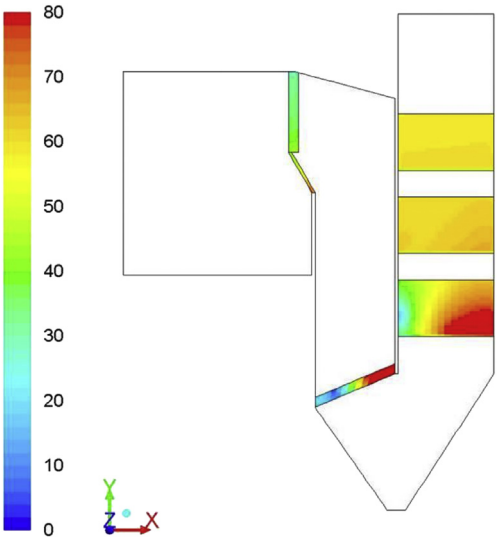

Fig. 10 – Heat transfer coefficient ($W \cdot m^{-2} \cdot K^{-1}$) on the flue gas side in the symmetry plan of the simulated plant (case CS1).

To investigate the influence of an inhomogeneous flow field on the convective heat transfer and the pressure loss over the superheater tube bundles the results of the CFD simulation for CS1 have been compared with calculations according to the VDI heat atlas [17] Gg1 (heat transfer) and IDELCHIK - Handbook of hydraulic resistance [16] p.752 (pressure loss). The results of this comparison are shown in Tables 7–9.

Due to the homogenous flow field in the superheater tube bundles 1 and 2 the calculated pressure losses according to the CFD simulation and the empirical calculation are in good agreement. For the bundles 1 and 2 there are deviations regarding the amount of transferred heat by convection, due to effects of the radiation, which is not considered in the empirical correlation. In case of the final superheater (SH3), the results concerning pressure loss and heat transfer differ considerably, since the velocity and temperature gradient predicted with the CFD simulation cannot be considered by the empirical correlations, which assume a homogenous flow through the bundle.

4.5. *Application of the empirical high temperature corrosion model*

The model has been applied in a post-processing step based on the already calculated temperature and flow profile of the CFD simulation.

Table 7 – Comparison of the transferred heat by convection and the pressure loss according to the CFD simulation and the calculations based on [16] and [17] for SH1.

	Unit	CFD	Calculations
Flue gas temperature SH entry	°C	536	536
Flue gas temperature SH exit	°C	469	463
Mean surface temperature	°C	366	366
Transferred heat by convection	kW	3035	3205
Pressure loss	Pa	44	46

Table 8 – Comparison of the transferred heat by convection and the pressure loss according to the CFD simulation and the calculations based on [16] and [17] for SH2.

	Unit	CFD	Calculations
Flue gas temperature SH entry	°C	610	610
Flue gas temperature SH exit	°C	541	536
Mean surface temperature	°C	442	442
Transferred heat by convection	kW	3087	3296
Pressure loss	Pa	50	51

The CFD simulations of flow and heat transfer show that flue gas temperatures as well as the steel temperatures in the superheater tube bundles 1 and 2 are below the application range of the empirical model. Therefore, the empirical model is only applied to calculate the local corrosion potential for the final superheater.

The calculated local corrosion potentials for the three different cases can be found in Figs. 12–14. Since already very small leaks of the superheater tubes lead to a shut-down of the boiler, the maximum values of the calculated corrosion potentials of the final superheater are compared in Table 10.

The sensitivity study shows that a switch of the flow direction of the final superheater from parallel to counter-flow increases the maximum of the corrosion potential by a factor of 3.4. This result can be explained by the combination of the highest surface temperature with an increased flue gas temperature in the first part of the superheater tube bundle. An increase of the live steam temperature by ~30 °C, from 453 °C to 480 °C, leads to a maximum corrosion potential which is 7.4 times higher than that found within the actual state analysis of the plant.

It is proposed that the main corrosion mechanism prevailing is the oxidation by molecular oxygen and hence, time dependent. Therefore, the corrosion rates shown in Table 10 and Figs. 6 to 8 should only be interpreted qualitatively. There might be deviations between the predicted rates according to the empirical model and the corrosion rates found in real CHP plants. Nevertheless, the data gained under well-defined conditions from short-term measurements can be used to determine trends and allow a comparison of different cases.

In general, the danger of a material failure of the superheater tubes under full load conditions can be considered as low. This is in good agreement with long-term observations of the plant operator. Also one can see that corrosion becomes considerably higher when the steam temperatures are increased.

Table 9 – Comparison of the transferred heat by convection and the pressure loss according to the CFD simulation and the calculations based on [16] and [17] for SH3.

	Unit	CFD	Calculations
Flue gas temperature SH entry	°C	646	646
Flue gas temperature SH exit	°C	616	612
Mean surface temperature	°C	480	480
Transferred heat by convection	kW	1678	1528
Pressure loss	Pa	20	40

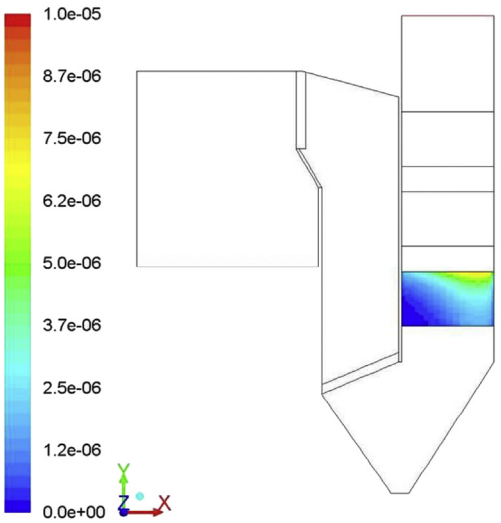

Fig. 12 – Calculated local corrosion potential (mm·h^{-1}) of the superheaters in the symmetry plan of the simulated plant under full load conditions (CS1).

5. Summary and conclusion

To investigate the high-temperature corrosion behavior of superheater tube bundles, online corrosion probe measurements have been carried out in a specially designed fixed bed/drop tube reactor. The investigated boiler steel 13CrMo4-5 is commonly used as steel for superheater tubes in biomass fired heat and power plants. The reactor used allows an independent variation of a single parameter of interest. Therefore, the quality of the measured correlations between the corrosion probe signal and the influencing parameters exceeds those already published. The corrosion probe measurements show a clear dependence on the parameters flue gas temperature and

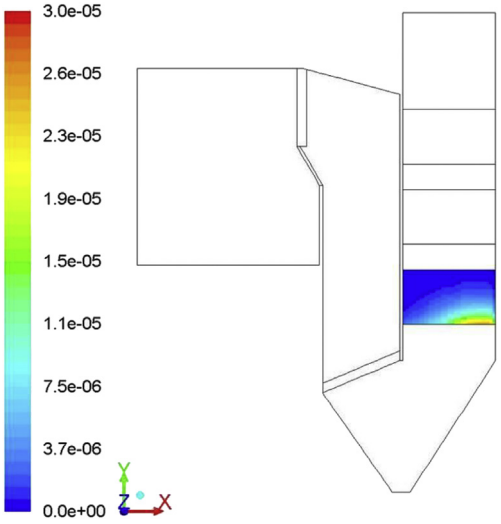

Fig. 13 – Calculated local corrosion potential (mm·h^{-1}) of the superheaters in the symmetry plan of the simulated plant for a changed flow in the final superheater (CS2).

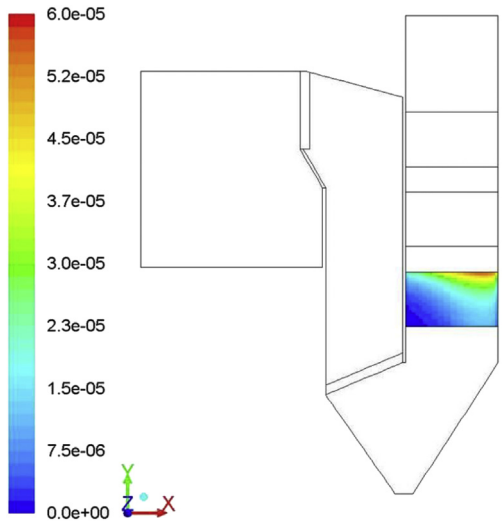

Fig. 14 – Calculated local corrosion potential (mm·h^{-1}) of the superheaters in the symmetry plan of the simulated plant for enhanced steam temperatures (from 453 °C to 480 °C) (CS3).

velocity as well as the steel temperature. The following variations have been carried out to investigate the influence on the corrosion behavior: flue gas temperature between 625 °C and 880 °C, steel temperature from 450 °C to 550 °C and flue gas velocity from 2 m·s^{-1} to 8 m·s^{-1}. Based on the experimental data gained, an empirical function has been developed which is a combination of an Arrhenius function describing the dependence on the flue gas and the steel temperature and a linear dependence on the flue gas velocity. This empirical function is able to reproduce the corrosion potential measured sufficiently accurate. The model is validated for the parameter range investigated within the test runs.

Although the model developed is not able to predict actual corrosion rates due to the fact that the measurement time of the test run has been kept rather short (~300 h), the general dependence on the parameters is comparable to those found during long-term measurements in a real-scale, forest wood chips fired biomass steam boiler [12].

Some restrictions have to be made regarding the applicability of the model. The use of a Cr or Ni rich superheater material can affect the corrosion behavior considerably. The empirical model developed is only validated for low alloy superheater materials such as 13CrMo4-5 or 16Mo3. Furthermore, the corrosion behavior strongly depends on the corrosion mechanism. It is suggested that the main corrosion mechanism prevailing within this work is the oxidation of the steel by molecular oxygen. Deviations in the fuel composition can lead to different corrosion mechanisms such as active Cl-induced corrosion or corrosion by molten salts. Therefore, the application of the model is restricted to chemically untreated wood chips as fuel. To increase the validity range of the model additional measurements with different superheater materials and different types of herbaceous fuels or agricultural residues should be performed.

Table 10 – Maximum values of the calculated corrosion potential for superheater 3.

	Unit	CS1	CS2	CS3
Max(corr.pot.)	mm·h^{-1}	7·10^{-6}	2.5·10^{-5}	5.5·10^{-5}

The newly developed model has been applied within a CFD simulation of flow and heat transfer to calculate the actual local corrosion potential of a biomass fired boiler (38 MW_{th}, 453 °C live steam temperature) under full load conditions. To consider the effects of an inhomogeneous flow field in the heat exchangers on the heat transfer and therefore, the local steel temperatures, a finite cell based heat exchanger model was applied in the CFD simulations. Furthermore, two additional cases have been simulated to determine the influences of enhanced steam temperatures and a switch of the steam flow through the final superheater on the high temperature corrosion potential.

The simulations show a rather low corrosion potential for the final superheater under the actual full load conditions. This is in agreement with long-term observations of the plant operator. Furthermore, the simulations show that an increase of the final steam temperature from 453 °C to 480 °C increases the maximum corrosion potential calculated by a factor of 7.4. A change of the flow direction of the final superheater leads to a 3.4 times higher corrosion potential.

Generally, an evenly distributed flow profile over the cross section of the superheater inlet can reduce the local corrosion potential considerably.

Concluding, the empirical model developed allows a comparison of the local corrosion potential of different live steam temperatures, plant geometries or interconnections of the superheater tube bundles. Furthermore, the empirical model allows for a quick estimation if high temperature corrosion is of relevance for a certain plant or not when using a low alloy steel like 13CrMo4-5 and comparable flue gas compositions.

The model is able to roughly estimate the local corrosion potential together with a CFD simulation of flow and heat transfer in a relatively short time and without detailed knowledge of the underlying chemical processes already in the design phase of a plant and hence is a helpful tool for boiler manufacturers.

Acknowledgments

The financial support by the Austrian Ministry for Transport, Innovation and Technology (BMVIT) (program: ModSim: project number: 828703) as well as by the companies BIOS BIOENERGIESYSTEME GmbH, KWB Kraft und Wärme aus Biomasse GmbH, POLYTECHNIK Luft-und Feuerungstechnik GmbH and Josef Bertsch GmbH & Co. is gratefully acknowledged. The online corrosion probe measurements were performed in cooperation with CORRMORAN GmbH, Germany.

REFERENCES

[1] Li YS, Spiegel M, Shimada S. Corrosion behaviour of various model alloys with NaCl-KCl coating. Mater Chem Phys 2005;93(1):217–23.

[2] Lehmusto J, Lindberg D, Yrjas P, Skrifvars BJ, Hupa M. The role of potassium in high temperature corrosion of superheater steels. In: Electric Power Research Institute 532 (EPRI), editor. Proceedings of the international conference Impacts of Fuel Quality on Power Production and Environment; 23–27 Sept 2012; Puchberg, Austria. Palo Alto, CA: Electric Power Research Institute 532 (EPRI); 2013.
[3] Uusitalo MA, Vuoristo PMJ, Mäntylä TA. High temperature corrosion of coatings and boiler steels below chlorine-containing salt deposits. Corros Sci 2004;46(6):1311–31.
[4] Grabke HJ, Reese E, Spiegel M. The effects of chlorides, hydrogen chloride, and sulfur dioxide in the oxidation of steels below deposits. Corros Sci 1995;37(7):1023–43.
[5] Jonsson T, Folkeson N, Svensson JE, Johansson LG, Halvarsson M. An ESEM in situ investigation of initial stages of the KCl induced high temperature corrosion of a Fe2.25Cr1Mo steel at 400 °C. Corros Sci 2011;53(6):2233–46.
[6] Frandsen FJ. Utilizing biomass and waste for power production - a decade of contributing to the understanding, interpretation and analyses of deposits and corrosion products. Fuel 2005;84(10):1277–94.
[7] Obernberger I, Brunner T. Depositionen und Korrosion in Biomassefeuerungen. In: VDI Wissensforum GmbH, editor. Tagungsband zur VDI-Fachkonferenz: Beläge und Korrosion in Großfeuerungsanlagen; June 2004; Göttingen, Germany. Düsseldorf, Germany: VDI-Wissensforum GmbH; 2004.
[8] Montgomery M, Jensen SA, Borg U, Biede O, Vilhelmsen T. Experiences with high temperature corrosion at straw-firing power plants in Denmark. Mater Corros 2011;62(7):593–605.
[9] Hansen L, Nielsen H, Frandsen F, Dam-Johansen K, Karlsson A. Influence of deposit formation on corrosion at a straw-fired boiler. Fuel Process Tech 2000;64(1):189–209.
[10] Gruber T, Schulze K, Scharler R, Obernberger I. Investigation of the corrosion behaviour of 13CrMo4-5 for biomass fired boilers with coupled online corrosion and deposit probe measurements. Fuel 2015 Mar;144:15–24.
[11] Waldmann B. Korrosion in Anlagen zur thermischen Abfallverwertung: Elektrochemische Korrosionserfassung und Modellbildung [PhD thesis]. Augsburg, Germany: University of Augsburg; 2007.
[12] Retschitzegger S, Brunner T, Obernberger I, Waldmann B. Assessment of online corrosion measurements in combination with fuel analyses and aerosol and deposit measurements in a biomass combined heat and power plant. Energy Fuel 2013;27(10):5670–83.
[13] Maisch S. Identifikation und Quantifizierung von Korrosionsrelevanten Parametern in Müllverbrennungsanlagen mittels Charakterisierung der deponierten Partikel und elektrochemischer Online-Messungen [PhD thesis]. Augsburg, Germany: University of Augsburg; 2011.
[14] Gellings PJ, Tostmann KH. Korrosion und Korrosionsschutz von Metallen: eine Einführung. München, Germany: Carl Hanser Verlag; 1981. ISBN: 3-446-12594-9.
[15] Scharler R, Forstner M, Braun M, Brunner T, Obernberger I. Advanced CFD analysis of large fixed bed biomass boilers with special focus on the convective section. In: ETA-Florence & WIP Munich, editor. Proceedings of the 2nd World Conference and Exhibition on Biomass for Energy, Industry and Climate Protection; 10–14 May 2004; Rome, Italy. Florence, Italy: ETA-Florence; 2004. p. 1357–60. ISBN: 88-89407-04-2.
[16] Idelchik I. Handbook of hydraulic resistance. 3rd ed. New York, USA: Begell House; 1996. ISBN: 1-56700-074-6.
[17] VDI. VDI-wärmeatlas. 10. Auflage. Berlin, Germany: Springer-Verlag; 2006. ISBN: 978-3-540-25504-8.
[18] Zukauskas A, Ulinskas R. High-performance single-phase heat exchangers. Washington DC, USA: Hemisphere Publishing Corporation; 1989. ISBN: 0891167153.

Paper III

Dominating high temperature corrosion mechanisms in low alloy steels in wood chips fired boilers

*Thomas Gruber** [1], *Stefan Retschitzegger* [1], *Robert Scharler* [1], *Ingwald Obernberger* [2, 3]

[1)] BIOENERGY 2020+ GmbH, Inffeldgasse 21b, A-8010 Graz, Austria

[2)] Institute for Process and Particle Engineering, Graz University of Technology, Inffeldgasse 13, A-8010 Graz, Austria

[3)] BIOS BIOENERGIESYSTEME GmbH, Inffeldgasse 21b, A-8010 Graz, Austria

* Telephone: + 43 (0) 316 873-9228, Fax: + 43 (0) 316 873-9202 e-mail: thomas.gruber@bioenergy2020.eu

KEYWORDS: high temperature corrosion, 13CrMo4-5, wood chips, natural gas, oxidation, active Cl-induced oxidation

ABSTRACT

Ash related problems such as slagging, fouling and high temperature corrosion in biomass fired boilers are still insufficiently explored due to the complexity of the underlying processes. Considerable research has already been done to identify the dominating corrosion mechanism when using low alloy steels like 13CrMo4-5 and chemically untreated wood chips as fuel. Up to now no satisfactory answer could be given, although it was suggested that the oxidation of the steel is the dominating mechanism in the material temperature range between 450 °C to 550 °C. To prove this assumption, test runs have been carried out in a specially designed drop tube reactor. To investigate the time-dependent corrosion behavior of 13CrMo4-5, a newly developed mass loss probe was applied under several constant parameter setups. In addition to these measurements, the time-dependent oxidation of 13CrMo4-5 under air was investigated in a muffle furnace. To gain relevant information regarding the corrosion mechanism prevailing, the deposits as well as the corrosion products have been examined subsequently to the test runs by means of scanning electron microscopy and energy dispersive X-ray analyses. With the experimental data gained it could be shown that the dominating corrosion mechanism strongly depends on the conditions prevailing (e.g. steel temperature, flue gas temperature and velocity) and can either be the oxidation of the steel by gaseous O_2 and H_2O or a combination of oxidation and active Cl-induced oxidation.

1. INDRODUCTION AND OBJECTIVES

High temperature corrosion in biomass fired furnaces and boilers is still insufficiently explored due to the complexity of the processes involved. In the last decades the following corrosion mechanisms have been identified as relevant in biomass fired boilers for low alloy steels: hot corrosion type II *(1)*-(*4*), oxidation/scaling of the steel (*5*)-(*7*), active Cl-induced oxidation (*8*),(*9*) and sulfidation corrosion (*10*) of the steel. Additional mechanisms involving the destruction of protective chromium or nickel oxide layers are known for high alloy steels (*11*). A good overview of the possible mechanisms can be found in (*12*).

In a previous work coupled online corrosion probe and deposit probe measurements have been used to investigate the corrosion behavior of the steel 13CrMo4-5 during the combustion of chemically untreated wood chips (*13*). In this work it was concluded that the oxidation of the steel seams to be the main corrosion mechanism prevailing, due to the absence of a molten deposit layer and the missing of chlorine. Thereby, chlorine could neither be detected in the deposits formed on the corrosion probe nor in the corrosion products.

However, the oxidation of iron by gaseous O_2 or H_2O is in general controlled by solid state diffusion of O^{-2} or Fe^{+2} ions (*5*). The temperature of the online corrosion probe is controlled via the steel temperature on the inward air-cooled side of the sample rings. Due to the good heat conductivity of 13CrMo4-5 (38 W/mK at 20°C), the temperature gradient over the sample rings is negligible. Therefore, the outer surface temperature is approximately the same as the

controlled steel temperature on the inside. Therefore, the oxidation rate should be nearly independent of the flue gas temperature and velocity. This is in contrast to the findings of the online corrosion probe test run which showed an exponential dependence on the flue gas temperature and a linear dependence on the flue gas velocity (*13*).

To clarify whether the oxidation of the steel is the main corrosion mechanism prevailing and to validate the corrosion rates measured with the online corrosion probe, additional test runs have been carried out using a newly developed mass loss probe (MLP) (*14*). These tests were carried out in the same coupled biomass packed bed / drop tube reactor as for the earlier online corrosion probe test runs (*13*).

Retschitzegger et al. (*14*) have already performed a test run with the MLP under a constant parameter setup to investigate the initial phase of the high temperature corrosion process using forest wood chips as fuel. The following constant parameter setup was applied in their test run: flue gas temperature at the measurement port of (T_{FG}) 745 ± 13 °C; probe steel temperature (T_S) of 480 ± 1 °C and flue gas velocity (v_{FG}) of 2.7 ± 0.1 m/s.

In the present work, an additional test run was performed to approve that the oxidation of the steel by O_2 and H_2O is the main corrosion mechanism prevailing when firing wood chips. For this test run, the same parameter setup was used, but instead of wood chips natural gas was used as fuel. Natural gas is basically free of the two corrosive species Cl and S. Additionally no dust is formed during the combustion of natural gas. Hence, the formation of a corrosive deposit layer is prevented. Therefore, it is assumed that high temperature corrosion occurring is solely caused by oxidation. In the case of oxidation being the main corrosion mechanism in wood chips fired boilers, this test run and the MLP test run of Retschitzegger et al. should show a comparable corrosion behavior.

In a further test run again forest wood chips have been used as fuel. The flue gas temperature and velocity have been increased compared to the other two test runs. The parameter setup was: T_{FG} = 905 ± 13 °C; T_S = 480 ± 1 °C and v_{FG} = 3.6 ± 0.1 m/s. This test run had the purpose to check if the rate of corrosion truly depends on the flue gas temperature and velocity, which would mean that an additional or another corrosion mechanism then oxidation is the dominating corrosion mechanism prevailing.

Supplementary, the oxidation of 13CrMo4-5 was investigated in a muffle furnace to get a reference value for the mass loss by oxidation over time in an air environment.

Additionally to the time-dependent mass loss the deposits as well as the corrosion products of one sample ring of each test run have been analyzed by means of scanning electron microscopy (SEM) and energy dispersive x-ray (EDX) analyses. This detailed investigation was applied to clarify which corrosion mechanism is dominating for a low alloy steel like 13CrMo4-5 when using chemically untreated woody biomass as fuel.

2. MATERIALS AND METHODS

2.1. Biomass reactor

The mass loss experiments have been carried out using a combined packed bed / drop tube reactor with which well-defined conditions regarding flue gas temperature and composition, typically prevailing in biomass fired boilers, can be achieved. A detailed description of the setup used can be found in (*13*). A schematic view of the reactor is shown in

Figure 1. The setup applied consists of a packed bed reactor (biomass grate furnace with air staging and flue gas recirculation), an additional natural gas burner and an upper transition part to a heated vertical tube with isothermal conditions (the so-called drop tube). The gas burner and

the biomass furnace can each be operated on their own or in combination. The electric heating of the drop tube allows a compensation of the fluctuation of the grate furnace operation and, therefore, to achieve constant and adjustable flue gas temperatures in front of the corrosion probe. Hence, the flue gas temperature can be adjusted independently of the thermal load of furnace and gas burner and therefore, enables corrosion measurements under defined flow and temperature conditions. Finally, the flue gas is transferred via a lower transitional part to a water cooled heat exchanger before it enters the chimney.

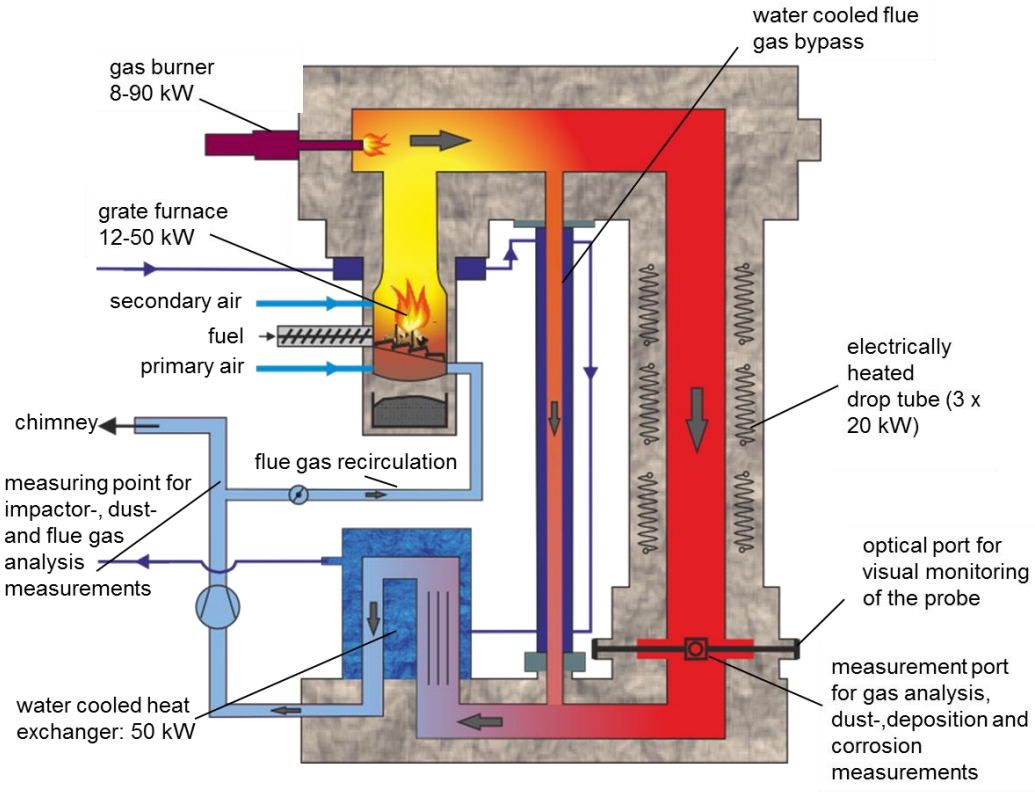

Figure 1: Schematic view of the combined packed bed/drop tube reactor with relevant units and measurement ports. The figure was adapted from (*13*).

2.2. Steel 13CrMo4-5

The material investigated was 13CrMo4-5 (material number 1.7335) which is commonly used as steel for superheater tubes in biomass fired boilers. The composition of this heat resistant ferritic steel can be found in Table 1.

Table 1: Composition of 13CrMo4-5 (1.7335)

Element		C	Si	Mn	P	S	Al	Cu	Cr	Mo	Ni	Fe
min.	[wt-%]	0.10	-	0.40	-	-	-	-	0.70	0.40	-	remaining
max.	[wt-%]	0.17	0.35	0.70	0.025	0.02	0.04	0.30	1.15	0.60	0.30	remaining

2.3. Mass loss probe

To determine the time-dependent mass loss caused by high temperature corrosion a newly developed mass loss probe was inserted into the flue gas of the drop tube reactor. A detailed description of this probe can be found in *(14)*.

The mass loss probe consists of a carrier-lance with five test rings on top, which is cooled by air. The temperature of the sample rings is measured on the inside of a sample ring by a thermocouple. A PID controller regulates the amount of cooling airflow and hence, the steel temperature of the sample rings.

To gain a time-dependent mass loss, the individual test rings are removed from the probe after different times. To determine the mass loss of the test rings, the rings are weighted before being exposed to the flue gas. After the test run, the corrosion products are removed according to ASTM G1-03 and the mass loss is determined gravimetrically.

2.4. Suction pyrometer

To correct the flue gas temperature measured with the reactor internal thermocouples regarding radiation, suction pyrometer measurements according to standards of the International Flame Research Foundation (IFRF) have been performed at the position of the measurement port (see Figure 1).

2.5. Biomass fuel sampling and analysis

To investigate the composition of the wood chips, two representative samples of the fuel were taken during the test run with the elevated flue gas temperatures and velocities. The sample preparation was carried out according to CEN/TS 14780. The ash content is determined according to CEN/TS 14775. The determination of C, H and N is carried out according to CEN/TS 15104:2011 04 01. The chlorine content is determined according to CEN/TS 15289. Major and minor ash forming elements were determined by multi-step pressurized digestion of the fuel with HNO_3 (65%) / HF (40%) / H_3BO_3 followed by measurement by inductively coupled plasma optical emission spectroscopy (ICP-OES) or inductively coupled plasma mass spectroscopy (ICP-MS) depending on detection limits. The moisture content of the fuel sample is determined according to CEN/TS 14774.

2.6. SEM/EDX analyses and sample preparation

To gain more information regarding the structure and the chemical composition of the deposit layer, the oxide layer and the corrosion front, SEM/EDX analyses of the cross section of the MLP sample rings were performed subsequently to each test run. To investigate the elemental distribution, first the ring was embedded in epoxy resin, afterwards the profile was grinded using sand papers until a smooth and plane surface was achieved. The cross sections were prepared under dry conditions without the use of a lubricant. Afterwards, the ring was coated with a thin carbon layer. Between the various steps the probe rings were stored in a desiccator. The systems used for the elemental mappings are a Zeiss Ultra 55 field emission scanning electron microscope equipped with an EDAX Pegasus X-ray analysis system. Within these mappings, the oxygen content was measured and not stoichiometrically calculated to detect oxides and to achieve a clear separation between the corrosion layer and the original steel surface. The elemental mappings show the relative distribution of each element over the area investigated. Thereby, bright colors mean a high concentration whereas a weak color represents a low concentration of the element.

An accelerating voltage of 12 kV was used for the analyses to minimize the damage on the deposits caused by the electron beam. However, because of the limited resolution of the energy-dispersive spectrometer (EDS) the exited S K-line, Pb M-line and Mo L-line are overlapping in the spectrum. Hence, these elements are hard to distinguish accurately, especially if only small amounts of these elements are present. Also the accuracy of the quantitative analyses of these elements is limited.

2.7. Test runs and operating conditions

Within the work presented two test runs have been carried out to identify the dominating corrosion mechanism prevailing when using 13CrMo4-5 as a boiler steel and chemically untreated wood chips as fuel in the steel temperature range between 450 °C to 550 °C.

The results of these two test runs have been compared to those obtained from Retschitzegger et al. *(14)*. In the test run of Retschitzegger et al. the MLP has been used together with an online corrosion probe to investigate the influence of temperature variations on the high temperature corrosion rate. In this test run chemically untreated wood chips have been used as fuel. The test run has been divided in two parts. The following constant parameter setup was applied in the first part of the test run: T_{FG} = 745 ± 13 °C; T_S = 480 ± 1 °C and v_{FG} = 2.7 ± 0.1 m/s.

In the second phase, the so-called variation phase, the flue gas temperature has been varied between 740 and 865 °C by electric heating of the drop tube. For each flue gas temperature the probe surface temperatures have been varied between 400 and 550 °C. The results of the MLP for the constant parameter setup in the first part of the test run have been used for comparison in this work. The effect of parameter variations on the high temperature corrosion as well as a detailed description of the experimental setup can be found in *(14)*. Relevant operating data of this test run are summarized in Table 2.

In the first test run of this work the drop tube reactor was operated using natural gas as fuel. Here, only the MLP was used to investigate the time dependent corrosion behavior. The same constant parameter setup as the one used by Retschitzegger et. al. *(14)* was used. Since natural gas is basically free of Cl and S, it is assumed that corrosion occurring in this case is solely caused by the oxidation of the low alloy steel by gaseous O_2 or H_2O. In the case of oxidation being the main corrosion mechanism both test runs should show a comparable corrosion behavior. Since the combustion of natural gas is basically free of dust emissions 54 mg/Nm³ (related to 13% O_2 and dry basis) of powdery $Ca(OH)_2$ were injected into the flue gas. The powder injected had the following particle size distribution: D10% = 1.1 µm, D50% = 5 µm, D90% = 15 µm. Due to this measure the dust concentrations and in the following the deposit build-up and hence, heat transfer on the MLP probe of the test campaigns became more comparable. In the temperature range and conditions prevailing it is assumed that $Ca(OH)_2$ forms an inert deposit layer due to the absence of a liquid phase. To ensure this, SEM/EDX measurements of the probe ring cross section have been performed (see Section 3.3).

In the second test run, again forest wood chips have been used as fuel. The flue gas temperature and velocity have been increased compared to the other two test runs. The parameter setup in the second test run was: T_{FG} = 905 ± 13 °C; T_S = 480 ± 1 °C and v_{FG} = 3.6 ± 0.1 m/s. The fuel used in this test run was chemically untreated forest wood chips mainly consisting of spruce. The biomass mainly consists of logging residues, but also contains bark, stem wood as well as a low fraction of fine particles and needles. The biomass originated from a local supplier close to Graz, Austria and was harvested within a radius of approximately 50 km around Graz. The fuel had the following specifications according to EN 14964-1:2010: origin … 1.1.4.4 and 1.1.4.5; particle … P45Ac; moisture … M35; ash … A2.0; bulk density …. BD200.

The fuel composition is presented in Table 3. If oxidation is the dominating corrosion mechanism, the results of this test run should be comparable to the other two MLP test runs performed in the fixed bed drop tube reactor.

Table 2: Relevant operating conditions of the drop tube reactor and the mass loss probe
Explanations: Nm³ … m³ at 0 °C and 101 325 Pa; T_{FG} … flue gas temperature at measurement port; v_{FG} … flue gas velocity at entrance of measurement port; T_S … probe surface temperature; d.b. … dry basis; w.b. … wet basis;

		Retschitzegger et. al. *(14)*	gas burner	wood chips with elevated flue gas velocity/temperature
parameter	unit	mean value ± standard deviation	mean value ± standard deviation	mean value ± standard deviation
fuel power related to NCV	kW	23.2 ± 2.1	22.6 ± 0.2	24.0 ± 1.9
O_2	vol.% d.b.	8.6 ±1.6	13.1 ± 0.8	10.3 ± 0.9
CO_2	vol.% d.b.	12.0 ±1.6	7.4 ± 0.8	9.9 ± 0.9
CO	mg/Nm^3 d.b.	3.1 ± 2.1	0.2 ± 0.1	10.8 ± 5.1
H_2O	vol.% w.b.	15.4	7.7	11.6
T_{FG}	°C	745 ± 13	734 ± 4	905 ± 13
v_{FG}	m/s	2.7 ± 0.1	2.8 ± 0.1	3.6 ± 0.1
T_S	°C	480 ± 0.1	480 ± 0.1	480 ± 0.1

2.8. Oxidation of the steel in a muffle furnace

In addition, the mass loss of 13CrMo4-5 by oxidation was investigated using a *Carbolite AAF 11/18* muffle furnace to get a reference value for the mass loss over time by oxidation in an air environment. The oxide formation and hence, mass loss of steel was determined in the same way as described in Section 2.3. The muffle furnace was operated at a constant temperature of 480 °C during the test run. The water content varied between 1-2 vol-% wet basis depending on the weather conditions and humidity of the surrounding air. Ambient air circulation occurred due to natural convection via a small chimney in the muffle furnace.

3. RESULTS AND DISCUSSION

3.1. Fuel analyses

Two fuel samples have been taken during the test runs to investigate the fuel composition. The obtained fuel composition is given in Table 3.

The analyses confirm that the fuel used in the biomass fired test run is comparable to the fuel used by Retschitzegger et al. within the deviations typical for biomass fuels. The corrosion potential of a fuel correlates to the molar 2S/Cl ratio (see (*15*)-(*17*)). According to this basic fuel characterization method fuels with a 2S/Cl ratio below 2 are assumed to cause severe corrosion. The general corrosion potential for the wood chips used can be considered as low.

Table 3: Results of fuel analyses
Explanations: w.b. … wet basis; d.b. … dry basis; std.-dev. … standard deviation; mean … mean value; data from Retschitzegger et al. is adapted from *(14)*.

		Retschitzegger et.al.		wood chips elevated flue gas velocity/temperature	
		n=4		n=2	
		mean	std-dev	sample 1	sample 2
moisture content	wt% w.b.	31.6	3.9	28.4	33.2
ash content	wt% d.b.	2.7	1.2	1.4	1.9
C	wt% d.b.	48.1	0.4	49.8	49.7
H	wt% d.b.	6.0	0.1	6.0	6.0
N	wt% d.b.	0.3	0.1	0.2	0.1
S	mg/kg d.b.	262	70	144	198
Cl	mg/kg d.b.	117	71	52	58
Si	mg/kg d.b.	3654	3009	408	840
Ca	mg/kg d.b.	4723	1207	3590	5340
Mg	mg/kg d.b.	614	193	451	372
K	mg/kg d.b.	1875	449	1360	1250
Na	mg/kg d.b.	128	92	34	41
P	mg/kg d.b.	242	71	129	172
Al	mg/kg d.b.	615	424	126	241
Fe	mg/kg d.b.	313	237	72	143
Mn	mg/kg d.b.	88	26	46	160
Zn	mg/kg d.b.	15	5	12	14
Pb	mg/kg d.b.	4	5	3	4
2S/Cl ratio	mol/mol	7.6	2.7	6.1	7.5

3.2. Mass losses

The mass losses of the steal obtained within the two drop tube reactor test runs and the muffle furnace test run as well as the findings of Retschitzegger et al. are presented in Figure 2. The measured data has been fitted using a parabolic function and standard least square method to highlight the parabolic character of measurement data.

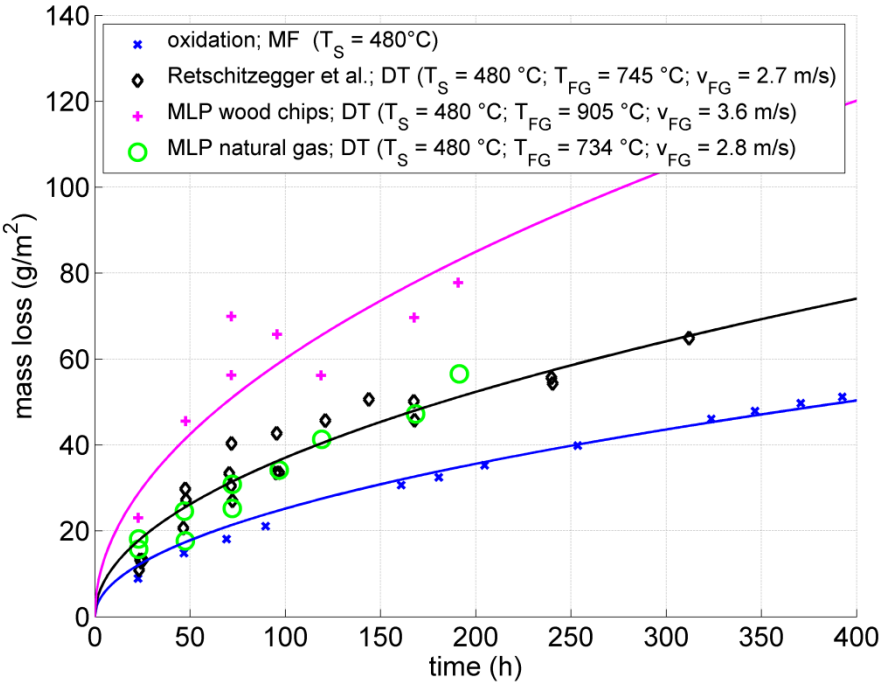

Figure 2: Mass loss for various test runs as a function of time.

Explanation: MLP … mass loss probe; T_S … steel surface temperature; T_{FG} … flue gas temperature; MF … muffle furnace; DT … drop tube reactor, solid lines … parabolic fit

One can clearly see that the mass loss in the muffle furnace test is the smallest. In the MLP test runs the same parameter setup for wood chips and natural gas: T_S = 480°C, T_{FG} ~ 740 °C and v_{FG} ~ 2.8 m/s leads to approximately the same mass loss over time. Finally, the test run with wood chips and elevated flue gas temperatures and velocities produces significantly higher mass losses. The findings are discussed in detail in Section 3.4.

3.3. Analyses of deposit and corrosion layer

The corrosion behavior of the steel is not solely determined by the chemical composition of the deposits formed on a superheater tube. Also the structure and porosity as well as the aggregate state of the deposit have a considerable effect on the heat transfer and the high temperature corrosion behavior. Here, higher deposit temperatures might not only enhance the speed of corrosion, but lead also to other or additional corrosion mechanism (e.g. hot corrosion). Pictures of the deposits formed on the MLP during the various test runs are shown in Figure 3. One can see that the deposits on the windward side have a comparable thickness in all cases investigated. Although the duration of the test run of Retschitzegger et al. was nearly 2.5 times longer than

those of the two MLP test runs performed within this work. This can most certainly be explained by the fact that the deposits formed on the windward side of the probe are all powdery and loosely bound to the MLP and no sintering occurred. Therefore, the deposits can easily be degraded by the flue gas flow (erosion of the deposit layer) as well as during the changing procedure of the mass loss probe rings.

In the case of the wood chips test runs, the leeward side of the probe was covered with a thin layer consisting of condensed ash vapors. This layer is missing in the case of the gas burner test run, due to the missing ash forming vapors.

In addition, the $Ca(OH)_2$ injected into the flue gas during the gas burner test run does not form the same uniformly shaped deposit layer as those formed during the two wood chips test runs. However, since the deposits formed on the MLP are generally thin, it is expected that this has only a weak influence on the overall corrosion behavior.

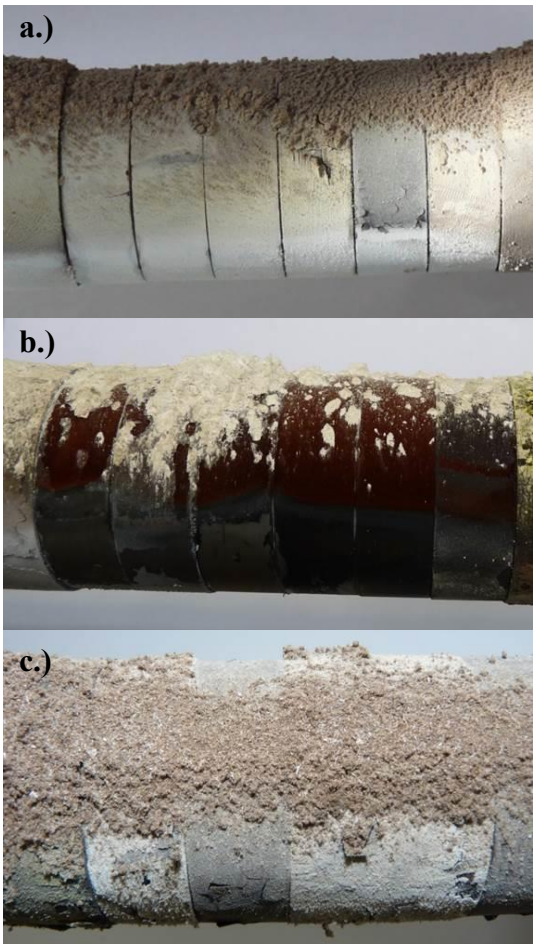

Figure 3: Photos of the MLP after the test runs: a.) wood chips as fuel; T_{FG} ~ 740 °C; T_S = 400-550 °C; v_{FG} ~ 2.7 m/s; maximum test run duration = 480 h; profile view b.) gas burner ;: T_{FG} ~ 740 °C; T_S = 480 °C; v_{FG} ~ 2.8 m/s; maximum duration = 192 h; profile view c.) wood chips: T_{FG} ~ 900 °C; T_S = 480 °C; v_{FG} ~ 3.6 m/s; maximum duration = 191 h; top view

To gain information regarding the chemical composition and structure of the corrosion products and the deposit layer, SEM/EDX element mappings have been carried out on the windward, windward + 50 and leeward side of a MLP probe ring. The results of these analyses

are presented in Figure 4. Since the general information obtained for the various ring sides is similar, only the results of the leeward side are shown.

The deposits formed in the test run of Retschitzegger et al. consist mainly of K_2SO_4 (see Figure 4, left). This is in good agreement with similar measurements (see (*13*)). In addition, also small fractions of Si and Ca oxides originating from coarse fly ash particles can be found. No traces of chlorine can be attested neither in combination with potassium nor with iron which is often reported in the case of active Cl-induced oxidation being the main corrosion mechanism *(8)*,*(9)*. Therefore, one can only see the equally distributed background noise of the EDX analysis in the Cl mappings. Sulfur can be found in two combinations. In the deposit sulfur coexists in combination with potassium and oxygen which indicates the presence of K_2SO_4. At the corrosion front, sulfur can also be found in combination with iron. These findings are in agreement with those of (*13*).

In the case of the gas burner test run (see Figure 4, middle), the only dust source available is the injected $Ca(OH)_2$. One can see in Figure 3, that the coarse fly ash, respectively the $Ca(OH)_2$ is solely located on the windward side ± 50 ° of the MLP. Hence, only traces (lower 1 Atomic-%) of Ca can be found on the leeward side of the sample ring. The Si spots most likely originate from the sandpaper used for the grinding process. As already mentioned an acceleration voltage of 12 kV has been used for the SEM/EDX analyses. The low acceleration voltage makes a correct analysis of the elements S, Mo and Pb hardly possible. Especially when only traces (< 1 at-%) of the elements are present, as in the current case. However, the bright spots in the S/Mo/Pb mapping most likely originate from Mo since Mo is part of the steel 13CrMo4-5 (see Table 1). Further, the elements S and Pb are not or only in traces present in the flue gas of the gas burner test campaign.

The results of the test run with wood chips at elevated flue gas temperature and velocity are presented in Figure 4 on the right side. One can see, that also in this case the outer deposit layer mainly consists of K_2SO_4. However, the inner deposit layer is clearly made of KCl. Si and Ca can only be found in local spots. These findings and their impact on the corrosion mechanism are discusses in detail in Section 3.4.

3.4. Corrosion Mechanism

- Oxidation of the steel 13CrMo4-5 in air environment

In the last decades considerable research has been done to investigate and identify the processes occurring during the oxidation of iron. It is generally accepted that solid state diffusion is the rate limiting process during the oxidation of iron *(5)-(7)*. Further it is known that such processes show a strong dependence on the steel temperature and generally follow an Arrhenius law *(5)-(7)*. According to *(6)* both iron and carbon steels show a comparable oxidation behavior. In addition, a “general rule” exists that iron based alloys containing less than 2 wt-% Cr show a similar oxidation behavior than iron *(7)*, since the Cr content is too low to form a passivating Cr_2O_3 layer (*18*). Hence, the oxidation behavior of 13CrMo4-5 should be comparable to those of iron in a first approximation.

In general diffusion controlled processes are characterized by parabolic kinetics. Hence, the rate of oxidation is very fast in the beginning, but significantly slows down with increasing thickness of the oxide layers. One can see in Figure 2 that the oxidation behavior of the steel 13CrMo4-5 found within the muffle furnace experiments indeed follows such a parabolic rate law.

In the temperature range relevant for high-temperature corrosion in biomass fired boilers (<570 °C) the oxidation of iron produces a relatively thin Fe_2O_3 (hematite) layer on top of a thicker Fe_3O_4 (magnetite) layer *(19)*. Hence, the growth rate is mainly dominated by the

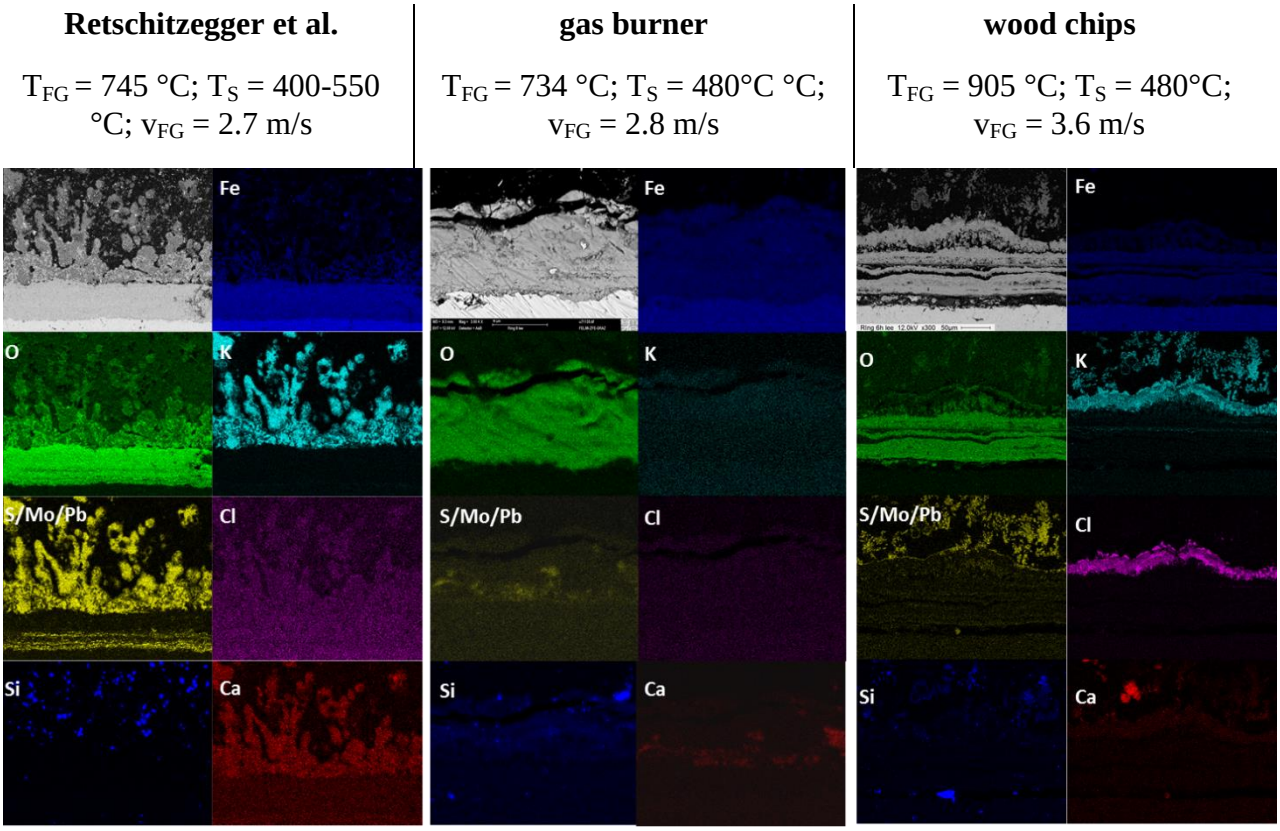

Figure 4: EDX elemental mappings of the deposit and corrosion layer on the leeward side of the MLP sample rings for the test runs: Retschitzegger et al. (left), gas burner (middle) and wood chips at elevated temperatures and velocities (right).

formation of magnetite. According to *(5)* the formation of the magnetite layer is limited by the outward diffusion of iron ions. Due to this, the rate of iron oxide formation below 570 °C hardly depends on the oxygen content of the flue gas. This was also experimentally validated for various carbon steels at 500 °C for oxygen pressures between 0.013 atm and 0.92 atm *(20)*. Due to the comparable oxidation behavior of iron, carbon and low alloy steels also the oxidation behavior of 13CrMo4-5 in the boiler sections of biomass fired boilers should be nearly independent of the oxygen content of the flue gas.

Since the trend found within the muffle furnace experiments is comparable to those of iron also modelling approaches such as the theory of Wagner *(5),(21)* can be used as a first approximation to describe the growth of iron oxide on 13CrMo4-5 in the temperature range of interest. A detail discussion on the oxidation of iron and the modelling approach of Wagner can be found in *(5)*.

- Influence of water vapor on high temperature corrosion

As shown in Figure 2 the mass loss of the two MLP test runs (parameter setup: T_S = 480 °C, T_{FG} ~ 740 °C and v_{FG} ~ 2.8 m/s) exceeds that of the muffle furnace significantly. The negligible temperature gradient over the sample ring as well as the different oxygen content in the gas environment in the case of the MLP test runs are not accountable for this difference as already discussed earlier. Another difference between the muffle furnace experiments and the drop tube reactor experiments is the higher water content of the gas environment of the MLP test runs (see Table 2).

It was already shown that the oxidation rate of iron in the presence of water vapor can significantly be increased compared to the oxidation in dry atmosphere *(22)*. The influence of water vapor on the oxidation behavior was investigated using the following two atmospheres *(22)*: O_2 = 5 vol-%, H_2O = 40 vol-%, N_2 = 55 vol-% and O_2 = 5 vol-%, H_2O = 0 vol-%, N_2 = 95 vol-%. The measured increase of the oxidation rate, between the two gas atmospheres investigated, thereby strongly depended on the temperature prevailing. It hardly had an effect at 400 °C, while it increased the parabolic rate constant at 600 °C by a factor of 2.5. In *(22)* it is argued that the presence of the water vapor leads to the formation of hematite whiskers. Further it is argued that these whiskers have a high density of grain boundaries. Due to this grain boundary diffusion most likely becomes the dominating transport mechanism, which results in a faster transport of the iron cations and in further consequence in increased oxidation rates. Although, the amount of water vapor in the gas atmosphere used in *(22)* is considerably higher than those of the MLP test runs performed within this work, the basic mechanism proposed in *(22)* should generally be transferable to the work presented.

Hence, it is proposed that the enhanced water vapor content in the flue gas is responsible for the higher oxidation rates of 13CrMo4-5 in the MLP test runs compared to the oxidation rates determined in the muffle furnace.

- Influence of HCl on high temperature corrosion

The concentration of HCl in the flue gas is typically very low (< 10 ppm) when chemically untreated wood chips are used as fuel *(13)*, which minimizes the danger of active Cl-induced corrosion caused by gaseous chlorides *(23)*. However, according to the knowledge of the authors no studies are available which have investigated the influence of HCl on the high temperature corrosion of low alloy steels or iron. Due to the very low concentrations of HCl it seems plausible that the influence of gaseous HCl on the overall corrosion behavior is negligible.

- Influence of KCl on high temperature corrosion

As discussed in the previous section, the differences between the muffle furnace test run and the two MLP test runs in the drop tube reactor can most probably be explained with the different water contents in the gas environment. However, the water and oxygen contents in the flue gas of the different MLP test runs are comparable (see Table 2). Therefore, it is assumed that a different O_2 and H_2O content of the flue gas is not responsible for the higher mass losses obtained in the case of the MLP test run with elevated flue gas temperatures and velocities. Similar combustion conditions and chemically untreated wood chips with comparable chemical compositions have been used in both test runs. Hence, it is argued that different compositions of the flue gas should also not be responsible for the different corrosion behavior found within the two test runs. Furthermore, an increased steel temperature caused by the increased heat flux can be excluded as

reason for the higher mass loss as already discussed in the introduction of this work. Therefore, it can only be explained by a significant speed-up of a process in the deposit layer.

It is known that solid K_2SO_4, the main component of the deposit layer, has only a minor effect on the corrosion behavior under the framework conditions investigated *(12)*. The only known mechanism involving sulphates is hot corrosion type II which requires a molten deposit layer. Due to the absence of such a molten deposit layer, this mechanism can be excluded.

In order to investigate the chemical composition and structure of the initially formed deposit layer, short term deposit probe measurements have been carried out in earlier work (see (*13*)).

These deposit probe measurements confirmed that the layers mainly consisted of potassium sulphate. Chlorine could be found in small amounts in the case of 480 °C steel temperature. No chlorine could be found in the test run with a steel temperature of 550 °C. This indicates that the condensation temperature of the gaseous chlorides lies somewhere between 480 °C and 550 °C which is also in good agreement with results obtained from chemical equilibrium calculations.

As already mentioned no traces of chlorine could be found neither in the final deposit nor in the final corrosion layer of the test runs performed by Retschitzegger et al. (see Figure 4, left). This is in agreement with other work performed using a similar experimental setup (*13*). There it was argued that the condensed chlorine species in the initial state of the test runs get sulphated and that the supply of chlorine species cannot be maintained due to increasing surface temperatures over time.

In the MLP test run with elevated flue gas temperatures and velocities a layer of KCl was found on top of the corrosion products formed (see Figure 4). The existence of this KCl layer is assumed to be the result of multiple factors.

The higher temperature gradient and flue gas velocity lead to a higher heat transfer coefficient. As a result also the mass transfer coefficient was increased according to the Lewis analogy. Hence, the condensation of gaseous KCl was enhanced in the case of the MLP test run with elevated flue gas temperatures and velocities. In addition, the surface temperature of the deposit was probably always below the condensation temperature of KCl. Therefore, the supply of KCl was possible throughout the entire test run. Furthermore, in the test run of Retschitzegger et al. *(14)* steel temperature variations up to 550 °C have been performed after the initial phase (see Section 2.7) whereas the MLP was operated at a constant steel temperature of 480 °C. Since the condensation temperature of KCl lies somewhere between 480 and 550 °C, it is most likely that the condensed KCl became evaporated during the temperature variations performed in the test run of Retschitzegger et al *(14)*.

Many authors (e.g. *(8)*,*(9)*) reported a compact inner corrosion layer, consisting of $FeCl_2$, in the case of active Cl-induced oxidation. Although no $FeCl_2$ could be found at the corrosion front, the presence of KCl and the significantly increased mass loss in the case of enhanced flue gas temperatures and velocities lead to the assumption that active Cl-induced oxidation is an additional corrosion mechanism prevailing for this test.

Active Cl-induced oxidation can be ruled out as corrosion mechanism in the case of the natural gas MLP test run. Since the corresponding MLP test run shows a very similar corrosion behavior as the one with wood chips for the same parameter setup, it is concluded that the influence of active Cl-induced oxidation strongly increases with increasing flue gas temperature. Due to the low heat conductivity of the deposit layer *(25)*, an increased heat flux, caused either by a higher flue gas temperature or velocity, leads to increased temperatures in the deposit layer. It is known that the sulphation process of KCl follows an Arrhenius law *(26)*,*(27)*. Hence, the release rate of Cl, due to the sulphation of KCl, will strongly increase with increasing temperatures of the

deposit layer. The released chlorine is then able to cause active Cl-induced oxidation and therefore, accelerate the overall high temperature corrosion rate considerably (see Figure 2). Thereby, it is assumed that the severity of corrosion caused by active Cl-induced corrosion is proportional to the amount of chlorine released near the steel surface and therefore, strongly increases with rising deposit temperature

- Corrosion mechanism prevailing

Based on the findings presented it is suggested that the overall high temperature corrosion results from a combination of the two well-known mechanisms oxidation and active Cl-induced oxidation. From literature it is known that the oxidation of the steel is mainly influenced by the steel temperature and follows parabolic kinetics *(5)*. Due to this it is concluded, that the oxidation of the steel is similar in all three MLP test runs. Hence, the increased mass loss, found in the test run with the elevated temperatures, is presumably solely caused by an increased share of active Cl-induced oxidation.

The combined mechanism proposed is only possible as long as a source of chlorine, e.g. KCl, is available in the deposits. As already discussed, it is most certain that already deposited KCl evaporates at higher temperatures and the condensation of new KCl may be suppressed. In this case the high temperature corrosion should be dominated by the oxidation of the metal. Additional test runs using natural gas and wood chips as fuels should be carried out at steel temperatures above the condensation temperature of KCl to confirm this assumption.

With the explanation of a combined corrosion mechanism consisting of oxidation and active Cl-induced oxidation the dependence on the flue gas temperature and velocity, reported in *(13)* becomes plausible. Both parameters considerably influence the heat flux and hence, the temperature profile in the deposit layer, which in further progress leads to a significant speed up of the overall corrosion process.

4. SUMMARY AND CONLCUSION

Earlier high temperature corrosion measurements performed in a coupled biomass fired drop tube reactor (*13*),*(28)*(28) led to the assumption that the oxidation of the steel by O_2 and H_2O is the dominating corrosion mechanism for the steel 13CrMo4-5 in the steel temperature range between 450 °C – 550 °C, when firing chemically untreated wood chips. However, the exponential dependence of the corrosion rate on the flue gas temperature, respectively the linear dependence on the flue gas velocity cannot be explained with the oxidation of the steel being the main corrosion mechanism. To identify the dominating corrosion mechanism two additional test runs have been carried out in the same reactor, using a newly developed mass loss probe. In addition the oxidation of the steel under air environment as a reference value has been investigated in a muffle furnace. In these test runs the time dependent mass loss of steel was determined and the deposit and corrosion products formed have been analyzed using SEM/EDX.

The mass losses and SEM/EDX analyses of the deposit and corrosion layers from these test runs lead to the following results:

- The oxidation of the low alloy steel depends on the H_2O content of the atmosphere. This result is in good agreement with other literature.
- For the fuel chemically untreated wood chips in the steel temperature range between 480 °C and 550 °C under the framework conditions used within this work it is proposed that the overall corrosion behavior is determined by a combination of the two corrosion mechanisms oxidation and active Cl-induced oxidation.

- The share of active Cl-induced oxidation strongly increases with increasing deposit temperatures. Thereby, the deposit temperature can be considerable influenced by the local heat flux and hence, local temperature gradient as well as the flue gas velocity.
- Within the combined mechanism proposed, the strong dependence of the corrosion rate on the flue gas temperature and velocity found in earlier work *(13),(14),(28)* becomes plausible.
- Condensed KCl in the deposits represents the main source of Cl needed for active Cl-induced oxidation. However, the appearance of KCl in the deposits depends on various parameters. The condensation temperature of KCl lies between 480 °C and 550 °C, under the framework conditions investigated. Hence, the supply of KCl from the flue gas is suppressed as soon as the deposit surface temperature exceeds the condensation temperature of KCl.
- Further it is suggested that no KCl could be detected in earlier work *(13),(14),(28)*, since the steel temperature variations performed exceeded the condensation temperature and hence, led to evaporation of the condensed KCl from the deposit layer.

Even though the model proposed is able to explain the measurement results found, it is suggested to perform additional measurements using both wood chips and natural gas as fuel at higher steel temperatures to confirm the model. If the surface temperature exceeds the condensation temperature of KCl throughout the test run, both mass losses found should be caused by oxidation and hence, be similar.

5. ACKNOWLEDGEMENTS

The financial support by the Austrian Ministry for Transport, Innovation and Technology (BMVIT) (programme: ModSim: project number: 828703) as well as by the companies BIOS BIOENERGIESYSTEME GmbH, KWB Kraft und Wärme aus Biomasse GmbH, POLYTECHNIK Luft- und Feuerungstechnik GmbH and Josef Bertsch GmbH & Co. is gratefully acknowledged.

6. REFERENCES

(1) Rapp, RA. Hot corrosion of materials: a fluxing mechanism? *Corrosion Sci.* **2002**, *44 (2)*, 209-221.

(2) Zhang, Y; Wu, W. Summary of studies on hot corrosion of iron-based alloys by sodium sulfate in O2/SO2/SO3 environment. *J. Phys. IV* **1993**, *3 (C9)*, 319-326.

(3) Spiegel, M. Salt melt induced corrosion of metallic materials in waste incineration plants. *Mater. Corros.* **1999**, *50 (7)*, 373-393.

(4) van Lith, S; Buchardt, C; Frandsen, FJ. Final report (D20) for SES6-CT-2003-502679: Ash and aerosol related problems in biomass combustion and cofiring (BIOASH), task 2.3: Lab-scale investigation of the potential for corrosion of deposits. CHEC Research Centre, Technical University of Denmark, Denmark; **2007**.

(5) Atkinson, A. Transport processes during the growth of oxide films at elevated temperature. *Rev. Mod. Phys.* **1985**, *57 (2),* 437-470.

(6) Chen, R; Yeun W. Review of the High-Temperature Oxidation of Iron and Carbon Steels in Air or Oxygen. *Oxid. Met.* **2003**, *59 (3)*, 433-468.

(7) Schütze, M. Corrosion and environmental degradation, 2nd Vol. Weinheim, Germany: *Wiley VCH* **2000**. ISBN 9783527299713

(8) Reichel, H; Schirmer, U. Waste incineration plants in the FRG: construction, materials, investigation on cases of corrosion. *Mater. Corros.* **1989**, *40*, 135-141.

(9) Nielsen, HP; Frandsen, FJ; Dam-Johansen, K; Baxter LL. The implications of chlorine-associated corrosion on the operation of biomass-fired boilers. *Prog. Energy Combust. Sci.* **2000**, *26*, 283-298.

(10) Gesmundo, F; Young, DJ; Roy, SK. The high temperature corrosion of metals in sulfidizing–oxidizing environments: a critical review. *High Temp. Mater. Processes* **1989**, 8, 149-189.

(11) Pettersson, J; Asteman, H; Svensson, JE; Johansson, LG. KCl induced corrosion of a 304-type austenitic stainless steel at 600 °C; the role of potassium. *Oxid. Met.* **2005**, 64, 23-41.

(12) Antunes, RA; de Oliveira, MCL. Corrosion in biomass combustion: a materials selection analysis and its interaction with corrosion mechanisms and mitigation strategies. *Corrosion Sci*. **2013**, *76*, 6-26.

(13) Gruber, T; Schulze, K; Scharler, R; Obernberger, I. Investigation of the corrosion behavior of the 13CrMo4-5 for biomass fired boilers with coupled online corrosion and deposit probe measurements. *Fuel* **2015**, *144*, 15-24.

(14) Retschitzegger, S; Gruber, T; Brunner, T; Obernberger, I. Improvement of the accuracy of short-term corrosion probe measurements by addition of a mass-loss probe. *Fuel Process. Technol.* **2015**, 137, DOI:10.1016/j.fuproc.2015.03.026

(15) Sommersacher, P.; Brunner, T.; Obernberger, I. Fuel Indexes: A Novel Method for the Evaluation of Relevant Combustion Properties of New Biomass Fuels, *Energy Fuels* **2012**, 26, 380-390.

(16) Salmenoja, K. Field and laboratory studies on chlorine-induced superheater corrosion in boilers fired with Biofuels, Ph.D. Dissertation, Abo Akademi, Abo/Turku, Finland, **2000**.

(17) Krause, H. H. Corrosion by Chlorine in Waste Fuelled Boilers, Presented at International Conference on Fireside Problems while Incinerating Municipal and Industrial Waste, Palm Coast, FL, USA, **1989**.

(18) Werner, E; Kalpakjian, S; Schmid, SR. Werkstofftechnik. 5. Auflage. Munich, Germany: *Pearson Studium* **2011**. ISBN: 978-3868940060.

(19) Birks, N; Meier, G; Pettit, F. Introduction to High Temperature Oxidation of Metals. Cambridge, England: *Cambridge University Press* **2006**. ISBN-13 978-0-521-48042-0.

(20) Boggs, WE; Kachik, RH. The oxidation of iron-carbon alloys at 500 °C. *J. Electrochem. Soc.* **1969**, 116, 424-430.

(21) Wagner, C. Beitrag zur Theorie des Anlaufvorgangs, *Z. Phys. Chem.* **1933**, B41, 25-42.

(22) Pujilaksono, B; Jonsson, T; Halvarsson, M; Svensson, JE; Johansson, LG. Oxidation of iron at 400-600 °C in dry and wet O_2. *Corrosion Sci.* **2010**, 52, 1560-1569.

(23) Grabke, HJ; Spiegel, M; Zahs, A. Chloridation and oxidation of iron, chromium, nickel and their alloys in chloridizing and oxidizing atmospheres at 400±700°C. *Corrosion Sci.* **2000**, 42, 1093-1122.

(24) Gellings, PJ; Tostmann, KH. Korrosion und Korrosionsschutz von Metallen: eine Einführung. München, Germany: *Carl Hanser Verlag* **1981**. ISBN: 3-446-12594-9.

(25) EU project no.SES-CT-2003-502679, BIOASH – Ash and aerosol related problems in biomass comubstion and co-firing. Publishable final activity report. Project coordinator: Ingwald Obernberger, TU Graz, Graz, Austria **2007**.

(26) Boonsongsup, L; Iisa, K; Frederick, WJ. Kinetics of the Sulfation of NaCl at Combustion Conditions. *Ind. Eng. Chem. Res.* **1997**, *36*, 4212-4216

(27) Matsuda, H; Ozawa, S; Naruse, K; Ito, K; Kojima, Y; Yanase, T. Kinetics of HCl emission from inorganic chlorides in simulated municipal wastes incineration conditions. *Chem. Eng. Sci.* **2005**, *60*, 545-552

(28) Retschitzegger, S; Brunner, T; Obernberger, I; Waldmann, B. Assessment of online corrosion measurements in combination with fuel analyses and aerosol and deposit measurements in a biomass combined heat and power plant. *Energy Fuels* **2013**, 27, 5670–5683.